EPFL

Thèse n° 9296

An integrative approach to elucidate the mechanisms and dynamics of Huntingtin aggregation and inclusion formation in neuronal models of Huntington's Disease

Présentée le 18 février 2022

Faculté des sciences de la vie
Laboratoire de neurobiologie moléculaire et neuroprotéomique
Programme doctoral en neurosciences

pour l'obtention du grade de Docteur ès Sciences

par

Nathan Alain Denis RIGUET

Acceptée sur proposition du jury

Prof. B. D. McCabe, président du jury
Prof. H. Lashuel, directeur de thèse
Prof. L. M. Thompson, rapporteuse
Prof. E. E. Wanker, rapporteur
Prof. A. Radenovic, rapporteuse

École polytechnique fédérale de Lausanne

2022

Acknowledgments

First and foremost, I would like to thank and express my sincere gratitude to my advisor Professor **Hilal A. Lashuel,** for his continuous support, mentorship and great scientific guidance during my Ph.D. He first placed his confidence in me when I joined the lab for my master thesis internship. I did not have a lot of experience at the time, but he trusted my motivation and enthusiasm to accept me in the lab and to conduct scientific research. During my PhD., he was always supportive by giving inputs and new ideas. It is always a bit frustrating to receive extra comments and additional suggestions after hard and dedicated work, but it defines the rigorous and meticulous critical thinking that Hilal taught me, and is crucial in research. Hilal once said to me, “It’s easy to do experiments, but doing the correct one is complicated”, which emphasizes the careful design and planning of the experiments required to be successful. The Ph.D. is a very long journey, and Hilal was present to help and guide me during good and difficult periods. I was also lucky that Hilal invited me to join many meetings to discuss with visiting professors and to travel abroad for seminars and establish great collaborations. I am extremely grateful for the opportunity and everything I learned over the past four years. Thanks a million, Hilal.

I would like to thank the members of the Jury: Prof. **Brian McCabe**, Prof. **Aleksandra Radenovic**, Prof. **Leslie M. Thompson** and Prof. **Erich E. Wanker**, for their valuable time in evaluating my work.

Thanks to my mentor, Prof. **Graham Knott,** for all his advice, enthusiasm and successful collaboration with the BioEM platform.

Special gratitude goes to **Anne-Laure Mahul-Mellie**r, who trained me from the very beginning, encouraged me, and from whom I learned a lot. She taught me how to perform almost all lab experiments I had conducted during this journey, but also gave me plenty of scientific feedbacks on presentation and writing, and therefore is responsible for a great part of the scientist I am today. Thanks a lot for all your dedicated time, advice and support. I could not have wished for a better mentorship.

I deeply thank **Niran Maharjan,** who was always present to answer all the questions I could have in the lab at the beginning of my Ph.D. I was very lucky to have his support in the lab and as a friend. I had the chance to do my Ph.D. next to great colleagues and friends, **Bryan Frey, Rajasekhar Kolla, Senthil Kumar, Pedro Magalhães, Enzo Morro**, **Jonathan Ricci** and

Ahmed Sadek, where we always helped each other and created a positive and fun atmosphere. It was a real pleasure and very comforting to be part of this group.

A great thanks also go to all current and previous members of the Lashuel lab for their fruitful discussions, help in the lab and to create a nice work environment: **Lorène Aeschbach, Firat Altay, Loay Awad, Driss Boudeffa, Manel Boussouf, Nadine Aït Bouziad, Johannes Burtsher, Anass Chiki, Sonia Donzelli, Elena Gasparotto, Mahmood Haj-Yahya, Janna Hastings, Ramanath Hegde, Khalid Ibrahim, Somanath Jagannath, Yllza Jasiqi, Deepthy Kavungal, Galina Limorenko, Sergey Nazarov, Salvatore Novello, Theodora Panagaki, Gopinath Pushparathinam, Andreas Reif, Joan Romani, Iman Rostami, Till Ryser, Julian Shillcock, Mohammed Syed, Sophie Vieweg, John Warner, Laura Weerens, Lixin Yang, Zhidian Zhang.** Many thanks to **Marie Rodriguez** for all her great administrative support over the past years.

My sincere thanks to **Alice Patin** and **Flore Munier-Jolain** for the dedicated work and efforts that they placed on working on some of my projects during my Ph.D. They greatly contributed to the advancement of my thesis through their valuable time and scientific investments.

I had the pleasure to work with a great team at the BioEM platform with **Mary Croisier, Stephanie Rosset, Anaelle Dubois, Jerome Blanc, Graham Knott** and **Davide Demurtas,** which led to successful results. I also want to thank **Romain Guiet, Olivier Burri, Thierry Laroche, José Artacho, Nicolas Chiaruttini, and Arne Seitz** from the Biop platform, EPFL, who helps me with the design of the imagery pipeline and for their insightful comments. Many thanks to the proteomic facility and especially **Romain Hamelin, Florence and Diego Chappe** for all their discussions, technical help and analysis during my Ph.D.

During my PhD, I had the chance to collaborate and learn from **Hesso Farhan**, **Veronika Reiterer**, **Kristin Grußmayer**, **Vytautas Navikas**, **Kristin Grußmayer, Richard Faull**, **Malvindar Singh-Bains** and **Magda Zachara**, and I would like to deeply thank all of them.

Special thanks to **Hilal A. Lashuel**, **Anne-Laure Mahul-Mellier**, **Rajasekhar Kolla**, **Pedro Magalhães**, **Salvatore Novello** and **Galina Limorenko** for their valuable inputs on the manuscript.

I am grateful to the EPFL for providing an exciting and innovative work and teaching environment. Also, I would like to express my deepest appreciation to the **CHDI foundation** for helping and providing the funding for this work.

I was fortunate to join the Défi Parkinson association and meet extraordinary people starting with **Yves Auberson**, **Michel Zryd**, **Luc Levan** and **Claude Molteni** in order to raise

awareness about Parkinson's disease. I am thankful to all of them and especially to Yves, who is a great source of inspiration and motivation.

I want to thank all my **friends**, who were not afraid to ask me the topic of my research for most of them, and especially the **Maxipotes** who helped me to evade during tough times and always made me happy.

I am extremely grateful to my **family** and especially my parents **Serge** and **Sophie,** who always supported me and never questioned my choices during my studies. It was not always easy to be far away during my thesis and especially during COVID time, but we always managed to get together and spend precious time. I want to dedicate this thesis to my grandparents **André**, **Dett**, **Charles** and **Jacqueline.**

I specifically thank **Rafaël** for his meticulous review of the references, as well as **Martine** and **Marion** to correct the French part of the manuscript.

Finally, I want to express my warmest gratitude to **Marion** for her continuous and perpetual support. Marion was the key element for maintaining a correct work-life balance, and despite all the work I had during my Ph.D., she always helped me in so many ways and allowed for great moments together. She gave me a lot of strength and confidence during the past years, and I am eternally grateful–Merci beaucoup Bibou.

Abstract

Despite the fact that the gene responsible for Huntington's disease (HD) is known, we still do not understand the underlying mechanisms leading to neurodegeneration and death. Identifying and understanding the mechanisms controlling mutant huntingtin (mHtt) aggregation and inclusion formation using different cellular and animal models is crucial to elucidate the molecular mechanisms underpinning the disease and to develop effective treatments to prevent or slow the progression of HD.

At the mechanistic level, our work shows that mHtt aggregation and inclusion formation in the cytosol and nucleus occur via different mechanisms and lead to the formation of inclusions with distinct biochemical and ultrastructural properties. We show that mHtt cytoplasmic inclusion formation occurs via two phases: 1) a first phase involves the rapid formation of a dense fibrillar core and is driven predominantly by intermolecular interactions involving the polyQ domain via phase separation-like mechanisms; 2) a second phase is associated with the recruitment of soluble mHtt, fibril growth, and the active recruitment and sequestration of lipids, proteins, and membranous organelles. Our work points to this second phase as an important contributor to mHtt toxicity and suggests that targeting inclusion growth and maturation represent a promising therapeutic strategy. These observations suggest that the two types of inclusions may exert their toxicity via different mechanisms and may require different strategies to interfere with their formation, maturation and toxicity. Using primary neurons, we demonstrated that neuronal intranuclear inclusions evolve over time from small aggregates to large granulo-filamentous inclusions associated with cellular toxicity. In addition, our work underscores the failure of the cellular degradation machineries to clear mHtt inclusions, as well as the sequestration of other proteins, lipids and organelles.

Finally, we would like to emphasize that our comparative analysis of tag-free and GFP-tagged mutant mHtt aggregation and inclusions formation will inform future efforts to develop models that reproduce HD pathology more faithfully and underscore the need for developing label-free techniques to investigate disease-relevant mechanisms that underpin inclusion formation.

Keywords

Huntington's Disease, Huntingtin protein, mHtt, Httex1, aggregation, cellular inclusions, polyglutamine, confocal microscopy, correlative light electron microscopy, proteomic, HEK cells, primary neurons.

Résumé

Bien que le gène responsable de la maladie de Huntington soit connu, nous ne comprenons toujours pas les mécanismes sous-jacents conduisant à la mort des neurones et à la neurodégénérescence. L'identification et la compréhension des mécanismes contrôlant l'agrégation et la formation d'inclusions de la protéine huntingtine mutante (mHtt) –à l'aide de différents modèles cellulaires et animaux— est cruciale pour élucider les mécanismes moléculaires à la base de la maladie et pour développer des traitements efficaces afin de prévenir ou ralentir la progression de la maladie de Huntington.

Nos travaux montrent que l'agrégation de mHtt dans le cytosol et le noyau se produisent via différents mécanismes et conduisent à la formation d'inclusions avec des propriétés biochimiques et ultra-structurales distinctes. Nous montrons que la formation d'inclusions cytoplasmiques mHtt se produit en deux phases: 1) une première phase implique la formation rapide d'un dense noyau fibrillaire, principalement entraînée par des interactions intermoléculaires impliquant le domaine polyQ via des mécanismes de type « séparation de phases »; 2) une deuxième phase est associée au recrutement de mHtt soluble, à la croissance des fibrilles, ainsi qu'au recrutement et à la séquestration active des lipides, des protéines et des organites membranaires. Nos études indiquent que cette seconde phase contribue fortement à la toxicité de mHtt et suggèrent que cibler la croissance et la maturation des inclusions représente une stratégie thérapeutique prometteuse. Ces observations suggèrent que les deux types d'inclusions peuvent exercer leur toxicité via des mécanismes différents et peuvent nécessiter des stratégies différentes pour interférer avec leur formation, leur maturation et leur toxicité. En utilisant des cultures primaires de neurones, nous démontrons que les inclusions intranucléaires neuronales évoluent à partir de petits agrégats pour devenir de larges inclusions granulo-filamenteuses, associées à une toxicité cellulaire. De plus, nos travaux soulignent l'incapacité des mécanismes de dégradation cellulaire à éliminer les inclusions de mHtt, ainsi que la séquestration d'autres protéines, lipides et organites.

Enfin, nous tenons à souligner que notre analyse comparative d'agrégation et de formation d'inclusions de mHtt avec et sans marqueur fluorescents, éclairera les efforts futurs pour développer des modèles qui reproduisent plus fidèlement la maladie de Huntington. De ce fait, nous mettons en avant le besoin de développer des techniques sans marqueurs afin de comprendre les mécanismes intrinsèques de la maladie qui régulent la formation des inclusions.

Mots-clés

Maladie de Huntington, protéine huntingtine, mHtt, Httex1, agrégation, inclusions cellulaires, polyglutamine, microscopie confocale, microscopie corrélative, protéomique, cellules de HEK, neurones primaires.

Abbreviations

a.a.:	amino acids
AAV:	adeno-associated virus
Amyloid-beta:	Aβ
AFM:	Atomic force microscopy
ASO:	Antisense oligonucleotide
ASOs:	Gene antisense oligonucleotides
Alpha-Synuclein:	aSyn
BAC:	Bacterial artificial chromosome
BDNF:	Brain-derived neurotrophic factor
BiFC:	Bimolecular complementation cellular assay
C.elegans:	Caenorhabditis elegans
CAG:	Cytosine-adenine-guanine
Cas9:	CRISPR associated protein 9
CBP:	(Creb)-binding protein
CFP:	Cyan fluorescent protein
CLEM:	Correlative light electron microscopy
CREB:	Camp-response element (creb)-binding protein
CRISPR:	Clustered Regularly Interspaced Short Palindromic Repeats
cryo-EM:	Cryogenic electron microscopy
DNA:	Deoxyribonucleic acid
E. coli:	Escherichia coli
e.g.:	*exempli gratia* (For example)
eGFP:	Enhanced green fluorescent protein
EM:	Electron microscopy
ER:	Endoplasmic reticulum
FDA	Food and Drug administration (USA)
FL-Htt	Full-length Htt
FRET:	Förster resonance energy transfer
GABA:	Gamma-aminobutyric acid
GFP:	Green fluorescent protein
GST:	Glutathione-s-transferase
HAP1:	Huntingtin-associated protein 1
HAP40:	Huntingtin-associated protein 40
HD:	Huntington's disease
HDACs:	Histone deacetylases

HEAT:	Huntingtin, elongation factor 3 (ef3), protein phosphatase 2a (pp2a), and the yeast kinase tor1
HEPES:	4-(2-hydroxyethyl)-piperazin-1-ethanesulfonsaure
HIP1:	Huntingtin-interacting protein 1
Hsp:	Heat-shock proteins
htt:	Huntingtin gene
Htt:	Huntingtin protein
Httex1:	Huntingtin exon 1
IBs:	Inclusion bodies
i.e.:	*id est* (That is)
INDELs	nucleotide insertions and deletions
kDa:	Kilodalton
KI	Knock-In
LB:	Lysogeny broth
LC/MS:	Liquid chromatography–mass spectrometry
M8P:	Methionine at position 8 to proline
MALDI:	Matrix-assisted laser desorption ionization
mHtt:	mutant huntingtin, with an expanded polyQ-length
MAO:	Monoamine oxidase
MSN:	Medium spiny neurons
NES:	Nuclear export signal
NeuroD:	Neuron-specific transcription factor
NF-kB:	Nuclear factor kb
NMDA:	N-methyl-d-aspartate
NRSF:	Neuron-restrictive silencer factor
Nt17:	First 17 N-terminal amino acids of Htt
NUMA:	Nuclear mitotic apparatus
p53:	Tumor suppressor protein 53
PBS:	Phosphate-buffered saline
PDE10A:	Phosphodiesterase 10A
PMSF:	Phenylmethanesulfonyl fluoride
PolyP:	Poly proline
polyQ:	Poly glutamine domain
PPII:	Polyproline type II
PRD:	Proline Rich Domain
pS13:	Phosphorylated serine 13
pS16:	Phosphorylated serine 16
pT3:	Phosphorylated threonine 3
PTMs:	Post-translational modifications
REST:	Repressor element-1 transcription factor

RISC:	RNA-induced silencing complex
RNA:	Ribonucleic acid
RNAi:	RNA interference
ROS:	Reactive oxygen species
SDS-PAGE:	Sodium dodecyl sulfate polyacrylamide gel electrophoresis
SH3:	Src homology-3
SIG1R:	sigma 1 receptor
SNPs:	single nucleotide poly morphisms
TALEN:	transcription activator-like effector nuclease
TEV:	Tobacco etch virus
ThT:	Thioflavin T
TrkB:	Tyrosine receptor kinase b
WB:	Western blot
WT:	Wild type
WT Htt:	Wild type Huntingtin, with an unexpanded polyQ-length
YFP:	Yellow fluorescent protein
ZFP:	zinc-finger protein
3-NPA	3-nitropropionic acid

Content

List of Figures

Chapter I

Chapter II

Chapter III

Chapter IV

Supplementary figures

Chapter II

Chapter III

List of Tables

Chapter I

Chapter I: Introduction

1. Huntington's disease

Huntington's disease (HD) is a genetic and progressive neurodegenerative disease characterized by a triad of motor, cognitive, and psychiatric symptoms[1–4]. It is a rare disorder with a predominant prevalence in Caucasian populations (5 to 10 per 100,000 individuals) and a rate of occurrence of less than 1 per 100,000 individuals in Asia and Africa, but with an increasing worldwide trend throughout the preceding decades[5–8]. Chorea is one of the clinical hallmarks of HD, appearing early in the progression of the disease, also characterized by motor impairments such as bradykinesia, incoordination, and rigidity appearing at later stages[9]. Consistent with the disease progression, chorea seems to reflect the neuronal dysfunction and motor impairment resulting from neuronal death[10]. Cognitive symptoms gradually manifest and can be detected several years before diagnosis[11]. Pathologically, the HD brain is characterized by brain atrophy due to neuronal death altering mainly striatal and cortico-striatal neurons. The highest neuronal loss is observed in the striatal part of the basal ganglia, affecting predominantly striatal medium spiny neurons (MSN) involved in motor coordination[12]. MSN are GABAergic neurons and constitute 95% of striatal neurons, with the remaining being interneurons. The specific vulnerability of MSN remains unclear; however, it can arise from cell-autonomous defects such as impairments in protein quality machinery[13,14], transcription[15,16], mitochondrial homeostasis[17,18], and excitotoxicity[19], as well as from non-cell-autonomous mechanisms with the dependence of brain-derived neurotrophic factor (BDNF) from the cortex[20,21]. Different levels of neuronal loss and atrophy are also observed in other brain regions such as the amygdala, hippocampus, globus pallidus, substantia nigra, thalamus, and cerebellum at different stages of disease progression[22–24]. Brain atrophy results in approximately 30 % brain weight reduction, associated with a volumetric loss of 20-30 % in cortical areas, ≈ 60 % in the striatum and ≈ 30 % in the thalamus[25] (Figure 1). Vonsattel and colleagues defined a grading system based on the macroscopic and microscopic analysis of

postmortem brain tissues from the striatum[26]. The system is divided into five grades ranging from grade 0, with no detection of neuropathological abnormalities, to grade 4, affiliated with severe striatal atrophy, and intermediate grades ranging from 1 to 3.

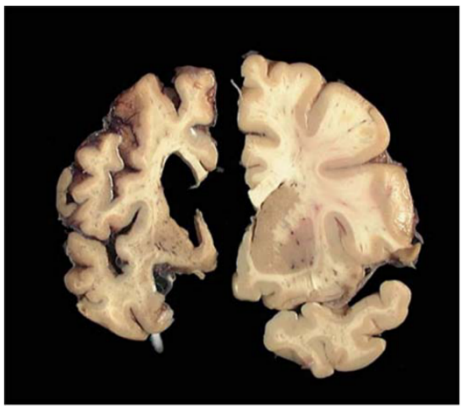

Figure 1. Coronal slice comparison between a grade 4 HD brain (left) and a normal brain (right).
The cortex and caudate (dorsal striatum) are strongly reduced in the HD brain, causing ventricular expansion. Image courtesy of the Harvard Brain Tissue Resource Center.

HD is an autosomal dominant disorder identified by a mutation in the huntingtin gene (*htt*) mapped on chromosome 4[27]. The gene discovery was first referred to as the "interesting transcript 15" (IT-15) by the Huntington's Disease Collaborative Research Group in 1993[28]. The mutation results in an abnormal expansion of the CAG repeats coding for an expanded polyglutamine (polyQ) tract at the amino-terminal (N-ter) part of the huntingtin protein (Htt)[9,28]. The polyQ domain has a median of 18-19 repeats for a non-HD population and becomes pathogenic above 35Q, rendering Htt more prone to aggregate[29,30]. Expanded polyQ domains are associated with eight other neurodegenerative disorders, including six spinocerebellar ataxias, dentatorubral-pallidoluysian atrophy, and spinobullar muscular atrophy[31–33]. In HD, both affected and unaffected individuals were reported to have repeats from 36 to 39, indicating a potentially reduced penetrance of the disease[34] or a role for other disease-modifying genes and mechanisms. Although the majority of cases arise from affected parents, it is estimated that 10 to 15 % are *de novo* mutations resulting from parents with a polyQ length below the pathogenic threshold, *i.e.*, between 27 and 35Q[35].

The length of the polyQ domain is inversely correlated with the age of onset, with the juvenile forms of HD associated with a polyQ repeat length of 75 or more[36,37]. Nevertheless, there is large variability in the age of onset for patients with the same polyQ repeat length, indicating that other factors such as the uninterrupted CAG repeat, gene polymorphisms, and environmental factors modulate the age of onset[38,39]. Indeed, investigations based on human studies have shown that expansion of the CAG repeat is the causative mutation of HD but not the only contributor to disease onset, duration, and severity[37,40,41]. Interestingly, one early study by Wexler *et al.* did not show great differences between homo- and heterozygotes for the mutant allele in terms of clinical expression[42], though a more recent study by Squitieri and colleagues demonstrated that homozygotes had faster disease progression and a different phenotype[43].

Wild type (WT) and mutant huntingtin proteins are ubiquitously expressed in the body[44,45]. However, mRNA and protein expressions vary according to different tissues and organs, with the highest expression levels found in the brain[46] (Figure 2A). Brain mRNA expression levels are also region-specific. For example, Htt is detected at higher levels in the cerebral cortex and the cerebellum compared to the basal ganglia. Therefore, Htt levels do not correlate with the pattern of neurodegeneration observed in HD patients' brains (Figure 2B-C). In addition to brain atrophy, HD affects peripheral tissues, leading to different secondary effects such as weight loss, cardiac failure, skeletal muscle atrophy, testicular atrophy, and impaired glucose tolerance[44]. Those peripheral abnormalities were shown to be directly related to mutant Htt expression in peripheral tissues and not only as a consequence of the neuropathology[47–49]. Interestingly, studies in mice revealed that Htt homozygous knock-out was lethal at the embryonic stage, implying that Htt is indispensable to the early development of several tissue types[50,51].

The major causes of death in HD patients are respiratory complications (predominantly pneumonia) and heart disease (myocardial infarction, heart failure, coronary disease)[52].

Recent studies suggest that HD should be considered as a global and systemic disorder affecting many tissues[44].

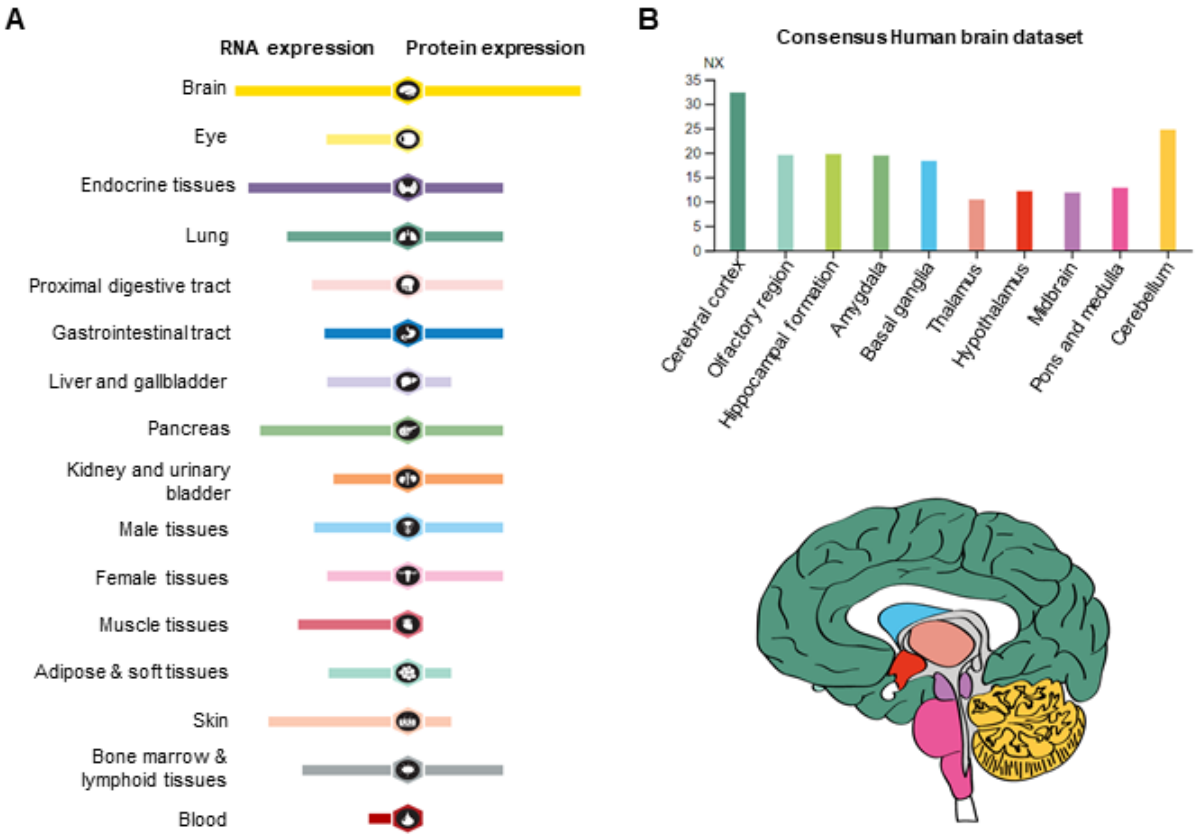

Figure 2. mRNA and protein expression in the human body and brain areas.

A. Normalized RNA and protein expression of Htt in the different tissues. **B.** Consensus normalized RNA levels (NX) of Htt according to brain areas depicted in the bottom (color-match). The figure was adapted from proteinatlas.org (*https://www.proteinatlas.org/ENSG00000197386-HTT*)[53].

2. Huntingtin protein

2.1 Sequence and structure

Htt is a well-conserved 348 kDa protein composed of 3,144 amino acids (a.a.). The huntingtin gene contains 67 exons, but Htt variants can be generated by alternative splicing and can lack

exons 10, 12, 29 and 46[54,55]. Htt is mostly cytoplasmic but is also found in the nucleus and other organelles such as the endoplasmic reticulum (ER)[56]. Htt translocation between the cytoplasm and the nucleus is directed by Nuclear Export Signal (NES) sequences at the N- and C-termini, which also regulate its normal functions[57,58]. Additionally, Htt contains several HEAT (Huntingtin, Elongation factor 3, protein phosphatase 2A, and TOR1) domains known to regulate protein-protein interactions (Figure 3). The highly dynamic conformation of Htt precluded efforts to solve its 3D structure for decades. To address these challenges, Guo *et al.* relied on the fact that the protein becomes more compact and stable once it is bound to one of its substrates and determined, for the first time, the 3D structure of Htt complexed with the Htt-associated protein 40 (HAP40) using cryo-electron microscopy (cryo-EM), at a resolution of 4 Å (Figure 3B)[59]. The segment corresponding to exon 1 could not be resolved due to its high flexibility. In addition, a large portion from residues 403 to 660 and other disordered short sequences at the C-terminal of the protein were not resolved. However, the cryo-EM analyses revealed a rich alpha-helical structure of Htt, with three major domains consisting of HEAT repeats at the N- and C- terminal part of the protein connected by a smaller flexible bridge. The N-terminal 21 HEAT repeat forms a typical α-solenoid and comprise membrane-binding regions as well as a large disordered insertion, whereas the C-terminal 12 HEAT repeats form an elliptical ring composed of helical and unstructured domains. These HEAT repeats are formed by anti-parallel alpha-helices leading to intra- and inter-molecular interactions, consistent with a cellular scaffolding function of Htt[56]. Htt partners such as HAP40 bind within the cleft defined by the two HEAT domains and the small linker through hydrophobic and electrostatic interactions. Htt can adopt various 3D conformations based on intramolecular interactions, such as the interaction of the N-terminal domain with the C-terminus of the protein to give the Htt protein a solenoidal shape and form an internal cavity[56]. Recent work by Harding and colleagues characterized the Htt structure in its apo form (not ligand-bound) and could reach a resolution of only 12 Å, indicating that Htt itself is very flexible[60,61]. These structural features emphasize the role of Htt as a protein-protein interaction hub.

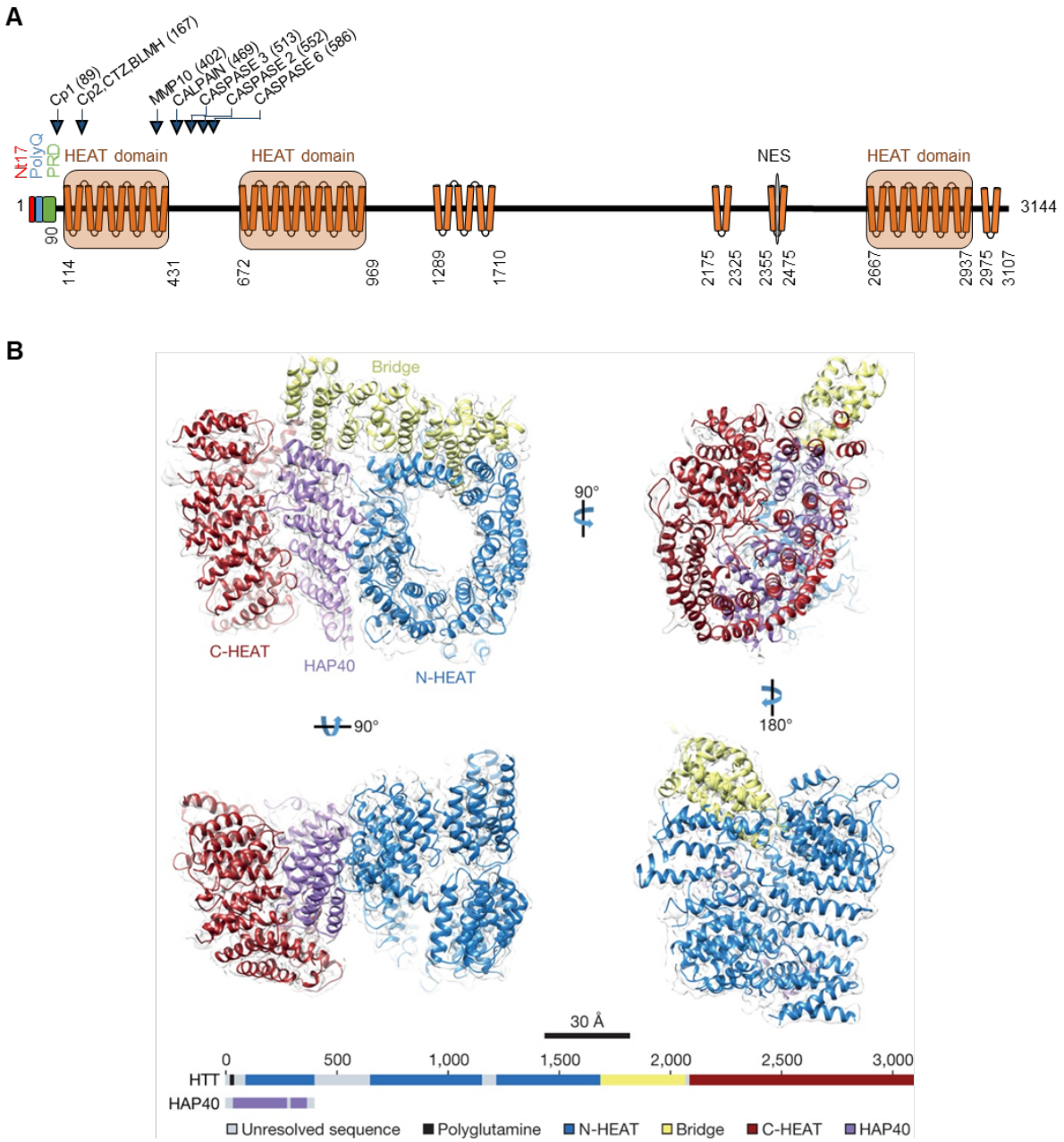

Figure 3. Schematic representation of human huntingtin protein.

A. Full-length Htt (23Q) contains an Nt17 region (red), an expanded polyQ tract (blue), a Proline-Rich Domain (PRD, green), and several alpha-helical HEAT (Huntingtin, Elongation factor 3, protein phosphatase 2A, and TOR1) repeats (orange). Three major HEAT domains are indicated. Blue arrows represent the amino acid positions of protease cleavage sites. Cp1 and Cp2: unknown protease; CTZ: cathepsin Z; BLMH: bleomycin hydrolase; MMP10: metalloproteinase 10; Calpain and several caspases. 469: calpain, 513: caspase 3, 552: caspase 2, 586: caspase 6. An NES was identified at positions 2,397–2,406[57]. **B.** Cryo-electron microscopy of Htt and HAP40 complex. The figure was produced from Guo *et al.*[59] (panel B*)* with permission.

2.2 Signaling pathways, functions, and partners

Htt interacts, directly or indirectly, with many partners (*e.g.*, HAP1, HIP1, CBP, NUMA, HAP40), supporting the scaffolding function of Htt[62–64], and has been implicated in various cellular pathways, including vesicular transport[65], cell division[66], cilliogenesis[67], and transcriptional regulation[58] (Figure 4).

Vesicular transport: One of the major functions of Htt is related to the control of vesicles and organelles' transport and internalization through its interaction with Huntingtin-Associated Protein 1 (HAP1) or dynein directly[68,69]. Htt can form a complex through HAP1 with the dynactin and kinesin proteins, involved in the microtubule-mediated anterograde and retrograde transport of diverse vesicles and organelles such as endosomes, lysosomes and autophagosomes[66,70–72]. Moreover, Htt mediates the transport of Brain-Derived Neurotrophic Factor (BDNF) along the cortico-striatal pathway[65,72]. Htt's role in vesicular transport is even more important considering that the striatum is dependent on the cortico-striatal BDNF transport as it is not locally produced, making it very sensitive to a BDNF diminution[73]. Therefore, a decrease in BDNF production or transport might contribute to HD pathogenesis by the specific death of MSN[12].

Cell division: Htt also coordinates cell division by mediating spindle orientation through additional interactions with dynein[66]. It was demonstrated that Htt is essential for mitotic spindle positioning on astral microtubules via the recruitment of the nuclear mitotic apparatus protein (NuMA) and the G-protein-signaling modulator 2 (LGN)[66,74].

Cilliogenesis: Htt is also required for cilliogenesis regulation in photoreceptor cells, ependymal cells, and neurons[67,75]. Htt mediates the transport of the pericentriolar material 1 protein (PCM1) via the HAP1/dynein/dynactin complex, needed for cilliogenesis[76]. Defects in cilia formation impede protein trafficking and cell-type-specific structural and functional features.

Transcriptional regulation: Htt was shown to bind many transcription factors such as TrkB, NeuroD[77], NF-κB[78], p53[79], and the C-AMP Response Element-binding protein (CREB-binding

protein: CBP)[79]. Moreover, Htt interacts with transcriptional activators and repressors, in particular with the repressor element-1 transcription factor/neuron restrictive silencer factor (REST/NRSF)[80]. The sequestration of REST/NRSF in the cytoplasm by Htt prevents its binding to the neuron restrictive silencer element (RE1/NRSE) acting on the BDNF promoter II. Therefore, Htt act as a positive transcriptional regulator for genes regulated by NRSF-RE1 like BDNF. Overall, Htt acts as a transcriptional regulator in the cell cycle, DNA repair, cellular development and survival, inflammatory responses, and cellular stress[56].

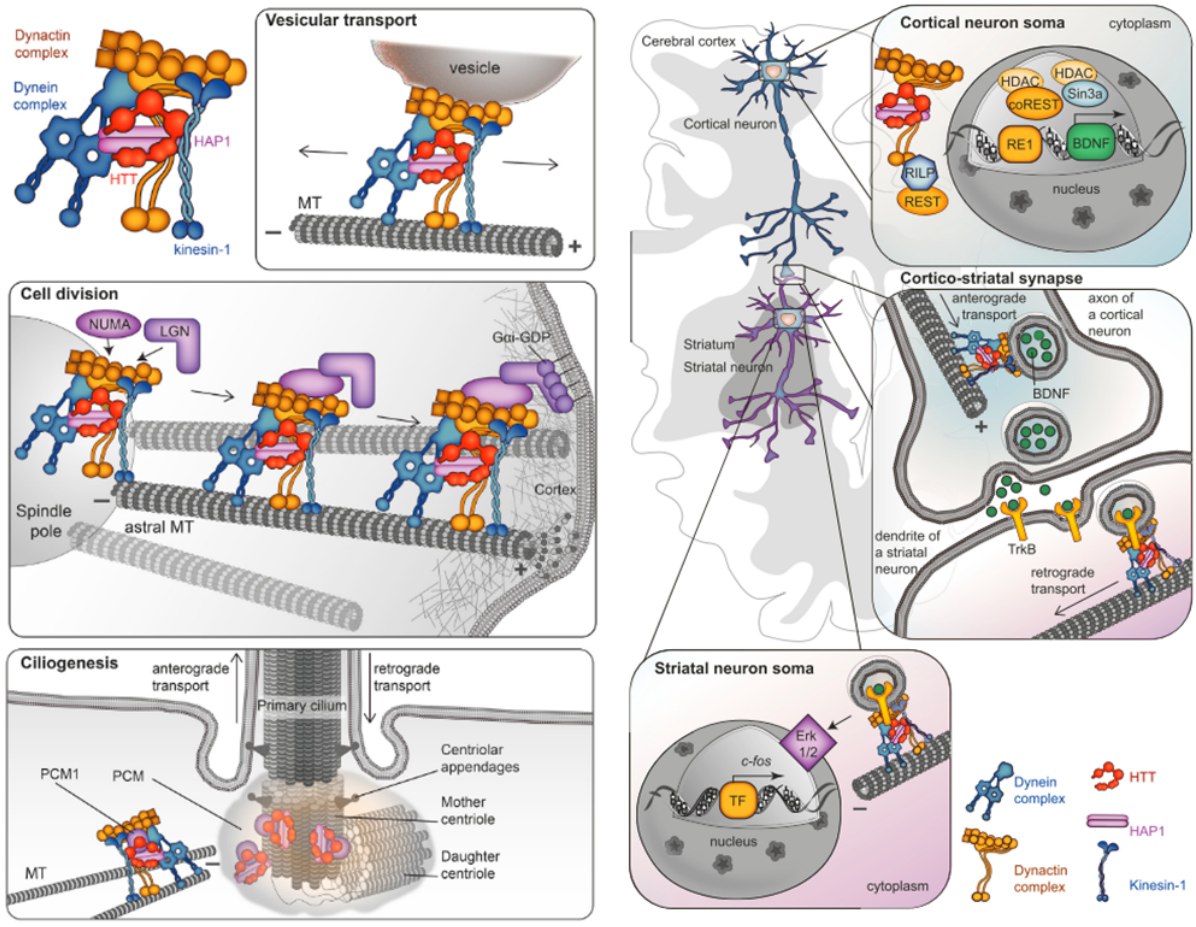

Figure 4. Biological functions of huntingtin.

Huntingtin is a scaffold protein and forms a Dynein/Dynactin/HAP1 complex involved in microtubule-mediated transport and playing a role in various cellular functions (non-exhaustive list): vesicular transport, cell division, cilliogenesis, and transcription. The figure is adapted from Saudou and Humbert[56], with permission.

2.3 Proteolytic cleavage and aberrant splicing generate Htt variants in HD

Post-mortem analyses of HD patients' brains and cellular studies have consistently shown the existence of several N-terminal fragments containing the aggregation-prone expanded polyQ domain[81–88]. Studies reporting on the detection of Htt fragments by immunohistochemistry (IHC) in human HD brain tissues are summarized in table 1.

Antibodies and epitopes	Intranuclear immunoreactivity	Cytoplasmic or neuritic immunoreactivity	References
Ab1 (1-17)	✓	✓	DiFiglia *et al*. 1997[81]
AP78, AP194, Htt1-17 (1-17)	✓		Becher *et al.* 1998[89] Schilling *et al.* 2007[90]
N-Del (1-23 and 69-92)	✓		Schilling *et al.* 2007[90]
Ab1259 and 2B4 (50-64)	✓		Lunkes *et al.* 2002[84]
Htt55-65 (55-65)	✓		Schilling *et al.* 2007[90]
Htt81-90 (81-90)	✓		
1C2 (polyQ)	✓	✓	Gourfinkel-An *et al.* 1998[91] Sieradzan *et al*. 1999[82] Maat-Schieman *et al.* 2007[92] Herndon *et al*. 2009[93]
EM48/MAB5374 (aggregates from Htt 1-256)	✓	✓	Gutekunst *et al.* 1999[94] Van Roon-Mom et al. 2006[95]
CAG53b (1-118, expanded polyQ)	✓		Sieradzan *et al*. 1999[82]
HP1 (80-113)	✓		
1H6 (115-129)		✓	Lunkes *et al.* 2002[84]
HD1 (1-173)		✓	Sieradzan *et al*. 1999[82]
214 (214-229)		✓	Lunkes *et al.* 2002[84]
4C8 (414-503)		✓	Gourfinkel-An *et al.* 1998[91]
AP81 (650-663)		✓	Becher *et al.* 1998[89]
Ab585 (585-725)		✓	DiFiglia *et al*. 1997[81]

Table 1. Htt fragments detected by IHC in HD patients' brains.

The great majority of extreme N-terminal Htt antibodies are preferentially detected in the nuclei of neurons in human HD brain tissues.

Furthermore, an increase in proteolytic activity has been detected in HD patients' brains, which correlates with the production and accumulation of these small N-terminal fragments, including the first exon fragment of Htt (Httex1), from 1 to 90 a.a.[96]. Interestingly, the pattern of N-terminal Htt fragments in the human post-mortem HD striatum differs from that of the healthy control striatum[97]. Biochemistry analyses of human HD brain samples by gel-based protein separation and Western blot (WB) reported the detection of several Htt fragments ranging from 180 to 200 kDa, predominantly with antibodies targeting the N-terminal parts of the Htt protein (< 503 a.a.)[87,88,97–101]. These observations suggest that Htt fragmentation could be a potential modifier of the HD pathology. Consistent with this hypothesis, there is clear evidence from animal models that smaller N-terminal fragments of mutant Htt are more toxic[102–104] and induce a more severe phenotype[105–107].

Various cellular models and *in vitro* experiments have reported that Htt is cleaved by several proteases such as caspases, calpain, cathepsin, and metalloproteinase MMP10, leading to the production of N-terminal fragments of different lengths. Moreover, Htt contains proteolysis-sensitive regions called PEST (Figure 3), sequences enriched in proline, glutamic acid, serine, and threonine[108] that are more susceptible to targeting for proteolysis cleavage. These proteolytic sites of interest are common for both WT and mHtt proteins[56]. Importantly, observations in HD mice suggested that some proteolytic cleavages are more toxic than others, independent of the difference in the lengths of the resulting fragments[109].

In addition, several *in vivo* and human studies have reported aberrant *Htt* mRNA splicing that leads to the production of smaller Htt variants such as Httex1[96,110] or Htt proteins lacking exons 10, 12, 29, and 46[56]. Incomplete splicing of *Htt* leading to Httex1 protein expression has been shown to occur in HD patients' brains[110] and Httex1 protein was previously described as a key component of intracellular protein inclusions found in HD *post-mortem* brains[85,90,110].

Htt is also subjected to sense and antisense repeat-associated non-ATG (RAN) translation that generates novel expansion proteins (poly-Alanine, poly-Serine, poly-Leucine, and poly-

Cysteine). The accumulation of HD-RAN proteins was observed in HD patients' brains and to aggregate depending on the CAG length, causing toxicity in neuronal cells[111].

Altogether, the generation of N-terminal Htt fragments, and especially Httex1, results in their accumulation in neurons and potentially drives toxicity.

3. Htt protein aggregation and Httex1 pathology

The accumulation of Htt-positive intraneuronal aggregates in the cortex and striatum of *post-mortem* brains of HD patients has led to the hypothesis that Htt aggregation plays a central role in the pathogenesis of HD[81,82,94,112,113]. Htt aggregates are found in both the neuronal nuclei (neuronal intranuclear inclusions, NII) and cytoplasm or neurites of HD brain tissues[81,94,95]. Neuronal inclusions were characterized predominantly by IHC using mHtt antibodies (Table 1) and co-stained for ubiquitin, indicating insufficient protein degradation[82,93]. In parallel, a limited number and relatively old biochemical analyses of HD brains were performed, revealing the presence of insoluble Htt aggregates and oligomers[86,88,98]. Additionally, EM analyses conducted in post-mortem HD brains demonstrated the presence of intranuclear and cytoplasmic inclusions with the detection of granules and filaments[81,113].

The heterogeneity of Htt inclusions may explain why aggregates containing the polyglutamine region could be either toxic or neuroprotective[114]. Early neuropathological studies suggested that the pathogenic HD gain of function could be related to the formation of ubiquitinated aggregates formed by N-terminal mHtt fragments generated due to the enhanced cleavage and aggregation of the expanded polyglutamine stretch[81,82,94,112]. The formation of cellular inclusions composed of misfolded mHtt supports the gain of the toxic function hypothesis. However, the loss of the normal Htt protein function and discrepancies in the correlation between the extent of inclusion formation and neuronal loss suggest the involvement of more complex mechanisms with a differential contribution of loss- and gain- of toxic functions[115–117].

The formation of intracellular inclusions composed of misfolded mutant Htt (mHtt) was also reported in animal and cellular models of HD and is considered one of the hallmarks of HD neuropathology[9,102,118,119]. *In vivo*, mHtt forms fibrillar aggregates, which were shown to be composed of Htt and other proteins associated with HD[120], including proteins involved in degradation, transcription regulator factors, and different chaperons sequestered by mHtt[121,122]. mHtt inclusions were also detected in the peripheral tissues of HD patients[123,124] and HD transgenic mice[125–127], such as in skeletal muscles, the pancreas, the liver, the adrenal gland, and the kidney. The length of the polyQ stretch, as well as the flanking regions, also contribute to the regulation of mHtt proteostasis, aggregation, and toxicity[128].

Together, these findings suggest that the process of Htt aggregation plays a central role in the pathogenesis of HD and that understanding the sequence and molecular and structural determinants of this process is crucial to advancing and enabling new insights into novel strategies to treat HD.

3.1 Httex1 is a pathophysiological fragment in HD

Httex1 is composed of three main domains: the first 17 a.a. (Nt17), the polyQ domain, and a Proline-Rich Domain (PRD) (Figure 5). The presence of Httex1 in the post-mortem brains of HD patients suggested a potential role of this fragment in the pathogenesis of HD[81,82,94,112]. Therefore, several animal and cell culture models have been developed to test this hypothesis. In addition, knock-in (KI) and transgenic mice for the full-length human *htt* gene (*e.g.*, YAC128) produce the Httex1 protein, and disease progression in KI-mice was shown to correlate with the level of incomplete gene splicing and appearance of protein aggregates[96,129].

Remarkably, the overexpression of Httex1 containing the polyQ repeats (from 80 to 175 glutamine residues) is sufficient to recapitulate the key features of HD human pathology (e.g., N-terminal Htt aggregation, cellular toxicity) in mice[102,119,130] or Drosophila[85,131] and in cell culture models[83,84,132]. Furthermore, *in vitro*, Httex1 aggregates in a polyQ repeats and

concentration-dependent manner[133–136]. These *in vitro* models reproduce different aspects of Htt aggregation and have been instrumental in advancing our understanding of the sequence, molecular, and structural determinants of Htt aggregation and inclusion formation[137–143]. Therefore, the Httex1 fragment is commonly used to study *in vivo* and *in vitro* models of Htt aggregation, structure and toxicity.

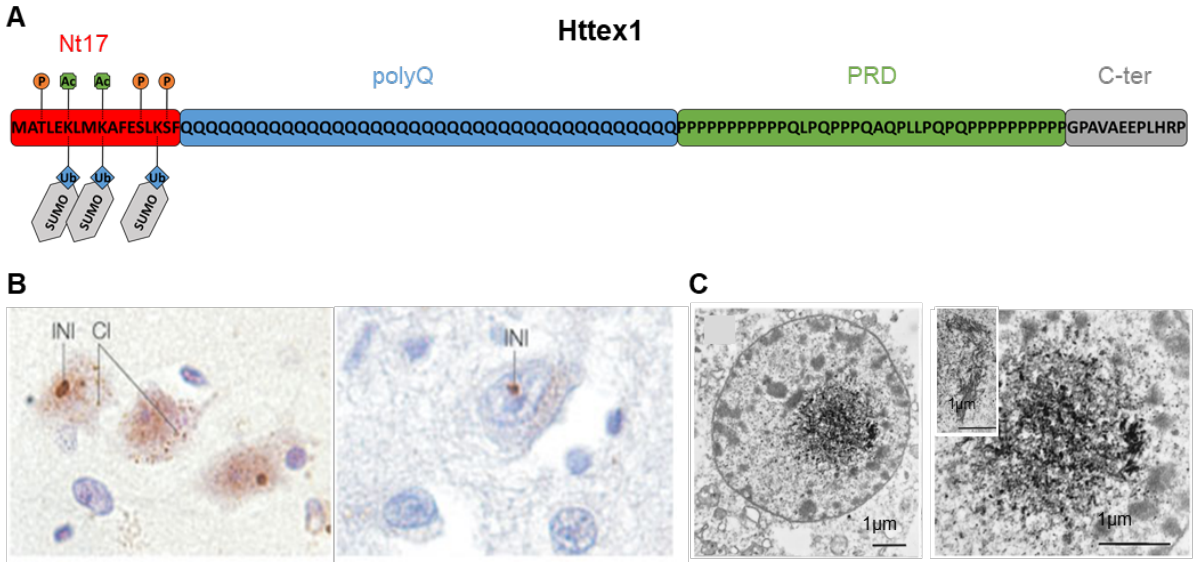

Figure 5. Httex1 protein and N-terminal Htt inclusions in HD brain.

A. Scheme representing Httex1 39Q and Nt17 post-translational modifications (PTMS). Nt17 domain (red), the polyQ domain (blue), and the PRD (green). The Nt17 domain is subject to different PTMs: P: Phosphorylation; Ac: Acetylation; Ub: Ubiquitination; and SUMO: Sumoylation. **B.** Intranuclear inclusion (INI) and cytoplasmic inclusion (CI) detection in an HD patient brain with the 1C2 antibody (expanded polyglutamine specific [MAB1574]). **C.** Electron microscopy of a human neuronal intranuclear inclusion (NII) in the HD cortex with immunoperoxidase labeling (Ab1). The figure was adapted from Ross and Poirier[144] (panel B) and DiFiglia *et al.*[81] (panel C), with permissions.

3.2 Nt17 domain

The toxicity and high aggregation propensity of N-terminal Htt fragments, such as Httex1, have been attributed to the presence of the polyQ domain, which is directly linked to the genetic cause of HD[145]. However, increasing evidence suggests that the Nt17 domain plays a critical

role in modulating the subcellular localization, cellular trafficking, protein-protein interaction, aggregation, and toxic properties of the Htt protein and its N-terminal fragments[136,145,146].

Over the past years, several biophysical studies have enabled a better understanding of the structure and function role of the Nt17 domain. *In vitro*, Nt17 forms a transient amphipathic α-helix with a hydrophobic face and a polar face, which mediates membrane binding and regulates the aggregation properties of Httex1[138,147] and interactions with its partners[140,148]. Numerous *in vitro* aggregation studies based on synthetic Httex1-like peptides and Httex1 fusion proteins have shown that the Nt17 domain accelerates Httex1 aggregation[149]. For example, Httex1 aggregation is significantly slower *in vitro* in the absence of Nt17 or by substitution of the hydrophobic residues with alanines[140,150]. However, there is a discrepancy between the *in vivo* and *in vitro* findings, as Httex1 aggregation was increased in HD transgenic mice in the absence of the Nt17 domain[151]. It has been proposed that the Nt17 domain mediates inter- and intramolecular interactions with other Nt17 and polyQ domains, thus facilitating Htt oligomerization and fibril formation[139,140].

The Nt17 domain was also shown to modulate the subcellular localization of Htt between the nucleus and the cytosol compartments via its pseudo-Leucine-rich NES composed of four residues (Leucine 4, Leucine 7, Phenylalanine 11, and Leucine 14). Interestingly, the disruption of the Nt17 α-helical structure by substituting a methionine at position 8 by a proline residue (M8P) leads to an accumulation of Httex1 in the nucleus along with an increase in toxicity[138]. These findings highlight how small sequence changes in this large protein could significantly modulate the aggregation and toxicity of Httex1. Therefore, it is important to elucidate the sequence and structural factors regulating the biophysical, cellular, and functional properties of this domain and its role in Htt pathophysiology.

The Nt17 domain contains several residues that can undergo PTMs, such as phosphorylation[141,146,152–154], acetylation[141,155,156], ubiquitination[81,82,90,94] and SUMOylation[137,157]. Nt17 PTMs are known to influence protein structure, subcellular localization, aggregation, and toxicity, and are thus likely to influence Htt functions[158,159]. Remarkably, Nt17 PTMs were

shown to modulate Nt17 structural properties, Httex1 membrane binding capacities and subcellular localization in primary neurons[136].

More specifically, phosphorylation of threonine at position 3 (pT3) stabilizes the Nt17 alpha-helix and decreases its propensity to aggregate[135]. Acetylation at lysine 6 (Ack6) can reverse the inhibitory effect induced by pT3 when the two modifications are introduced simultaneously[156]. On the other hand, phosphorylation of both serine 13 and serine 16 (pS13/pS16) is induced by cellular stress and inhibits the aggregation of Httex1[145].

The IκB kinase (IKK) was shown to phosphorylate S13 and induce Htt clearance by the proteasome and lysosomal pathways[141]. Moreover, the recent discovery of the TANK-binding kinase 1 (TBK1) as a kinase that efficiently and specifically phosphorylates Htt at S13 enabled studying the role of Httex1 phosphorylation. Increased S13 phosphorylation by TBK1 induced an enhanced autophagy clearance of mutant Httex1 along with reduced aggregation and Htt-induced toxicity[160]. The decreased levels of pT3 in HD, its inhibitory influence on Htt aggregation, and the beneficial effect of S13 phosphorylation on Htt clearance suggest that Nt17 PTMs modulation may be a promising therapeutic approach[154].

3.3 Proline-Rich Domain (PRD)

The PRD in the C-terminal part of the polyQ domain (Figure 5A) consists of 2 polyproline domains, forming a stable polyproline helix (PPII) secondary structure[161–163]. The two polyproline repeats of 11 and 10 proline residues are separated by 17 a.a. composed principally of proline and glutamine residues. It was previously reported that removal of the PRD extends the half-life of Httex1-GFP[149]. Shen *et al.* also reported that the PRD destabilizes fibril formation *in vitro* and that its removal increased Httex1 aggregation, nuclear localization and toxicity in neurons[149]. In addition, the PRD was shown to be involved in regulating Htt protein-protein interactions, in particular with the SH3 and WW domains[164]. Qin and colleagues demonstrated that the PRD is essential for the formation of the core and shell structural

arrangement of cellular inclusions and especially for the interaction of binding partners such as HIP1, SH3GL, Dynamin, and FIP2[165].

3.4 Httex1 fibrilization

At the molecular level, monomeric Httex1 is disordered and can assemble into a more energetically favorable conformational state when it transitions to oligomers or fibrils (Figure 6). Early models of Httex1 aggregation focused mostly on the polyQ domain as the main initiator and driver of Httex1 aggregation and fibrilization[166,167]. However, subsequent studies demonstrated the important role of the flanking domains in regulating the early steps of Httex1 fibrilization (Nt17 and PRD, described above). One early model by Wetzel and colleagues proposed that the Nt17 domain-mediated oligomerization increases the local concentration of the polyQ repeat domain, leading to a conformational switch toward a more structured beta-sheet amyloid core and fibril formation[168] (Figure 6A-B). Then, the elongation of the beta-sheet-rich nucleus generates amyloid fibrils by the addition of monomers to both ends of the fibril[169]. Similar to other amyloid proteins, Httex1 was shown to self-assemble into oligomeric and fibrillar species of different morphologies[170,171]. This polymorphism is the result of the conformational heterogeneity of the protein and its ability to form various supramolecular arrangements driven by the lateral association of the fibrils, secondary nucleation, and multi-filament fibril branching[172].

NMR studies suggested that Httex1 fibrils are arranged as a “bottle brush” with the polyQ domain forming the core of the fibrils, the Nt17 partially absorbed, and the PRD adopting flexible structures that decorate the surface of the fibrils (Figure 6C)[173]. Importantly, recent findings also suggest that the Nt17 domain in the fibrillar state is partially solvent-exposed and able to interact with the plasma membrane, as well as susceptible to proteolysis by trypsin *in vitro*[136]. Boatz *et al.* proposed a new structural model of the Httex1 filament based on TEM, X-ray, and solid-state NMR[172]. In this model, the authors suggest that Httex1 polymorphism is the result of Httex1’s ability to self-assemble into fibrils which then self-associate to form

different supramolecular arrangements. The Nt17 domain does not appear to be crucial for interactions between filaments but is important for the initiation of fibril branching.

Recently, cryo-EM analyses of Httex1 fibrils from our group also revealed a high degree of polymorphism[174]. In this study, Nazarov *et al.* demonstrated that Httex1 fibrils are composed of multiple protofilaments, where the number of protofilaments is strongly dependent on the length of the polyQ repeat. Interestingly, the removal of the Nt17 domain was shown to increase the heterogeneity of the fibrils, alter the arrangement of the polyQ amyloid core, and decrease the propensity of Httex1 fibrils to laterally associate.

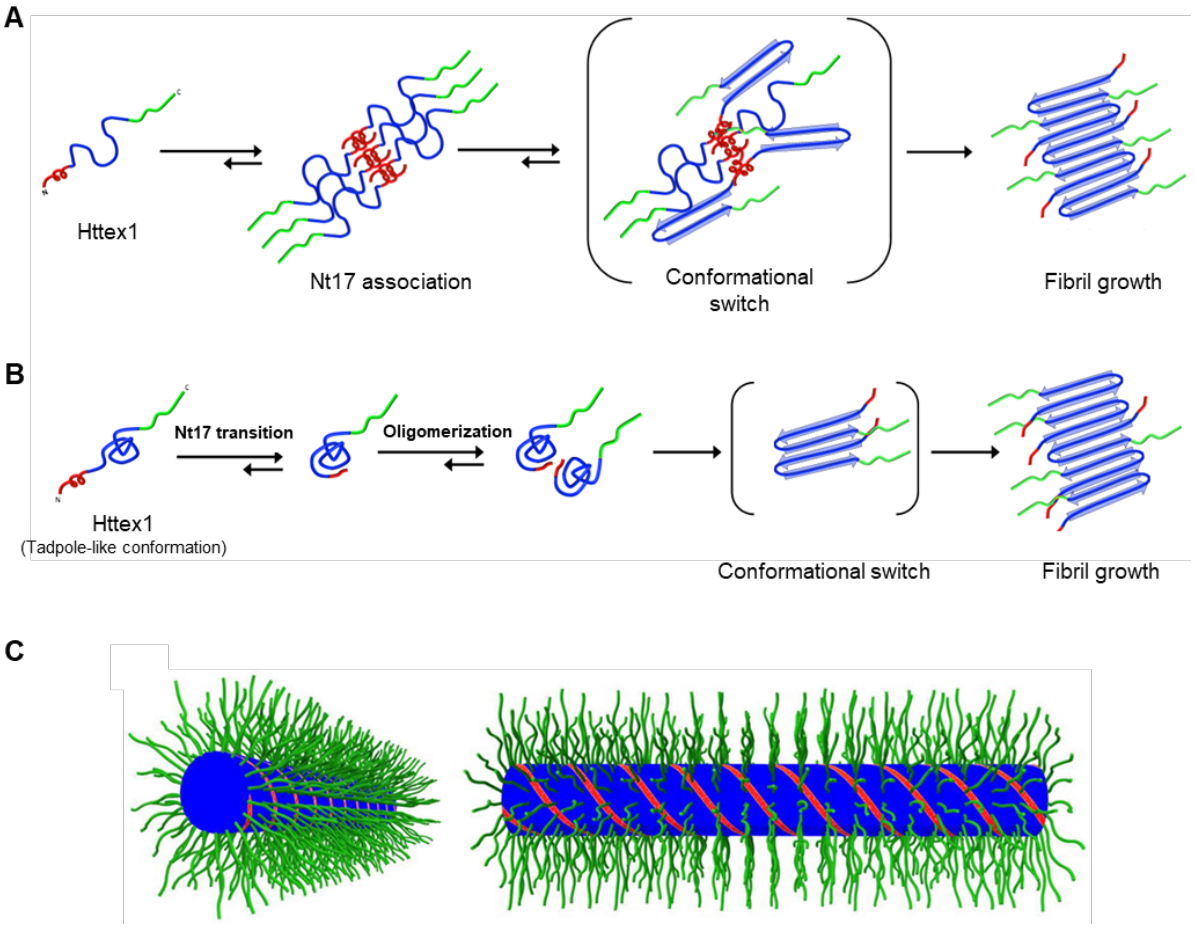

Figure 6. A schematic model for Httex1 aggregation.

The Nt17 domain is represented in red, the polyQ domain in blue, and the PRD in green. **A.** Httex1 aggregation is initially driven by the association of the Nt17 domain due to its alpha-helical conformation. The Nt17 promotes aggregation by gathering Httex1 monomers into oligomers. Then, Httex1 undergoes a conformational switch of the polyQ into beta-sheets followed by fibril growth. **B.** Httex1 can also adopt a tadpole-like conformation in the monomeric

form. The Nt17 can interact and be partially adsorbed on the polyQ, and the oligomerization can arise from intermolecular hydrophobic interactions between the Nt17 domains. Similar to the first Httex1 aggregation model, the increased concentration of polyQ leads to a conformational switch of the polyQ into beta-sheets and fibril growth. **C.** Httex1 "bottle brush" model with the polyQ domain forming the core of the fibril (blue); the Nt17 is partially absorbed and accessible on the polyQ (red) and the PRD is flexible and extruding on the outside of the fibril. The figure is adapted with modifications from Kolla *et al.*[175] (panels A and B) and from Isas *et al.*[173] (panel C), with permissions.

4. How do tags influence amyloid proteins, fibrilization, and aggregate formation *in vitro* and in cellular models?

The discovery of genetically encoded fluorescent tags such as the green fluorescent protein (GFP) isolated from the jellyfish *Aequorea Victoria* has revolutionized molecular and cell biology by facilitating the visualization of proteins and monitoring their expression and dynamic properties in cells and living organisms[176–178]. The structure of GFP was solved in 1996 by Yang and colleagues using protein crystallization and multiwavelength anomalous dispersion at a resolution of 1.9 Å[179]. They reported that the global shape of GFP is a cylinder formed by eleven beta-strands and one alpha-helix in the center, forming a beta-barrel with an approximate size of 3 nm by 4 nm. GFP absorbs blue light (488 nm) and emits green light with a maximum emission peak at 509 nm. The introduction of mutations close to the chromophore (F64L and S65T) resulted in GFP mutants with better folding and brighter emission, renamed enhanced GFP (eGFP)[180,181]. In recent studies, most of the experiments are done with eGFP but are often referred to as simply "GFP" compared to the original "wild type" GFP.

The detection and visualization of amyloid proteins in living cells are crucial for understanding the mechanisms of aggregation, fibrilization, and inclusion formation. Despite the significant advantages of using GFP in cell biology, some limitations of this approach have been reported. For example, Swenson *et al.* reported variable ectopic GFP expressions among transgenic mouse lines and detected a loss of GFP fluorescence after the fixation of the cells[182,183]. GFP

and other GFP-like proteins such as DsRed[184] also showed deleterious effects, such as impacting the cellular pathways, impairing cell growth and viability[185–188]. However, the great majority of the studies do not address or mention the potential influences of such tags in their experimental designs.

4.1 The fusion of GFP influences the biophysical properties of amyloid fibrils.

The detection and visualization of amyloid proteins in living cells are crucial for understanding the mechanisms of aggregation, fibrilization, and inclusion formation. However, the fusion of large fluorescent proteins such as GFP (27 kDa) might influence the aggregation of smaller amyloid proteins (Httex1: 9-17kDa; alpha-Synuclein: 14 kDa; Amyloid-beta: 4 kDa; the core of Tau: ~12-13 kDa). Below, I present an overview of studies illustrating the impact of protein tags on the biophysical, cellular, and aggregation proteins of proteins linked to neurodegenerative diseases.

Huntingtin

Several studies used additional sequences or tags (e.g., GST, GFP, YFP) to facilitate the purification or detection of Htt[133,189–192]. However, many studies have shown that fusing peptides and proteins of various sizes to Htt could alter its structural, biochemical, aggregation, and interactome properties[193,194]. Dahlgren and colleagues studied Httex1 aggregation *in vitro* with and without GFP fused to the C-terminus, together with a GST tag fused to the N-terminus of each construct[192]. They observed by EM and atomic force microscopy (AFM) that GST-Httex1-GFP fibrils were ~3 nm thicker than GST-Httex1. They also reported that the presence of GFP did not alter the branched-type morphology of the aggregates but led to a decreased branching efficiency. This result indicates that the GFP tag was generating steric perturbations during fibrilization and aggregation processes and possibly altering the surface properties of fibrils in ways that disrupted secondary nucleation events and branching. In addition, Bäuerlein

and colleagues reported an increased stiffness of fibrils formed in primary neurons by Httex1 97Q-GFP due to the presence of globular densities on the surfaces of the filaments, corresponding to GFP dimers (≈ 6 nm in diameter)[195]. Furthermore, they reported that the fusion of GFP to the C-terminal part of Httex1 resulted in a 50% reduction in fibril density inside the cytoplasmic inclusions formed in primary neurons and a 25% increase in fibril stiffness due to the GFP decoration along fibrils. Therefore, compiling evidence suggests that in addition to altering the kinetics of fibrilization of amyloid proteins and the biophysical properties of amyloid fibrils, the presence of large tags may alter the final structure and compositions of protein aggregates in cells.

Alpha-Synuclein (aSyn)

GFP or split GFP fused to aSyn is commonly used in cellular[196–200] and animal[201–205] models of Parkinson's disease (PD). Volpicelli-Daley and colleagues developed a seeding model of PD based on the addition of aSyn pre-formed fibrils (PFFs) to a neuronal culture. It is thought that, once internalized, the PFFs recruit endogenous aSyn, corresponding to the formation of intracellular aggregates[206]. The generation of aSyn-GFP fibrils *in vitro* resulted in significantly delayed aggregation kinetics and the formation of wider fibrils[204]. In the study by Afitska *et al.*, the authors even reported that the fusion of GFP to the C-terminus completely inhibited the primary nucleation of aSyn[207]. To follow the internalization of aSyn fibrils, Jarvela and colleagues developed a model based on aSyn-GFP PFFs with a TEV protease site to cleave the GFP tag and differentiate the internalized PFFs to PFFs outside the cells that will lose their GFP by TEV protease induction in the extracellular media[208]. In this study, electron microscopy (EM) characterization revealed that the presence of GFP did not prevent the fibrilization of aSyn *in vitro*. Moreover, using the thioflavin T (ThT) assay, the authors showed that the aSyn-GFP fibrillized alone, seeded aSyn monomers and increased the PFFs' seeding. However, the formation of cellular aggregates or Lewy-body (LB)-like inclusions was not assessed in this study. In a different study, Karpowicz *et al.* used aSyn-GFP PFFs and took advantage of trypan

blue to quench the fluorescence outside of cells[209]. Unfortunately, the authors did not show any biochemical or EM characterization of the aSyn-GFP fibrils, preventing direct comparisons of the aSyn-GFP fibrils to the fibrils formed without GFP in terms of Coomassie staining, fibril morphology, and aggregation kinetics. The treatment of primary neuronal cultures with aSyn-GFP PFFs resulted in the internalization of the fibrils, which were rapidly directed into the endolysosomal pathway. However, almost no seeding (recruitment of endogenous aSyn) or formation of pS129-positive aSyn inclusions was detected in the cells without pharmacological perturbation of lysosomes.

In addition, the use of aSyn-GFP overexpression-based cellular models did not lead to the formation of LB-like inclusions but, rather, showed the formation of GFP puncta[196–200]. Unfortunately, the vast majority of these GFP puncta lack comprehensive biochemical characterization, such as insolubility, and the presence of high molecular weight protein species and fibrils, and therefore could not be accurately defined as aggregates. Comparably, animal models of PD expressing aSyn-GFP could not faithfully reproduce LB-like inclusions. Transgenic aSyn-GFP mice models led to the accumulation of GFP or pS129 staining in the neurons, but no other LB-like features such as morphology, the presence of fibrils, and specific markers (*e.g.*, ubiquitin, p62) were detected[201–204]. In the study by Schaser *et al.*, A53T mutant aSyn-GFP mice were injected with PFFs, which resulted in the formation of amyloid, pS129, and ubiquitin-positive filaments but did not form the LB-like round inclusions[205]. Similarly, Trinkaus and colleagues performed cryo-electron tomography (cryo-ET) from neurons expressing A53T aSyn-GFP and treated with recombinant or brain-derived PFFs[210]. In both cases, the detected aSyn neuronal aggregates were composed predominantly of aSyn fibrils in the middle of cellular organelles and membranes, but never formed LB-like spherical inclusions.

Overall, the results from these previous studies showed that the presence of GFP on aSyn did not prevent the formation of fibrils or seeding *in vitro*[208,209], but there is no clear evidence that they could effectively seed endogenous aSyn, or form LB-like inclusions in cells, compared to

native (tag-free) aSyn PFFs[206,211]. In addition, no direct comparison of fibrillar features – morphology (width, size, branching) or kinetics – was performed or reported to compare aSyn and aSyn-GFP PFFs.

Amyloid-beta (Aβ)

Ochiishi and colleagues showed that the linker length between Aβ and GFP was influencing the fluorescence capacities of GFP in aggregating conditions[212]. They observed that a linker of 14 a.a. allowed GFP to fluoresce in aggregating conditions, compared to a linker of 12 a.a previously used[213,214] and only 2 a.a. in their study, resulting in the quenching of GFP fluorescence. Despite the impact of GFP on the detection of Aβ aggregates, no precise evidence revealed the alteration of GFP on the structural arrangement of amyloid proteins. Additional discrepancies were observed in the aggregation of Aβ when fused to GFP compared to Aβ alone[215]. In this study by Hussein and colleagues[215], they observed that Aβ42-GFP was not seeded by Aβ42 labeled with a small fluorophore Aβ42-ATTO (ATTO size: 0.3-1.2 kDa) in HEK cells and did not form SDS-insoluble aggregates. Therefore, the authors concluded that GFP was altering the physical and biochemical features of Aβ42, thus changing its conformational properties and propensities to fold and aggregate. Based on these results, even if the presence of GFP did not alter the fibrilization capacity of Aβ42 *in vitro*, it was altering its seeding capacity and its capacity to form aggregates in cells. In addition, Azizyan *et al.* studied the effect of the fusion of globular domains representing large fluorescent tags on the formation of amyloid fibrils[216]. They modeled Aβ-GFP fibril formation and revealed that a short linker leads to the steric repulsion of the globular domains (GFP) and perturbed the stacking of the amyloid core of the aggregating proteins. The authors underscored the importance of using the right tools, especially the correct linker size, to study the fibrilization of cross-β amyloid fibrils when fused to a large fluorescent tag.

Tau

Aggregation of Tau is commonly monitored using the aggregation-prone Tau repeat domains (Tau^{RD}) or full-length Tau (Tau^{FL}) fused to fluorescent tags by Fluorescence Resonance Energy Transfer (FRET) assays[217,218]. A FRET signal occurs when the donor and acceptor fluorophores are in close proximity (> 10nm). However, the distance between two beta-strands in the amyloid formation is ~ 0.47 nm[219] compared to the large size of the GFP tag (~ 3 nm by 4 nm). Therefore, the high propensity of Tau to generate a β-sheet-containing structure cannot be efficiently evaluated using this technique, and may also alter the correct formation of Tau amyloid packing to form paired helical filaments (PHF). Recently, Kaniyappan and colleagues reported experimental evidence that GFP was disturbing the β-strands packing of the amyloidogenic protein Tau[220]. The authors fused GFP to full-length Tau (Tau^{FL}-GFP) or the short repeat domain Tau containing a pro-aggregating mutation ($Tau^{RD\Delta K}$-GFP), separated by a 13-14 a.a linker. Using light scattering and EM, they revealed that the addition of GFP to Tau proteins led to a three-fold aggregation reduction for $Tau^{RD\Delta K}$-GFP and almost complete inhibition when GFP was added to the N-terminal part of the peptide (GFP-$Tau^{RD\Delta K}$). In addition, AFM showed that the fibrils formed by Tau^{FL}-GFP were enlarged with the presence of an additional halo of height corresponding to GFP (≈ 3 nm). Similarly, $Tau^{RD\Delta K}$-GFP oligomers were detected as being almost two times wider than non-GFP fibers. Moreover, mass per length analysis by scanning transmission electron microscopy (STEM) demonstrated a different subunit packing of GFP-tagged Tau fibers compared to non-GFP Tau, incompatible with the paired helical filament (PHF) model. Overall, the authors demonstrated that the fusion of GFP to Tau directly modified the fibrilization of monomers into fibrils *in vitro*, and did not represent naturally occurring fibers in diseased brains.

4.2 The fusion of GFP reduces the surface accessibility of amyloid fibrils

The presence of large tags could also reduce the surface accessibility of the fibrils. Even if an amyloid protein is fused to a fluorescent reporter with a recommended linker size by Azizyan and colleagues[216], the decoration of the fibril with the globular tags might decrease its surface accessibility and prevent interactions with proteins or other molecules. Secondary nucleation, which occurs on the surfaces of fibrils, represents another mechanism for oligomer formation, seeding, and fibrilization and, thus, could be affected by the lack or disruption of surface accessibility[221]. In addition, surface occlusion could alter post-aggregation post-translational modification of the fibrils, which were recently shown to play key roles in the regulation of inclusion formation and maturation and pathological diversity in several neurodegenerative diseases[154,158–160,211,222]. Surface accessibility alterations were supported by the change in width and morphology observed in fibrils that present an additional tag[192,220]. Moreover, the reduced branching observed in GST-Httex1-GFP compared to GST-Httex1 indicates a lack of surface accessibility due to GFP, thus preventing secondary nucleation events[192]. Recently, coarse-grained simulations from our group showed that the use of fluorescent tags such as GFP induced a size-dependent surface occlusion of amyloid fibrils and impacted their interactome[221].

The biophysical and cellular influence of GFP on amyloid fibrilization and inclusion formation *in vitro* and in cells is summarized in Figure 7.

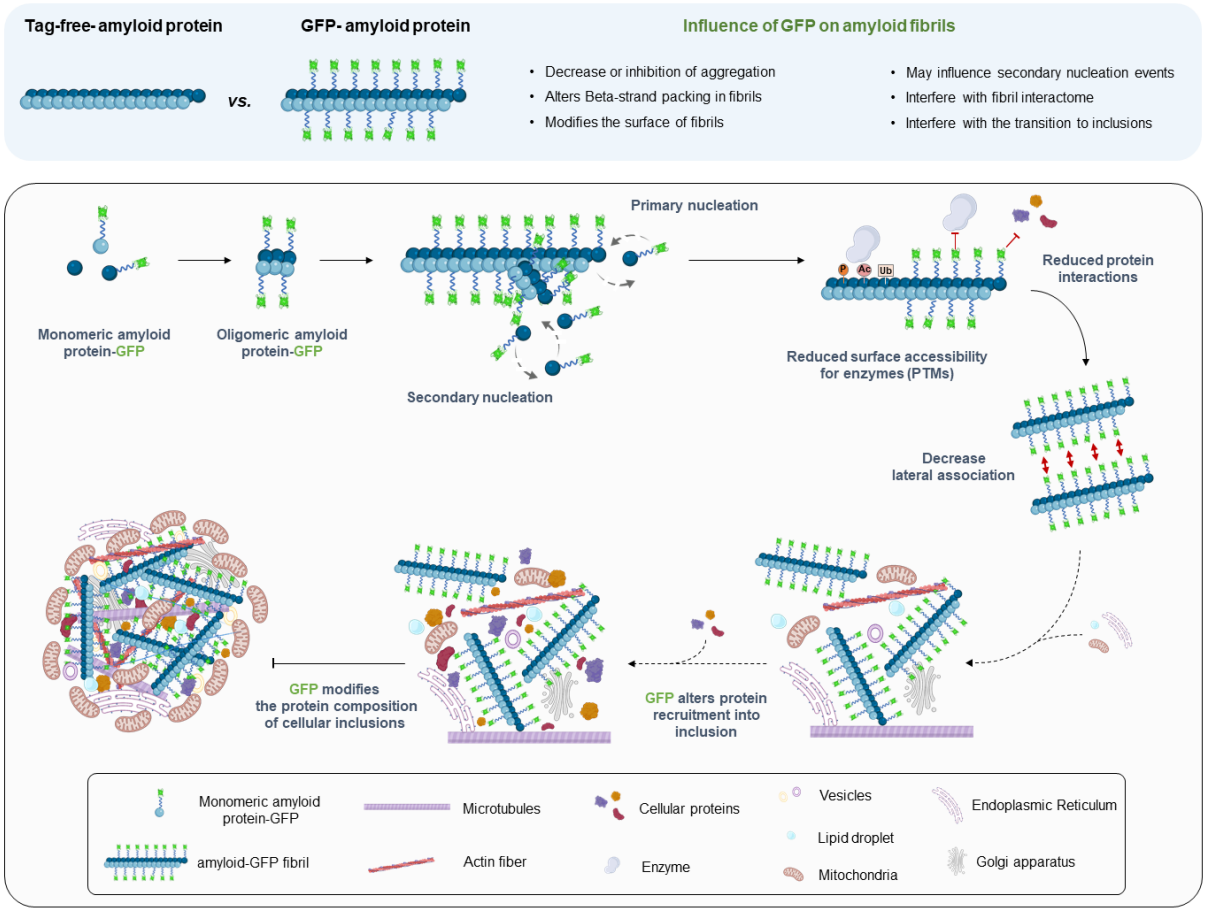

Figure 7. Schematic depiction illustrating the effects of GFP on the various stages of protein aggregation and inclusion formation based on published studies and from our work[221].

The depicted mechanisms illustrate the various stages associated with the mechanisms of amyloid protein oligomerization, fibrilization, and inclusion formation[211,223].

Altogether, even if the addition of fluorescent tags on aggregation-prone amyloid proteins does not appear to prevent fibril formation, it could still affect the fibrilization processes and the formation of pathological aggregates. Therefore, it is important to underscore that the use of large tags in cellular and animal models of HD might interfere with the reproducibility of the disease and should be considered in the interpretation of the results.

5. Animal models of HD

Animal models of HD have been instrumental in advancing our understanding of the biology of Htt, its aggregation mechanisms and its role in the pathogenesis of HD. Over the past decades, several animal models have been generated from different species and using various Htt fragments[224–226].

Early animal models of HD, which preceded the discovery of the *htt* gene, used neurotoxins such as ibotenic acid, kainic acid, and quinolinic acid, to mimic the specific loss of GABAergic striatal neurons in rodents and non-human primates[227–232]. In addition, to reproduce HD-linked energy metabolism defects, mitochondrial toxins like 3-nitropropionic acid (3-NPA) and malonate were directly injected into the mouse striatum[233,234]. Although these models were characterized by local neuronal loss and mitochondrial defects, they did not reproduce the progressive and neuropathological features of HD in all brain regions.

Since the discovery of the *htt* gene, genetic models of HD became the golden standard for investigating Htt pathophysiology. Several transgenic models have been generated based on different expressions of the Htt protein, including the full-length or truncated fragments, varying size of polyQ repeats, transgenic or knock-in (KI) Htt expression, and the use of different gene promoters[224–226].

5.1 Rodent models of HD

Rodents, especially mice, are the most commonly used animal model in HD. The main transgenic models expressing human FL-Htt employ either a yeast artificial chromosome (YAC) or a bacterial artificial chromosome (BAC), with a polyQ tract ranging from 48 to 128, under the human *htt* promoter[115,235–237]. HD48 and HD89 mice also express human FL-Htt but under a CMV promoter[238]. Unlike these mice, the YAC and BAC HD models express the genomic Htt including the introns, as well as upstream and downstream regulatory elements, representing a more natural expression of Htt with intronic features and alternative splicing of

Htt. The majority of these transgenic mice displayed behavioral and motor abnormalities along with brain atrophy and the presence of intranuclear inclusions, although the severity and pathological burden at the cellular level varied among the different models. In contrast, KI FL-Htt mice express an endogenous chimeric mouse Htt with a humanized exon 1 specifically inserted in the Htt gene, such as the HdhQ111[239], CAG140[240], HdhQ150[241,242], and Q175 models[243]. These models use mutated Htt with a polyQ stretch ranging from 72 to 200Q, far beyond the pathogenic threshold in humans. KI mice have also been shown to develop neurological and neurodegenerative phenotypes, including cytoplasmic and nuclear striatal inclusions, and neuronal defects. Overall, the behavioral and neuropathological phenotypes, as well as disease progression, were more severe in transgenic FL-Htt compared to KI FL-Htt, though both approaches tend to reproduce many features of HD.

Interestingly, the use of Htt N-terminal fragments was sufficient to reproduce HD pathology, which was often more severe than that of FL-Htt animal models. Among these, mice expressing Htt586, Htt171, and Httex1, are the most commonly used. The R6/2 mouse model was generated, along with three other lines (R6/0, R6/1 and R6/5), which expressed Httex1 under the human promoter. R6/2 expresses human Httex1 with around 150 CAG repeats and is one of the most commonly used and extensively studied mice models due to its severe and early phenotype[130]. R6/2 mice exhibit intranuclear and neuropil aggregates, brain atrophy, and cognitive and motor defects, along with a reduced lifespan[130].

Globally, neuronal inclusions were largely observed in all rodent models of HD, but the spatial and temporal distribution varied depending on the model, with early appearance correlating with the shortening of the N-terminal Htt fragment expressed[224].

5.2 Non-rodent genetic animal models of HD

Most of the non-rodent animal models of HD express truncated N-terminal fragments of mHtt.

Caenorhabditis elegans. C. elegans models express Htt fragments with the first 57, 79, or 171

a.a. with an expanded polyQ from 88 to 150Q[244–246]. Mutant Htt expression was targeted to a specific subset of neurons and resulted in Htt aggregate formation, neuronal dysfunction, neurodegeneration, mechanosensory defects and reduced lifespan[244–246].

Drosophila *(Drosophila melanogaster).* Several lines were generated using Drosophila by expressing the first 58 to 548 a.a. of Htt, as well as one FL-Htt model[247–250]. The vast majority expressed the complementary DNA (cDNA) – thus, without introns – of human Htt fragments in photoreceptor neurons and other targeted specific cellular populations (UAS-GAL4 system)[251]. HD fly models showed Htt neuronal aggregation, degeneration, motor defects, and reduced lifespan.

Zebrafish (*Danio rerio*). A zebrafish HD model was developed by injecting embryos with Httex1. This resulted in the formation of perinuclear aggregates and increased cellular apoptosis, making this model useful for the screening of protein aggregation inhibitors[252].

Sheep, along with pigs and non-human primates, are considered large-animal models of HD.

Sheep (*Ovis aries*). The sheep model of HD expresses human FL-Htt with 73Q[253,254]. Early IHC analyses in 7-month-old sheep showed a reduction in the MSN marker DARP-32; however, no protein aggregation and no detectable neuronal loss were observed[253]. Further characterization of the model revealed the presence of S830-positive cortical neuropil aggregates (mHttex1 targeted antibody) at 18-months and additional neuronal intranuclear inclusions in the piriform cortex at 36-months[255].

Pigs (*Sus scrofa*). The first Tibetan miniature pig model of HD expressed by nuclear transfer the N-terminal 208 a.a. of Htt with a polyQ of 105 glutamines, but led to an early postnatal death with increased apoptotic markers[256]. More recently, Yan and colleagues used CRISPR/Cas9 and somatic nuclear transfer to generate a KI pig model of HD expressing a humanized exon 1 with 150 CAG repeats[257]. The KI pig model resulted in the specific neurodegeneration of MSN with the detection of some small mHtt-positive nuclear and neuropil aggregates, as well as motor and respiratory dysfunctions.

Non-human primates (*Macaca mulatta or fascicularis*). Finally, non-human primate models of HD were developed, first by employing toxin-based methods[258,259] and, later, genetically expressing Htt171-82Q[260] or Httex1[261] via lentiviral overexpression. The Httex1 model with around 84Q displayed a severe HD phenotype with extensive inclusion formation, although the great majority of non-human primates did not survive after six months.

Overall, numerous animal models of HD were generated and are important to answering specific questions on the pathogenesis of HD, despite some limitations and discrepancies among the literature. Interestingly, animal models expressing truncated N-terminal fragments of Htt, and especially Httex1, brought strong evidence that they are relevant models and could recapitulate many features of HD pathology.

6. Cellular models of HD

Cellular models of HD are complementary to animal models in order to better dissect Htt aggregation and inclusion formation properties in a controlled environment. The use of cellular models allows for the genetic modulation and expression of various Htt constructs in selected cell types as well as a robust characterization in a relatively short time. Moreover, the modeling of the HD pathology in cells can be monitored at the subcellular level and provides a good resolution to decipher molecular pathways and toxicity events.

6.1 First cellular models of HD and detection of aggregates

Since the discovery of the *htt* gene in 1993, very few studies have shown evidence of inclusion formation in cells expressing FL-Htt[119,262,263]. Most of the studies on FL-Htt were based only on fluorescence microscopy and rarely exhibited inclusion formation. Furthermore, even if inclusions were detected, it was not clear whether they were formed by FL-Htt or N-terminal

Htt fragments. Moreover, the formation of Htt aggregates was not validated and characterized at the biochemical level. For example, Cooper *et al.* reported only 1% of cells containing aggregates using FL-Htt with 18 or 82Q in N2a cells compared to 82% in Htt171 with 82Q based on fluorescence microscopy[264]. In order to study Htt aggregate formation in cellular models, smaller N-terminal fragments of Htt were also generated (Httex1, Htt171, Htt586). Studies in cellular models have consistently shown that Httex1 is associated with more robust inclusions formation compared to Htt171 or longer caspase fragments (Htt500-600)[103,119,262,264]. Similar to animal studies, early models of Htt inclusion formation showed an increased aggregate formation in N-terminal fragments of Htt, associated with increased nuclear relocalization in neuronal cell types, as well as increased toxicity.

Although different types of techniques, based primarily on imaging, have been used to identify the accumulation of Htt proteins, the criteria for defining protein aggregates or pathological inclusions are not always clear. Most of the early studies classified Htt inclusions/aggregates based on the detection of puncta by fluorescent imaging. Indeed, early models of cellular Htt aggregation relied mostly on antibody-based detections or the use of a short tag (*e.g.*, Flag) before the fusion of fluorescence proteins such as GFP was used[262–264]. Fluorescent microscopy is very useful for subcellular localization and colocalization studies, but the detection of puncta or accumulation of fluorescence should be combined with specific markers or techniques to be precisely defined as aggregates. EM analysis can give a stronger indication of the presence of protein aggregates and fibrils, as found in *post-mortem* HD brains[81,113]. However, EM-based techniques are more challenging, require heavy processing of the samples, and do not allow for multiplexing. Also, Htt inclusions are more robustly defined based on their biochemical properties and considered to be insoluble protein aggregates when resistant to detergent or protease-resistant. Biochemical techniques are very diverse and can be adjusted depending on the desired detergent fractionation and to isolate aggregates. Moreover, isolated fractions can be coupled to additional analytic techniques such as mass spectrometry and proteomic analysis for in-depth and quantitative characterization[265].

Altogether, previous studies indicate that it is crucial to rely on an integrative approach for the robust investigation of protein aggregation and inclusion formation in cells.

6.2 Htt fragments used to model HD in cells

Httex1 is the most commonly used N-terminal fragment to investigate Htt aggregation in cells[120,136,143,149,160,195,266–270]. However, other longer N-terminal fragments containing the Httex1 sequence with the polyQ stretch are also employed (*e.g.*, Htt171[271,272] and Htt586[273,274], Figure 8), in line with the detection of Htt epitopes outside exon 1 in the human brain (Table 1). Investigating the aggregation of longer N-terminal fragments containing Httex1 is important for assessing the influence of sequences outside exon 1 on Htt aggregation and cellular properties, as well as for assessing modulators of Httex1 cleavage. It has recently been shown that Htt171 aggregation occurs via distinct mechanisms compared to Httex1[175]. Although polyQ-mediated processes initially drive Httex1 aggregation, the aggregation of Htt171 is driven by phase separation events mediated by a complex interplay between the helical domain comprising residues 104-171 and the polyQ domain. Moreover, site-specific phosphorylations of Htt outside exon 1 (*e.g.*, T107 and S116) have been shown to modulate Htt aggregation. Other N-terminal fragments of Htt that are naturally occurring by proteolysis in the brain, *in vivo,* and in cells are also used in cellular models of HD[81–87], such as Htt167 (mediated by calpain 2)[274,275] and Htt586 (mediated by caspase 6) (Figure 3A). However, though the Htt586 fragment is naturally produced by caspase 6 cleavage of the Htt protein[85,104,131,276], almost no studies have reported robust aggregation and inclusion formation in cells expressing this fragment[273,274]. Other, less frequently used N-terminal fragments such as Htt287[277], Htt511[275], Htt969[14,165,263], and other mutated or partially truncated variants[138,149,278] are also expressed in cells to assess their aggregation of cellular properties.

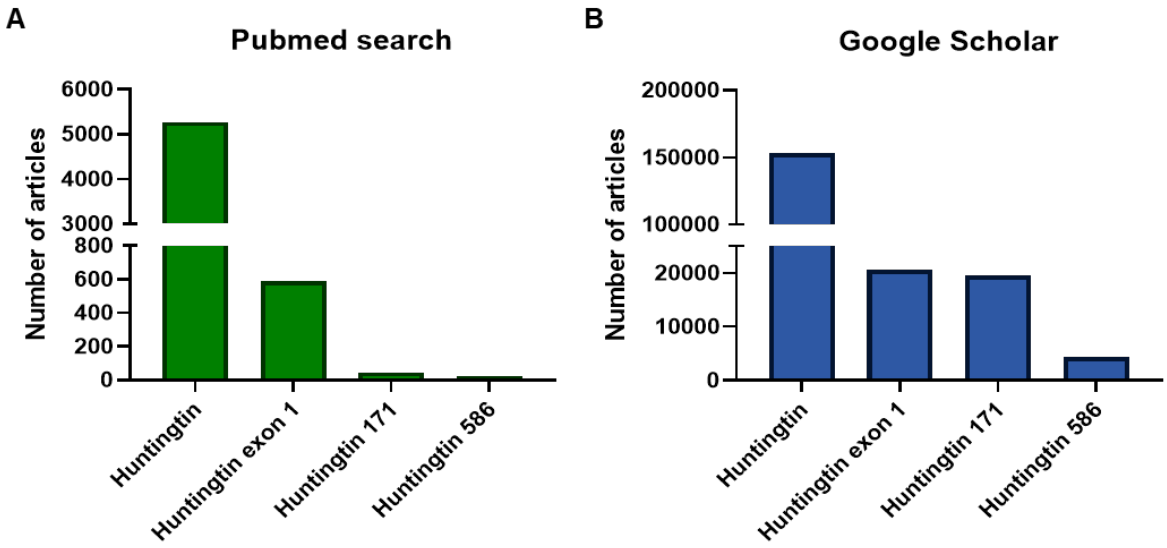

Figure 8. Comparison of literature mining depending on the size of Htt fragments

A. PubMed search provides many much more articles with the keywords “Huntingtin exon 1” (589) compared to “Huntingtin 171” (46) and “Huntingtin 586” (24). **B.** Google Scholar search is less stringent than PubMed, resulting in 20 500 articles for “Huntingtin exon 1”, relatively similar to “Huntingtin 171” with 19 600 articles, and only 4 380 articles for “Huntingtin 586”.

6.3 Influence of non-natural sequences on cellular models of HD

Similar to animal models of HD, many cellular studies often use a polyQ length greater than 75 repeats, associated mostly with rare juvenile forms of the disease, to induce aggregate formation[90,195,279–283]. Some models use Htt constructs of 100-130 polyQ repeats[281,284–286], which are far from human mutations predominantly around 40 to 50 polyQ[29,36]. In addition, most studies rely on the use of large fluorescent proteins fused to Htt to investigate the cellular properties and dynamics of Htt inclusion in cells[117,149,270,279,287]. As discussed earlier in the introduction, “*How do tags influence amyloid proteins, fibrilization, and aggregate formation in vitro and in cellular models*”, the presence of these large proteins can influence the aggregation mechanism and the final structure and biochemical properties of the inclusions, as well as Htt cellular interactors.

6.4 Cell types used to model Htt expression and aggregation

In the past decades, a plethora of cell types has been used to express the Htt fragments from diverse lengths, with or without the presence of tags. Non-differentiating mammalian cells such as HEK, HeLa, COS-7, M17, and CHO can easily be manipulated in lab cell culture and transfected to overexpress Htt. As an example, Httex1 expression in HEK cells results in the formation of abundant and predominantly cytosolic Htt aggregates/inclusions. This remains one of the most commonly used cellular models of Htt aggregation and inclusion formation[90,143,268,275,288–296]. Neuronal cell lines like N2a, SH-SY5Y, and PC12 will also grow *in vitro* by cell division if non-differentiated and have features similar to those of the previous non-neuronal dividing cell types. Cell lines can be engineered to endogenously express Htt but take more resources to develop and do not allow for modifications of the protein sequence afterward. For example, the STHdh mouse striatal cell line expressing a humanized exon 1 (Q111/Q111) must follow a strict differentiation protocol to correctly differentiate and display neuronal features. Although the level of Htt inclusion formation in these cells is very low, STHdh$^{Q111/Q111}$ cells displayed calcium homeostasis impairments and increased vulnerability[297–299].

While Htt dysfunctions are also present in peripheral tissues, it is essential to conduct studies in differentiated neuronal cells, heavily affected in HD. Primary cultures of neurons are commonly used and originate mostly from mice and rats. One challenge with primary neuronal cultures is that they are more resistant to transfection; therefore, viral-based methods are often required[120,143,155,160]. The differentiation of primary cells requires around seven days *in vitro* to obtain a neuronal network, and the presence of glial cells as supporting cells can be maintained in the culture if no specific treatments are employed. Interestingly, cytoplasmic inclusions seem to occur more frequently in dividing and non-differentiating mammalian cells, whereas nuclear inclusions are found predominantly in differentiated neuronal cell types.

Neuronal and non-neuronal models of HD have been instrumental in deciphering specific mechanisms linked to Htt expressions such as subcellular localization, inclusion formation, and

cellular impairments[90,120,141,143,160,268,288,293–295]. However, these studies focused mainly on the polyQ domain, often lack a detailed characterization of the inclusions at both the biochemical and structural levels, and rely mostly on the use of additional sequences or tags. The employment of a multitude of cell types, Htt sequences, polyQ lengths, additional mutations, and tags makes it challenging to compare and reconcile cellular results. In addition, most of the studies did not combine multiple techniques for an integrative characterization of Htt aggregation, inclusion formation, and their impacts on cells.

Increasingly, publications reported the use of animal- or human/patient-derived embryonic stem cells (ESCs) and induced pluripotent stem cells (iPSCs) to monitor Htt cellular expression[300]. In these models, HD-related cellular defects such as transcriptional, metabolism, and electrophysiology dysfunctions, as well as oxidative stress, were observed[301–303]. Recently, Victor and colleagues used the microRNA-based conversion of HD patient fibroblasts to generate MSN and could observe small nuclear and cytoplasmic puncta, mitochondrial dysfunction, DNA damage, and toxicity[304]. However, no robust Htt aggregation was observed, and the challenging reproducibility makes it difficult for these models to investigate Htt inclusion formation in cells. Remarkably, stem cells do not serve solely as cellular models of HD but can be engineered for cell replacement therapy[305].

6.5 Cellular toxicity of Htt aggregation and inclusion formation

Despite decades of work dissecting the molecular mechanisms and signaling pathways underlying Htt inclusion formation and maturation, the direct link between Htt aggregation, neuronal cell death, and HD pathogenesis and clinical symptom progression is still missing. In HD brains, a significant increase in neuronal loss in the striatal and cortical areas and longitudinal brain atrophy occurs during disease progression[12,26,306] and are associated with the deposition and accumulation of intraneuronal aggregates of mHtt, making these inclusions the pathological hallmark of HD[81,89,94]. However, the pattern of neurodegeneration is not similar

to the presence of inclusions with more aggregates detected in the cortex, despite stronger brain atrophy observed in the striatum and the specific loss of MSN[94]. Thus, the question of whether Htt inclusions are harmful and directly cause neuronal cell death[307] or whether they have protective effects[117,308,309] is still under debate[310]. Several *in vivo* and cellular models have been developed to evaluate the potential correlation between Htt aggregation level and neurodegeneration.

First, it has been shown that the formation and accumulation of Htt aggregates together with neurodegeneration were observed concomitantly in most of the HD transgenic mice models expressing N-terminal fragments of Htt[102,115,225,239–241,243], suggesting that the increased burden of Htt inclusions is toxic. Although nuclear and cytoplasmic or neuropil Htt aggregates are considered a hallmark of HD, no direct link was demonstrated between inclusion formation and toxicity.

In addition to animal models of HD, several Htt overexpressing cell-based models have been developed to provide more insight into how Htt aggregation and inclusion formation could be cytotoxic. Using these cellular models, several mammalian cell types (*e.g.*, HeLa[311], N2a[312,313], HEK 293 cells[314], SH-S5Y5[315], and striatal cell lines[316]), including rodent primary striatal neurons[317,318], have been shown to be more prone to death when mHtt is overexpressed with an expanded polyQ stretch[310]. Furthermore, some of these studies demonstrated that Httex1-overexpressing cells are sensitive to aggregates in a dose- and time-dependent manner[136,314]. The cytotoxicity effects of overexpressing Htt in cells have been linked to several pathways, including mitochondrial dysfunction and oxidative stress[311], transcriptional dysregulation[319], inhibition of neuritic out-growth[312], and neuritic degeneration[320]. Recent studies have also suggested that the sequestration inside the Htt inclusions of key proteins such as chaperones[321,322], transcription factors[323], and proteins involved in regulating proteostasis overload or dysfunction[324] could cause the loss of protein functions (including Htt). Such a wide range of functional changes might render the cells more susceptible to death. Additional

evidence of a correlation between Htt inclusions burden and neuronal toxicity came from studies showing that lowering the Htt aggregation level is protective. Yamamoto and colleagues demonstrated that halting the expression of mHtt in mice led to protein inclusions clearance and improved behavioral features[325]. Moreover, the inhibition of mHtt oligomerization by Congo red promotes inclusion clearance and survival in HeLa cells and R6/2 mice[326]. Similarly, Hedge *et al.* recently showed that preventing Htt aggregation and inclusion formation suppresses toxicity in primary neurons and *Caenorhabditis elegans* HD models[160]. These results reinforce the potentially toxic role of inclusion formation and accumulation in the pathogenesis of HD. However, the nature of the aggregate species (soluble oligomeric form vs. fibrillar aggregates) and their protein composition, size, subcellular localization (nuclear vs. cytoplasmic), and brain location of the Htt aggregates greatly vary. Therefore, our difficulty in establishing a causal link between aggregate formation deposition and neuronal loss during pathogenesis and the progression of HD may also be due to our lack of knowledge about the nature of the toxic species.

Due to the diversity of Htt inclusions formed, it is also possible that not all types of Htt aggregates are pathogenic but that some may have beneficial effects. In line with this hypothesis, several animal[327] and cellular studies have shown that the presence of Htt inclusions does not necessarily correlate with cell death[263,308,328]. Arrasate *et al.* have shown that in primary neuronal culture overexpressing Httex1 47Q, neurons able to form inclusion survived and had an increased lifespan while those expressing Httex1 47Q as diffuse intracellular proteins rapidly died[117]. Additional work from Finkbeiner's group confirmed that the formation of Htt inclusion bodies in neurons reduce the risk of neuronal cell death[329]. Moreover, it has been shown that preventing the formation of Htt inclusions significantly increased neuronal cell death[308] while promoting inclusion formation is neuroprotective[330]. All these studies have suggested that neurons promote Htt inclusion formation as a protective response to either reduce the level of the toxic Htt proteins and/or to sequester more toxic Htt species (*e.g.*, small soluble oligomeric or aggregated forms) that may otherwise impair cellular

functions due to aberrant interactions and/or direct damage to cellular compartments and machineries. Despite the difficulties involved in clearly identifying and quantitatively assessing soluble oligomer formation, several studies demonstrated that soluble oligomers were more toxic than larger inclusions, and therefore their sequestration should be protective[331–334].

Thus, the formation of Htt inclusions could start as a beneficial neuronal response, but ultimately, their maturation into large inclusions in which many proteins, organelles, membranes, and lipids are eventually sequestered over time has become a cause of cellular dysfunction and neuronal cell death. The toxicity of these inclusions may also depend on the stage of disease progression.

6.6 Challenges of modeling HD in cells

The introduction of non-natural sequence modifications, combined with the lack of biochemical and structural assessment of Htt inclusions, has led to the generation of several models with limited characterization and, therefore, that are less efficient for deciphering such a complex process. Moreover, the great majority of the models allow for detailed investigation of only the final step of inclusion formation without assessing the mechanisms responsible for initiating and regulating Htt misfolding, oligomerization, fibrillization and inclusion formation. The mechanisms of intracellular Htt aggregation and toxicity can be fully understood only if the models reproduce features of the human pathology and allow for a thorough characterization at the different steps of the aggregation pathways with the appropriate tools. A better understanding of the cellular and molecular mechanisms of Htt aggregation will pave the way to potential therapeutic interventions.

7. Therapeutic approaches

Although there is currently no cure for HD, recent advancements in understanding the biology of Htt have paved the way for the development of disease-modifying strategies, many of which are currently under clinical assessment. These include lowering Htt levels, modulating neuroinflammation, synaptic transmission and protein homeostasis[324,335–337]. Unlike other neurodegenerative diseases, HD is monogenic and can be diagnosed by genetic testing prior to symptomatic manifestations[9,338]. Despite the availability of genetic testing, biomarkers and symptomatic grading are needed to assess disease progression and the efficacy of novel therapies. For example, the Unified Huntington's Disease Rating Scale (UHDRS) is commonly used to measure and rate the clinical outcomes of HD patients based primarily on motor, cognitive, behavioral, and functional capacities[339].

7.1 Symptomatic drug treatment

Initial therapies for HD focused on targeting the symptoms rather than the underlying causes of HD. On the other hand, targeting symptoms is fundamental to improving the quality of life of HD patients, even if it does not influence the progression of the disease. These included anti-chorea drugs tetrabenazine (Xenazine)[340,341] and deutetrabenazine (Austedo)[342], as well as other neuroleptics and antidepressants[343] approved by the FDA. Most of the clinical trials did not lead to clinical benefits, except the controlled trial of deutetrabenazine, which resulted in significantly improved motor signs of HD patients but did not prevent or slow disease progression[342]. Recently, the Huntington study group has been working on a phase III clinical trial (KINEC-HD) to assess the efficacy of valbenazine on dyskinesia by inhibiting dopamine release[344]. In parallel, Sage Therapeutics is conducting a phase I/II clinical trial on a drug (SAGE-718) aimed at improving the cognitive symptoms of HD patients by modulating NMDA receptors.

7.2 Htt lowering strategies

Due to the significant aggregation of mHtt in HD and the beneficial and reversible effects of mHtt suppression in mice[325], considerable efforts were focused on reducing Htt and mHtt levels (Figure 9). The consequences of Htt lowering are controversial because lowering Htt levels also leads to a loss of its physiological functions, especially in the absence of therapeutic approaches that selectively target the mutated form of Htt. Animal studies in which Htt has been inactivated yielded contrasting results, reporting both no defects[345] and severe abnormalities[346]. However, a decrease in Htt levels in humans and other animal models seems to be well tolerated and without detectable phenotypes, although long-term assessment is still required[347–350].

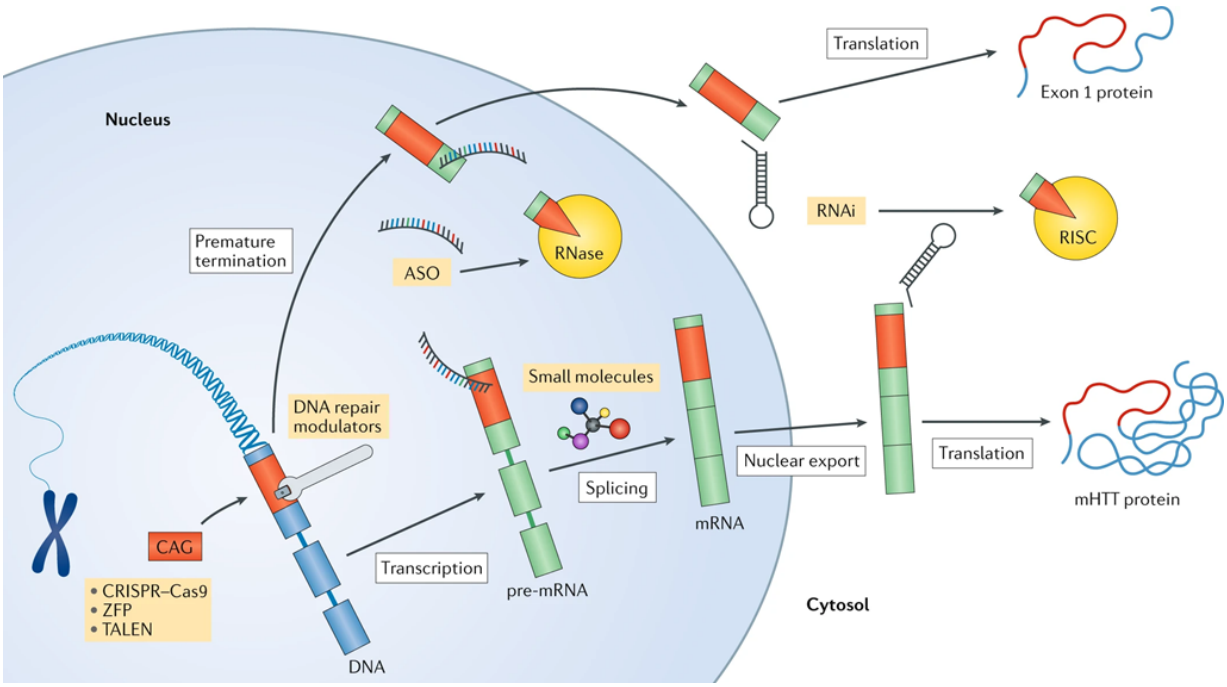

Figure 9. Htt lowering strategies.

Htt expression can be targeted at different steps from DNA to translation: CRISPR-Cas9, zinc-finger protein (ZFP), transcription activator-like effector nuclease (TALEN), DNA repair modulators, antisense oligonucleotide (ASO), small molecules, and RNA interference (RNAi). The CAG and polyQ repeats represented in red are mutated forms of Htt (< 36 repeats). RNA-induced silencing complex: RISC. Ribonuclease: RISC. The figure is adapted from Tabrizi *et al.*[337], with permission.

Allele-specific therapies are direct and probably safer and can be achieved by targeting extended CAG repeats[351,352], specifically identified mHtt single nucleotide polymorphisms (SNPs)[353,354] or nucleotide insertions and deletions (INDELs)[355,356]. However, even allele-specific agents can have off-target effects, such as targeting other CAG repeat-containing regions[357]. The subsequently described Htt-lowering strategies can target either both alleles or the aberrant isoform only.

RNA interference (RNAi): Small interfering RNAs (siRNAs), artificial microRNAs (miRNAs) and short hairpin RNAs (shRNAs) are part of the RNA machinery and induce the degradation of mature mRNA via the RNA-induced silencing complex (RISC)[358,359]. Synthetic interfering RNA does not cross the blood-brain barrier and is hardly internalized in neuronal cells; thus, it needs delivery strategies. The viral-based delivery of RNAi effectors resulted in Htt lowering in cells[360] and *in vivo*[361,362]. As an example, adeno-associated virus (AAV) delivery of shRNA via striatal injection in Htt171 82Q mice led to a reduction in the mHtt mRNA level and inclusion formation and resulted in improved motor performance[361]. Moreover, Htt mRNA was reduced by 45% in WT *Rhesus Macaques* using AAV delivery of miRNA via injection in the putamen[350]. The normal Htt reduction in the putamen was safe and did not induce neurodegeneration or the presence of symptoms. In addition, the first gene therapy for HD currently in phase I/II uses the drug AMT-130 from uniQure (rAAV5 miRNA) to reduce both WT and mHtt, based on brain delivery of recombinant adeno-associated virus[363,364].

Antisense oligonucleotide (ASO): ASOs are synthetic single-stranded DNA molecules with sequences complementary to mRNA. ASOs can bind pre-mRNA and induce their degradation via RNase H[359,365]. One major drawback of ASOs is the need for repeated spinal injection for the delivery of the drug. Recently, the clinical trial using an ASO directed to both WT and mutant Htt from Roche (Tominersen, GENERATION-HD1)[364] was halted because it did not prevent or reduce HD symptomatology, although it was safe and well-tolerated. In parallel, the clinical trial using the ASO candidate from Wave targeting only mHtt was discontinued because

it did not lower mHtt levels, although an improved form of the drug is currently under development.

Zinc-finger nucleases (ZFNs): At the DNA level, transcription can be inhibited by ZFN repressors via nucleotide-binding. ZFNs can bind to DNA and target specific nucleotides through an array of zinc-finger proteins (ZFP), each capable of binding three to five nucleotides[366]. The binding of ZFP alone can reduce gene expression levels or be associated with a transcriptional repressor or nuclease. ZFP targeting pathogenic CAG repeats was shown to reduce the Htt protein level by 95% in cells and up to 60% in R6/2 mice[367]. mHtt reduction in R6/2 mice was beneficial with a decrease in aggregate load and improved motor behavior.

Transcription activator-like effector nucleases (TALENs): Similar to ZFNs, TALENs can specifically bind DNA nucleotides but at higher efficiency and specificity and suppress the transcription of Htt[368,369].

CRISPR–Cas9: Recently, the discovery of CRISPR-Cas9 opened new ways of lowering Htt levels and selectively targeting CAG repeats or associated SNPs[370–374]. Unlike ZFNs or TALENs, the CRISPR-Cas9 technique is based on a guide RNA to target DNA sequences. mHtt expression was shown to be permanently inactivated using CRISPR-Cas9 in BACHD mice[372] and HD patient-derived cells[373] by targeting SNPs correlated with pathogenic CAG repeats.

Small molecules: The great advantages of small molecules are their ability to cross the blood-brain barrier and act throughout the whole body, as well as their oral bioavailability. Small molecules aimed at lowering Htt levels are splice modulators targeting the splicing of pre-mRNA into RNA. Novartis is planning a human trial with the Branaplam drug (originally developed for spinal muscular atrophy) to alter Htt splicing[375]. In addition, the splice modulator from PTC Therapeutics (PTC518) is under safety assessment in a phase I clinical trial after successfully lowering Htt levels in BACHD mice.

Overall, RNA or DNA targeted approaches could lead to long-term treatments of HD, but the difficult delivery and potential off-target effects are problematic to ensuring safe and efficient treatments.

7.3 Other therapeutic strategies

Neuroinflammation has been shown to play a role in the pathogenesis of neurodegenerative diseases and especially in HD with the detection of reactive microglia and astrocytes in the brains of HD patients[376,377]. The overactivation of immune cells in HD induces the production of pro-inflammatory cytokines, quinolinic acid, and ROS, contributing to neurotoxicity[378,379]. Neuroinflammation is a complex process that is not fully understood, but the development of anti-inflammatory drugs is already being tested in HD[380–382]. For example, Laquinimod was tested in a phase II clinical trial and showed reduced secretion of pro-inflammatory factors as well as a significant reduction in caudate atrophy[382–385]. However, the primary outcome was not successfully reached, as the UHDRS total motor score (TMS) did not significantly differ from the baseline[364,386].

In addition, thanks to the evolvement of cell replacement therapies in regenerative medicine, the use of pluripotent stem cells is under investigation for HD[305,387]. Patient-derived iPSCs are potentially safer and more ethical for transplantation, but they will still carry the HD mutation unless they are also edited with CRISPR/CAS-9 before transplantation. Even in this case, the environment might still lead to cytotoxicity and neurodegeneration in a non-cell-autonomous way. Thus, this therapy would need complementary approaches.

Other strategies are explored at the protein level, such as the modulation of Htt PTMs[142,388], N-terminal cleavage inhibition[389,390], anti-aggregation agents[391] (Congo red[392], trehalose derivatives[393], C2-8 small molecule[394], and QBP1 peptide inhibitor[395]), chaperone induction[396–398], and enhancing mHtt clearance via the proteasome and autophagy[324,388]. However, the

impact of such modulations and their influence on normal Htt functions is still not fully understood.

Another interesting therapeutic approach is to modulate synaptic function to prevent excitotoxicity, impaired Ca^{2+} metabolism, and MSN pathway dysfunctions observed in HD[336]. Neuroprotective effects were observed by the inhibition of 1) the extra-synaptic N-methyl-d-aspartate (NMDA) receptor[399,400]; 2) the sigma 1 receptor (SIG1R) resulting in BDNF increase and reactive oxygen species (ROS) reduction[401,402]; 3) Monoamine oxidase (MAO) inducing monoamine neurotransmitter increase (dopamine, noradrenaline, and serotonin)[403,404]; and 4) Phosphodiesterase 10A (PDE10A), shown to restore cellular signaling[405].

Altogether, even if Htt lowering approaches are promising by targeting the upstream causes of the pathology, efficient treatment of HD might require combined therapies acting on neuroinflammation, synaptic function, and protein homeostasis at an early stage.

8. Objectives of the thesis

The primary objective of this thesis was to develop cellular models of HD that enable investigating the mechanisms of Htt cytoplasmic and nuclear inclusion formation and to recapitulate some of the key features of human pathology. The generation of such cellular models is an essential first step toward elucidating the molecular, structural and cellular determinants of Htt aggregation and inclusion formation and how different cell types regulate and respond to these processes.

To achieve this goal, we first assessed the importance of the polyQ length, the Nt17 domain and the PRD in the mechanisms of inclusion formation and maturation in mammalian cells. Ultrastructural and protein content characterization of cytoplasmic and nuclear inclusions allowed us to unravel specific processes and pathways that regulate Htt aggregation and inclusion formation depending on the cellular milieu (Chapter II). We then conducted a time-dependent study on nuclear Htt inclusions formed in primary neurons to investigate the level and kinetics of aggregation, as well as the morphology of neuronal inclusions. We also characterized the biochemical and ultrastructural features of neuronal Httex1 inclusions, as well as their toxic properties (Chapter III). Finally, we discussed our results in the context of the generation of cellular models of HD that are phenotypically, biochemically, and structurally closer to the human pathology and the perspective on label-free methods needed to monitor inclusion formation (Chapter IV).

Chapter II: Disentangling the cellular, molecular and ultrastructural determinants of Huntingtin inclusion formation in mammalian cells

Abstract

Despite the strong evidence linking the aggregation of the Huntingtin protein (Htt) to the pathogenesis of Huntington's disease (HD), the mechanisms underlying Htt aggregation and neurodegeneration remain poorly understood. Herein, we investigated the ultrastructural properties and protein composition of Htt cytoplasmic and nuclear inclusions in mammalian cells overexpressing mutant exon1 of the Htt protein. Our findings provide novel insight into the ultrastructural properties of cytoplasmic and nuclear Htt inclusions and their mechanisms of formation. We show that Htt inclusion formation and maturation are complex processes that, although initially driven by polyQ-dependent Htt aggregation, also involve 1) polyQ and PRD domain-dependent sequestration of lipids and cytoplasmic and cytoskeletal proteins related to HD dysregulated pathways; 2) recruitment and accumulation of remodeled or dysfunctional membranous organelles, and 3) impairment of the protein quality control and degradation machinery. We also show that nuclear and cytoplasmic Htt inclusions exhibit distinct biochemical compositions and ultrastructural properties, suggesting different mechanisms of aggregation and toxicity.

1. Introduction

Although several studies have investigated specific cellular mechanisms linked to Htt aggregation, the current models often lack detailed characterization of the inclusions at both the biochemical and structural levels. Furthermore, while some of the previous studies explored the effect of polyQ repeat length on the ultrastructure properties of mutant Htt, there are no reports on the role of the first N-terminal 17 amino acids (Nt17) of Htt – which regulates many aspects of the aggregation and cellular properties of Htt proteins[141,145,147,149] – on the organization and ultrastructure properties of cytoplasmic and nuclear Htt inclusions. Finally, the vast majority of the previous studies used mutant Htt constructs fused to either peptide-based tags or large fluorescent proteins like GFP that could interfere with the cellular and aggregation properties of Htt[195,266,268,406].

Here, we employed a cellular model of Htt aggregation and inclusion formation to gain insight into how sequence modifications influence the final ultrastructural and biochemical properties of cytoplasmic and nuclear Htt inclusions and their impact on cellular organelles and functions. The cellular models used in this study are based on the overexpression of N-terminal fragments of mutant Htt comprising the Exon 1 region (Httex1), which contains the polyQ expansion. Incomplete splicing of *HTT* leading to Httex1 protein expression has been shown to occur in HD patients' brains[110], and Httex1 protein was previously described as a key component of the intracellular inclusions found in HD *post-mortem* brains[85,90,110]. Moreover, the expression of pathogenic Httex1 (polyQ tract > 43Q) is sufficient to induce HD-like features, including aggregates formation and toxicity in mice[102,119,130], Drosophila[131], C. elegans[407] and cell culture models[132,137–139,143,149,195,268,270,408,409]. *In vitro* and cellular studies also showed that Httex1 aggregates in a polyQ repeat length and concentration-dependent manner[133–135]. Therefore the mutant Httex1-based models are useful to study the pathogenesis of HD as they reproduce different aspects of Htt aggregation and have been instrumental in advancing our

understanding of the sequence, molecular, and structural determinants of Htt aggregation and inclusion formation[137–143].

We applied Correlative Light and Electron Microscopy (CLEM) and proteomics-based approaches to investigate the structural and biochemical properties of the cytoplasmic and nuclear Httex1 inclusions in HEK 293 cells. We also investigated the role of the Nt17 domain and the polyQ tract length in modulating the composition and the structural properties of mutant Httex1 inclusions. Finally, given that a large body of published cellular studies on the mechanisms of Httex1 aggregation and inclusion formation is based on constructs in which Httex1 is fused to the GFP[58,147,149,195,410–412], we also compared, for the first time, the composition, ultrastructural properties, and toxicity of inclusions formed by native (tag-free) and GFP-tagged mutant Httex1.

2. Results

2.1 Httex1 cytoplasmic inclusions exhibit a distinctive core and shell morphology and are composed of highly organized fibrils, cytoplasmic proteins and membranous structures

To investigate the ultrastructural properties of Htt inclusions, we first used a mammalian cell model system of HD, in which overexpression of mutant Httex1 with polyQ repeats > 39 has been shown to result in a robust and reproducible formation of cytoplasmic Htt inclusions[143,268]. In this model, nuclear inclusions are also observed in ~ 15% of transfected cells by Httex1 72Q[292], thus providing an opportunity to investigate and compare the ultrastructural features of cytoplasmic and nuclear Htt inclusions under identical conditions. This model system is widely used to investigate molecular, cellular, and pharmacological modulators of Htt aggregation and inclusion formation[132,137,287,408,409,138,139,143,149,195,268,270,279], though very often using Htt constructs with extra non-natural sequences such as Myc, FLAG and GFP tags. Previous studies have shown that the presence of such tags significantly alters the aggregation properties of N-terminal fragments of mutant Htt[193,216,413]. Therefore, in this work, we opted to maintain the native sequence of the protein and investigated mutant Httex1 aggregation and inclusion formation in the absence of additional sequences or tags. Tag-free Httex1 72Q was overexpressed in HEK 293 cells (HEK cells), and the morphology and structural properties of Httex1 inclusions were assessed. Despite the formation and abundance of inclusions formed by Httex1 72Q, we did not observe overt toxicity in HEK cells. The initiation of apoptotic events was apparent only after 96 h, as indicated by Caspase 3 activation without loss of plasma membrane integrity[292].

Next, we assessed the morphology of Httex1 72Q inclusions by immunocytochemistry (ICC) using nine antibodies against different epitopes along the sequence of Httex1 (Figures 1A and S1). Interestingly, all the antibodies presented a strong immunoreactivity to the periphery of the Httex1 72Q inclusions, and none of these antibodies labeled the core of these inclusions (Figures 1B and S2A). This observation suggests either an absence of Htt in the center of the

inclusions or poor accessibility of the used antibodies to the core of the inclusions, possibly due to the high compactness of the Htt aggregates in the core compared to the periphery of the inclusions. In addition, we observed high colocalization of the filamentous actin (visualized by phalloidin) with Httex1 inclusions (Figure 1B, white arrowheads), indicating a possible involvement of the cytoskeleton proteins in Htt inclusion formation.

2.2 CLEM of the cytoplasmic Httex1 inclusion reveals a complex structural organization of HTT aggregates and membranous structures, with a distinctive core and shell

To gain more insight into the structural and organizational features of Httex1 inclusions formed in cells, we turned to electron microscopy (EM). We first employed a correlative approach to analyze the ultrastructure of the inclusions by EM and their subcellular environment seen with CLEM (Figure 1C-D). Httex1 72Q positive inclusions were immunostained and imaged by confocal microscopy (Figure 1C) and then subjected to serial sectioning for analysis by EM (Figure 1D). The EM micrographs of the Httex1 72Q inclusions revealed a surprisingly complex morphology characterized by a halo-like structure with a dense core and a heavily stained outer shell. The outer layer of the inclusions contained fibrillar structures that appeared to be tightly packed and radiating from the core of the inclusion. EM-dense cytoplasmic structures were detected in both the core and the periphery and could reflect the incorporation or sequestration of disrupted organelles inside the inclusion[165,195,414] (Figure 1D, white arrowheads). The halo-morphology of Httex1 inclusions was consistent across many imaged inclusions (Figure S3A).

To further characterize the structural properties and distribution of Httex1 within the inclusion, we used cryo-fixation via high-pressure freezing, which preserves the cellular ultrastructure in its native state. EM imaging revealed radiating fibrils at the periphery and more tightly organized and stacked fibrils in the core (Figure S4A). Electron-dense membranous structures

were observed in the core and more to the periphery. These results suggest that both the core and shell contain aggregated fibrillar forms of mHtt with but a distinct structural organization.

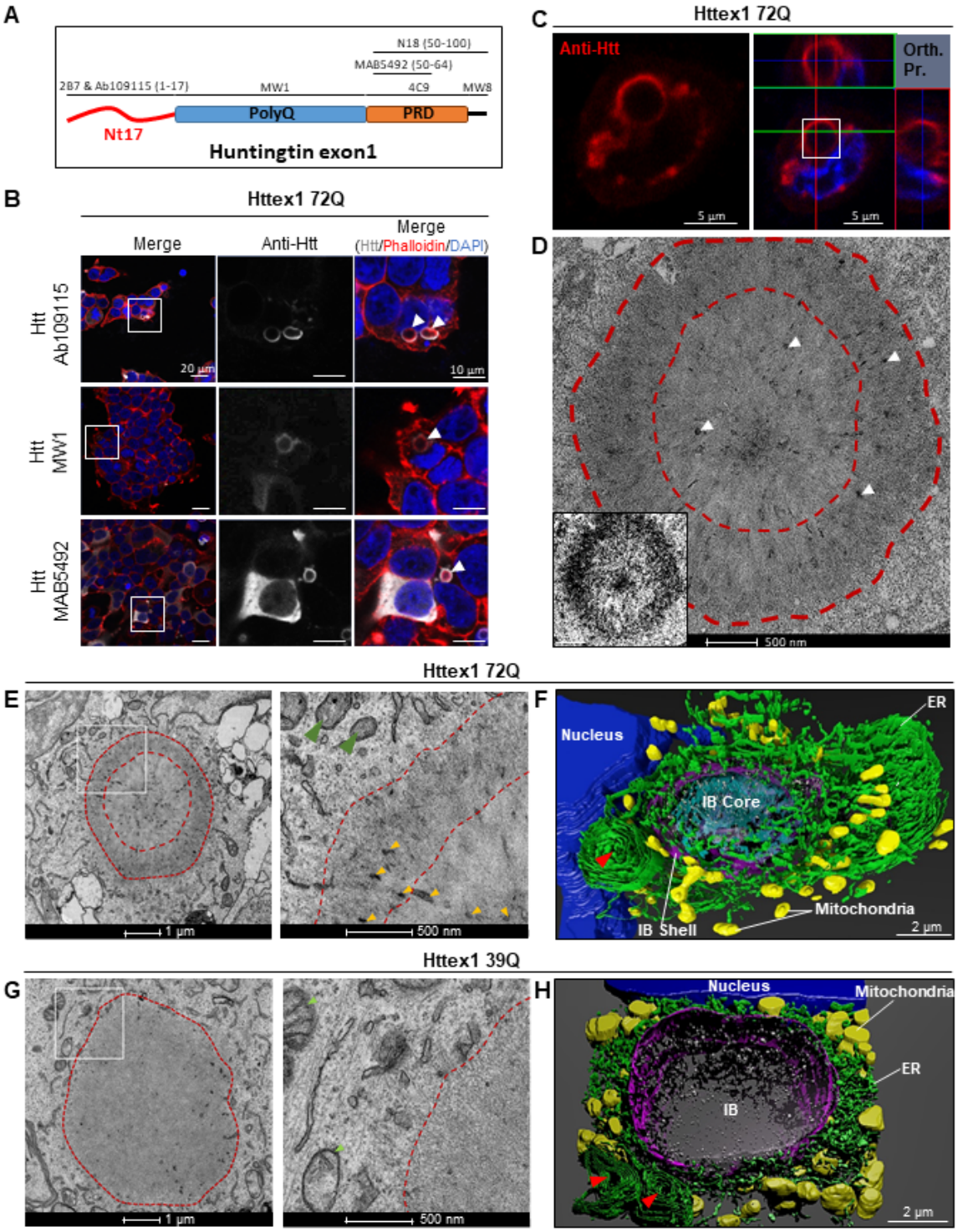

Figure 1. Confocal microscopy and CLEM revealed the ring-like structure of the Httex1 72Q inclusions formed in HEK cells.

A. Epitope mapping of the Httex1 antibodies. **B.** Httex1 72Q inclusions that formed 48 h after transfection in HEK cells were detected by ICC staining combined with confocal imaging. All

the Htt antibodies showed strong immunoreactivity to the periphery of the Httex1 inclusions. The nucleus was counterstained with DAPI (blue) and the F-actin with phalloidin (red). White arrows indicate the colocalization of the F-actin with the ring-like structure of Httex1 inclusions. Scale bar = 20 µm (left-hand panels) and 10 µm (middle and right-hand panels). **C-D.** 48 h post-transfection, HEK cells were fixed, and ICC against Httex1 was performed and imaged by confocal microscopy (**C**). The selected area of the cells (white square) was then examined by EM. Orthogonal projection (Orth. Pr.), Scale bars = 5 µm. (**D**). Pieces of membranes and vesicles are indicated by the white arrowheads. A binary image (inset) was generated from the electron micrograph using a median filtering and Otsu intensity threshold, allowing for a better distinction between the core and the shell ultrastructure of the tag-free Httex1 inclusion. Scale bar = 500 nm. **E.** Representative electron micrograph of Httex1 72Q cellular inclusion and higher magnification (white square) shown in the right panel. Dashed lines delimit the aggregate and the core of the inclusion. Internalized membranous structures and the mitochondria are indicated by the orange arrowheads and the green arrowheads, respectively. Scale bar = 1 µm (left panel) and 500 nm (right panel) **F.** 3D model of Httex1 72Q cellular inclusion and surrounding organelles (top view). The Httex1 inclusion body (IB) shell is represented in purple and the IB core in cyan. ER membranes are shown in green, intra-inclusion membranous structures are displayed in white, the nucleus is shown in blue, and the mitochondria are shown in yellow. A red arrow highlights the formation of stacked ER cisternae. Scale bar = 2 µm. **G.** Representative electron micrograph of Httex1 39Q inclusion formed 48 h after transfection in HEK. The white square indicates the area shown in the right panel at higher magnification. Dashed lines delimit the inclusion. Httex1 39Q inclusions appeared less dense than the Httex1 72Q inclusions. Scale bar = 1 µm (left panel) and 500 nm (right panel). **H.** 3D model of the Httex1 39Q inclusion body (IB) is shown in purple, surrounded by mitochondria (yellow) and ER structures (green). A red arrow highlights the formation of stacked ER cisternae close to the Httex1 39Q inclusion. Intra-inclusion membranous structures are shown in white. The nucleus is highlighted in blue. Scale bar = 2 µm.

The structural organization of Httex1 72Q inclusions combined with the primary localization of Htt antibodies in their periphery suggests that Htt fibrils in the outer layer of these inclusions serve as active sites for the recruitment of soluble Htt, the growth of Htt fibrils, and the interaction of Htt with other proteins and cellular organelles. The ultrastructure of inclusions formed by the Httex1 72Q suggests that their formation is not simply the result of the interactions between Htt monomers but may also involve interactions and the recruitment of other proteins and cellular components. Consistent with this hypothesis, it has been previously reported that Htt intracellular inclusions interact with and/or contain cellular endomembranes, especially of the endoplasmic reticulum (ER)[195] and the mitochondria [18,267,268,414,415], and alter the organization and functions of these organelles.

To determine whether the formation of cytoplasmic inclusions involves interactions with or recruitment of membranous structures such as ER and mitochondria, we imaged inclusion positive cells by EM under conditions that preserve the internal membranes of cellular organelles, i.e., in the absence of detergents commonly used in the ICC procedure. EM images revealed that the core and periphery of the Httex1 72Q inclusion contained many small membranous structures (Figure 1E, yellow arrowheads). An ER network and mitochondria were present at the periphery of these inclusions, suggesting that these regions might act as active sites for the recruitment and interaction of soluble Htt with other proteins and cellular compartments during inclusion formation and maturation. Most of the mitochondria surrounding the cytoplasmic Httex1 72Q inclusions exhibited damaged or markedly reduced numbers of cristae (Figure 1E, green arrowheads).

Next, we sought to identify the endomembrane compartments within Httex1 72Q inclusions using a panel of antibodies or dyes labeling intracellular compartments. The mitochondrial (Tom 20 and Mitotracker) and ER (BiP/Grp78) markers were strongly detected near Httex1 72Q cytoplasmic inclusions (Figure S5A-C). The autophagy flux marker, p62, was enriched in the periphery of Httex1 72Q inclusions (Figure S5D). Markers of aggresome formation, such as Vimentin and HDAC6, were also enriched in the periphery and in close proximity to Httex1 72Q inclusions (Figure S5E-F). Moreover, when cytoskeletal proteins such as actin and tubulin were overexpressed (fused with RFP), they were observed mainly at the periphery of the Httex1 72Q inclusions (Figure S5G-H). This observation is consistent with the colocalization of F-actin (stained by phalloidin) with Httex1-72Q inclusions (Figure 1B, white arrowheads). None of the organelles' markers were detected inside the core of these inclusions (Figure S5), although the EM images clearly showed the presence of membranous structures in the center (Figure 1E). This confirms the poor accessibility of antibodies and dyes to stain the core of the Httex1 inclusions, likely due to their compactness and highlights the importance of using EM to decipher the ultrastructural properties and composition of the pathological inclusions.

2.3 3D reconstruction of Httex1 inclusions indicate perturbation of the ER organization

To further investigate the structure of Httex1 inclusions and their impact on cellular compartments, we generated a 3D model of the inclusions and the organelles in their vicinity. In cells containing Httex1 72Q inclusions, serial EM images were captured, aligned, and the different features segmented (Figure 1E). These segmentations were then used to create a 3D model of the inclusion and surrounding cellular components (Figure 1F and movie 1). This model showed that the inclusion formed in a crowded region with the presence of ER and mitochondria all around it. The 3D model suggests that the electron-dense membranous structures recruited inside the Httex1 inclusions were mostly composed of endomembranes and vesicles (labeled in white), consistent with a previous report[195,414]. Interestingly, the ER adopted a specific “rosette-like” or “stacked cisternae” morphology (highlighted by a red arrowhead) in the periphery of some Httex1 72Q inclusions. Finally, it is noteworthy that the mitochondria (labeled in yellow) were not detected inside the inclusion but rather at the periphery of the inclusions. Interestingly, despite the proximity of the cellular inclusions to the nucleus, the inclusion did not compromise the nuclear membrane integrity (Figure S3A).

2.4 Cytoplasmic and nuclear Httex1 inclusions in HEK cells exhibit distinct ultrastructural properties

Both cytoplasmic and nuclear inclusions have been observed in HD patients’ brains and transgenic mouse models of HD[314,416,417]. Therefore, we compared the structural and organizational properties of Httex1 72Q inclusions in the cytoplasm (~85%) and nucleus (~15%) of the transfected HEK cells containing inclusions[292]. Using immunofluorescence-based confocal microscopy, we did not observe significant differences in the size or overall morphology between the Httex1 72Q inclusions in the nucleus and the perinuclear region (Figure 2A). However, EM clearly showed that the nuclear inclusions formed by the Httex1 72Q were enriched in fibrillar structures (Figure 2B) but did not exhibit the classical core and

shell organization, nor did they contain the membranous structures trapped within the cytoplasmic inclusion (Figure 1D-E). This suggests that the intracellular environment is a key determinant of the structural and molecular complexity of the inclusions and that nuclear and cytoplasmic inclusion formation occurs via different mechanisms.

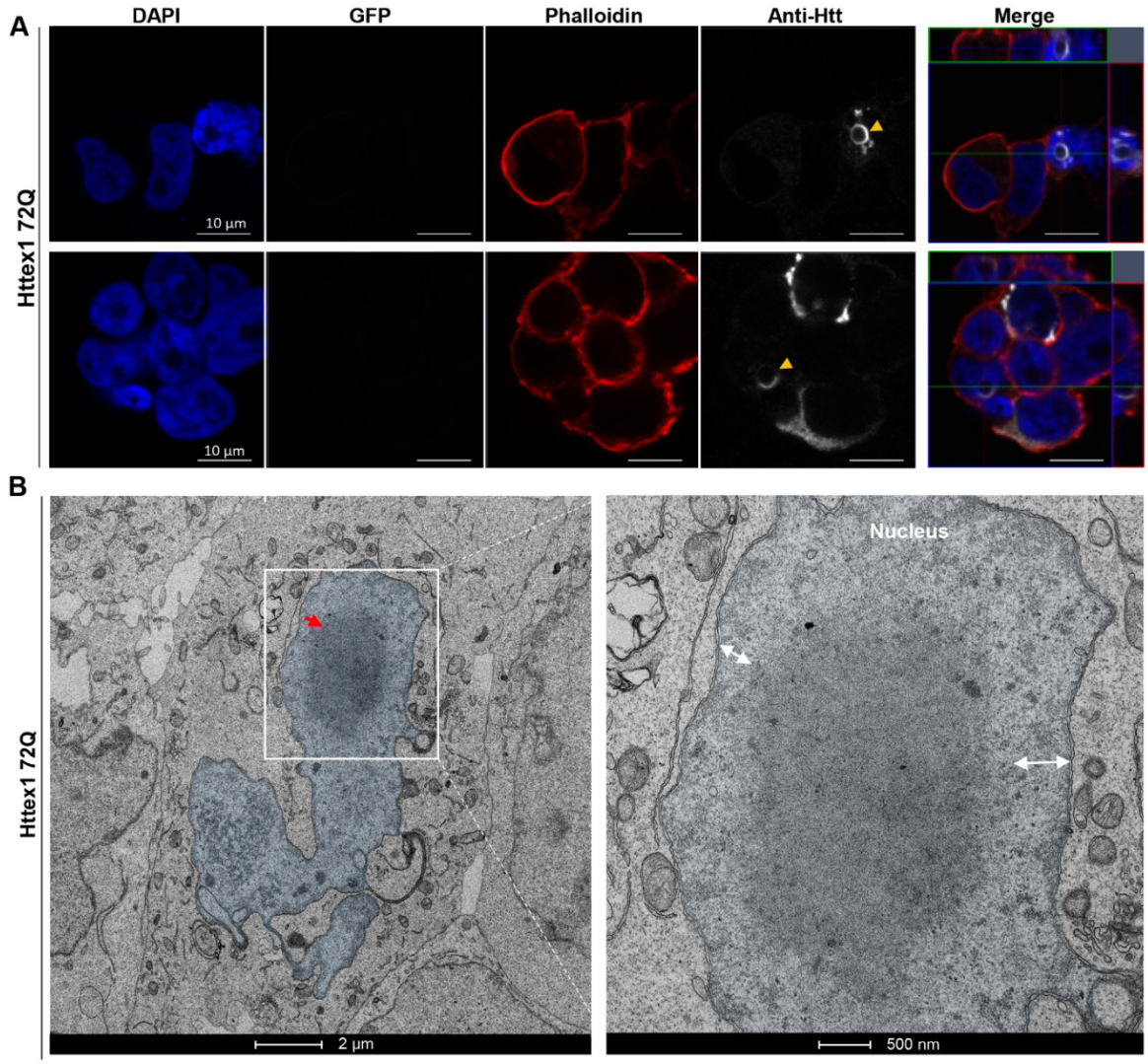

Figure 2. The nuclear inclusions formed by Httex1 72Q do not exhibit the classical core and shell organization observed for the cytosolic inclusions.

A. Representative confocal images of Httex1 72Q nuclear inclusions, 48 h after transfection. Httex1 expression (grey) was detected using a specific primary antibody against the N-terminal part of Htt (amino acids 1-17; 2B7 or Ab109115). The nucleus was counterstained with DAPI (blue), and phalloidin (red) was used to stain the actin F. Httex1 nuclear inclusions are indicated by the yellow arrowheads. Scale bars = 10 µm. **B.** Electron micrograph of a representative nuclear Httex1 72Q inclusion. The white square indicates the area shown at higher magnification in the right-hand panel. The nucleus is highlighted in blue, and the double arrows indicate the distance between the nuclear inclusion and the nuclear membrane. No

interaction between the nuclear inclusion and the nuclear membrane was observed. Scale bars = 2 µm (left-hand panel) and 500 nm (right-hand panel).

2.5 The length of the polyQ domain is another key determinant of inclusion formation

We and others have previously shown that the polyQ repeat length strongly influences the conformation and aggregation properties of Httex1, with higher polyQ favoring the formation of a more compact polyQ domain and accelerating Htt aggregation *in vitro* and *in vivo*[135,193,418]. However, the polyQ dependence on Htt inclusion formation has predominantly been assessed mainly by ICC and in the context of Htt fused to fluorescent proteins and polyQ repeats much longer than the pathogenic threshold (64Q-97Q[195]; 64Q-150Q[409]; 43Q-97Q[266]). Therefore, we next investigated whether the length of the polyQ repeat also influences the organization and ultrastructural properties of cytoplasmic Htt inclusions in HEK cells. Toward this goal, we investigated the level of aggregation and the structural organization of the Httex1 inclusions carrying different polyQ lengths (16Q, 39Q vs. 72Q). Consistent with previous data from our group, no significant cell death was observed in HEK cells overexpressing Httex1 16Q or 39Q constructs even after 96 h[292]. However, cells expressing Httex1 72Q underwent apoptosis after 96 h. As expected, no inclusions were formed upon overexpression of Httex1 16Q even after 72 h post-transfection (Figure S6). Httex1 39Q inclusions were detected predominantly in the cytoplasm of the HEK cells at all the time points examined (24-72 h), though at lower numbers than in the Httex1 72Q conditions: Httex1 39Q (16%) vs. Httex1 72Q (38%) of transfected cells[292].

Characterization of the inclusions by EM revealed that the polyQ tract length dramatically influences the ultrastructure properties of the Httex1 inclusions. The dark shell structure that delimits the core from the periphery of the Httex1 72Q inclusions (Figure 1D-E) was absent in the Httex1 39Q inclusions (Figure 1G). In addition, the Httex1 39Q inclusions appeared less dense compared to those of the Httex1 72Q. These observations were consistent for all eight inclusions imaged per condition (Figure S3B).

Similar to what we observed for Httex1 72Q, the 3D reconstruction of the Httex1 39Q inclusions clearly showed alteration of the ER organization, as well as the localization of mitochondria near the inclusions (Figure 1H and movie 2). The electron-dense membranous structures found inside the inclusions were identified as endomembranes and vesicles. Httex1 39Q expressing cells also contained specific ER-cisternae at the periphery of the inclusions (Figure 1H, red arrowheads). Altogether, our data establish that polyQ expansion plays a critical role in determining the final architecture and ultrastructural properties of the Httex1 inclusions.

2.6 Removal of the Nt17 domain reduces aggregation formation but does not influence the organization and ultrastructural properties of the inclusions

The Nt17 domain functions as a Nuclear Export Signal (NES) and has been shown to play an important role in regulating the intracellular localization of Htt as well as its kinetics of aggregation and extent of inclusion formation[142,146]. Therefore, we sought to assess the role of Nt17 in regulating the ultrastructural properties of Htt inclusions. Towards this goal, we generated Httex1 39Q and 72Q mutants lacking the entire Nt17 domain (ΔNt17) and compared the structural properties of the inclusions formed by these mutants to those formed by Httex1 39Q and Httex1 72Q. Quantitative confocal microscopy revealed a strong reduction in the number of inclusions (~50% reduction) of cells transfected by Httex1 ΔNt17 72Q compared to Httex1 72Q[292]. Surprisingly, inclusions formed by the Httex1 ΔNt17 72Q (Figure S7A-B) exhibited an architecture and organization (central core and peripheral shell) similar to those formed by Httex1 72Q (Figure 1D-E and Figure S8A). Furthermore, similar to Httex1 39Q, the Httex1 ΔNt17 39Q cytoplasmic inclusions did not exhibit a core and shell architecture. These observations suggest that the Nt17 domain – while playing a crucial role in regulating the kinetics and early events of Htt aggregation – does not influence the morphology or structural organization of Htt cytoplasmic and nuclear inclusions.

2.7 Neutral lipids are incorporated into Httex1 cellular inclusions in a polyQ length-dependent manner

Recent studies showed that the formation of pathological inclusions, Lewy bodies in Parkinson's disease, involves the recruitment of lipids and membranous organelles[211,223]. Although several studies have shown dysfunction of cholesterol metabolism in various cellular and animal models of HD[419,420], the role of lipids in Htt inclusion formation and the lipid composition of cellular huntingtin inclusions remains unknown[421,422]. To gain further insight into the role of lipids in the formation and structural organization of Httex1 inclusions, we next assessed their presence using fluorescent probes targeting different lipid classes. We did not observe the recruitment of ceramide, cholesteryl ester, or phospholipids into mutant Httex1 inclusions (Figure S9 A-C). Interestingly, neutral lipids were not found in the center of Httex1 39Q inclusions (Figure S9D white arrowheads) but were enriched in Httex1 72Q inclusions (Figure S9E). This could contribute to the polyQ length-dependent differences in the ultrastructural properties of the Httex1 inclusions (Figures 1E and 1G). Neutral lipids were also detected in nuclear inclusions (Figure S9E, yellow arrowheads). Although the Nt17 domain has been shown to act as a lipid- and membrane-binding domain, neutral lipids were also detected in the Httex1 ΔNt17 72Q inclusions, though not inside Httex1 ΔNt17 39Q inclusions (Figure S10A). These results demonstrate that polyQ-dependent interaction between Htt and neutral lipids plays an important role in Httex1 aggregation and the formation of both nuclear and cytoplasmic inclusions. Interestingly, these interactions are not dependent on the Nt17 domain, which has been reported to interact with membranes and phospholipids. Whether mutant Httex1 interactions with lipids occur prior to aggregation and help initiate its oligomerization or represent late events associated with the maturation of inclusions remains unknown.

2.8 Quantitative proteomics reveals that the formation of Httex1 72Q inclusions involves the active recruitment and sequestration of proteins and organelles

Our EM studies combined with 3D reconstructions showed that the formation of Httex1 72Q inclusions is accompanied by the sequestration of disrupted ER and vesicles inside the inclusion while mitochondria and membranous organelles surround its periphery. To gain further insight into the biochemical composition of Htt inclusions, we investigated the proteome of Httex1 72Q inclusions. Toward this goal, we first established a detergent fractionation protocol to isolate strongly insoluble proteins due to the formation of Httex1 inclusions in HEK cells, 48h post-transfection. Httex1 inclusions were isolated using ultracentrifugation and dissolved using Sarkosyl supplemented by 8M urea and sonication. Western Blot analysis of the Urea fraction confirmed the presence of Httex1 72Q within inclusions, while non-pathogenic Httex1 16Q was only detected in the soluble fraction (Figure S11A). We then performed quantitative proteomic analysis and compared the differentially abundant proteins between the Urea soluble fractions of HEK cells overexpressing Httex1 72Q or Httex1 16Q (see experimental details, Figure S11A-C).

The volcano plot shown in Figure 3A results from three independent experiments (FDR <0.05 and S0 of 0.5). As expected, no proteins were significantly enriched in the insoluble fraction of HEK cells expressing Httex1 16Q compared to those expressing GFP (Figure S11D). This is in line with our previous findings showing that Httex1 16Q overexpression does not result in the formation of inclusions (Figure S6). In contrast, 377 proteins were significantly enriched in the insoluble fraction of HEK cells overexpressing Httex1 72Q compared to cells overexpressing Httex1 16Q (Figure 3A). Among these proteins, we identified the endogenous HTT protein (Figure S11E). This suggests that the aggregation process triggered by the overexpression of Httex1 also leads to the recruitment of endogenous HTT protein.

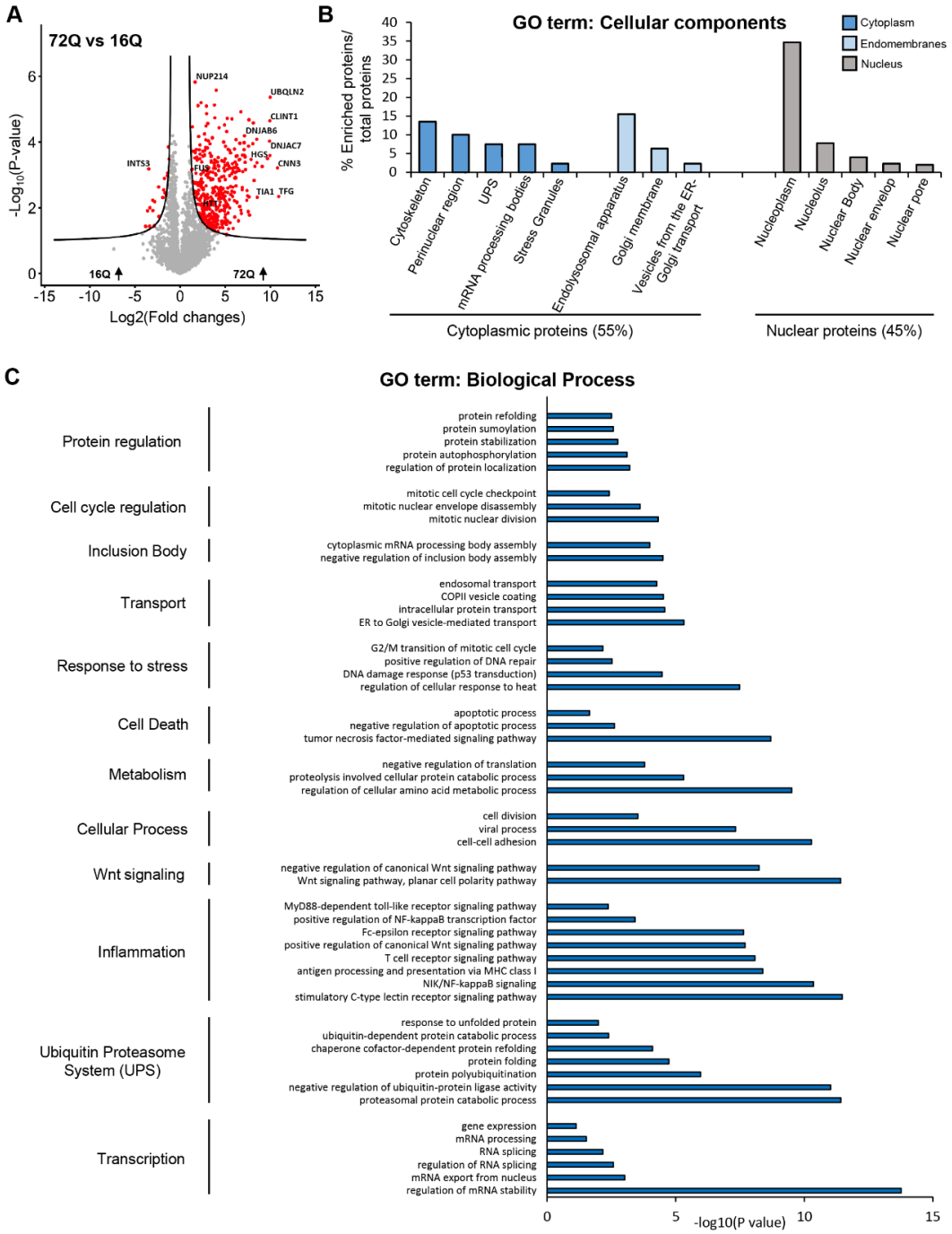

Figure 3. Proteomic analysis of the enriched protein contents found in the insoluble fraction of HEK expressing Httex1 72Q reveals protein aggregation and stress response pathways.

Urea soluble proteins from HEK expressing Httex1 72Q or Httex1 16Q of 3 independent experiments were extracted 48 h after transfection and analyzed using LC-MS/MS. **A.** Identified proteins were plotted using a volcano plot. Black lines represent the threshold of significance at a false discovery rate (FDR) <0.05 and an S0 of 0.5, which were used for the subsequent analysis. **B-C**. Proteins significantly enriched in Httex1 72Q (red dots in the right part of the volcano plot) were classified by cellular component (**B**) or biological processes (**C**) using Gene Ontology (GO) term and DAVID enrichment ($-\log_{10}$(p-value) >1) analyses.

The Gene Ontology (GO) term analysis combined with the database for annotation, visualization, and integrated discovery (DAVID) analysis was used to classify these proteins by cellular component (Figure 3B) and biological process (Figure 3C). Upregulated signaling pathways were investigated using the Ingenuity Pathway Analysis (IPA) (Figure S12).

Classification by cellular component (CC, Figure 3B) using the Gene Ontology (GO) showed that 55% of the proteins enriched in the insoluble fractions of HEK cells containing Httex1 72Q inclusions were part of the cytoplasmic compartment, with 24% of these proteins belonging to the endomembrane system, including the endolysosomal apparatus (clathrin-coated endocytotic vesicles, early endosome, endosomes, recycling endosomes, exosomes, and autophagosomes), the vesicles involved in Golgi-ER transport, and membranes from the Golgi and trans-Golgi network. These data are in line with the EM data showing that the Httex1 72Q inclusions were composed of small membranous structures and vesicles. Approximately 14% of the proteins enriched in the insoluble fraction were classified as pertaining to the cytoskeleton compartment, with the actin cytoskeleton being the most predominant, consistent with our confocal results (Figure 1B). The absence of mitochondrial proteins in the soluble Urea fraction confirms that mitochondria are not sequestered inside the inclusions but, rather, accumulate at the periphery, as shown by our EM imaging. The rest of the cytoplasmic proteins sequestered in the insoluble fraction of the Httex1 72Q-transfected HEK cells were mainly from the perinuclear region or from macromolecular protein complexes such as the ubiquitin-proteasome system (UPS), the mRNA processing bodies, and the stress granules. Interestingly, the insoluble fraction of the Httex1 72Q-transfected HEK cells was also significantly enriched by proteins of the nuclear compartment (~ 45%). Among the nuclear proteins, ~ 71.6% belonged to the nucleoplasm. Proteins from the nucleolus, the nuclear bodies, the nuclear envelope, and the nuclear pore were also significantly enriched.

To better understand how the sequestration of functional proteins during the process of Httex1 72Q inclusion formation and maturation could impact the biological functions of the cells, we

next classified the proteins enriched in the Httex1 72Q-transfected HEK by biological process (Figure 3C) and signaling pathways (Figure S12). In line with the cellular compartment analysis, our proteomic data showed that the most highly enriched terms for the biological process and the signaling pathways were related to the proteins involved in the proteasomal ubiquitin-dependent protein degradation. In addition, proteins related to the chaperone machinery (e.g., DNAJB6, DNAJB2, and other proteins from the Hsp40 and Hsp70 families) were enriched in the insoluble fraction of the HEK cells with Httex1 72Q inclusions. Altogether, our data suggest that the formation and maturation of the Httex1 72Q inclusions are accompanied by the sequestration of the proteins involved in the degradation machinery and the protein quality control pathway. This might potentially result in the failure of the protein degradation machinery to clear off the Httex1 72Q inclusions.

Finally, several signaling pathways and biological processes related to toxicity, oxidative stress, and inflammation responses were upregulated in the HEK cells with Httex1 72Q inclusions (Figure 3C and Figure S12). These include Huntington's disease signaling and several apoptosis processes, such as death receptor signaling and TWEAK signaling, but also the iNOS and the oxidative stress signaling pathways. The inflammation signaling pathways, such as Toll-like receptor signaling, interleukins signaling, and NFκB signaling, were among the top canonical pathways shown as upregulated in the insoluble fraction containing the Httex1 72Q inclusions. Oxidative stress and inflammation responses are closely interrelated and have been suggested to be key players in disease progression for HD and neuronal dysfunctions.

Together, our proteomic and CLEM data provide strong evidence that the formation of the Httex1 72Q inclusion formation involves the active recruitment and sequestration of cellular proteins, lipids, and organelles. This also suggests that sequestration of the key transcription regulators and depletion of key proteins from the autophagolysosomal, UPS, and chaperone pathways, due to their sequestration inside the Httex1 pathological inclusions, are major

contributors to cellular dysfunction and neurodegeneration in HD of the degradation and quality control machinery, as reported in HD human brain tissue[423].

2.9 Httex1 72Q cytoplasmic inclusion formation induces mitochondrial fragmentation, increases mitochondrial respiration and leads to ER-exit site remodeling

The remarkable accumulation of damaged mitochondria at the periphery of Httex1 72Q inclusions prompted us to investigate how Htt inclusion formation impacts mitochondrial functions. Quantification of mitochondrial length from EM-micrographs revealed a shorter mitochondrial profile associated with Httex1 72Q inclusions, as compared to HEK cells transfected with empty vector (Figure 4A-B). Similar levels of the outer mitochondrial membrane protein VDAC1 suggest that this mitochondrial fragmentation was not associated with a decrease in mitochondrial density (Figure S13A). We hypothesized that the fragmentation and recruitment of mitochondria to Httex1 inclusions might be associated with respirational dysfunction. Therefore, we performed high-resolution respirometry on cells transfected with Httex1 16Q and 72Q for 48 h. Aggregates were only detected in mutant Httex1 72Q transfected cells (Figure S13B). We assessed different respirational states of mitochondria by high-resolution respirometry (Figure S13C-D). Httex1 72Q transfection resulted in significantly higher mitochondrial respiration than Httex1 16Q (Figure S4C). Together, our results demonstrate a clear impact of Httex1 72Q inclusion formation on mitochondrial morphology and function.

Our EM analysis and 3D reconstruction further revealed the presence of ER cisternae at the periphery of the Httex1 inclusions. Stacked ER cisternae are usually formed by an increasing concentration of specific resident proteins or stress conditions[424].

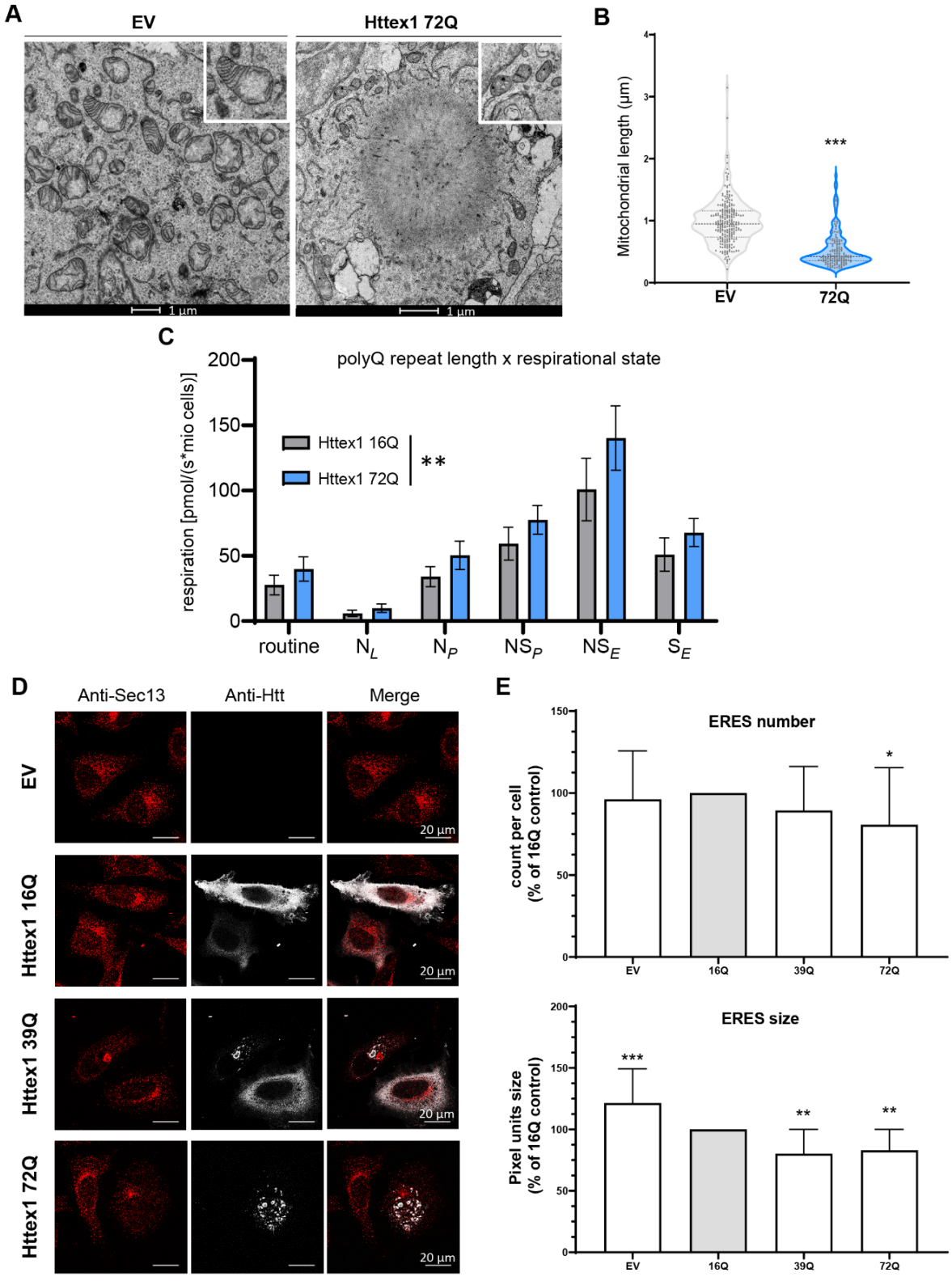

Figure 4. Formation of Httex1 72Q inclusions induces mitochondrial alterations and induces the reduction of ER-exit sites.

A. Electron micrographs of mitochondria in HEK cells overexpressing empty vector (EV) or Httex1 72Q. The insets depict higher magnification of the mitochondria found at the periphery

of the Httex1 72Q inclusions or representative in EV controls. Scale bars = 1 µm. **B.** Measurement of the mitochondrial length with FIJI reveals a significant reduction in the size of the mitochondrial profile located in the proximity of the inclusions. **C.** HEK cells from 4 independent experiments were gently detached for high-resolution respirometry (HRR) 48 h after transfection with indicated constructs. HRR was performed in respiration media (MIR05). After the measurements of routine respiration, cells were chemically permeabilized by digitonin, and different respirational states were subsequently induced using a substrate-uncoupler-inhibitor titration (SUIT) protocol. Routine respiration, NADH-driven, or complex 1-linked respiration after the addition of ADP (OXPHOS state) (NP), NADH- and succinate driven, or complex 1 and 2-linked respiration in the OXPHOS state (NSP), and in the uncoupled electron transport system (ETS) capacity (NSE), as well as succinate driven, or complex 2-linked respiration in the ETS state (SE) were assessed. (B) An unpaired t-test was performed. (C) The graphs represent the mean ± SD of 4 independent experiments. (C) Two-way ANOVA showing a significant interaction between the respirational states and the polyQ repeat length. **D.** Representative confocal images of HeLa cells transfected with Httex1 16Q, 39Q, or 72Q or the empty vector (EV) as the negative control. Cells were fixed 48 h after transfection and immunostained. Httex1 was detected with the MAB5492 Htt antibody (grey), and ER exit sites were detected with Sec13 (red). Scale bars = 20 µm. **E**. ERES number and size quantification from confocal imaging was performed using FIJI. The graphs represent the mean ± SD of 3 independent experiments represented as the relative percentage of the Httex1 16Q control. ANOVA followed by a Tukey honest significant difference [HSD] post hoc test was performed. *P < 0.05, **P < 0.005, ***P < 0.001.

The changes we observed in ER organization, together with the enrichment of proteins related to ER-Golgi trafficking inside the inclusions, prompted us to investigate whether ER functions were impaired upon the formation of the Httex1 inclusions. A major function of the ER is the biogenesis of COPII carriers that ferry proteins and lipids to distal compartments. COPII carriers form at ER exit sites (ERES), which are ribosome-free domains of the rough ER.

To determine whether the formation of Httex1 inclusions interferes with the homeostasis of the ERES, we used confocal imaging and quantified the number of ERES, labeled specifically by the COPII component Sec13 protein in HeLa cells expressing Httex1 72Q, Httex1 39Q, or Httex1 16Q (Figure 4D). Our data show that the number of ERES was significantly reduced (~ 20%) only in cells containing Httex1 72Q inclusions (Figure 4E, upper panel). We next quantified the size of the ERES using the same imaging pipeline (Figure 4E, lower panel). Overexpression of Httex1 16Q caused a 20% reduction in the size of the ERES compared to EV. However, the reduction became much more significant in the cells carrying Httex1 39Q or

Httex1 72Q, with a ~40% decrease compared to empty vector and ~20% compared to Httex1 16Q. These results demonstrate that the formation of the Httex1 inclusions interferes with the formation and fusion of ERES. The remodeling of ERES in cells has been described primarily as an adaptive response to the protein synthesis level of ER with the number of ERES proportional to the cargo load. Interestingly, our proteomics results (Figure 3A) showed that the TGF (Transforming Growth Factor) protein—which plays a central role in the biogenesis and organization of ERES—is sequestered in mutant Httex1 inclusions[425]. In line with our results, it has been previously shown that the depletion of TGF induced a dramatic reduction of the ERES sites[426]. Alternatively, the reduction of the ERES sites could represent early signs of cell vulnerability and toxicity induced by the presence of the Httex1 inclusions in cells.

2.10 The addition of GFP to the C-terminal part of Httex1 induces a differential structural organization revealed by CLEM.

Given that the great majority of cellular models of HD rely on the use of fluorescently tagged Htt constructs, we next investigated the aggregation properties of mutant Httex1 fused to GFP (Httex1 72Q-GFP and Httex1 39Q-GFP). First, we assessed the morphology of Httex1 72Q-GFP cytoplasmic inclusions in HEK cells by immunocytochemistry (ICC) using a panel of Httex1 antibodies (Figures 5A-B and S14A). Confocal imaging revealed a diffuse GFP signal throughout the inclusions. Conversely, the Htt antibodies labeled mainly the outermost region of Httex1 72Q-GFP inclusions, but also faintly stained their centers (Figure 5B). In contrast, the tag-free inclusions' cores were not labeled by all the Htt antibodies tested. Thus, we hypothesized that the presence of the GFP tag results in the formation of less compact Httex1 inclusions. While Actin-F was found to colocalize with tag-free Httex1 inclusions [(Figure 1B, Httex1 72Q), 39Q (Figure S9D, Httex1 39Q), and ΔNt17 Httex1 72Q (Figure S10A, ΔNt17 Httex1 72Q)], no specific enrichment of Actin-F was detected in the core or periphery of the Httex1 72Q-GFP inclusions. Furthermore, actin filaments were found exclusively at the

periphery of the tag-free Httex1 72Q and 39Q (+/- ΔNt17) cytoplasmic inclusions (Figures 1B and S10A). These results suggest a potential role of actin in the formation of Httex1 inclusion formation or maturation. Consistent with these observations, the actin cytoskeleton was one of the most dysregulated pathways according to a proteomic analysis conducted in human HD brains[427], underscoring its importance in the development of HD pathology.

Next, we performed a more in-depth analysis of the Httex1 72Q-GFP cellular inclusions formed in HEK by CLEM (Figure 5C-D). The Httex1 72Q-GFP inclusions were organized as a highly dense network of fibrils, which were more homogenously stained (Figures 5D and S14C) and did not exhibit the core and shell architecture that is characteristic of the tag-free Httex1 72Q inclusion (Figure 1D and S14D). Closer examination of the inclusions showed that they were composed of densely packed fibrils that exhibited a striking resemblance to the fibrillar aggregates formed by mutant Httex1 proteins in a cell-free system (Figures 5D and S14B). Structural analysis of Httex1 72Q-GFP by high-pressure freezing fixation (Figure S4B) also revealed densely packed fibrils radiating from the inclusions. The center of the inclusions was not well resolved, but thicker fibrils could clearly be observed radiating at the periphery with increased spacing between them compared to tag-free Httex1 72 inclusion (Figure S4A). A portion of Httex1 72Q-GFP inclusions exhibited perinuclear localization. In some cases, the accumulation of fibrils near the nuclear membrane leads to apparent distortion of the nucleus but without membrane disruption (Figure 5D and S15A). Overall, we observed no significant differences in diameter and distance from the nucleus for all the Httex1 (+/-GFP) inclusions imaged in HEK cells (Figure S16).

Next, we investigated the ultrastructure properties of Httex1 72Q-GFP inclusions present in the nucleus of the HEK cells (Figures 5E-F). No significant differences in terms of organization were observed between nuclear and cytoplasmic Httex1 72Q-GFP inclusions by both GFP detection and antibody staining (Figure 5E). The Httex1 72Q-GFP nuclear inclusions were also enriched in fibrillar structures.

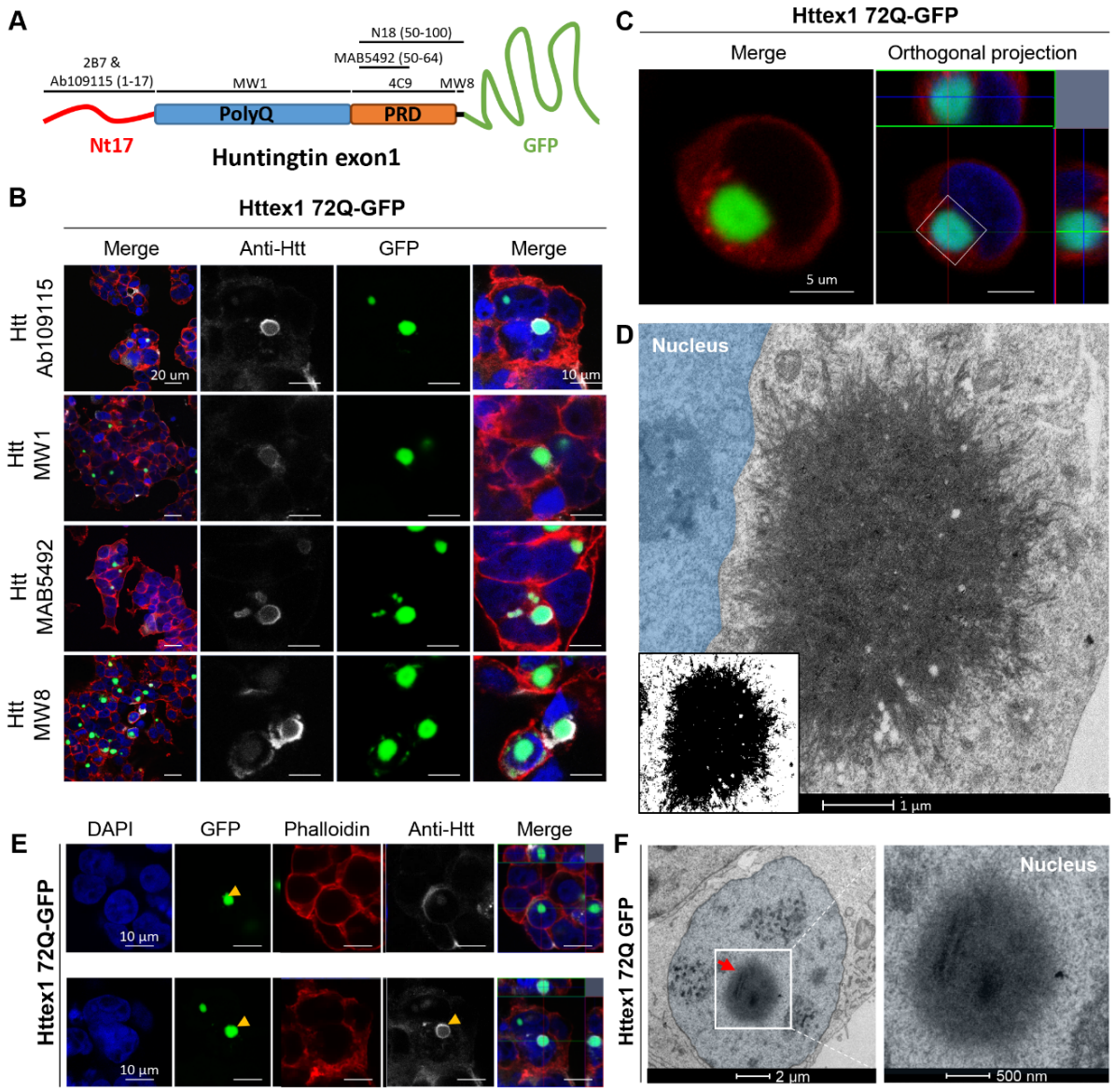

Figure 5. The addition of GFP to the C-terminal part of Httex1 induces a differential structural organization as revealed by ICC and CLEM.

A. Epitope mapping of the Httex1 antibodies. **B.** Httex1 72Q-GFP inclusions formed 48 h after transfection in HEK cells were detected by ICC staining combined with confocal imaging. All Htt antibodies showed strong immunoreactivity to the periphery of the Httex1 inclusions and modest immunoreactivity to the core. The nucleus was counterstained with DAPI (blue) and the F-actin with phalloidin (red). Scale bar = 20 µm (left-hand panels) and 10 µm (middle and right-hand panels). **C-D.** 48 h post-transfection, HEK cells were fixed, and ICC against Httex1 was performed and imaged by confocal microscopy (**C**). Scale bars = 5 µm. The selected area of the cells (white square) was then examined by EM (**D**). A binary image (inset) was generated from the electron micrograph using a median filtering and Otsu intensity threshold, allowing for a better distinction of the inclusions' morphology. Scale bar = 500 nm. **E.** Representative confocal images of Httex1 72Q-GFP nuclear inclusions formed in HEK cells 48 h after transfection. Httex1 expression (grey) was detected using a specific antibody against the N-terminal part of Htt (amino acids 1-17; 2B7 or Ab109115), and GFP (green) directly visualized

in the appropriate channel. The nucleus was counterstained with DAPI (blue), and phalloidin (red) was used to stain filamentous actin. Httex1 nuclear inclusions are indicated by yellow arrowheads. Scale bars = 10 µm. **F.** Electron micrograph of a representative Httex1 72Q-GFP inclusion. The white square indicates the area shown at higher magnification in the right-hand panel. The nucleus is highlighted in blue. Scale bar = 2 µm (left-hand panel) and 500 nm (right-hand panel).

The 3D reconstruction generated from the series of electron micrographs revealed much fewer membranous structures in both Httex1 39Q-GFP and Httex1 72Q-GFP inclusions (Figure S17) compared to tag-free Httex1 inclusions (Figures 1F and 1H). Moreover, consistent with EM observations, no neutral lipids were found in Httex1 39Q-GFP and Httex1 72Q-GFP inclusions (Figure S10B-C). Interestingly, neither the length of the polyQ repeat nor the presence or removal of the Nt17 domain seem to significantly alter the size, morphology or structural properties of the inclusions formed by mutant Httex1 proteins fused to GFP (Figure S18). This is different from what we observed for cells expressing tag-free Httex1, in which the increase of the polyQ length led to inclusions with distinct morphologies and organizational features. These findings suggest that the addition of GFP significantly alters the mechanism of Httex1 aggregation and inclusion formation.

To obtain an even clearer picture of these differences, we next performed EM under detergent-free conditions to preserve the internal membranes and structures of the inclusions. We observed that the length of the polyQ repeat did not influence the size of the Httex1 39Q-GFP and 72Q-GFP inclusions (Figure S16B) or their overall architecture in HEK cells. The Httex1 39Q-GFP inclusions are composed of radiating fibrils and are thus similar to the Httex1 72Q-GFP inclusions, although slightly less dense. The 3D reconstruction of the inclusions showed the presence of ER and mitochondria in their periphery, but few membranous structures were internalized (Figure S17B yellow arrowhead) as compared to tag-free Httex1 39Q and Httex1 72Q inclusions. A similar analysis of Httex1 ΔNt17 39Q-GFP and Httex1 ΔNt17 72Q-GFP inclusions (found in cells) (FigureS18A-D) also revealed no effect of Nt17 deletion on the ultrastructure of the inclusions or their interactions with the surrounding organelles. These

results confirm that mutant Httex1 aggregation and inclusion formation mechanisms are significantly altered by the addition of the GFP.

2.11 Phase transition of Httex1 GFP aggregate formation is mediated by the polyQ domain

To gain further insights on the role of the polyQ expansion in Httex1 aggregation mechanisms, we next investigated the dynamics of aggregate formation in live cells. Although we have shown that the GFP tag dramatically influences the morphology of the Httex1 inclusions, it is still a reliable tool to monitor the kinetics of early events during the aggregation of Htt in live cells. Therefore, we took advantage of the GFP tool to assess how the polyQ expansion might influence the dynamic of aggregation by live imaging, as the polyQ-dependent morphology was also observed in Httex1-GFP aggregates.

Our real-time study showed that once the aggregation has started, Httex1 39Q-GFP or Httex1 72Q-GFP inclusions grew extremely fast into larger and highly bright inclusions as reflected by the increase of the GFP intensity (Figure 6A-C and 6D-F). Strikingly, almost all the soluble Httex1 proteins were recruited to the Httex1 72Q-GFP or the 39Q-GFP inclusions from 10 to 30 min after the start of visible aggregation in one part of the cell.

To further analyze the kinetics of Httex1-GFP inclusion formation, we measured the intensity of Httex1-GFP cellular inclusion formation during the aggregation process (Figure 6B and 6E). To better analyze the GFP intensity change over time, we generated a sigmoidal interpolation corresponding to a first basal expression of GFP followed by an exponential increase to finally reach a plateau of intensity. The analysis of the interpolated curve demonstrated a faster inclusion formation for Httex1 72Q-GFP (relative slope: 8.65) compared to Httex1 39Q-GFP (relative slope: 2.57), Figure 6B and 6E. This result indicates that the long polyQ length (72Q) is associated with a reduced inclusion formation time from the start of aggregation to the final intensity plateau of the inclusion. In addition, our live imaging data also demonstrated that the

aggregates formed were highly dynamics and could undergo fusion and fission events at the early stages of the inclusion formation process (Figure S24). These processes have been recently described as a liquid-liquid phase transition[266] and suggested to be highly dynamic.

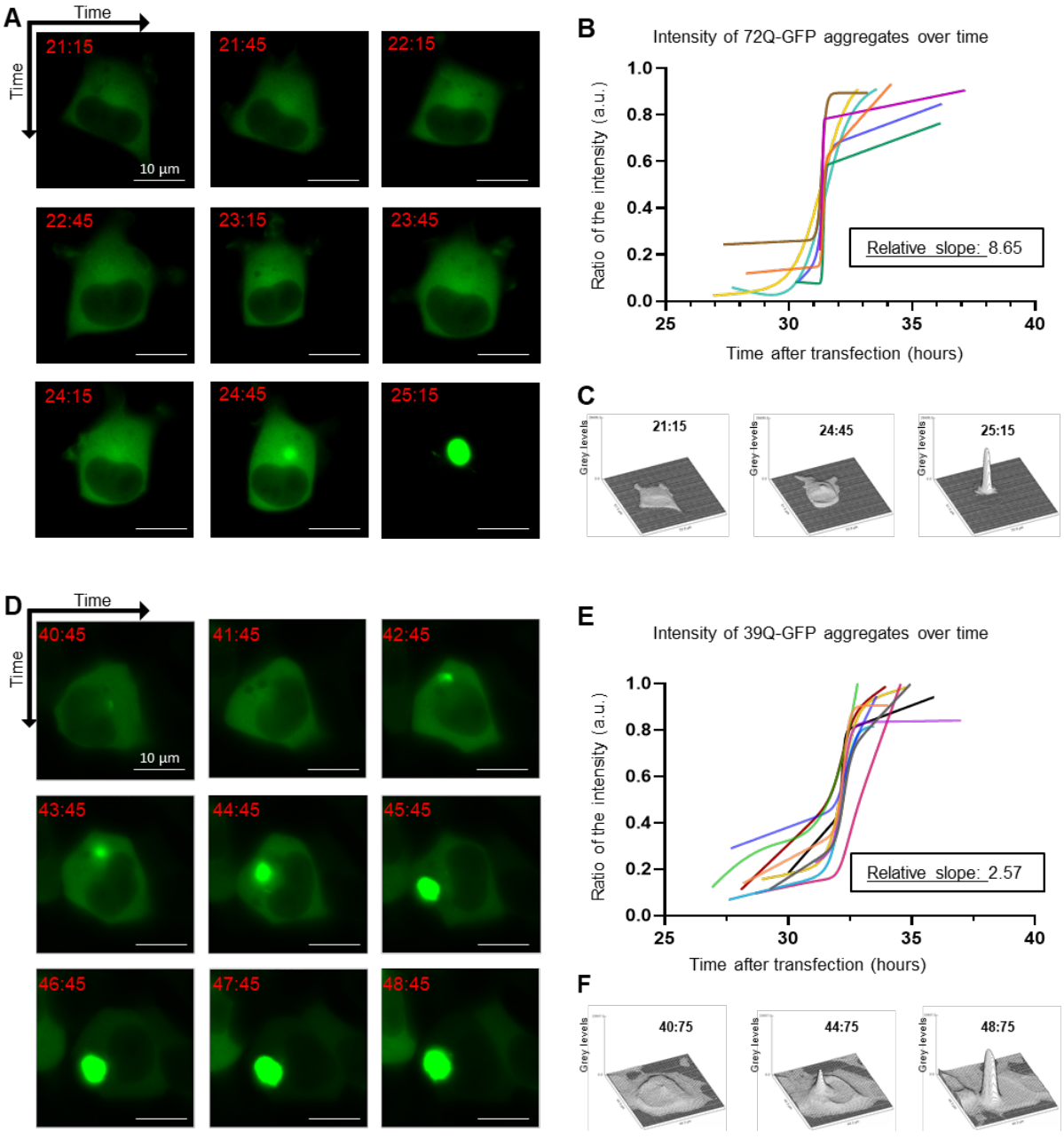

Figure 6. The dynamic of Httex1-GFP inclusions is driven by the polyQ domain.

A. Time-lapse of the GFP fluorescence observed by live-cell microscopy imaging of Httex1 72Q-GFP aggregation. **B.** Intensity of GFP over time of transfected cells with Httex1 72Q -GFP rescaled on the IC50. The mean of the relative slope of Httex1 72Q-GFP intensity at the inflection point of aggregation is indicated on the graph. **C.** Surface plot display of the GFP intensity over time of cell (A). **D.** Time-lapse of the GFP fluorescence observed by live-cell

microscopy imaging of Httex1 39Q-GFP aggregation. **E.** Intensity of GFP over time of transfected cells with Httex1 39Q-GFP rescaled on the IC50. **F.** Surface plot display of the GFP intensity over time of cell (D). The mean of the relative slope of Httex1 72Q-GFP intensity at the inflection point of aggregation is indicated on the graph. Scale bars = 10 µm.

Our results are consistent with previous studies demonstrating that Httex1 inclusions formation is polyQ dependent. Moreover, our EM studies showed that the early dynamic inclusions go on to form mature and fibrillar inclusions, likely via a liquid to solid transition (Figure 1D and 5D). The rapidity of inclusion formation might play a role in the architectural differences of the inclusions depending on the polyQ length and could explain the higher density of Httex1 72Q-GFP compared to Httex1 39Q-GFP.

2.12 The Httex1 72Q and Httex1 72Q-GFP inclusions exhibit distinct proteome composition

To further assess the similarities and differences in the proteome composition of cellular Httex1 inclusions formed by the tag-free and GFP mutant Httex1-72Q, we performed a quantitative proteomic analysis of the insoluble fractions from lysates of cells expressing these constructs (see experimental workflow, Figure S11A). Volcano plot analysis showed 492 proteins significantly enriched in the insoluble fraction of the HEK cells overexpressing Httex1 72Q-GFP as compared to those expressing GFP (Figure 7A). We observed a significant enrichment of the endogenous HTT protein, suggesting that, as for the tag-free Httex1 72Q, mutant Httex1-GFP inclusions can recruit the endogenous HTT protein (Figure S11E).

The cytoplasmic components enriched in the insoluble fraction of Httex1 72Q-GFP were similar to those found with tag-free Httex1-72Q and were part of the endomembrane system (~50%, light blue Figure 7B), the cytoskeleton, the perinuclear region, the UPS, mRNA processing bodies, and stress granules (Figure 7B, dark blue). However, in contrast to the tag-free Httex1 72Q insoluble fractions, in which no mitochondrial protein was found to be enriched, 10% of

the proteins enriched in the Httex1 72Q-GFP insoluble fraction were related to the mitochondria compartment (purple Figure 7B). The nuclear proteins found in the Httex1 72Q-GFP insoluble fraction belong to similar nuclear compartments as those identified previously in the Httex1 72Q insoluble fraction (Figure 7B, grey).

Biological process (Figure S19) and canonical pathway (Figure S20) analyses revealed that the UPS and chaperone machinery were the most enriched terms, as previously observed in the tag-free insoluble fraction. This indicates that the process of aggregation of Httex1 itself, regardless of the presence of the GFP tag, leads to the sequestration of the key cellular machinery responsible for protein folding and protein degradation. This could compromise the cell's ability to prevent the accumulation or clearance of Httex1 aggregates. Although in different proportions, most of the biological processes and pathways significantly enriched in the tag-free Httex1 72Q insoluble fraction, such as inflammation, transcription, HD signaling, and cell death, were also detected in the Httex1 72Q-GFP insoluble fraction.

Having identified the proteins significantly enriched in both tag-free and GFP-tag 72Q inclusions, we next determined which proteins were unique to each type of inclusion. Toward this goal, we used a Venn diagram to compare the lists of proteins significantly enriched in our volcano plot analyses [(Httex1 72Q vs. Httex1 16Q insoluble fractions) vs. (Httex1 72Q-GFP vs. Httex1 16Q insoluble fractions)] (Figures 3A and S11C). Figure 7C shows that ~45% (256 proteins) were found in both the tag-free and the GFP-tag Httex1 72Q inclusions. In total, 120 proteins (20.9%) were unique to the Httex1 72Q insoluble fraction, and 198 proteins (34.5%) were unique to the Httex1 72Q-GFP. Overall, we found 55% different proteins among the proteins that co-aggregate with or are sequestered in Httex1 72Q vs. 72Q-GFP inclusions, both compared to Httex1 16Q. We used the Kyoto Encyclopedia of Genes and Genomes (KEGG) pathway analysis to classify the list of proteins in Httex1 inclusions (Figure 7D). The proteasome, protein processing in the endoplasmic reticulum, and endocytosis were among the most enriched pathways from the common co-aggregated proteins. Those 3 terms were

also enriched significantly for Httex1 72Q-GFP, indicating the involvement of other unique proteins enriched in those pathways compared to Httex1 72Q.

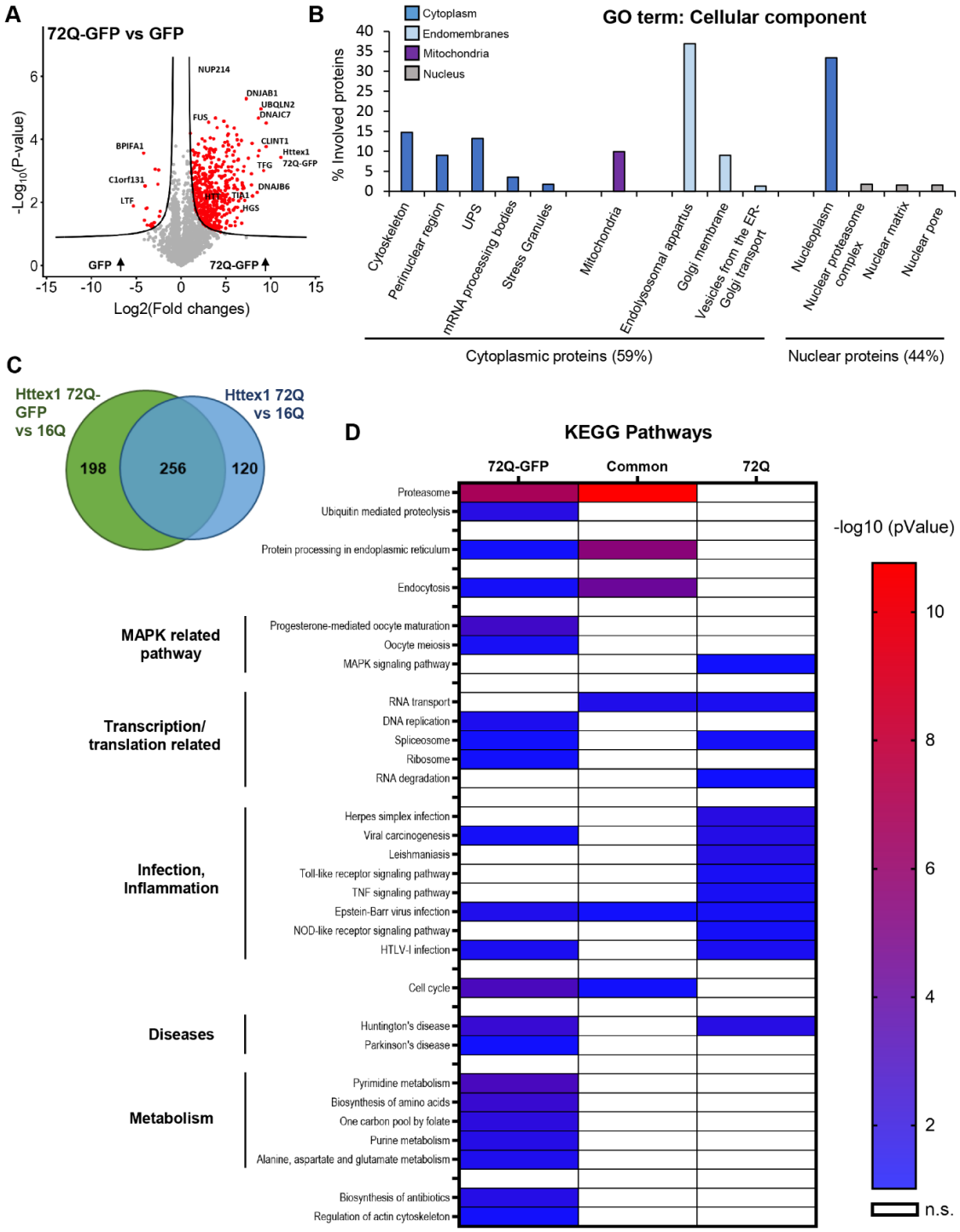

Figure 7. Proteomic analysis of Httex1 72Q-GFP in the Urea soluble fraction revealed 55% differences compared to tag-free Httex1 72Q for the proteins co-aggregated with Httex1 in HEK cells.

A. Identified proteins were illustrated using a volcano plot for the comparison of protein levels identified in the Urea soluble fraction 48 h after Httex1 72Q-GFP or GFP transfection in HEK cells, in 3 independent experiments. Mean difference (Log2 (Fold-Change) on the X-axis) between the Urea soluble fraction of HEK cells overexpressing Httex1 72Q-GFP or GFP were plotted against significance (Log10 (p-Value) on the Y-axis (T-Test)). A false discovery rate (FDR) of 0.05 and a threshold of significance S0=0.5 were assigned for the subsequent analyses. **B.** Cell compartment classification of the proteins significantly enriched in the Urea soluble fraction of the HEK cells overexpressing Httex1 72Q-GFP versus those expressing GFP. Gene Ontology (GO) enrichment analyses were determined by DAVID analysis (p values<0.05). **C.** To compare the results obtained with Httex1 72Q-GFP to tag-free Httex1 72Q, we represented the proteins enriched in Httex1 72Q vs. Httex1 16Q compared to the proteins enriched in Httex1 72Q-GFP vs. Httex1 16Q using a Venn diagram. In total, 256 proteins (44.6%) were found similar between the two conditions, 198 proteins (34.5%) were unique for Httex1 72-GFP enrichment, and 120 proteins (20.9%) were for Httex1 72Q enrichment. **D**. Kyoto Encyclopedia of Genes and Genomes (KEGG) Pathway Analysis of co-aggregated proteins with Httex1 72Q and Httex1 72Q-GFP. The heat map represents significant pathways (KEGG) enriched in the Urea soluble fractions extracted from the Venn diagram (**C**): co-aggregated proteins unique to Httex1 72Q, unique to Httex1-72Q-GFP, and common to both conditions, all compared to Httex1 16Q control.

The KEGG classification revealed two distinct clusters for Httex1 72Q and Httex1 72Q-GFP, as well as additional differences (Figure 7D). Proteins related to infection and inflammatory pathways (e.g., Herpes simplex infection, TNF signaling, and Toll-like receptor signaling) were found to be unique to Httex1 72Q, whereas proteins related to metabolism were specifically enriched for Httex1 72Q-GFP. Our proteomic analysis highlights that the addition of a fluorescent tag such as GFP significantly alters not only the mechanism of Htt inclusion formation but also the Htt interactome and thus the biochemical composition of inclusions.

2.13 What is the role of the proline-rich domain (PRD) in cellular Httex1 inclusion formation?

In addition to the Nt17 domain, the PRD flanking the polyQ stretch was also shown to modulate Httex1 aggregation[149]. Shen *et al.* previously showed that the PRD destabilizes the fibrils and decreases the aggregation kinetics of Httex1 *in vitro.* In order to assess the influence of the PRD on the morphology and the subcellular properties of Httex1 inclusions, we expressed in

HEK cells for 48 h Httex1 72Q and Httex1 72Q-GFP without the PRD (ΔPRD) and without half the PRD (1/2Δ PRD).

First, we characterized the expression of the Httex1 PRD mutants by biochemistry 48 h post-transfection. The soluble fraction was isolated, and the pellet was solubilized with 2% SLS and sonication (insoluble fraction). As expected, WB analysis showed that half and total removal of the PRD decreased the molecular weight of Httex1 and ran lower in the gel for both Httex1 72Q and Httex1 72Q-GFP constructs (red arrowheads, Figure 8A-B). Interestingly, the PRD mutations reduced the protein level of Httex1 and Httex1-GFP in both the soluble and insoluble fractions. This could suggest a role of the PRD on the expression stability of Httex1 at the mRNA level or at the protein level.

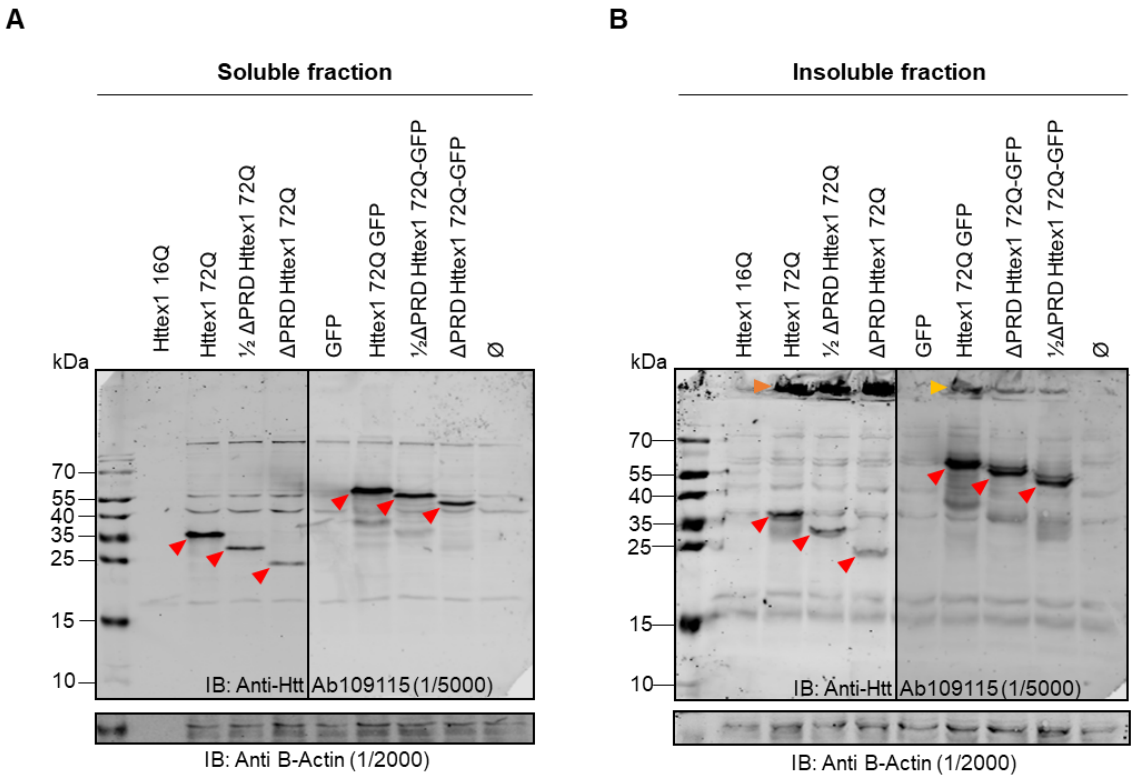

Figure 8. The removal of the PRD induces a decrease in protein level in the soluble and insoluble fractions.

Httex1 expression 48 h after transfection in HEK cells was analyzed by WB post detergent fractionation of the soluble and insoluble fractions. **A.** WB scan of the soluble fraction of tag-free and GFP Httex1 72Q, ΔPRD 72Q and 1/2ΔPRD 72Q as well as Httex1 16Q and GFP controls. Red arrows indicate the specific detection of Httex1. **B.** WB scan of the insoluble

fraction of tag-free and GFP Httex1 72Q, ΔPRD 72Q and 1/2ΔPRD 72Q as well as Httex1 16Q and GFP controls. Red arrows indicate the specific detection of Httex1. Large insoluble aggregates formed by Httex1 72Q constructs could not enter in the gel and are strongly detected for tag-free Httex1 in the stacking gel (orange arrowhead) and at a lower intensity for Httex1-GFP (yellow arrowhead). The results are representative of four independent experiments.

Looking carefully at the insoluble fraction, it appears that some of the aggregates cannot enter the gel and remain at the stacking (Orange and yellow arrowheads, Figure 8B). The same high amount of aggregates was detected for tag-free Httex1 72Q and PRD mutants (Orange arrowhead, Figure 8B) compared to a decreasing amount of aggregates in the stacking part for Httex1 72Q-GFP PRD mutants compared to Httex1 72Q-GFP. The results showed that the deletions of the PRD did not prevent the formation of cellular inclusions but seemed to impact the stability or degradation of Httex1.

Next, confocal imaging analysis revealed that total or partial removal of the PRD did not prevent inclusion formation or alter the morphology of the inclusions, *i.e.,* the formation of a strong immunoreactive “ring-like” inclusions seen for tag-free Httex1 72Q (orange arrowheads, Figure 9A). This result indicates that similar to cellular Httex1 72Q inclusions, ΔPRD and 1/2Δ PRD Httex1 72Q can form mature inclusions that are impermeable to Httex1 antibodies and that the epitopes detected by Ab109115 (Httex1 outside of the PRD) are still accessible at the periphery. In contrast, the expression of Httex1 72Q-GFP and PRD mutants (ΔPRD and 1/2Δ PRD) Httex1 72Q-GFP led to the formation of bright GFP inclusions also recognized only at the periphery by the Ab109115 antibody, but only faintly compared to tag-free Httex1 72Q (Yellow arrowheads, Figure 9B). In addition, small puncta were detected next to the inclusions with the Ab109115 antibody and not with the GFP fluorescence, which might correspond to Httex1 with cleaved GFP, also observed by WB (Figure 8B). However, such puncta were not observed with the tag-free constructs and are not dependent on the PRD.

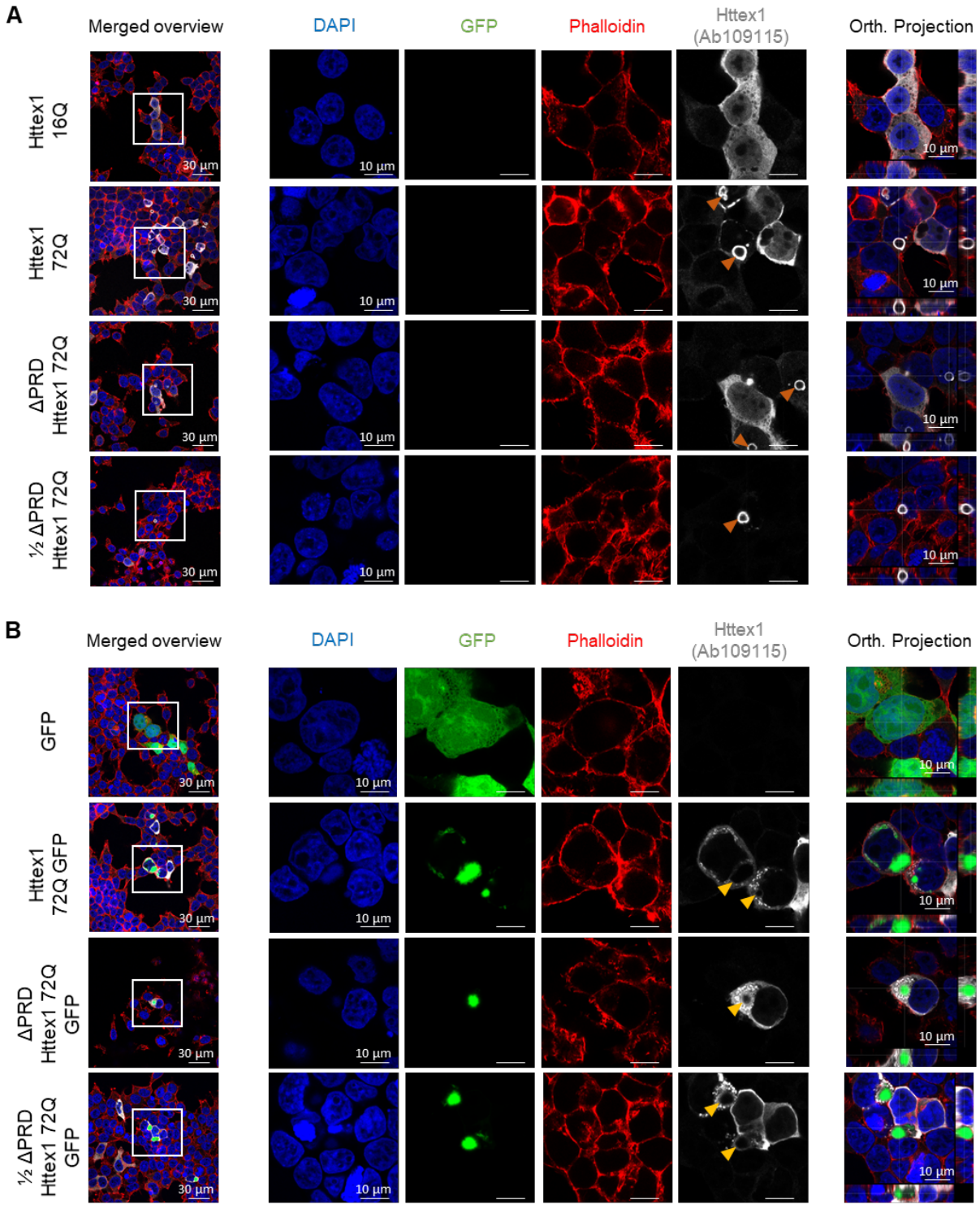

Figure 9. The removal of the PRD does not prevent the formation of cellular inclusions and to be detected as ring-like structures.

Httex1 expression 48 h after transfection in HEK cells was detected by ICC staining combined with confocal imaging. **A.** Representative confocal images of tag-free Httex1 16Q, 72Q, ΔPRD 72Q and 1/2ΔPRD 72Q. Httex1 72Q constructs reveal the formation of ring-like cellular inclusion with a strong immunoreactivity at the periphery, regardless of the deletion of the PRD

(orange arrowheads) and no detection to the core of the aggregate. The control Httex1 16Q did not show the formation of any inclusions but only diffuse Httex1. **B.** Representative confocal images of GFP and Httex1 72Q-GFP, ΔPRD 72Q-GFP and 1/2ΔPRD 72Q-GFP. Httex1 72Q-GFP constructs reveal the formation of cellular inclusion with a weak immunoreactivity at the periphery. The Httex1 antibody did not access the core of the inclusions that are clearly visible by the GFP signal. The control GFP does not show the formation of any inclusions but only a diffuse GFP signal. The nucleus was counterstained with DAPI (blue) and the F-actin with phalloidin (red). Orange arrowheads indicate the strong ring-like immunoreactivity of tag-free Httex1 inclusions. Yellow arrowheads indicate a faint ring-like immunoreactivity of GFP Httex1 inclusions. Scale bar = 30 μm (left-hand overview panels) and 10 μm (middle and right-hand panels). The results represent four independent experiments.

2.14 Httex1 72Q inclusions induce higher respirational dysfunction and a stronger decrease of ERES number compared to Httex1 72Q-GFP in HEK cells

Next, we investigated how the aggregation of mutant Httex1-GFP and the formation of cytoplasmic inclusions affect the mitochondrial and ER-related functions. First, we measured the mitochondrial respiration in different respirational states in HEK cells (Figure S13C-D). Compared to our findings with the tag-free mutant Httex1-72Q (Figure 4C), the increased mitochondrial respiration was significant but less pronounced for Httex1 72Q-GFP than for Httex1 16Q-GFP (Figure S13E). Given the role of mitochondria as a major source of reactive oxygen species (ROS), with implications of ROS in both neurodegenerative disease and cellular protective signaling cascades[428,429], we suspected that mitochondrial ROS production might be affected by the mitochondrial fragmentation observed in regions close to tag-free Httex1 72Q and absent for Httex1 72Q-GFP (Figure S21A-B). To test this hypothesis, we used an amplex red assay to measure mitochondrial ROS (superoxide and hydrogen peroxide) production concurrent with mitochondrial respiration (Figure S13D). We observed no significant differences in mitochondrial ROS production between the tag-free or GFP tagged Httex1 72Q or 16Q (Figure S21C).

Finally, we also investigated whether Httex1-GFP inclusions interfere with the homeostasis of ERES by comparing the size and the number of ERES in HeLa cells overexpressing Httex1 16Q-GFP to those expressing mutants GFP-tagged Httex1 39Q or 72Q (Figure S22A). We

found that cells containing Httex1 72Q-GFP inclusions caused a decrease in ERES number (Figure S22B, upper panel), although non-significant, compared to Httex1 72Q, which showed a 20% reduction (Figure 4E, upper panel). The reduction of ERES size was significant for cells expressing Httex1 72Q-GFP but not Httex1 39Q-GFP compared to Httex1 16Q-GFP (Figure S22B, lower panel). Thus, the effect of Httex1-GFP inclusions on ERES is present but is less pronounced compared to that observed in cells containing tag-free Httex1 inclusions. These observations are consistent with recent cryo-ET studies suggesting decreased ER dynamics near Httex1-GFP inclusions[195].

Overall, our results show that the cellular organelle responses and adaptation to inclusion formation were different for the Httex1 72Q-GFP inclusions than for the Httex1 72Q inclusions, consistent with the GFP-dependent changes observed in the proteome and the ultrastructural properties of Httex1 cytoplasmic inclusions.

3. Discussion

The detection of Htt aggregates and inclusions in HD brains, combined with the increased aggregation and inclusion formation by mutant forms of full-length and various N-terminal Htt fragments, led to the hypothesis that Htt aggregation and inclusion formation play a central role in the pathogenesis of HD. However, the exact mechanisms of Htt aggregation and inclusion formation in the brain and how these processes contribute to the initiation and progression of HD remain unknown. To address this knowledge gap, several animal and cellular models of HD have been developed, based mostly on overexpression of full-length or N-terminal fragments of Htt bearing an expanded polyQ tract of 46 to 160Q[143,263,270,287]. These HD models show robust aggregation and inclusion formation [103,130,262,264,308]. Cellular and neuronal models of HD provide several key advantages for investigating the mechanisms of Htt aggregation and inclusion formation, as they allow for 1) dissecting the key molecular and cellular events associated with these processes using advanced electron microscopy and imaging techniques; and 2) a more direct assessment of how modifying Htt aggregation and inclusion formation alters cellular functions and viability using a combination of proteomics, transcriptomics, and functional studies. This is illustrated by the recent application of electron tomography techniques to gain insight into the ultrastructural properties of Htt inclusions and how they interact with cellular organelles and influence their functions. In this work, we expanded on these studies and provided new insight into 1) the sequence determinants (polyQ repeat length and the role of the Nt17 domain) of Htt aggregation and inclusion formation; 2) the impact of different types of Htt inclusions on the structural and functional properties of cellular organelles; and 3) the role that the cellular environment and cell-type specificity play in determining the biochemical composition and ultrastructural properties of cytoplasmic and nuclear Htt inclusions. Finally, we provided a more in-depth analysis of the impact of fluorescent fusion proteins (GFP), which are commonly used to investigate the mechanisms of Htt inclusion formation and toxicity, on the biochemical and ultrastructural properties of Htt inclusions and their impact on cellular components and organelles.

3.1 Cytoplasmic Httex1 inclusion formation and maturation involves a complex interplay between Httex1 aggregates and organelles

Pathological inclusions in neurodegenerative diseases have been shown to have a complex organization and composition. For example, it has been recently demonstrated that Lewy bodies (LB) isolated from Parkinson's disease brains or LB-like inclusions in primary neurons are composed of not only filamentous and aggregated forms of alpha-Synuclein but also a complex milieu of lipids, cytoskeletal proteins, and other proteins and membranous organelles, including mitochondria and autophagosomes[211,223,430,431]. Studies in neuronal cultures also showed that the recruitment of lipids and membranous organelles during LB formation and maturation contribute to organelles' dysfunctions and lead to synaptic dysfunction and neurodegeneration. In line with these findings, our EM data, together with 3D reconstruction, revealed the presence of membrane fragments and vesicles entrapped in the core of the Httex1 inclusions. Consistent with these observations, our proteomic analysis revealed that 24% of the proteins enriched in the inclusions fraction belong to the endolysosomal compartments, the Golgi apparatus and the trans-Golgi network (Figure 3).

In addition, mitochondria and ER were found in the periphery of inclusions, as previously reported in cellular models[268] and human tissue[81,432]. We hypothesized that sequestration of key functional proteins, together with lipids, endomembranes and organelles inside the Httex1 inclusions, could challenge cellular homeostasis. In line with this hypothesis, our electron micrographs revealed that the mitochondria associated with Httex1 72Q inclusions were fragmented and often exhibited disorganized or depleted cristae (Figure 4A). These changes in mitochondrial morphology were associated with dysregulation of the mitochondrial respiration (Figure 4C), consistent with previous studies demonstrating that mutant Htt aggregates interact directly with outer mitochondrial membranes (in STHdh cells)[433] and induce mitochondrial fragmentation (in primary neurons)[434]. Defects in mitochondrial respiration have also been observed in HD patients' brains, especially defects of complexes II and IV of the respiratory chain may impair oxidative phosphorylation[435–437].

The ER at the periphery of the Httex1 72Q inclusions were also affected at the structural level, as shown by their morphological reorganization in rosette or “stacked cisternae”, and at the functional level, as evidenced by the dysregulation of the ERES homeostasis (Figure 4D-E). The formation of ER rosettes indicates the accumulation of proteins in the smooth ER[424] and is thought to result from low-affinity binding and export defects, which can be caused by unfolded Htt proteins but is not necessarily linked to ER stress. Kegel and colleagues[14] also reported the presence of ER cisternae next to aggregates formed by the expression of a large Htt fragment fused to a FLAG tag in clonal striatal cells. The formation of Httex1 inclusions seems to drive the reorganization of the ER network in their periphery but did not lead to ER protein sequestration, as shown by the quantitative proteomic analysis, which did not reveal significant ER proteins trapped inside the inclusions. The presence of ribosomes and ER membrane deformation was previously detected close to the periphery of Httex1 inclusions by cryo-ET[195] and was linked to a strong reduction in ER dynamics. In the same study[195], the periphery of the inclusions was immunoreactive to several components of the ER-associated degradation (ERAD) machinery (e.g., Erlin-2, Sel1L). These observations are consistent with our ICC data showing the presence of ER chaperone BIP at the outer periphery but not inside the inclusions (Figure S5). We also observed ERES modulation, which can be explained by the sequestration of specific proteins required for their fusion[438]. Consistent with these observations, our proteomic analysis showed the enrichment of proteins specific to the ER-Golgi trafficking. ERES modulation can also be explained by a reduction of the biosynthetic capacity of this compartment, as ERES have been shown to adapt to the amount of secretory burden to which they are exposed[439]. The recruitment and perturbation of the ER network might contribute to cytotoxicity during inclusion formation, but on its own does not appear to be sufficient to cause overt toxicity. Consistent with this hypothesis, the ERAD and Ca^{2+} signaling pathways have been extensively reported to be dysregulated in various cellular and animal models using different Htt fragments[274,332,440–443]. Altogether our data suggest that Httex1 aggregates could form at the surface of membranes as suggested by Suoponki and

colleagues[444], which could promote early aggregation events as well as membrane perturbation and their recruitment into cytoplasmic Httex1 inclusions.

3.2 Cytoplasmic and nuclear Htt inclusions exhibit distinct ultrastructural properties that are differentially influenced by the size of the polyQ repeats

Although previous studies have suggested the formation of ring-like nuclear inclusions, this architecture was defined by the peripheral staining of other proteins in the periphery of mutant Htt inclusions in several cellular models[113,120,165,414] and transgenic mice[445], and not by the peripheral staining of Htt as observed in the case of cytoplasmic inclusions (Figure 1). These results were obtained only using antibody-based techniques, thus, the ultrastructural and biochemical properties of the core of the inclusions remained poorly defined. Our results show that cytoplasmic Htt inclusions are composed of highly organized fibrils in both the core and the periphery, although we cannot rule out the presence of entrapped oligomers in the core or at the surface close to the growing fibrils in the periphery[167]. These observations are consistent with a previous report by Qin *et al*. based on a FLAG-tagged Htt1-969 fragment (100Q), demonstrating that the Htt species in the core of the inclusions are highly protease-resistant and that oligomeric forms of Htt accumulate with cytoplasmic proteins and vesicles in the periphery of the inclusions[165].

Our in-depth characterization of the Httex1 72Q inclusions at the ultrastructure level revealed distinct differences in the organization and architecture between the cytoplasmic and nuclear Htt inclusions. The cytoplasmic Httex1 72Q inclusions exhibit a dense core and shell morphology and are composed of highly organized fibrillar aggregates in both the core and the periphery. In contrast, nuclear Htt inclusions exhibited less complex ultrastructural properties, appeared as homogenous structures without the core and periphery morphology and were devoid of endomembranes or vesicles (Figure 2). These observations are consistent with most of the Htt nuclear inclusions found in HD mice models, which do not display the core and shell

organization[102,133]. Our results also suggest that the intracellular environment and interactions with lipids and endomembranes or vesicles are key determinants of the structural and molecular complexity of the inclusions and that different mechanisms drive the formation and maturation of the nuclear and cytoplasmic inclusions. Such differential characteristics between cytoplasmic and nuclear inclusions might account for the differential cellular dysfunction and toxicity associated with these two types of Htt inclusions[143,222,446–448].

Interestingly, the ultrastructural properties of the Httex1 cytoplasmic inclusions were strongly dependent on the length of the polyQ repeat[266] but not on the Nt17 domain (Figure 2). This is surprising given that *in vitro* and cellular studies have consistently shown that the Nt17 domain plays important roles in regulating the kinetics and structural properties of Htt aggregation[149] and Htt interactions with lipids and membranes[145,147,449–451]. Previous electron paramagnetic resonance (EPR) and solid-state nuclear magnetic resonance (solid-state NMR) studies of mutant Httex1 fibrils have proposed that mutant Httex1 form fibrils with a bottlebrush arrangement[173,452], with the polyQ domain making up the core of the fibrils[453], the Nt17 absorbed to the polyQ, and the flexible proline-rich domain (PRD) exposed on the surface of the fibrils. In a recent study using ssNMR, Boatz *et al.* confirmed that the polyQ domain forms the core mutant Httex1 and showed that the Nt17 domain and part of the PRD (PPII helices) are buried to the core, while the other part of the PRD (random coil) is dynamic and accessible, and regulates multifilament assemblies *in vitro*[172]. Together, these observations could explain why the deletion of the Nt17 domain does not interfere with the organization of the inclusion and suggest that the interactions between the fibrils and other proteins and/or organelles are most likely mediated by the flexible PRD domain. Consistent with this model, removal of the PRD domain has been shown to 1) disrupt interactions with specific cellular proteins and Htt binding partners[164]; 2) inhibit the recruitment of dynamin, Htt interacting protein 1 (HIP1), and SH3-containing Grb2-like protein (SH3GL3) to the periphery of Htt inclusions in cells[165]; and 3)

lead to a disorganization of the ultrastructural arrangement of the Htt inclusions[165]. In addition, we noticed that removal of the PRD was affecting the stability or the clearance of Httex1. It was previously reported that removal of either the Nt17 domain or the PRD was extending the half-life clearance of Httex1-GFP[149]. Shen *et al.* also reported an increased number of aggregates with higher cellular toxicity measured in neurons. We did not observe strong differences in our model at the cellular level, potentially due to the strong resilience of HEK cells. More analysis at the ultrastructural level of the inclusion should be conducted in order to assess how the PRD influences protein-protein interactions with Httex1 and with other proteins during inclusion formation.

We speculate that the formation of the core of the inclusions is guided predominantly by intermolecular interactions involving the polyQ domain and could be initiated by rapid events that are potentially driven by phase separation, as observed in our model (Figure 6) and also recently described by several groups[266,411,454,455]. The rapid formation of the aggregate's core does not allow for the regulated recruitment of other proteins and organelles (Figures 1, 2 and 7A), as evidenced by the fact that most antibodies against proteins found in Htt inclusion stain the periphery rather than the core of the inclusions[165]. The Nt17 domain most likely plays key roles in the initial oligomerization events and, possibly, the packing or lateral association of the fibrils. Once this core of dense fibrils is formed, the fibrils at the periphery continue to grow through the recruitment of endogenous soluble proteins (Figures 3 and 7A). Because this growth phase is slower, it allows the fibrils to interact with and/or recruit other proteins into the inclusions. Consistent with this hypothesis, Matsumoto and colleagues showed that the transcription factors TATA-binding protein (TBP) and CREB-binding protein (CBP)—containing a polyQ expansion—were present only at the periphery of the inclusions and not in the core[414]. Interestingly, although the length of the polyQ repeat did not seem to significantly influence the density of the fibrils at the core of the inclusions, the peripheral organization of the Htt fibrils and the formation of the outer shell showed strong polyQ repeat length

dependence (Figures 4 and 7A). This model is supported by studies from Hazeki *et al.* and Kim *et al.,* demonstrating that the detergent-insoluble core of cellular Httex1 inclusions

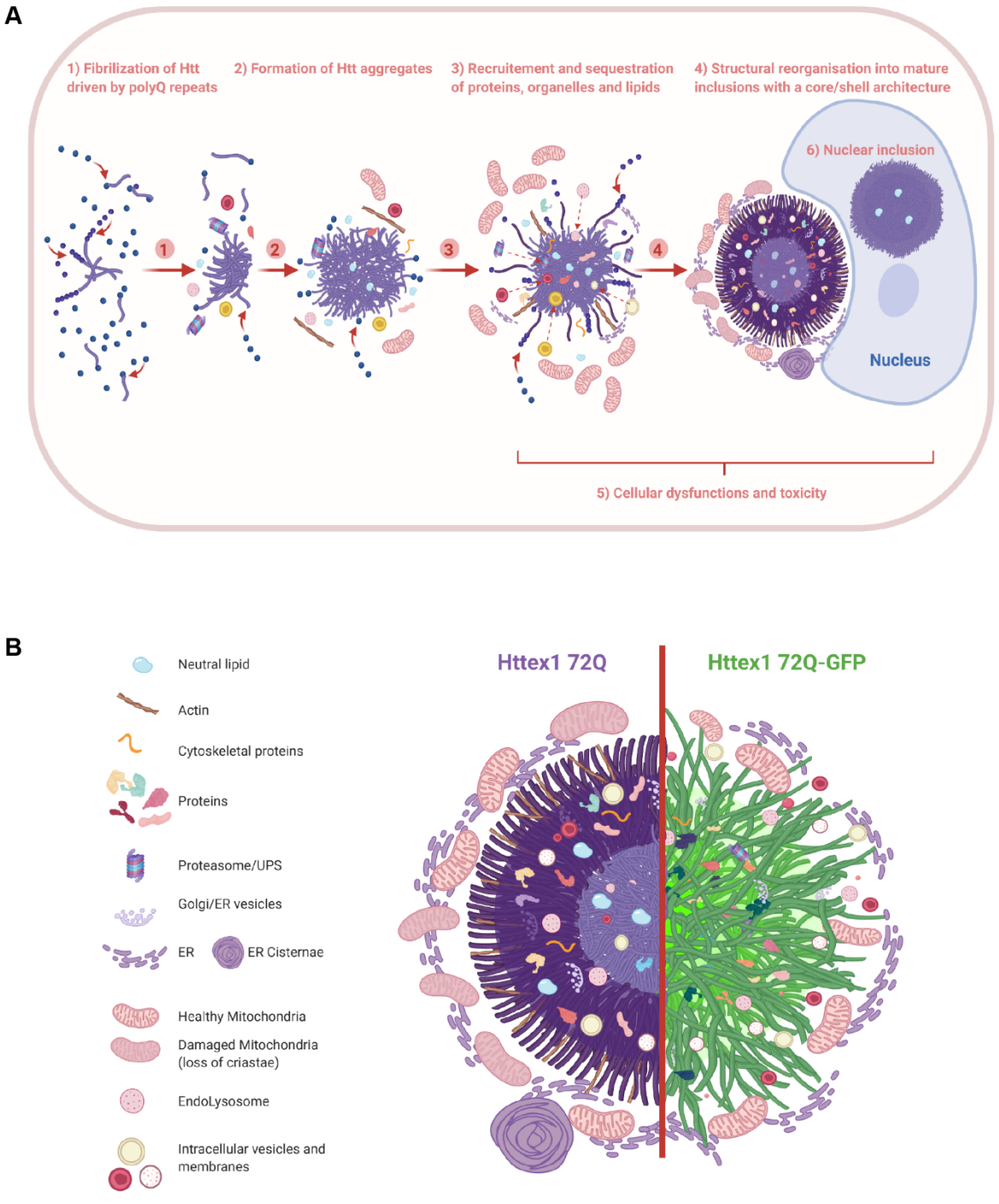

Figure 10. The formation of Huntingtin inclusions is driven primarily by the polyQ repeat domain and involves the active recruitment and sequestration of lipids, proteins, and membranous organelles.

A. We separated the formation and organization of cytoplasmic Httex1 inclusions in different elements: 1) Even though the Nt17 domain can play a major role in early oligomerization steps, we showed that the fibrilization is driven by the polyQ repeats; 2) The initiation of inclusion formation was previously demonstrated to occur in a phase transition mechanism[266,408] and could involve first the sequestration of proteins and organelles nearby either directly or indirectly; 3) During the growth of the inclusion, many cellular proteins, endomembranes, and lipids are recruited and sequestered inside the cytoplasmic inclusions; 4) Mature cytoplasmic Httex1 inclusions formed in cells display a core and shell structural organization if the polyQ length is relatively long (72Q) but not if it is close to the pathogenic threshold (39Q), even if inclusions are still formed in the second case. Cytoplasmic inclusion formation leads to the accumulation of mitochondria and ER network at the periphery; 5) Httex1 inclusion formation leads to the adaptation of the ER-mitochondrial network and respirational dysfunction, as well as significant toxicity after long-term incubation; 6) Nuclear inclusions do not display a distinct core/shell organization similar to the cytoplasmic inclusions, but they are still detected as a ring, as they are impervious for antibodies. Nuclear tag-free Httex1 inclusions are also enriched in neutral lipids. **B.** The depiction shows the distinct structural organization and cellular impact of Httex1 72Q (left) compared to Httex1 72Q-GFP (right). The arrangement and packing of Httex1 fibrils are different depending on the presence of GFP as well as the interactions, recruitment, and perturbation with surrounding organelles.

represents the skeletal structure of the inclusions, while the active surface dynamically interacts with Htt species and proteins being processed[409,410]. Altogether, our results highlight that the formation of Htt inclusions occurs in two major phases with, first, the formation of the core driven primarily by the polyQ repeat domain, and then the growth of the inclusions with the addition of Htt fibrils and the recruitment of other proteins and organelles. The second phase appears to be driven by interactions involving both the polyQ and PRD domains and involves the active recruitment and sequestration of lipids, proteins, and membranous organelles (Figure 10)**.**

3.3 Proteome analysis points to a failure of the protein degradation machinery to clear Httex1 inclusions

Proteins from the UPS system[456] including ubiquitin moiety, E3 ubiquitin ligases (e.g., ITCH, RNF34, TRIM32, MARCH7), 26S proteasome subunits, and deubiquitinases formed the major cluster of the differentially enriched proteins in the Httex1 72Q inclusions. These results are in line with previous studies showing that Htt inclusions formed in HD patients or several cellular

and *in vivo* models sequester several key components of the UPS system, including 26S proteasomes[457] (ADRM1[458]), deubiquitinases[283] (e.g., NEDD4 and USP5), and E3 ubiquitin ligases (e.g., ITCH, TRAF6, UBE3A, UHRF2, and Parkin) and induce impairment of the UPS[459–461]. In addition, our analysis revealed that among the proteins significantly up- or down-regulated in Httex1 72Q compared to Httex1 16Q, 42 proteins are known Htt interactors linked to the UPS, identified from the HDinHD database (Table S1). Proteins involved in autophagosome formation (optineurin[462]), maturation (ubiquilins[463]), and the process of autophagosome-lysosome fusion[464] (TOLLIP-interacting proteins and proteins involved in endolysosomal trafficking) were enriched inside the Httex1 72Q inclusions. Both TOLLIP[281,465,466] and optineurin[467–470] are critical for the efficient clearance of polyQ protein aggregates[471] and in particular, for the degradation of Htt aggregates. The depletion of TOLLIP in HeLa cells increases GFP-Htt-103Q-induced toxicity[465], while optineurin knockdown promotes Htt aggregation.

Finally, several chaperones from the Hsp70 and the DnaJ/HSp40 families, as well as ubiquilin-2, found previously enriched in Htt inclusions[265,409,472,473], were also sequestered inside the Httex1 72Q inclusions. This cluster of proteins was associated with the BAG2 signaling pathway (Figure S12), one of the top canonical signaling pathways that regulate the interplay between the chaperones from the Hsp70/Hsc70 family and ubiquitin. Interestingly, it has recently been shown that the Hsp70 complex, together with the Hsp40/110 chaperone family, formed a disaggregase complex that can directly bind to Htt aggregates[293]. After disaggregation, Ubiquilin-2 interacts with Htt and shuttles the disaggregated species to the proteasome to promote its complete degradation[474]. The enrichment of the disaggregase chaperones network in the Httex1 72Q inclusions suggests that they were actively recruited but failed in their attempt to clear the Httex1 72Q aggregates.

Together, these findings suggest that the cytosolic depletion of key proteins from the autophagolysosomal pathway, due to their sequestration inside the Httex1 pathological

inclusions, could contribute to cellular dysfunction of the degradation and quality control machinery, as reported in HD human brain tissue[423].

3.4 The fusion of fluorescent proteins to mutant Httex1 significantly alters the biochemical and structural properties of mutant Htt

To enable the investigation of Htt aggregation dynamics using live imaging techniques, N-terminal Htt fragments are usually fused to large fluorescent proteins such as GFP[117,149,270,279,287,408]. To determine whether the fusion of these proteins to Httex1 significantly alters its aggregation properties and the final structure of Httex1 inclusions, we compared the biochemical, structural, and toxic properties of mutant Httex1 fused (or not) to GFP in our cellular model. To the best of our knowledge, this is the first study to directly compare inclusions formed by tag-free mutant native Httex1 proteins to GFP-tagged mutant Httex1 at the structural, interactome and biochemical levels. Our results demonstrate that the fusion of the GFP tag to the Httex1 sequence significantly alters the proteome composition, structural organization and architecture of the Httex1 inclusions (Figures 1 and 5).

The ultrastructure of Httex1 72Q-GFP inclusions revealed radiating fibrils with homogenous staining and the absence of the core and shell morphology. In line with our findings, previous studies showed that cytoplasmic Httex1 72Q-GFP aggregates are fibrillar[266,475] and resemble other Httex1-GFP aggregates in COS cells[476], in primary striatal neurons[329] as well as aggregates formed by mutant Httex1 fused to a FLAG tag in HEK cells[268]. In a recent cryo-electron tomography (Cryo-ET) study, Bäuerlein *et al.* examined the ultrastructural properties of mutant Httex1 in the absence and presence of GFP and suggested that the presence of GFP does not significantly alter the organization of the cytoplasmic inclusions in HeLa and neurons[195]. Similar to our findings, they showed that the presence of the GFP tag 1) induces a 50% reduction in fibril density and a 25% increase in fibril stiffness; 2) results in increased

spacing between the fibrils in the Httex1-GFP inclusions; and; 3) does not influence the overall size of the inclusions.

However, when it comes to the ultrastructural properties of the tag-free mutant Httex1 inclusions, we observed very different results, as they did not observe the formation of inclusions with core and shell morphologies. Examination of the sequence of the constructs they used reveals a Myc-tag at the N-terminal side of their Httex1 proteins, whereas the constructs we used contain only the native sequence of mutant Httex1. While we showed that removal of the Nt17 domain does not influence the ability of tag-free Htt to form inclusions with the core and shell organization, the fusion of additional amino acids in the N-terminus could still significantly alter the kinetics, oligomerization, and aggregation pathway of Httex1 protein. In addition to differences at the ultrastructural levels, our studies showed the recruitment of membranous organelles and vesicles as disrupted structures inside the inclusions in both the core and shell but also in the form of intact ER-mitochondrial network at the periphery of the tag-free inclusions. Less internalized structures were observed in the Httex1-GFP inclusions, consistent with the findings of Bäuerlein *et al.*[195]. Another major difference between the two studies is that Bäuerlein *et al.* did not observe any polyQ-length effect on the size or ultrastructural properties of the inclusions formed by mutant Httex1-GFP over the polyQ repeat range of 64Q to 97Q. Although the presence of GFP can explain the differences between the two results, it is also possible that these differences are because the authors compared polyQ repeats that are far beyond the pathogenic threshold. We think that in this polyQ range, the difference in aggregation properties between 64 and 97Q would be small compared to what one would observe when comparing mutant Httex1 with polyQ repeats close to the pathogenic threshold (39-43Q). Therefore, in our study, we compared the ultrastructure properties of the inclusions of Httex1 containing 39 or 72Q repeats. In our experiments, the cytoplasmic inclusions formed by mutant Httex1 39Q were found to be less organized and did not exhibit a stable core and shell arrangement as in the case of Httex1 72Q.

In HEK cells, approximately 50% of the proteome of the tag-free inclusions were related to proteins involved in transcriptional pathways, while in the inclusions formed by Httex1 72Q-GFP, this biological process represents ~14%. Transcriptional dysregulation[477,478] is one of the major features of HD and occurs at the onset of the early neuropathological symptoms in HD patients. In addition, several proteins related to gene expression, the chromatin remodeling and histone acetylation process[479] (SETD2[480,481]), transcription initiation (TFIID subunit[482]), regulation (NF-Y[483]) and elongation (TCERG1[484]) factors, TATA-box binding proteins (TBP[472,485]) that have been shown to either lose their function in HD through their interaction with Htt and/or sequestration in the *bona fide* Htt inclusions[481,484] were specifically enriched in the tag-free inclusions but not in the GFP-Httex1 72Q inclusions. Similarly, although biological processes related to autophagy were found to be enriched, in both types of inclusions, ~33% of the identified proteins were different in the GFP-Httex1 72Q inclusions. For example, optineurin—an autophagy receptor implicated in HD pathology—was sequestered in the inclusions formed by the tag-free inclusions and the *bona fide* Htt inclusions in the HD brain[28] but not in the GFP-Httex1 72Q inclusions. Instead, CHMP2b was specifically enriched in the GFP-Httex1 72Q inclusions and found in the insoluble fraction of R6/2 mice[486]. CHMP2b, together with several proteins from the ESCRT complexes, is known as the ESCRTing autophagic complex involved in the clearance of specific aggregating proteins[487]. This suggests that selective autophagy pathways are engaged in response to different types of aggregates.

Several studies suggest the involvement of the cytoskeleton in HD and especially the microtubules on the formation of aggresomes[287,488]. In particular, the actin cytoskeleton was detected as one of the top dysregulated pathways from a proteomic analysis conducted in human HD brains[427]. In line with these findings, our study showed the presence of filaments of actin exclusively at the periphery of the tag-free Httex1 72Q and 39Q (+/- ΔNt17) cytoplasmic inclusions (Figure 1B). Actin was not detected in Httex1 72Q-GFP inclusions (Figure 5B). In addition, Actin-F was detected inside Httex1 39Q inclusions (Figure S9D) and in periphery

ΔNt17 Httex1 72Q inclusions (Figure S10A). The results suggest a potential role of the actin in the formation of Httex1 inclusions and, more specifically, in the core and shell organization observed by EM, indicating a distinct periphery.

In addition, proteins related to infection and inflammation pathways, including the TNF, the Toll-like receptor, and the NOD-like receptor signaling pathways, were only sequestered in the tag-free inclusion. This is particularly relevant because neuroinflammation has been implicated in HD pathology[378]. On the other hand, a significant number of metabolic proteins were exclusively enriched in the GFP-like inclusions. Our findings also support the hypothesis that the sequestrations of key proteins during the formation and maturation of Htt inclusions could be one of the causative mechanisms leading to neuronal dysfunctions and neurodegeneration, thereby favoring disease progression in HD. Therefore, despite the similarities in terms of general pathways impacted, the cellular responses or the mechanisms underlying cellular dysfunctions and toxicity are specific to the type of inclusions formed in the cells. Our results also strengthen the idea that inclusions formed from GFP-Httex1 72Q do not exhibit the same behavior as the tag-free inclusion.

Altogether, our data suggest that the aggregation processes of tag-free and GFP-tagged Httex1 are distinct (Figures 7B and S23), thus underscoring the potential limitations of using GFP to investigate the molecular, biochemical, and cellular determinants of Htt inclusion formation and mechanisms of toxicity.

3.5 Tag-free and GFP Httex1 inclusions differentially impact mitochondrial and ER-related functions in the cells

Mitochondrial fragmentation[489] and inflammation[380] are hallmarks of Htt-induced neurodegeneration. Recent studies reported the major role of mitochondrial fission and fusion homeostasis in HD and also revealed the specific mitochondrial fragmentation induced by mutant Htt using electron microscopy in STHdh neurons[490,491]. Interestingly, only tag-free

Httex1 72Q overexpression results in mitochondrial fragmentation and is characterized by the strong accumulation of inflammation-linked proteins in the aggregates. We speculate that the observed hyper-activation of mitochondrial respiration (in the absence of significantly increased ROS production) is an adaptation of the inclusion-bearing cells in order to generate sufficient energy by oxidative phosphorylation for increased energetic demands for unfolding or clearance of aggregating proteins. A similar hyperactivation of mitochondrial respiration has recently been reported for alpha-Synuclein aggregates[492]. These authors hypothesized that the hyper-respiration might represent a pathogenic upstream event to alpha-Synuclein pathology. We think that this may also be the case for untagged Httex1 72Q induced pathology. However, based on our extensive proteomic analyses of the inclusions formed by Httex1 72Q to or Httex1 72Q-GFP and the possibility of comparing the functionality of organelles in our cellular model, we can provide a more elaborate hypothesis. In the tag-free Httex1 72Q condition, mitochondrial hyperactivity coincided with both mitochondrial fragmentation and the detection of more inflammation-related proteins in the aggregates as compared to the GFP condition. We speculate that mitochondrial fragmentation initially may be protective, as it enhances mitochondrial mobility necessary for cell repair processes[493]. Upregulation of mitochondrial respiration would be a reasonable consequence of elevated ATP-requirements for mitochondrial and protein transport related to aggregation formation and proteostatic processes including ATP-requiring chaperone-, proteasome and autophagy processes.

We also demonstrated modulation of ERES with the presence of GFP at the C-terminal part of Httex1 72Q; the effect is reduced compared to tag-free Httex1 inclusions but still indicates ER perturbation consistent with the previous cryo-ET report[195], suggesting decreased ER dynamics near Httex1-GFP inclusions.

Overall, we demonstrated drastic differences in the architecture, composition, and impact on cellular organelles by the inclusions formed by Httex1 72Q in the absence and presence of GFP (Figures 7B and S23). Altogether, our data suggest that the aggregation processes of

unmodified and GFP-tagged Httex1 are distinct, thus underscoring the potential limitations of using GFP to investigate the molecular, biochemical, and cellular determinants of Htt aggregation and mechanisms of toxicity.

4. Conclusion

In summary, our integrative imaging and proteomic studies demonstrate that the process of Htt cytoplasmic inclusion formation occurs in at least two phases and involves the active recruitment of lipids, proteins, and organelles. The organization and ultrastructural properties of these inclusions are greatly influenced by the polyQ repeat length and the intracellular environment, as evidenced by the fact that cytoplasmic and nuclear Httex1 inclusions exhibit distinct ultrastructural properties. Equally important, our work emphasizes the importance of elucidating the role of Htt interactions with lipids and membranous organelles in regulating the process of Htt aggregation, inclusion formation, and toxicity. Extending the studies and approaches presented here to other HD model systems and other Htt fragments will pave the way to a better understanding of the mechanisms of Htt inclusion formation and how it contributes to the development of HD. We recently demonstrated that Htt171 aggregates *in vitro* via different mechanisms that are distinct from Httex1 and that the structured domains outside exon1 could play important roles in regulating early events associated with Htt oligomerization, initiation of Htt aggregation and inclusion formation[175]. This will also enable a more effective use of appropriate models to assess the therapeutic potential of targeting different stages and mechanisms of Htt inclusion formation and maturation.

5. Material and methods

DNA constructs and purification

pCMV mammalian expression vector encoding for Httex1 16Q, Httex1 16Q-GFP, Httex1 39Q, Httex1 39Q-GFP, Httex1 72Q, and Httex1 72Q-GFP were kindly provided by Andrea Caricasole (IRBM). ΔN17-Httex1 39Q, ΔN17-Httex1 39Q-GFP, ΔN17-Httex1 72Q, ΔN17-Httex1 72Q-GFP; ΔPRD-Httex1 72Q, 1/2ΔPRD-Httex1 72Q, ΔPRD-Httex1 72Q-GFP and 1/2ΔPRD-Httex1 72Q-GFP were purchased from GeneArt (Germany). Plasmids were transformed into Chemo-competent E. coli stable 3 cells (Stbl3) from Life Technologies (Switzerland), and Maxiprep plasmid purification (Life Technologies, Switzerland) was performed following the manufacturer's instructions.

Mammalian cell culture and plasmid transfection

HEK 293 cells were maintained in Dulbecco's modified Eagle's medium DMEM (Life Technologies, Switzerland) containing 10% FBS (Life Technologies, Switzerland), 10 µg/ml streptomycin and penicillin (Life Technologies, Switzerland) in a humidified incubator, and 5% CO_2 at 37°C. Cells were plated at a density of 100,000 per dish in glass-bottom µ-Dishes (IBIDI) or 50,000 cells/well in 24 well plates with a Thermanox Plastic Coverslip (round) 13mm in diameter (Life Technologies, Switzerland) in order to obtain cells at a 70-90% confluence the day after for the transfection procedure using a standard calcium phosphate procedure[494]. Briefly, 2µg of DNA was diluted in 30µl H2O and 30µl of 0.5M CaCl2 before the dropwise addition of 60µl of 2xHBS, pH 7.2 (50mM HEPES, pH 7.05; 10mM KCL; 12mM dextrose; 280mM NaCl; 1.5mM Na2PO4, pH 7.2 dissolved in H2O) under mild vortexing condition.

Immunocytochemistry (ICC)

At the indicated time-point, HEK 293 cells were washed twice with PBS pH 7.4 (1X) (Life Technologies, Switzerland) and fixed in 3.7% formaldehyde (Sigma-Aldrich, Switzerland) in PBS (PFA) for 15 min at room temperature (RT). After a blocking step with 3% BSA (Sigma-Aldrich, Switzerland) diluted in 0.1% Triton X-100 (Applichem, Germany) in PBS (PBST) for 30 min at RT, cells were incubated with the primary antibodies (Figure S1) anti-Htt raised against the Nt17 domain (2B7, CHDI [Cure Huntington's Disease Initiative]; Ab109115, Abcam) or the PolyQ (MW1, CHDI) or Proline-Rich Domain (PRD) (MAB5492, Millipore; 4C9, CHDI; N18, Santa-Cruz and EGT 414), or against Htt (S830) at a dilution of 1/500 in PBST for 2 h at RT. Cells were then rinsed five times in PBST and incubated for 1 h at RT with the secondary donkey anti-mouse Alexa647, donkey anti-rabbit Alexa647, or donkey anti-goat 568 antibodies (Life Technologies, Switzerland) used at a dilution of 1/800 in PBST and DAPI (Sigma-Aldrich, Switzerland) at 2µg/ml, all diluted in PBST. In addition, HEK cells were counterstained with Phalloidin Atto594 (Sigma-Aldrich, Switzerland), which has a high affinity to filamentous F-actin.

Cells were then washed five times in PBST, and a last one in double-distilled H2O, before being mounted in polyvinyl alcohol (PVA) mounting medium with DABCO (Sigma-Aldrich, Switzerland). Cells were examined with a confocal laser-scanning microscope (LSM 700, Zeiss, Germany) with a 40x1.3 oil objective (Plan-Apochromat) and analyzed using Zen software (Zeiss, Germany).

Immunofluorescence staining of ER exit sites

A total of 100,000 HeLa cells were seeded into a 6-well plate on glass coverslips. After 24 h, cells were transfected with the different variants of GFP-tagged or tag-free Httex1 using Fugene 6 according to the manufacturer's instructions. An empty vector was used as a

negative control. 48 h after transfection, cells were fixed in 4% PFA for 20 min and stained using an anti-Htt antibody (Millipore, mouse monoclonal (MAB5492)). Briefly, after cells were washed with PBS containing 20 mM glycine, slides were incubated in a blocking buffer composed of 3% BSA (Bovine Serum Albumin) in 0.1% Triton X-100 and PBS for 30 min at RT. Subsequently, cells were incubated with the primary antibodies against Htt and Sec13 (R&D Systems) to label ER exit sites, followed by washing and incubation with Alexa-Fluor tagged secondary antibodies. Slides were washed with PBS and embedded in polyvinyl alcohol mounting medium with DABCO (Sigma-Aldrich). Cells were imaged with 63x objective using a Zeiss LSM 700 confocal microscope.

In the case of Httex1-FP, cells were washed in PBS containing 20mM glycine followed by permeabilization in PBS containing 0.2% Triton X-100. Subsequently, cells were incubated with primary antibody to stain ER exit sites diluted in 3% BSA in PBS. After being washed with PBS, cells were incubated with the appropriate Alexa-Fluor tagged secondary antibodies in 3% BSA-PBS. Slides were washed with PBS and embedded in polyvinyl alcohol mounting medium with DABCO (Sigma-Aldrich). Cells were imaged with 63x objective using a Zeiss LSM 700 confocal microscope.

Quantification of ER exit sites' number and size was performed using the analyze particles tool in Image J after thresholding for pixel size and intensity.

Correlative light and electron microscopy (CLEM)

HEK 293 cells were grown at 600,000 cells/ml on 35 mm dishes with alpha-numeric searching grids etched on the bottom glass (MatTek Corporation, Ashland, MA, USA). 48 h after transfection with either Empty vector (EV), Httex1 72Q, or Httex1 72Q-GFP, cells were fixed for 2 h with 1% glutaraldehyde (Electron Microscopy Sciences, USA) and 2.0% PFA in 0.1 M phosphate buffer (PB) at pH 7.4. After washing with PBS, ICC was performed as described

above. Intra-cellular inclusions were stained with an Htt antibody (Millipore MAB5492, aa 1-82), and the cells of interest were imaged with a fluorescence confocal microscope (LSM700, Carl Zeiss Microscopy) with a 40x objective. The precise position of the selected cells was recorded using the alpha-numeric grid etched on the dish bottom. The cells were then fixed further with 2.5% glutaraldehyde and 2.0% PFA in 0.1 M PB at pH 7.4 for another 2 h. After five washes of 5 min with 0.1 M cacodylate buffer at pH 7.4, cells were post-fixed with 1% osmium tetroxide in the same buffer for 1 h and then washed with double-distilled water before being contrasted with 1% uranyl acetate water for 1 h. The cells were then dehydrated in increasing concentrations of alcohol (2 × 50%, 1 × 70%, 1 × 90%, 1 × 95%, and 2 × 100%) for 3 min each wash. Dehydrated cells were infiltrated with Durcupan resin (Electron Microscopy Sciences, Hatfield, PA, USA) diluted with absolute ethanol at 1: 2 for 30 min, at 1: 1 for 30 min, at 2: 1 for 30 min, and twice with pure Durcupan for 30 min each. After 2 h of incubation in fresh Durcupan resin, the dishes were transferred into a 65°C oven so that the resin could polymerize overnight. Once the resin had hardened, the glass CS on the bottom of the dish was removed by repeated immersion in hot water (60°C), followed by liquid nitrogen. The cell of interest was then located using the previously recorded alpha-numeric coordinates, and a razor blade was used to cut this region away from the rest of the resin. This piece was then glued to a resin block with acrylic glue and trimmed with a glass knife using an ultramicrotome (Leica Ultracut UCT, Leica Microsystems). Next, ultrathin sections (50–60 nm) were cut serially from the face with a diamond knife (Diatome, Biel, Switzerland) and collected on 2 mm single-slot copper grids coated with formvar plastic support film. Sections were contrasted with uranyl acetate and lead citrate and imaged with a transmission electron microscope (Tecnai Spirit EM, FEI, The Netherlands) operating at 80 kV acceleration voltage and equipped with a digital camera (FEI Eagle, FEI).

Sample processing for electron microscopy imaging without cell permeabilization

48 h after transfection, HEK 293 cells were fixed in PFA 2% and glutaraldehyde 2% in phosphate buffer 0.1M (pH 7.4) for 1 h and 30 min. To preserve the internal membranes of the cells, no ICC was performed. Cells were then washed 3 times for 5 min in cacodylate buffer (0.1M, pH 7.4). Next, they were post-fixed with 1% osmium tetroxide plus 1.5% potassium ferrocyanide in cacodylate buffer (0.1M, pH 7.4) at RT for 40min, followed by post-fixation with 1% osmium tetroxide in cacodylate buffer (0.1M, pH 7.4) at RT for 40min. Samples were washed twice for 5 min in distilled water, then further stained in 1% uranyl acetate in water for 40 min and washed once in double-distilled water for 5min. The samples were dehydrated in increasing concentrations of ethanol for 3 min each wash (2X50%, 1X70%, 1X90%, 1X95%, 2X100%) and then embedded in epoxy resin (Epon had the formula: Embed 812: 20g, DDSA: 6.1g, NMA: 13.8g, DMP 30: 0.6g) (Electron Microscopy Sciences, USA) through the continuous rotation of vials. The embedding process starts with a 1:1 ethanol:epon mix for 30min, followed by 100% EPON for 1 h. EPON was then replaced with fresh EPON for 2 h. Finally, samples were embedded between coated glass slides and placed in an oven at 65°C overnight. 50 nm thick serial sections were cut with an ultramicrotome (UC7, Leica Microsystems, Germany) and collected on formvar support films on single-slot copper grids (Electron Microscopy Sciences, USA) for transmission electron microscopy imaging (TEM). TEM images were taken at 80 kV filament tension with a Tecnai Spirit EM microscope, using an Eagle 4k x 4k camera. At least 8 cells were imaged per condition at 2900x and 4800x magnification.

Images were aligned using Photoshop software (Adobe, USA) and different organelles (Nucleus, Mitochondria, Endoplasmic Reticulum, Httex1 inclusions) were first segmented manually using the arealist function in the trackEM2 plugin in the FIJI software. We then moved to a custom-developed machine learning-based pipeline, tailored specifically to 3D microscopy data (www.ariadne-service.ch) after validation using the manual segmentation for reference.

At the end of the segmentation process, the different segmented areas were exported as serial image masks, then visualized as objects in the 3D viewer plugin in FIJI and exported as wavefront in the Blender® 3D modeling software (Blender Foundation). Using Blender®, the 3D axes were first corrected according to the model orientation and the Z scale was adjusted. Httex1 inclusion, mitochondria, and the nucleus were smoothed and the Httex1 inclusion was adjusted to visualize intra-aggregates membranous structures within the inclusion. Additional measurements were performed from electron micrographs in cells containing Httex1 inclusions using FIJI. The mitochondrial profile length corresponds to the maximal length of each mitochondria in one EM plane. The distance from the inclusion was not taken into account, as the measurements were performed in one plane. Instead, the average length of all detected mitochondria was taken into account and showed significant differences in the Httex1 72Q condition compared to the EV control.

High pressure freezing and embedding for TEM

48 h after transfection, HEK 293 cells were cultured on sapphire discs (6mm diameter) and frozen rapidly under high pressure (HPM100, Leica Microsystems). The discs were placed into cryo tubes containing acetone with 1% osmium tetroxide, 0.5% uranyl acetate, and 5% water at -90°C. They were then left at this temperature for 24 h before being warmed at 0°C over the next 72 h where they were then washed with pure acetone, and then infiltrated with increasing concentrations of Epon resin. Once in 100% resin the samples were left at room temperature for 24 h, and then the resin hardened in an oven at 65°C for 48 h. Serial sections were collected on single slot copper grids with a formvar support film, and then stained with lead citrate and uranyl acetate. These were imaged inside a transmission electron microscope at 80 kV (Tecnai Spirit, FEI Company), using a CCD camera (Eagle, FEI Company).

Live cell imaging

HEK cells were plated in at 15 000 cells per well in a glass-bottom 96 well plate (PerkinElmer, Switzerland), pre-coated with poly-L-lysine. 24 h post-plating, cells were transfected with Httex1-GFP constructs using Lipofectamine 2000 (Thermofisher, USA). Briefly, 100ng DNA mixed in 10 µl Optimem transfection media (Sigma-Aldrich, Switzerland) was added to 0.2 µl Lipofectamine 2000 mixed in 10 µl Optimem and added dropwise to the cells. Using the Operetta CLS High-content analysis microscope with the 40x Objective (PerkinElmer, Switzerland), cells were imaged in live conditions with imaging every 15 to 60 min. The exported images were analyzed with the PerlinkElmer Harmony software and Fiji. The intensity of GFP over time was plotted as a surface plot and rescaled on the IC50 (half intensity of the signal). The analysis of the interpolated curved based on the GFP intensity was based on the following equation: f(x) = b + a x + (t-b - (a+ c) x) /(1+ 10^((alpha-x) h)), with b: the value representing the bottom of the approximation (first “plateau”), t: value representing the top of the approximation (final “plateau”), a: coefficient of the first linear approximation, c: coefficient allowing a slope different from 0 in the final “plateau”, alpha: value of x at Ymid (with Ymid= mean of Ymax and Ymin) which Can be compared to the IC50 value, x: values on the x-axis (time in hours), h: “Hillslope”, slope of the exponential increase. The coefficient of division is a term allowing the curve to have an exponential behavior around the alpha value and to have a linear behavior when x is much higher than alpha.

Preparation of protein samples for biochemical analyses

Samples were generated, in duplicate, of the HRR experiment for analysis of mitochondrial markers by WB and FT. Transfected cells were lysed in 75µl of RIPA buffer (150Mm NaCl, 1µ NP40, 0.5% Déoxycholate, 0.1% Sodium dodecyl sulfate (SDS), 50Mm Tris pH 8). Cell lysates were incubated at 4°C for 20 min and then cleared by centrifugation at 4°C for 20 min at 16 000g. Supernatants were collected as soluble the protein fraction and stored at -20°C after

LB5x addition and 5 min of boiling. BCA was performed on the RIPA soluble fraction. Pellets were washed with 500ul of PBS, then centrifuged again for 5 min at 16,000g. Supernatants were discarded and the pellet resuspended in 30µl of PBS supplemented with SDS 2% and sonicated with a fine probe [3 times, 3 sec at the amplitude of 60% (Sonic Vibra Cell, Blanc Labo, Switzerland)]. Cellulose acetate membrane was first equilibrated with 2% SDS (in PBS) for 5 min and the main filter fold arranged on top of 2 Watman papers inside the Bio-Dot Apparatus (#1706545, USA). Samples were loaded and filtered by vacuum. The membrane was washed 3 times by 0.5% SDS in PBS and applying the vacuum. The acetate membrane was then removed and washed once in PBS-Tween 1%.

Samples were generated from four independent experiments for the analysis of PRD mutants by WB. 48 h post-transfection, HEK cells were washed with PBS and lysed using 75µl of PBS supplemented with 0,5% triton, 0,5% NP40, 1% protease inhibitor cocktail (Sigma-Aldrich, Switzerland) and 1% PMSF (lysis buffer). After 30 min incubation on ice and frequent vortexing, cells were centrifuged for 20 min at 20 000 g at 4°C. Supernatants were collected as a soluble fraction. Pellets were washed with the first lysis buffer. The insoluble pellet was then lysed using the lysis buffer supplemented with 2% Sarkosyl and sonicated during 9 s (3 s ON and 3 s OFF) and an amplitude of 60%. The protein concentration was estimated by BCA, and the same amount of total protein was loaded on 15 % SDS-Page prior to a transfer on nitrocellulose membrane (WB).

WB and FT membranes were blocked overnight with Odyssey blocking buffer (LiCor) and then incubated at RT for 2 h with different primary antibodies (anti-huntingtin MAB5492, Ab109115, anti-VDAC1 and Beta-actin for loading control) diluted in the same blocking buffer (1/5000). Membranes were washed in PBS-Tween 1% and then incubated with secondary antibody (680 or 800 form LiCor) diluted in blocking buffer (1/5000) for 1 h at RT before a final wash in PBS-Tween 1%. The protein detection was performed by fluorescence using Odyssey CLx from LiCor. The signal intensity was quantified using Image Studio 3.1 from LiCor.

Preparation of samples for mass spectrometry

Samples were generated in triplicate for quantitative mass spectrometry analysis. At the indicated time-point, HEK cells were lysed in PBS supplemented by 0.5% NP40, 0.5% Triton x100, 1% protease cocktail inhibitor (Sigma PB340), and 1% Phenylmethanesulfonyl Fluoride (PMSF, Applichem). Cell lysates were incubated at 4°C for 20 min and then cleared by centrifugation at 4°C for 20 min at 20,000g. Supernatants were collected as non-ionic soluble protein fractions. Pellets were washed and resuspended in PBS supplemented by 2% N-Lauroylsarcosine sodium salt (Sarkosyl, Sigma) with protease inhibitors. The pellets were briefly sonicated with a fine probe [3 times, 3 sec at the amplitude of 60% (Sonic Vibra Cell, Blanc Labo, Switzerland)], incubated 5 min on ice, then centrifuged at 100,000g for 30 min at 4°C. Supernatants were collected as Sarkosyl soluble fractions. Pellets were washed with the previous buffer and resuspended in PBS supplemented by 2% Sarkosyl and 8M Urea and briefly sonicated as done previously. Laemmli buffer 4x was added to samples before being boiled at 95°C for five minutes. Samples were then separated on a 16% SDS-PAGE gel before being analyzed by Coomassie staining and WB.

For WB analyses, nitrocellulose membranes were blocked overnight with Odyssey blocking buffer (LiCor, Switzerland) and then incubated at RT for 2 h with Htt primary antibodies (MAB5492, Millipore, Switzerland) diluted in PBS (1/5000). Membranes were washed in PBS-Tween 1% and then incubated with fluorescently labeled secondary antibody diluted in PBS (1/5000) for 1 h at RT before a final wash in PBS-Tween 1%. The protein detection was performed by fluorescence using Odyssey CLx from LiCor. The signal intensity was quantified using Image Studio 3.1 from LiCor.

For proteomic identification, the samples separated by SDS-PAGE were then stained with Coomassie blue (25% Isopropanol [Fisher scientific, United-States], 10% acetic acid [Fisher scientific, United-States], and 0.05% Coomassie brilliant R250 [Applichem, Germany]. Each gel lane was entirely sliced and proteins were In-gel digested as previously described[495].

Peptides were desalted on stagetips[496] and dried under a vacuum concentrator. For LC-MS/MS analysis, resuspended peptides were separated by reversed-phase chromatography on a Dionex Ultimate 3000 RSLC nano UPLC system connected in-line with an Orbitrap Lumos (Thermo Fisher Scientific, Waltham, USA). Protein identification and quantification were performed with the search engine MaxQuant 1.6.2.10[497]. The human Uniprot database and Httex1 Sequence was used. Carbamidomethylation was set as a fixed modification, whereas oxidation (M), phosphorylation (S, T, Y), acetylation (Protein N-term), and glutamine to pyroglutamate were considered as variable modifications. A maximum of two missed cleavages was allowed. "Match between runs" was enabled. A minimum of 2 peptides was allowed for protein identification, and the false discovery rate (FDR) cut-off was set at 0.01 for both peptides and proteins. Label-free quantification and normalization were performed by Maxquant using the MaxLFQ algorithm, with the standard settings[498]. In Perseus[499], reverse proteins, contaminants, and proteins identified only by sites were filtered out. Data from the Urea fraction were analyzed separately following the same workflow. Biological replicates were grouped together, and protein groups containing a minimum of two LFQ values in at least one group were conserved. Missing values were imputed with random numbers using a gaussian distribution (width = 0.7, down-shift = 1.9 for Urea fraction). Differentially expressed proteins were highlighted by a two-sample t-test, followed by a permutation-based correction (False Discovery Rate). Significant hits were determined by a volcano plot-based strategy, combining t-test P-values with ratio information[500]. Significance curves in the volcano plot corresponded to a S0 value of 0.5 and a FDR cut-off of 0.05. In the comparative analysis, known HTT interactor proteins were selected using the HDinHD dataset (https://www.hdinhd.org/) and restricted to the human and mouse datasets among cell- or animal-based studies exclusively.

Respirometry and amplex red fluorometry

Wild-type HEK 293 cells were transfected 24 h after plating with Htt 16Q, Htt 72Q, Htt 16Q-GFP, or Htt 72Q-GFP. 48 h after transfection, cells were gently detached using 0.05% trypsin, resuspended in DMEM, counted, and immediately used for high-resolution respirometry.

One million cells were transferred to MiR05 (0.5 mM EGTA, 3mM $MgCl_2$, 60 mM potassium lactobionate, 20 mM taurine, 10 mM KH_2PO_4, 20 mM HEPES, 110 mM sucrose, and 0.1% (w/v) BSA, pH=7.1) in a calibrated, 2ml high-resolution respirometry oxygraph chamber (Oroboros Instruments, Austria) kept stably at 37°C. Mitochondrial ROS production (O_2^- and H_2O_2) was measured using amplex red fluorometry and O2K Fluo-LED2 modules (Oroboros Instruments, Austria) as described previously[501]. Briefly, for amplex red fluorometry, cells were added to oxygraph chambers after the addition of 10 µM amplex red, 1 U/ml horseradish peroxidase, and 5 U/ml superoxide dismutase to MiR05 and calibration with known H_2O_2 concentrations. Fluorescence was measured during the subsequently applied high-resolution respirometry protocol.

Routine respiration (and mitochondrial ROS production) was measured from intact cells, after which plasma membranes were permeabilized by the application of an optimized (integrity of mitochondrial outer membranes verified by the cytochrome c test) concentration of digitonin (5 µg/mL).

Oxygen flux at different respirational states on permeabilized cells was then determined using the substrate-uncoupler-inhibitor-titration (SUIT) protocol described previously[502,503]. Briefly, NADH-pathway (N) respiration in the LEAK and oxidative phosphorylation (OXPHOS) state was analyzed in the presence of malate (2 mM), pyruvate (10mM), and glutamate (20 mM) before and after the addition of ADP (5 mM), respectively (N_L, N_P). The addition of succinate (10 mM) allowed for the assessment of NADH- and succinate-linked respiration in OXPHOS (NS_P) and in the uncoupled state (NS_E) after the incremental (Δ0.5 µM) addition of carbonyl cyanide m-chlorophenyl hydrazine (CCCP). The inhibition of Complex I by rotenone (0.5 µM)

yielded succinate-linked respiration in the uncoupled state (S_E). Tissue-mass specific oxygen fluxes were corrected for residual oxygen consumption, *Rox*, measured after additional inhibition of the mitochondrial electron transport system, ETS, Complex III with antimycin A. For further normalization, fluxes of all respiratory states were divided by ET-capacity to obtain flux control ratios, FCR. Terminology was applied according to http://www.mitoeagle.org/index.php/MitoEAGLE_preprint_2018-02-08.

Mitochondrial ROS values were corrected for background fluorescence and respirational states before the addition of the uncoupler used for analysis.

Statistical Analysis

All experiments were independently repeated at least 3 times. The statistical analyses were performed using Student's *t*-test, one-way ANOVA test followed by a Tukey-Kramer or HSD *post-hoc* tests, two-way ANOVA and repeated measures ANOVA using KaleidaGraph (RRID:SCR_014980) or GraphPad Prism 9.1.1. The data were regarded as statistically significant at $p<0.05$.

6. Contributions

This chapter was first sent to Nature Communications as a first version entitled:

"Disentangling the sequence, cellular and ultrastructural determinants of Huntingtin nuclear and cytoplasmic inclusion formation"

First Biorxiv version*:* *https://doi.org/10.1101/2020.07.29.226977*

Nathan Riguet[1], Anne-Laure Mahul-Mellier[1], Niran Maharjan[1], Johannes Burtscher[1], Alice Patin[1], Marie Croisier[2], Graham Knott[2], Veronika Reiterer[3], Hesso Farhan[3] and Hilal A. Lashuel[1]*

*Correspondence: hilal.lashuel@epfl.ch

Affiliations:

[1]Laboratory of Molecular and Chemical Biology of Neurodegeneration, Brain Mind Institute, Ecole Polytechnique Fédérale de Lausanne (EPFL), 1015 Lausanne, Switzerland.

[2]BIO EM facility (BIOEM), EPFL, 1015 Lausanne, Switzerland.

[3]Institute of Pathophysiology, Medical University of Innsbruck, Innsbruck, Austria.

Author contributions

H.A.L conceived and supervised the study. H.A.L, N.R and A.L.M.M designed all the experiments and wrote the paper. N.R performed and analyzed the confocal imaging, the electron microscopy and the 3D imaging reconstruction, quantitative proteomic experiments and the biochemistry experiments. A.L.M.M performed and analyzed the CLEM experiment and analyzed the proteomic data. N.M designed and analyzed the proteomic data. J.B designed, performed, and analyzed the high-resolution respirometry experiments. A.P helped to perform and analyze the confocal imaging experiments. M.C prepared the samples for CLEM and acquired the EM. G.K supervised the EM-related experiments and 3D imaging reconstruction and contributed to the interpretation of the data. V.R and H.F designed, performed, and analyzed the experiments related to ER. All authors reviewed and contributed to the writing.

7. Supplementary Figures

A

Primary Antibody	Reference	Company	Clone	RRID	Host	ICC Dilution	WB Dilution	Epitope
Anti-Htt	2B7	CHDI	2b7	-	Mouse monoclonal	1/500	-	Nt17 domain
Anti-Htt	Ab109115	Abcam	EPR5526	AB_10863082	Rabbit polyclonal	1/500	-	Nt17 domain
Anti-Htt	MW1	CHDI	MW1	AB_528290	Mouse	1/500	-	PolyQ
Anti-Htt	MAB5492	Millipore	2B4	AB_11213848	Mouse monoclonal	1/500	1/5000	50–64
Anti-Htt	4C9	CHDI	4C9	-	Mouse	1/500	-	PRD domain
Anti-Htt	N18 (sc-8767)	Santa-Cruz	3E10	AB_2123254	goat polyclonal	1/500	-	aa 50-100
Anti-Htt	MW8	CHDI	MW8	AB_528297	Mouse monoclonal	1/500	-	C-ter (mHtt)
Anti-Htt	S830	Bates lab	-	-	Sheep	1/500	-	mHttex1
Anti-Htt	Eurogentec (414- 4D3G9A12)	Lashuel lab	-	-	Mouse monoclonal	1/500	-	Httex1
Anti-Beta-actin	ab6276	Abcam	AC-15	AB_2223210	Mouse	-	1/5000	DDDIAALVIDNGSGK
Anti-BIP/Grp78	ab21685	Abcam	-	AB_2119834	Rabbit	1/500	-	-
Anti-Tom20	sc-17764	Santa-Cruz	F-10	AB_628381	Mouse	1/500	-	Raised against amino acids 1-145
Anti-p62	H00008878	Abnova	2C11	AB_437085	Mouse	1/500	-	Raised against a full length recombinant SQSTM1
Anti-Vimentin	ab92547	Abcam	EPR3776	AB_10562134	Rabbit	1/500	-	Synthetic peptide within Human Vimentin aa 400 to the C-terminus
Anti-HDAC6	ab1440	Abcam	-	AB_2232905	Rabbit	1/500	-	Synthetic peptide (Mouse) - N terminal
Anti-Sec13	MAB9055	R&D Systems	1280A	-	Rabbit monoclonal	1/500	-	
Anti-VDAC1	ab14734	Abcam	20B12AF2	AB_443084	Mouse	-	1/5000	Recombinant full length protein corresponding to Human VDAC1/ Porin.
Anti-MAP2	ab92434	Abcam	-	AB_92434	Chicken	1/1500	-	Recombinant MAP2 protein
Anti-NeuN	ab177487	Abcam	EPR12763	AB_2532109	Rabbit	1/500		Synthetic peptide within Human NeuN aa 1-100

B

Secondary Antibody	Reference	Company	RRID	ICC Dilution	WB Dilution
Donkey anti-rabbit Alexa Fluor 647	A31573	Invitrogen	AB_2536183	1/800	
Donkey anti-mouse Alexa Fluor 647	A31571	Invitrogen	AB_162542	1/800	
Goat anti-chicken Alexa Fluor 568	A11041	Invitrogen	AB_2534098	1/500	
Goat anti-mouse Alexa Fluor 680	A21058	Invitrogen	AB_2535724		1/5000
Goat anti-rabbit Alexa Fluor 680	A21109	Invitrogen	AB_2535758		1/5000
Goat anti-mouse Alexa Fluor 800	926-32210	Li-Cor	AB_621842		1/5000
Goat anti-rabbit Alexa Fluor 800	926-32211	Li-Cor	AB_621843		1/5000

Figures S 1. List of the antibodies used in this study.

Primary (**A**) and secondary **(B)** antibodies used in this study.

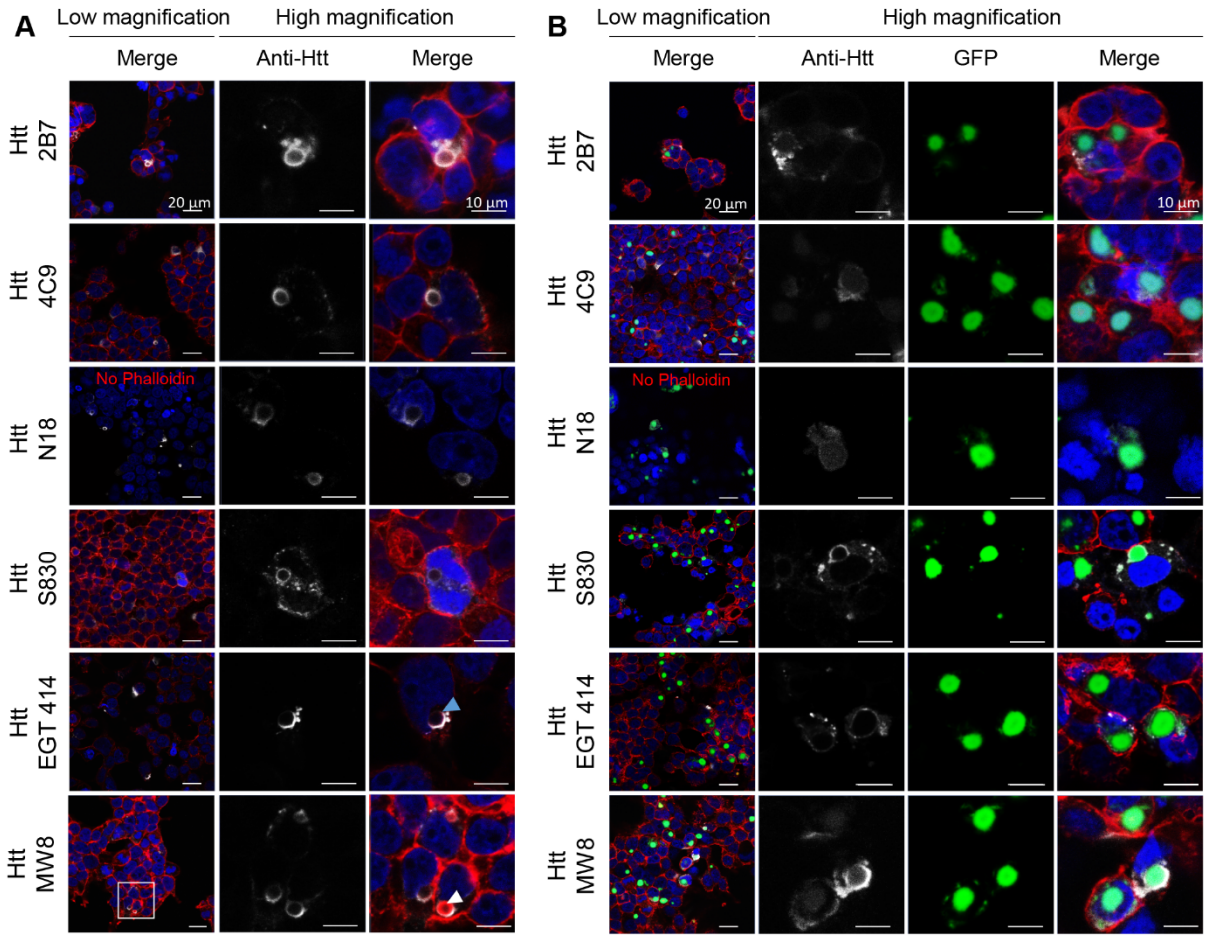

Figures S 2. Characterization of Httex1 72Q and Httex1 72Q-GFP inclusions by Immunocytochemistry with a panel of Httex1 antibodies revealed a ring-like detection.

A. ICC of HEK cells transfected with Httex1 72Q for 48 h. **B.** ICC of HEK cells transfected with Httex1 72Q-GFP for 48 h. (**A-B**) Httex1 72Q and Httex1 72Q-GFP inclusions were detected as a ring-like structure with all the Htt antibodies tested (grey) and as puncta with the GFP channel (green). Blue arrows indicate F-actin (red) colocalizing with the ring-like structure of some Httex1 72Q inclusion. DAPI was used to counterstain the nucleus. Scale bars = 20 µm (left-hand panels) and 10 µm (middle and right-hand panels).

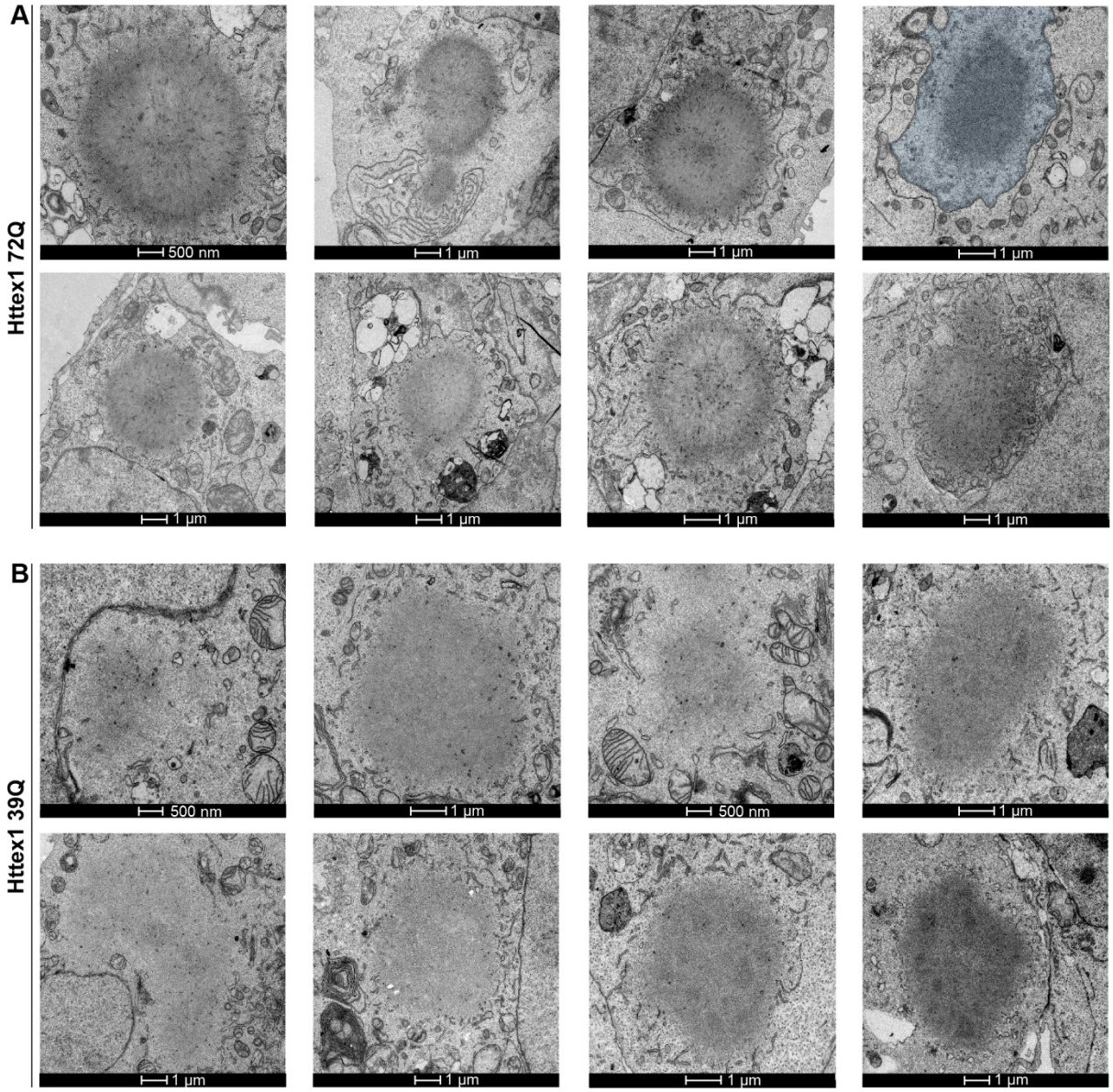

Figures S 3. Ultrastructural characterization of Httex1 72Q and Httex1 39Q inclusions.

A. 8 representative electron micrographs of Httex1 72Q inclusions in HEK cells 48 h post-transfection. **B**. 8 representative electron micrographs of Httex1 39 inclusions in HEK cells 48 h post-transfection. The nucleus was highlighted in blue. Scale bars = 1 µm or 500 nm as indicated below the micrographs.

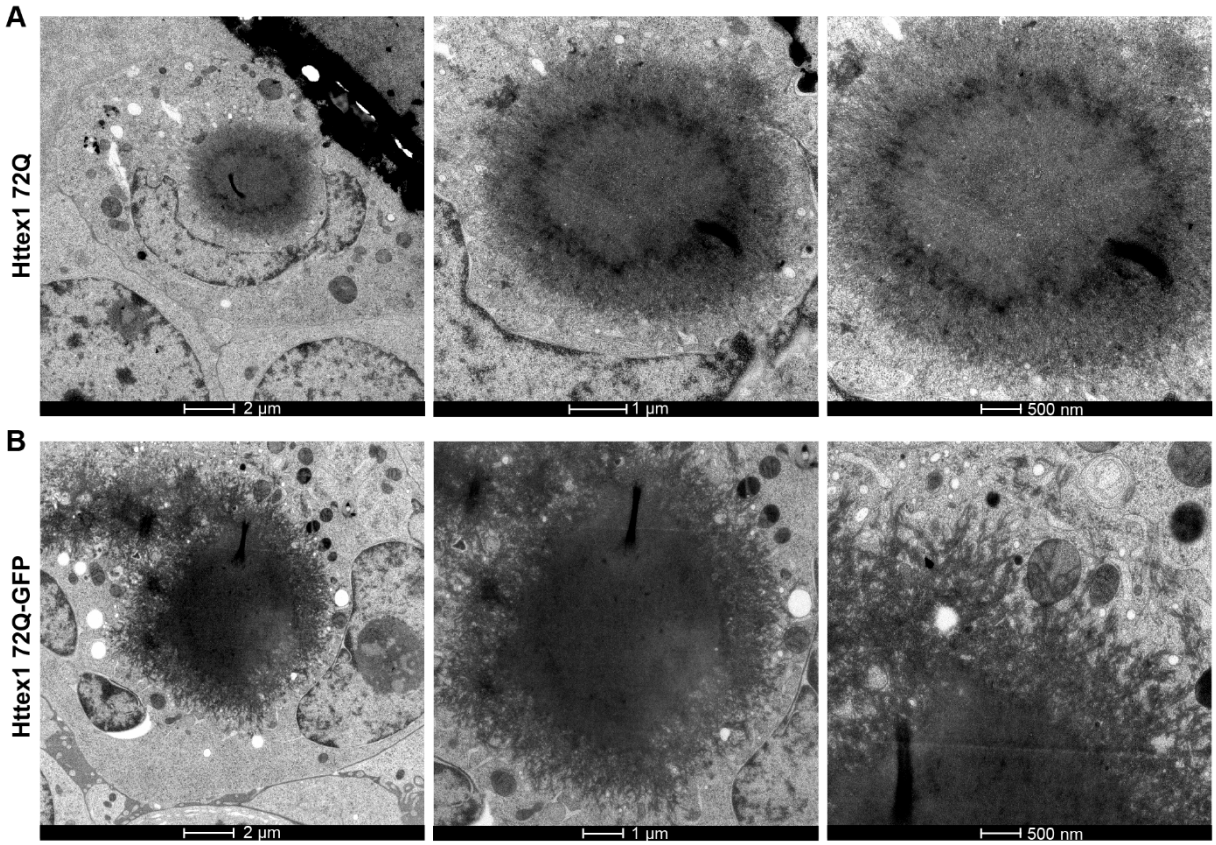

Figures S 4. Electron microscopy analysis of Httex1 72Q and Httex1 72Q-GFP cellular inclusions post-High-Pressure Freezing demonstrates a distinct fibrillar organization. HEK cells were fixed by HPF and freeze substituted for EM imaging 48 h after Httex1 transfection. **A**. Electron micrographs of Httex1 72Q inclusion show radiating stacked fibrils. **B**. Electron micrographs of Httex1 72Q-GFP inclusion reveal thick radiating fibrils at the periphery. Scale bars = 2 µm, 1 µm, or 500 nm as indicated below the micrographs.

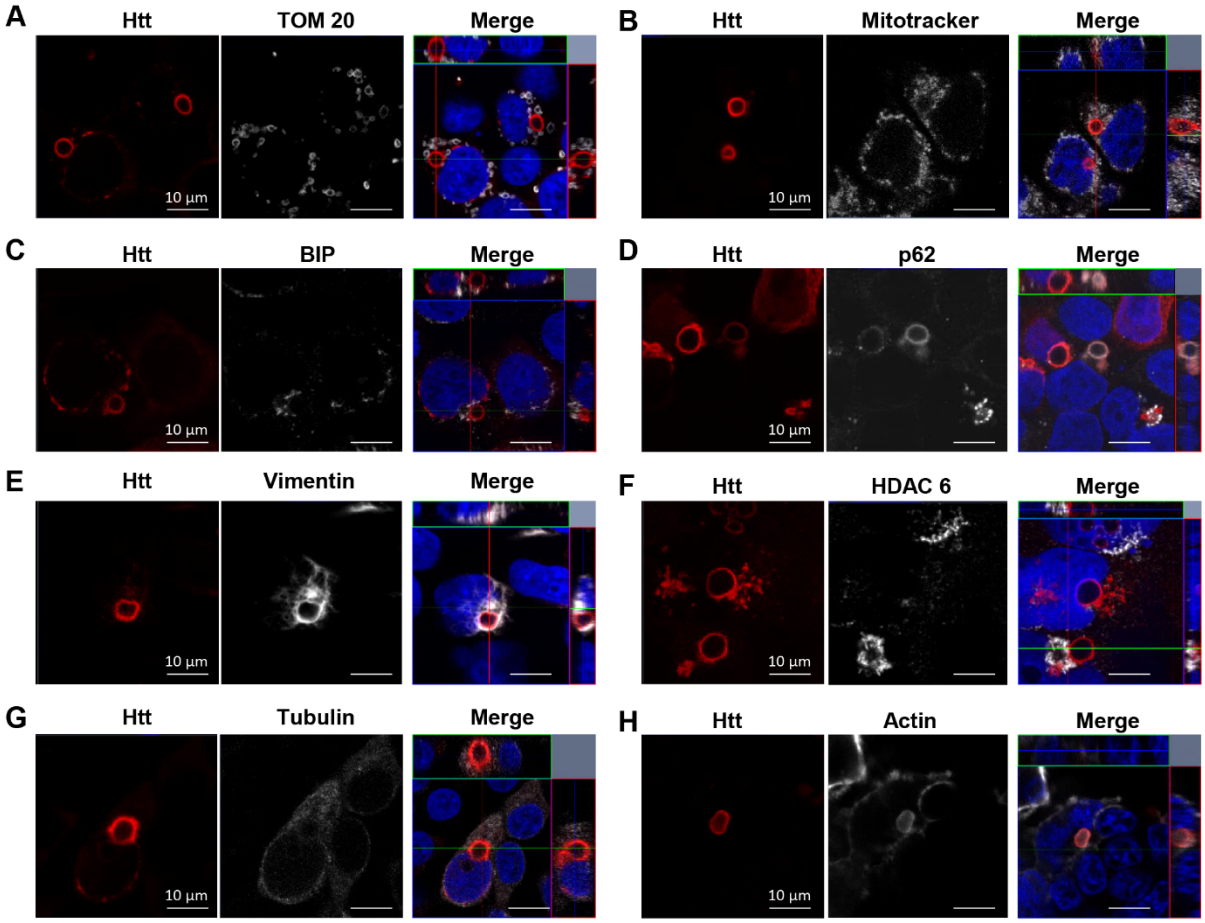

Figures S 5. The formation of the Httex1 72Q cellular inclusions is accompanied by the accumulation of organelles at their periphery.

Httex1 72Q inclusions formed in HEK cells 48 h post-transfection were stained by Htt antibody (MAB5492, grey) in combination with organelle markers Tom20 and Mitotracker (mitochondria) (**A-B**), BIP (ER) (**C**), p62 (autophagosomes) (**D**), Vimentin (**E**) and HDAC6 (aggresome) (**F**), tubulin (**G**) and actin (cytoskeleton) (**H**). The nucleus was counterstained with DAPI (blue). Scale bars = 10 µm.

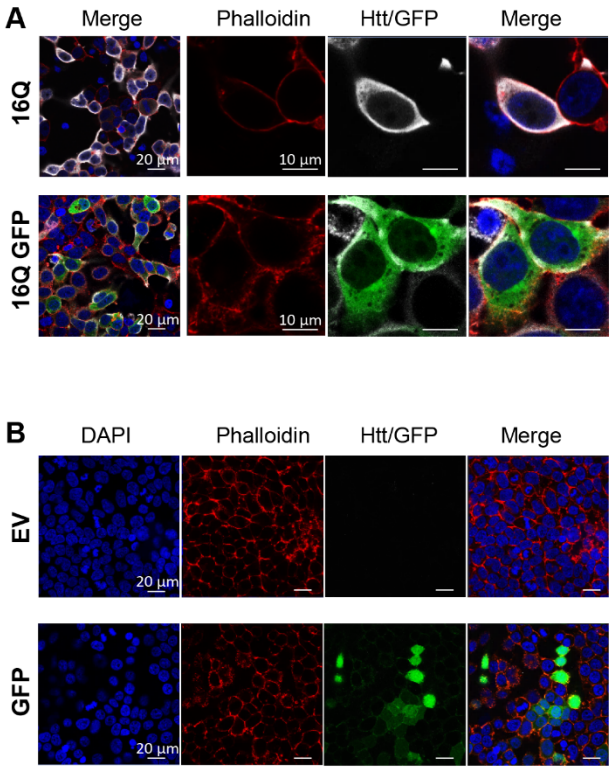

Figures S 6. Immunocytochemistry of HEK cells expressing Httex1 16Q (+/-GFP) and EV/GFP controls does not show any aggregate formation.

A. Representative confocal images of Httex1 16Q and Httex1 16Q-GFP do not display any aggregates 48 h after transfection. Scale bars = 20 µm (left-hand panels) and 10 µm (middle right-hand panels). **B**. Representative confocal images of empty vector (EV) and GFP do not display any aggregates or Htt staining 48 h after transfection. Scale bars = 20 µm.

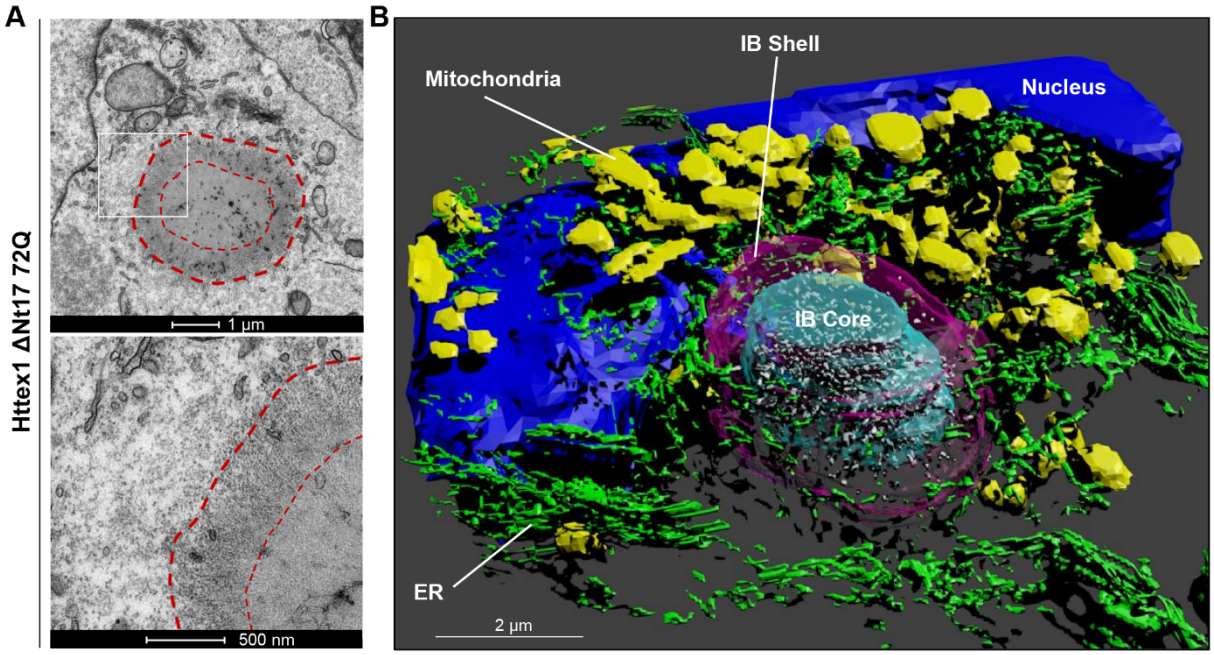

Figures S 7. The Nt17 domain does not influence the structural architecture of the Httex1 inclusions.

A. Representative electron micrograph of Httex1 ΔNt17 72Q inclusion formed 48 h after transfection in HEK. The white square indicates the higher magnification shown in the lower panel. Dashed lines delimit the inclusion and the core of the inclusion. Scale bar = 1 µm (top panel) and 500 nm (bottom panel). **B**. 3D model of the Httex1 ΔNt17 72Q inclusion. The Httex1 inclusion body (IB) shell is represented in purple, the core in cyan, the ER membranes in green, the intra-inclusion membranous structures in white, the nucleus in blue, and the mitochondria in yellow. Scale bar = 2 µm.

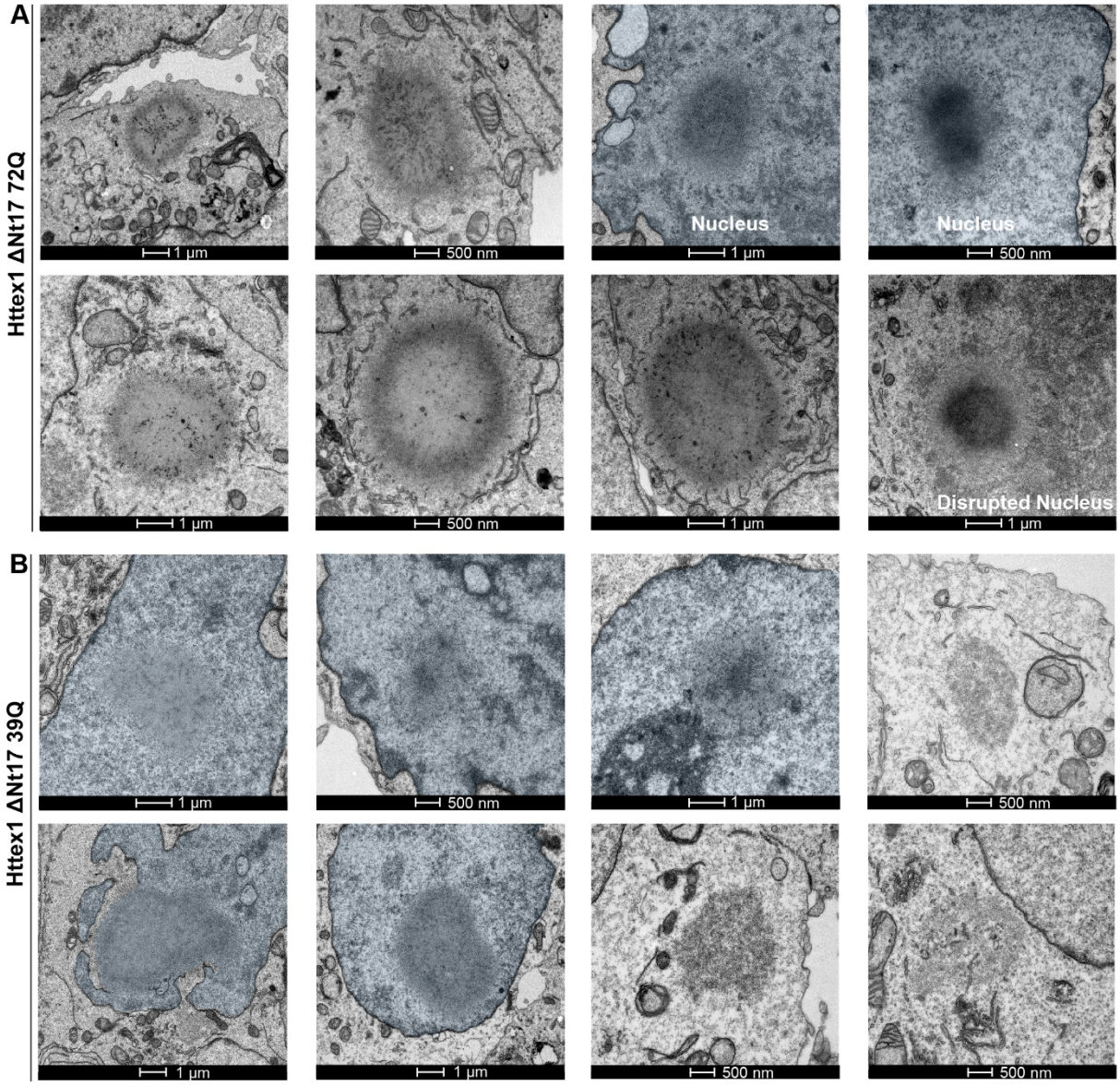

Figures S 8. Ultrastructural characterization of Httex1 ΔNt17 72Q and Httex1 ΔNt17 39Q inclusions.

A. 8 representative electron micrographs of Httex1 ΔNt17 72Q inclusions in HEK cells 48 h post-transfection. **B**. 8 representative electron micrographs of Httex1 ΔNt17 39 inclusions in HEK cells 48 h post-transfection. The nucleus is highlighted in blue. Scale bars = 1 µm or 500 nm as indicated below the micrographs.

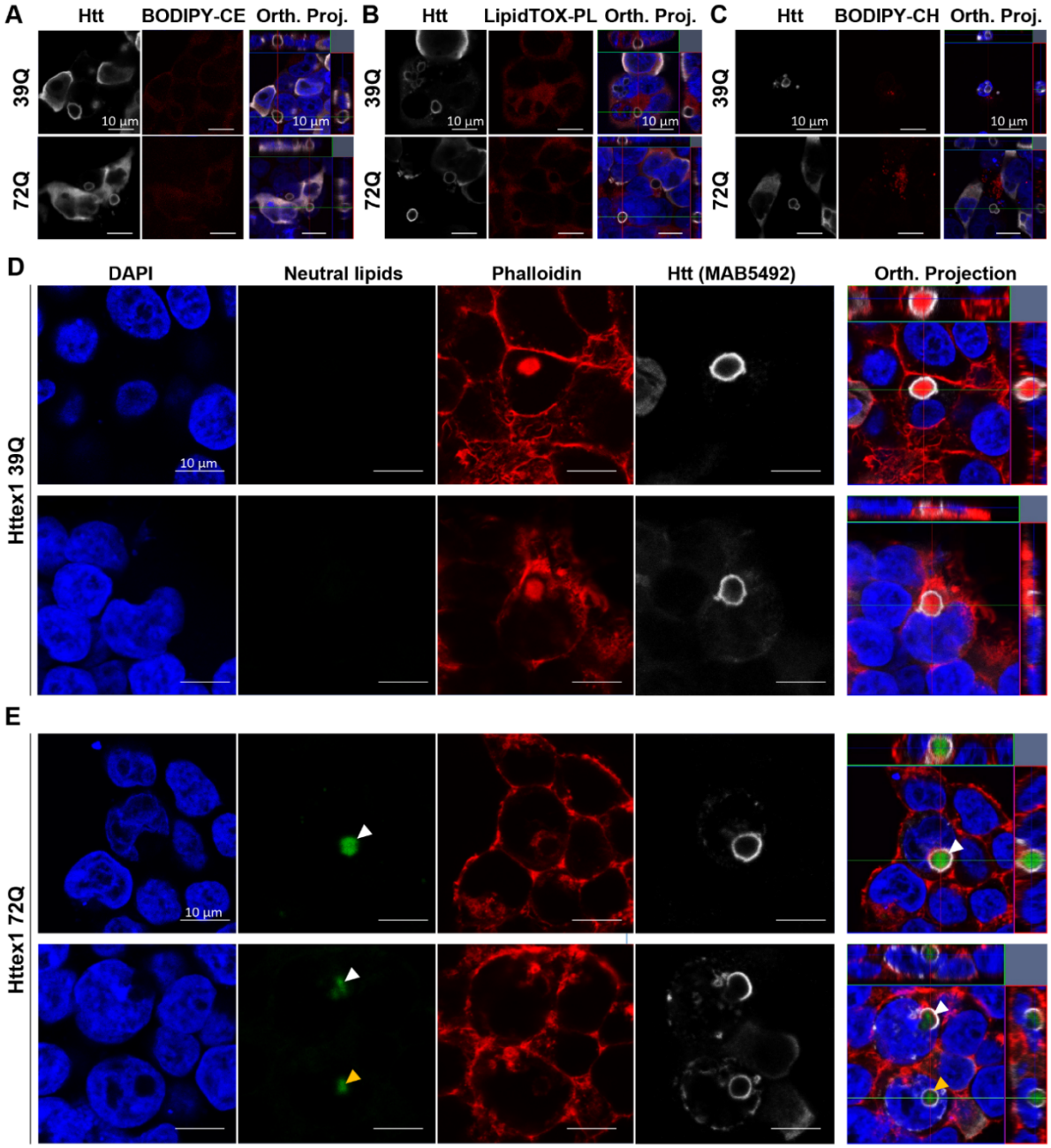

Figures S 9. Neutral lipid enrichment of Httex1 cellular inclusions is dependent on the polyQ length.

(**A-C**) Representative confocal images of Httex1 39Q and Httex1 72Q inclusions 48 h post-transfection stained by Htt antibody (MAB5492, grey) and different lipid dyes (red). **A**. The Ceramide BODIPY probe (BODIPY-CE) does not show any colocalization of inclusions with Ceramide. **B**. The LipidTOX™ Red phospholipid stain (LipidTOX-PL) does not show any colocalization of inclusions with phospholipids. **C**. The cholesteryl ester BODIPY probe (BODIPY-CH) does not show any colocalization of inclusions with cholesteryl ester. Scale bars = 10 µm. Representative confocal images of Httex1 39Q (**D**) and Httex1 72Q (**E**) inclusions

formed 48 h after transfection in HEK cells. Inclusions were stained by the Htt antibody (MAB5492, grey) in combination with a marker of the neutral lipids (non-Polar BODIPY probe, green). The nucleus was counterstained with DAPI (blue), and phalloidin (red) was used to stain the actin F. White arrowheads indicate neutral lipid enrichment only for Httex1 72Q inclusions. Orthogonal projections (Orth. Projection) were generated from a Z-stack through the selected cells. Scale bars = 10 µm.

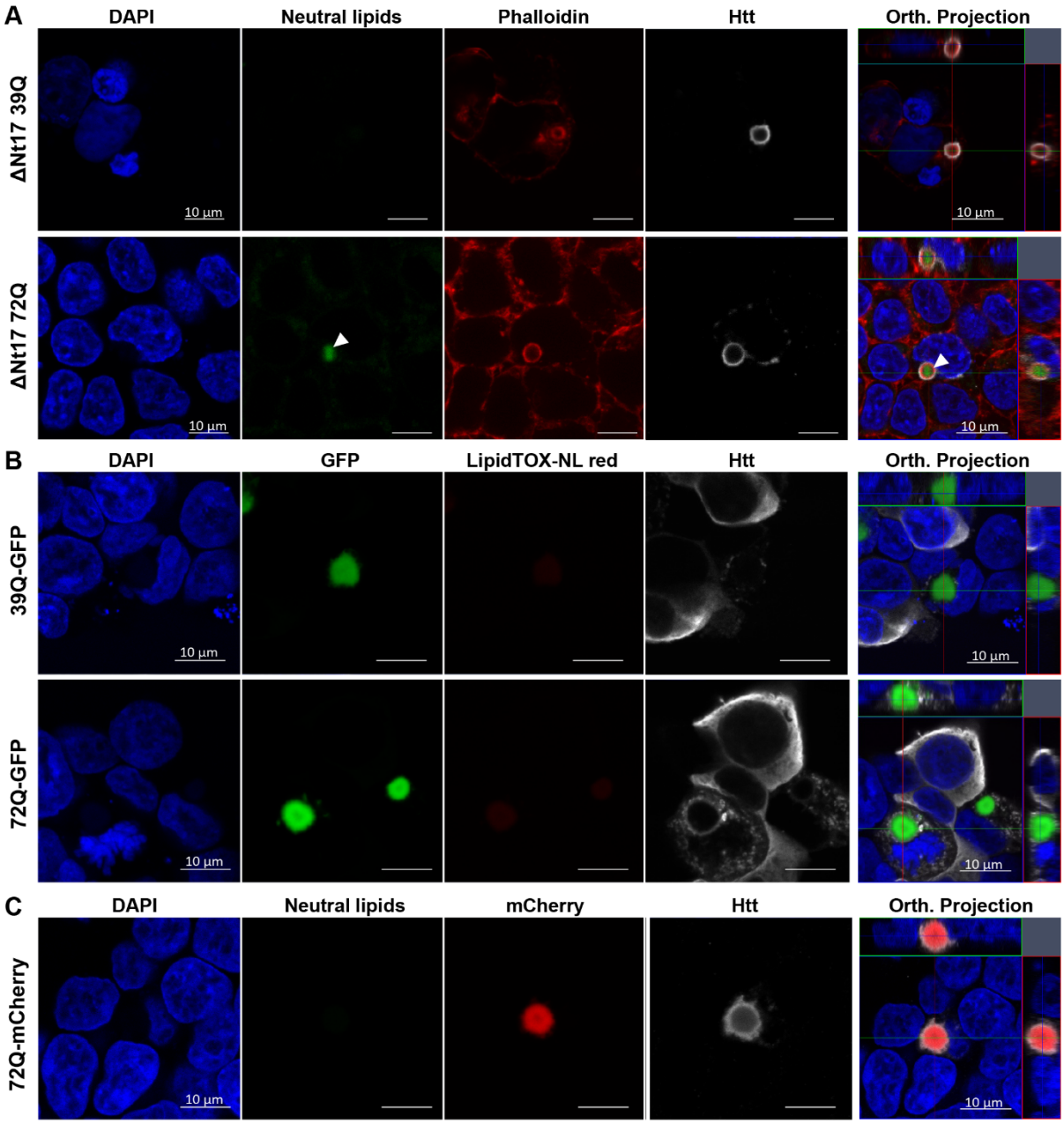

Figures S 10. No neutral lipid enrichment was observed in Httex1-GFP cellular inclusions but only for Httex1 ΔNt17 72Q.

A. Representative confocal image of Httex1 ΔNt17 39Q and 72Q inclusions 48 h post-transfection stained with the non-Polar BODIPY probe (493/503) targeting neutral lipids (green) shows a neutral lipid enrichment to the core of the inclusion for 72Q but not 39Q. Phalloidin (red) was used to stain the F-actin. White arrowheads indicate neutral lipid enrichment. Scale bars = 10 µm. **B**. Representative confocal images of Httex1 39Q-GFP and Httex1 72Q-GFP inclusions 48 h post-transfection stained with the LipidTOX™ Red stain targeting neutral lipids (LipidTOX-NL red). **C**. Representative confocal images of Httex1 72Q-mCherry inclusions 48 h post-transfection stained with the non-Polar BODIPY probe (493/503)

targeting neutral lipids. No lipid enrichment was observed for Httex1-GFP or Httex1-mCherry cellular inclusions. The nucleus was stained with DAPI (blue) and Httex1 with MAB5492 primary antibody revealed by a secondary antibody coupled to Alexa 647 (grey). Orthogonal projections (Orth. Projection) were generated from a Z-stack through the selected cells. Scale bars = 10 µm.

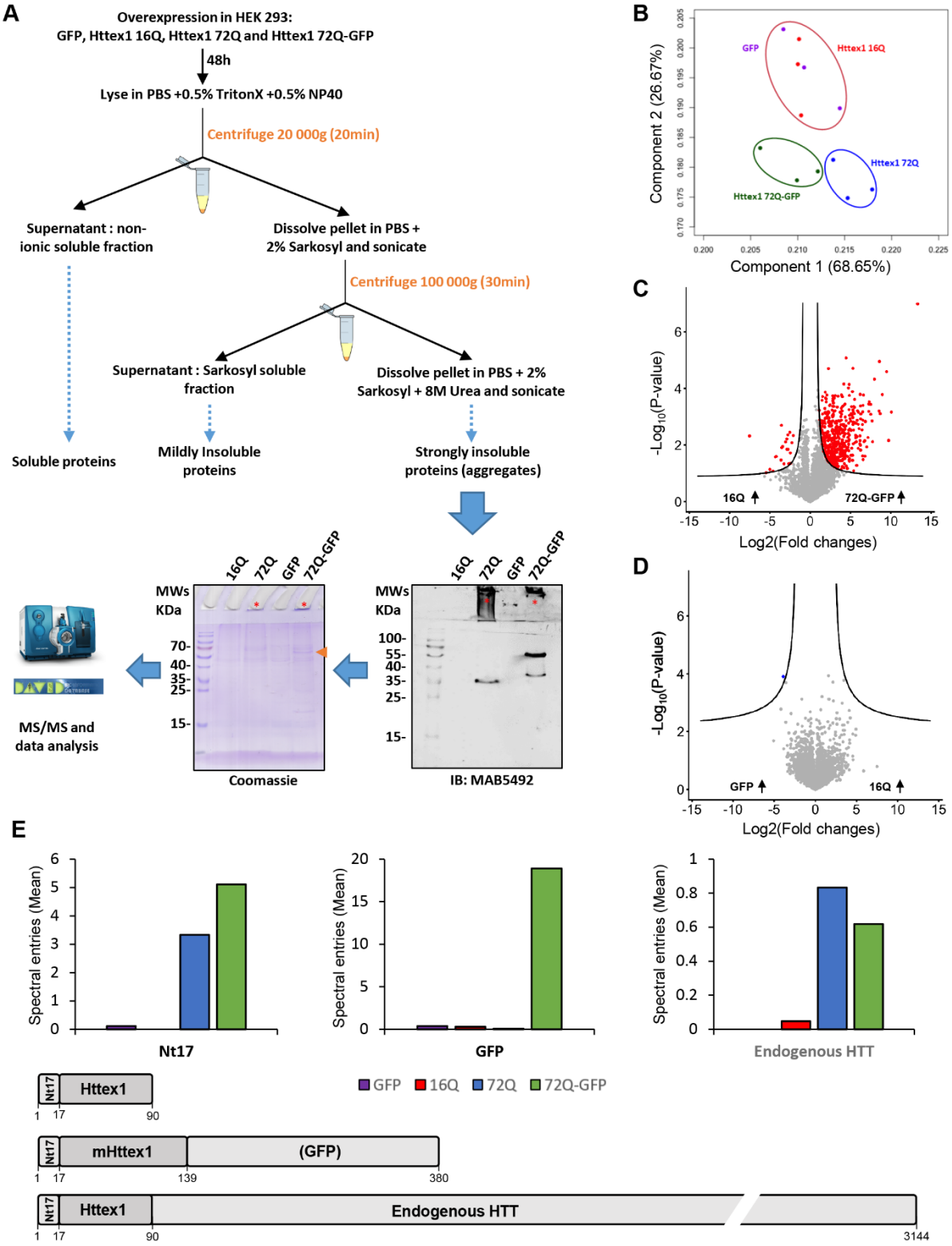

Figures S 11. Detergent fractionation and proteomic analysis of Httex1 transfected in HEK cells.

A. Overall workflow: HEK cells were transfected for 48 h with Httex1 and GFP indicated plasmids before detergent fractionation from mild to harsh solubilization to separate soluble Htt to aggregate species. Proteins from the last Urea soluble fraction containing Htt inclusions were separated on SDS-PAGE gel, followed by LC-MS/MS for protein identification and

quantification of 3 independent experiments. Red stars indicate the presence of aggregates in the stacking gel. The orange arrow indicates the expected size of Httex1 72Q-GFP. **B.** Principal component analysis of the Urea soluble fraction shows 3 clusters: 1) Httex1 16Q and GFP (non-aggregated controls, red and purple), 2) Httex1 72Q-GFP (green), and 3) Httex1 72Q (blue). **C-D.** Volcano plot with a false discovery rate (FDR) of 0.05 and S0 of 0.5 used to compare protein levels identified in the Urea soluble fraction. (**C**) The comparison of Httex1 72Q-GFP vs. Httex1 16Q showed a strong protein enrichment for Httex1 72Q-GFP. (**D**). Almost no significant differences were found in the comparison of the two negative controls Httex1 16Q and GFP. **E.** Peptide detection (mean spectral entries of the 3 independent experiments) along the Httex1 (+/-GFP) and full-length HTT. The schematic representation of Htt fragments shows non-mutated Httex1 that corresponds to Httex1 16Q, mHttex1 corresponding to Httex1 72Q, or Httex1 72Q-GFP when fused to GFP at the C-terminus and the non-mutated full-length HTT that corresponds to the endogenous protein. The different sequences were divided into 4 segments: Nt17 domain, mHttex1 (not detected), GFP, and the full-length sequence of HTT over the first exon.

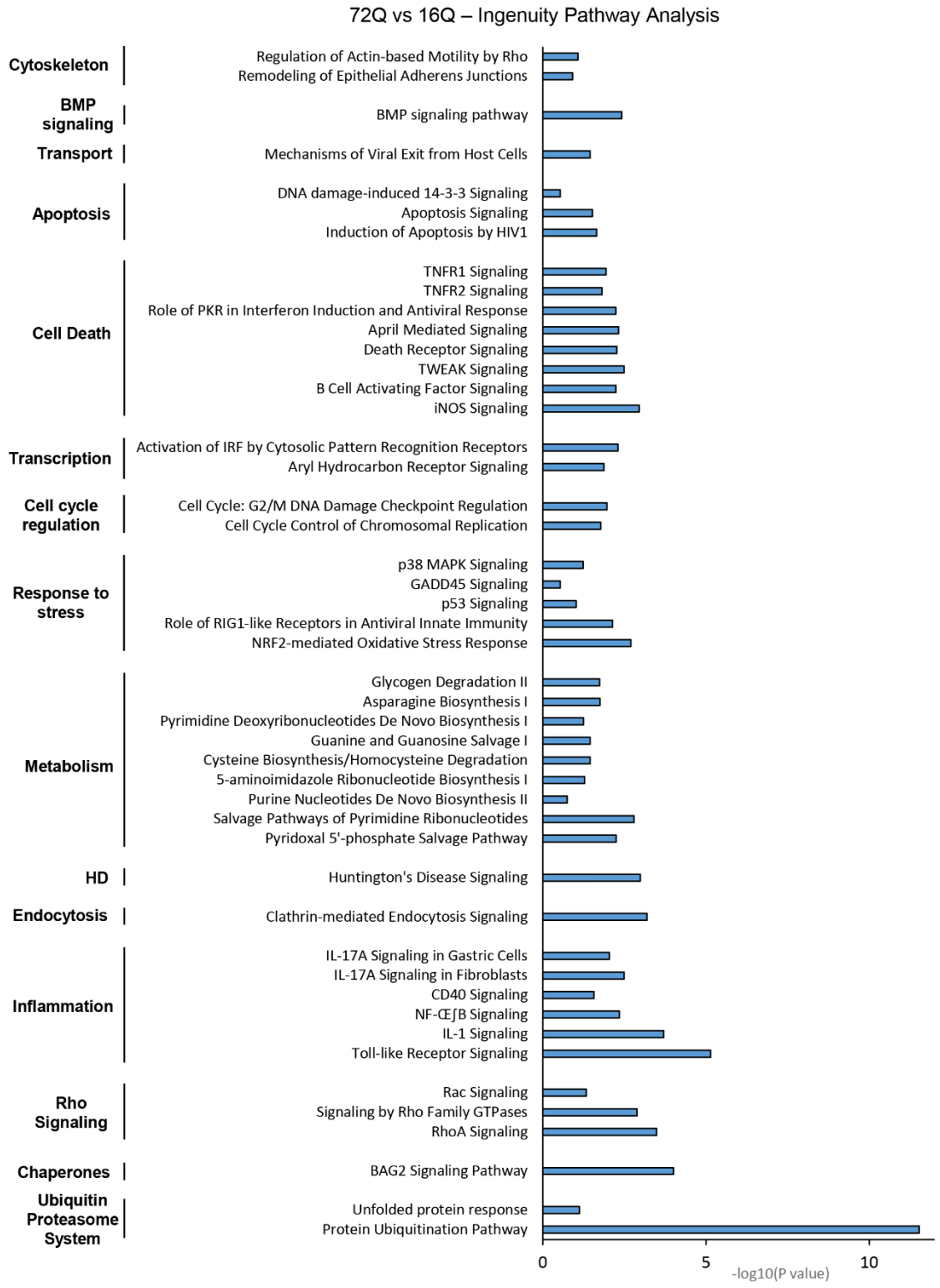

Figures S 12. **Ingenuity Pathway Analysis of Httex1 72Q vs. Httex1 16Q Urea soluble fraction reveals strong enrichment of the Ubiquitin-Proteasome System (UPS).**

Canonical pathways enriched in the Urea soluble fraction of Httex1 72Q vs. Httex1 16Q extracted from the volcano plot (Figure 3A) of the quantitative proteomic using Ingenuity Pathway Analysis (IPA).

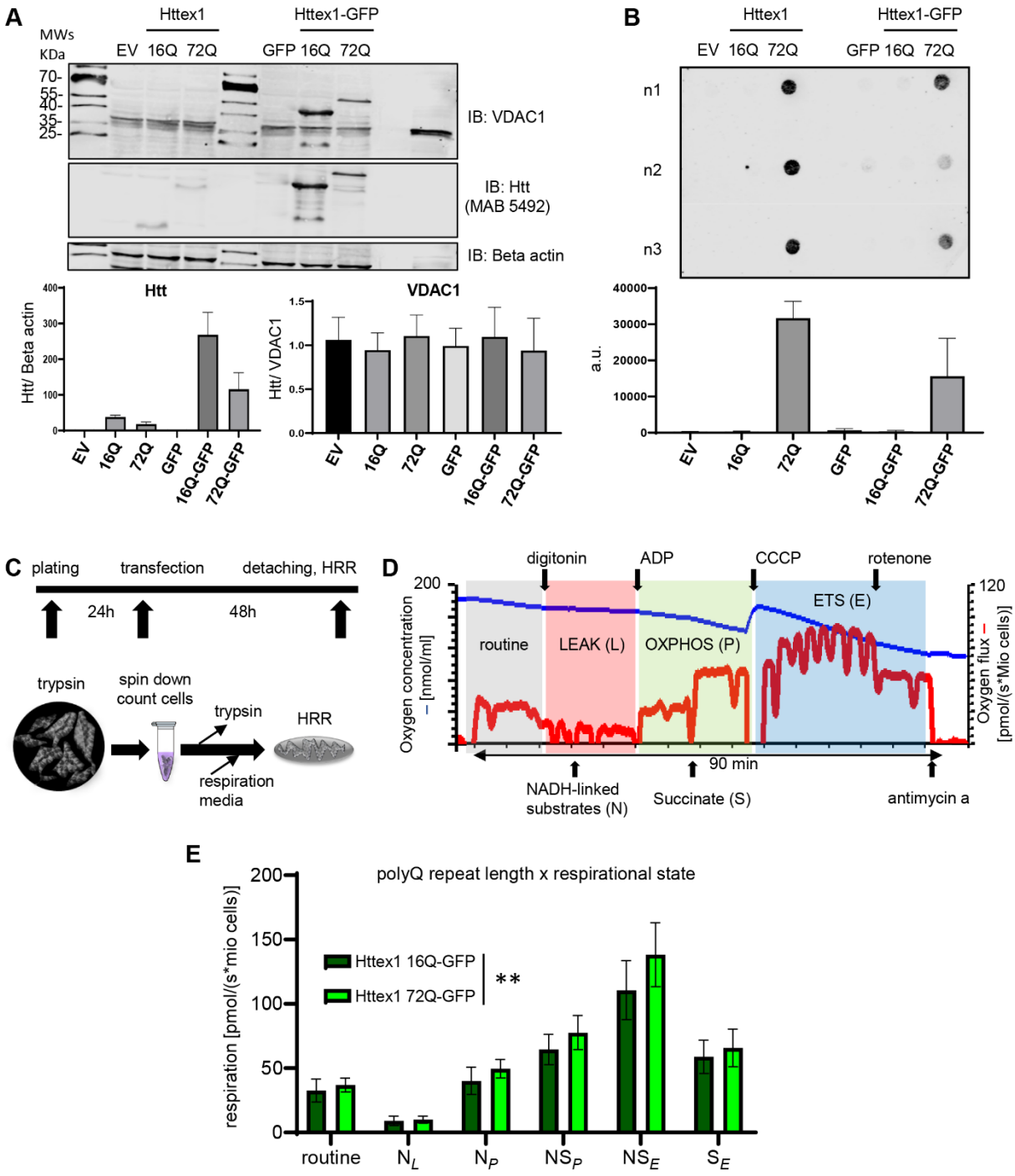

Figures S 13. High-resolution respirometry (HRR) revealed respiration differences in cells transfected with Httex1 72Q-GFP compared to Httex1 16Q-GFP.

A. Western Blot (WB) analyses of Httex1 transfected HEK cells in parallel with the HRR experiment. We quantified similar levels of the outer mitochondrial membrane protein VDAC1, indicating no decrease in mitochondrial density. Httex1 levels indicated higher Httex1 16Q(+/-GFP) levels compared to Httex1 72Q(+/-GFP) in the soluble fraction. Due to better transfection efficiency, Httex1-GFP constructs are expressed higher than the tag-free Httex1 constructs. **B.** Filter trap analyses of Httex1 transfected HEK cells in parallel with the HRR experiment. Only Httex1 72Q(+/-GFP) were detected on the filter trap after loading of the SDS-insoluble fraction, indicating the formation of large SDS-insoluble aggregates. **C.** Experimental setup of HRR

experiments. Cells were transfected with indicated constructs 24 h after plating in 4 independent experiments. 48 h after transfection, cells were gently detached and HRR was performed in respiration media (MIR05). **D.** After the measurement of routine respiration, cells were chemically permeabilized by digitonin. Different respirational states were subsequently induced using a substrate-uncoupler-inhibitor titration (SUIT) protocol. **E.** Routine respiration, NADH-driven, or complex 1-linked respiration after the addition of ADP (OXPHOS state) (NP), NADH- and succinate driven, or complex 1 and 2-linked respiration in the OXPHOS state (NSP), and in the uncoupled electron transport system (ETS) capacity (NSE), as well as succinate driven, or complex 2-linked respiration in the ETS state (SE) were assessed. Httex1 72Q-GFP significantly increased the respiration compared to Httex1 16Q-GFP. (C) Two-way ANOVA showing a significant interaction between the polyQ repeat length and the respirational states. *P < 0.05, **P < 0.005, ***P < 0.001.

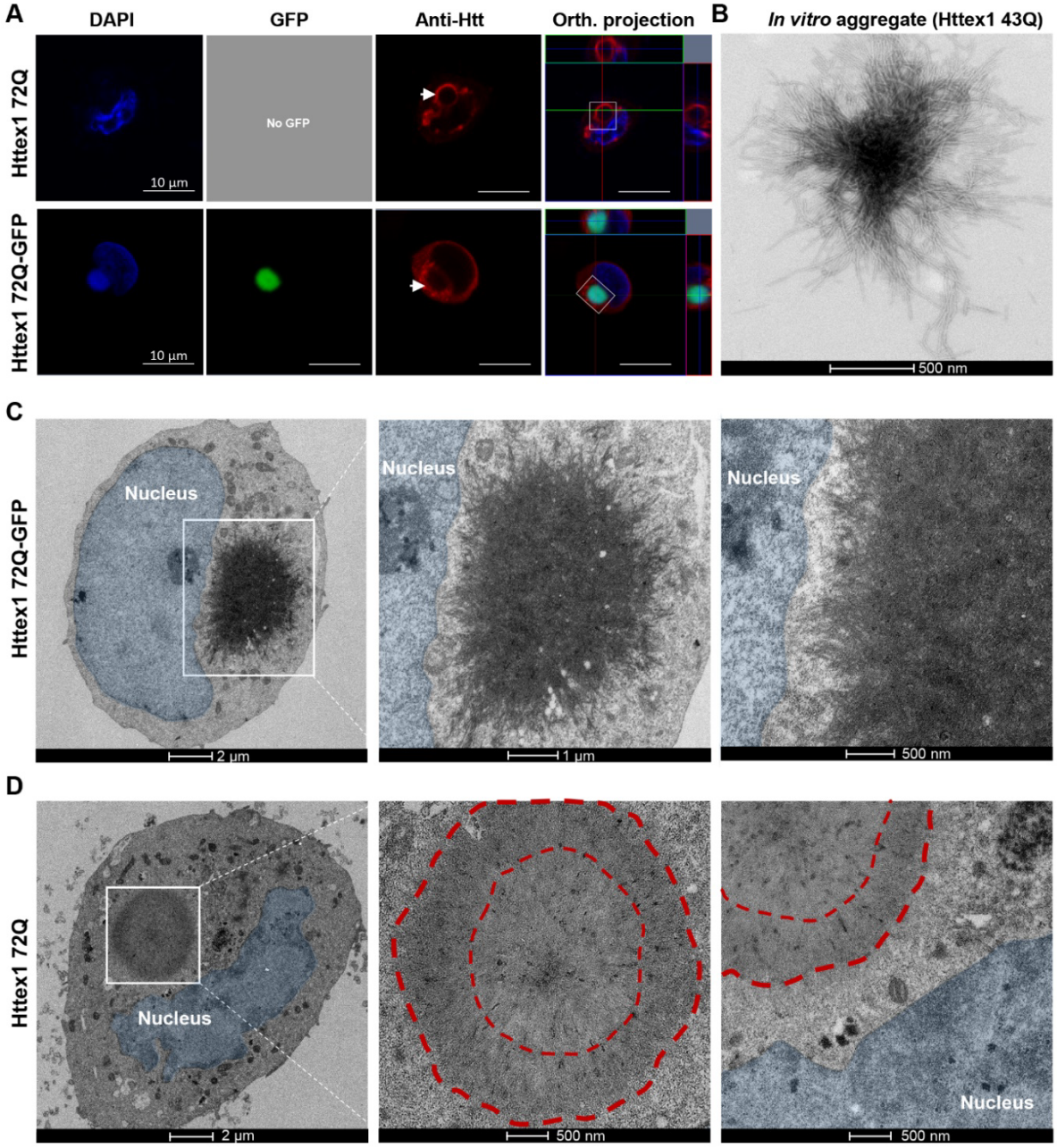

Figures S 14. **Correlative light- and electron microscopy (CLEM) of cells transfected with Httex1 72Q and Httex1 72Q-GFP.**

A. Confocal images of Httex1 72Q and Httex1 72Q-GFP, 48 h after transfection in HEK cells. Httex1 expression (red) was detected using a specific primary antibody against the N-terminal part of Htt (MAB5492) or GFP (green), and the nucleus was stained with DAPI (blue). Scale bars = 10 µm. The same cell was then processed for EM. **B.** Representative image of *in vitro* aggregate of Httex1 43Q assessed by EM. **C.** Electron micrograph of the transfected cell by Httex1 72Q-GFP previously imaged by confocal (**A**, bottom panels). Magnified micrographs of the inclusion (white square) and magnification close to the nuclear membrane are displayed on the middle and right-hand panels. **D.** Electron micrographs of the transfected cell by Httex1 72Q previously imaged by confocal (**A**, upper panels). Magnified micrographs of the inclusion (white square) and magnification close to the nuclear membrane are displayed on the middle and right-hand panels. Scale bars = 2 µm, 1 µm, or 500nm as indicated below the micrographs.

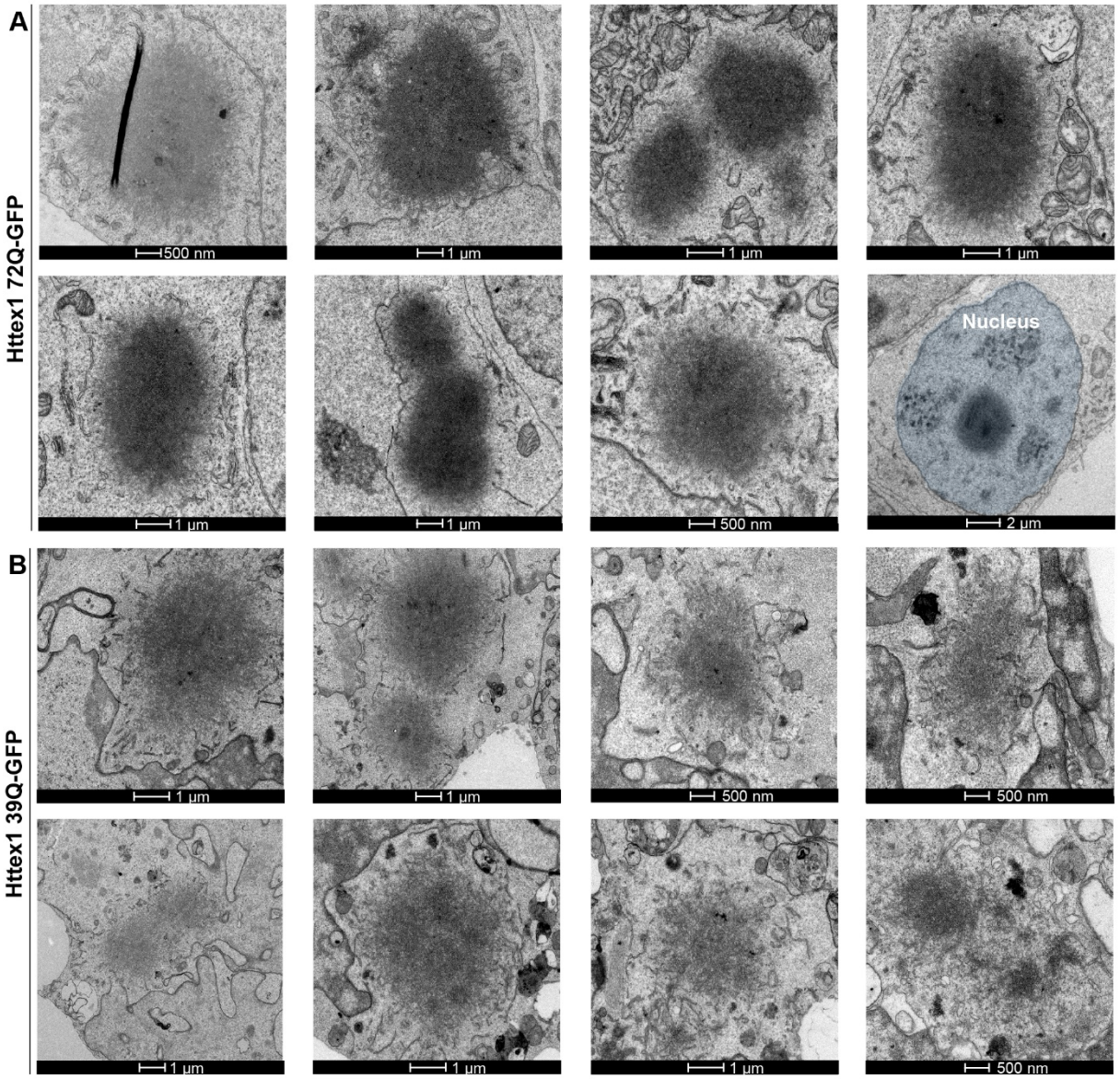

Figures S 15. Ultrastructural characterization of Httex1 72Q-GFP and Httex1 39Q-GFP inclusions.

A. 8 representative electron micrographs of Httex1 72Q-GFP inclusions formed in HEK cells 48 h post-transfection. **B.** 8 representative electron micrographs of Httex1 39-GFP inclusions formed in HEK cells 48 h post-transfection. The nucleus was highlighted in blue. Scale bars = 1 µm or 500 nm as indicated below the micrographs.

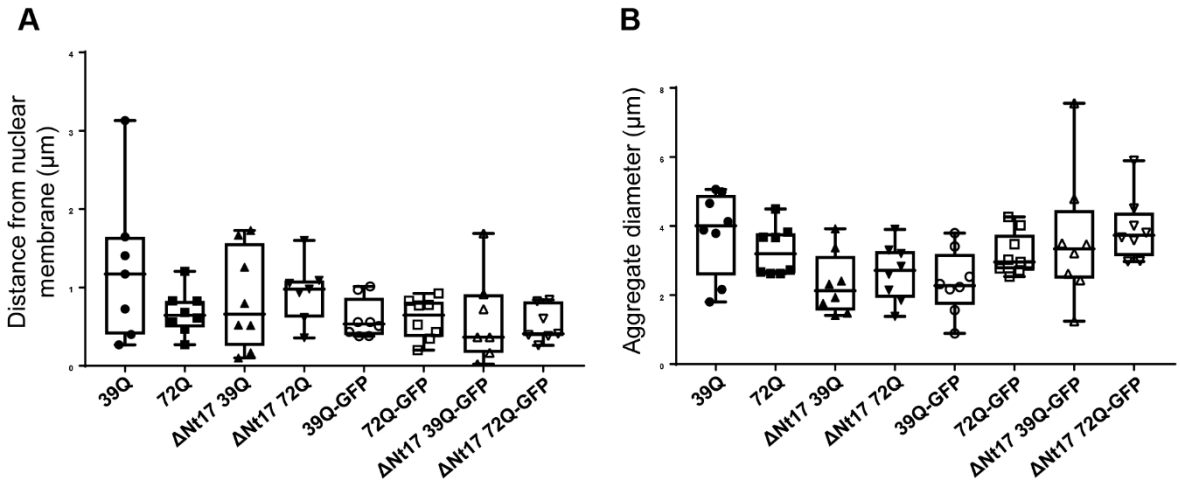

Figures S 16. **Subcellular localization and size of Httex1 inclusions based on electron micrographs.**

The distance of the inclusion from the nuclear membrane and the inclusion diameter was quantified from electron micrographs from Figures S3, S8, S15, and S18. **A.** Distance of the inclusion from the nuclear membrane. **B.** Httex1 inclusion diameter. No statistical differences were measured between the different conditions.

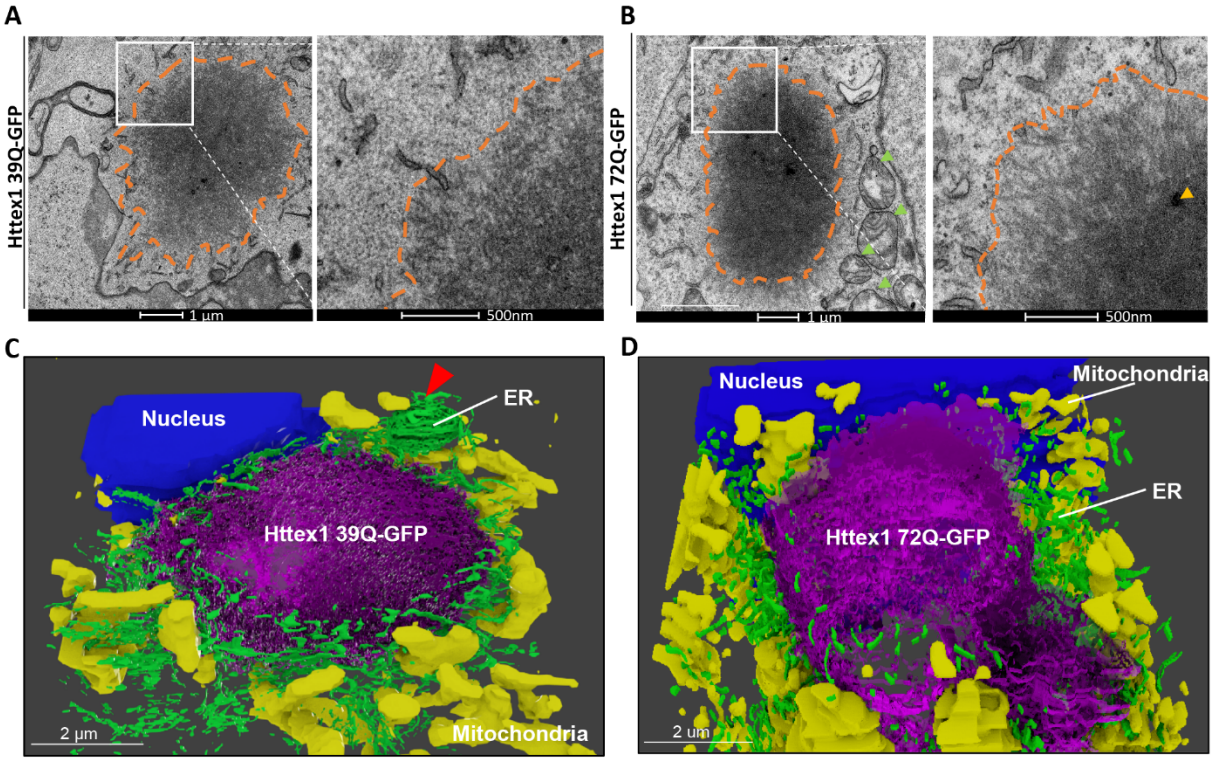

Figures S 17. EM and 3D models of cellular Httex1 39Q-GFP and 72Q-GFP inclusions show ER and mitochondria in their periphery.

A-B. Representative electron micrographs of Httex1 39Q-GFP (**A**) and Httex1 72Q-GFP (**B**) inclusions formed after 48 h expression in HEK cells. Higher magnifications (white square) are represented in the right-hand panels. Dashed lines delimit the inclusions. Orange arrowheads: internalized membranous structures. Green arrowheads: mitochondria. More electron micrographs of Httex1 72Q-GFP (Figure S15A) and Httex1 39Q-GFP (Figure S15B) were acquired. Scale bars = 1 µm (left-hand panel) and 500 nm (right-hand panels). **C-D.** 3D models of Httex1 39Q-GFP (**C**) and Httex1 72Q-GFP (**D**) inclusions (top views). Httex1-GFP inclusions (purple), ER membranes (green), nucleus (blue), and mitochondria (yellow). Scale bars = 2 µm.

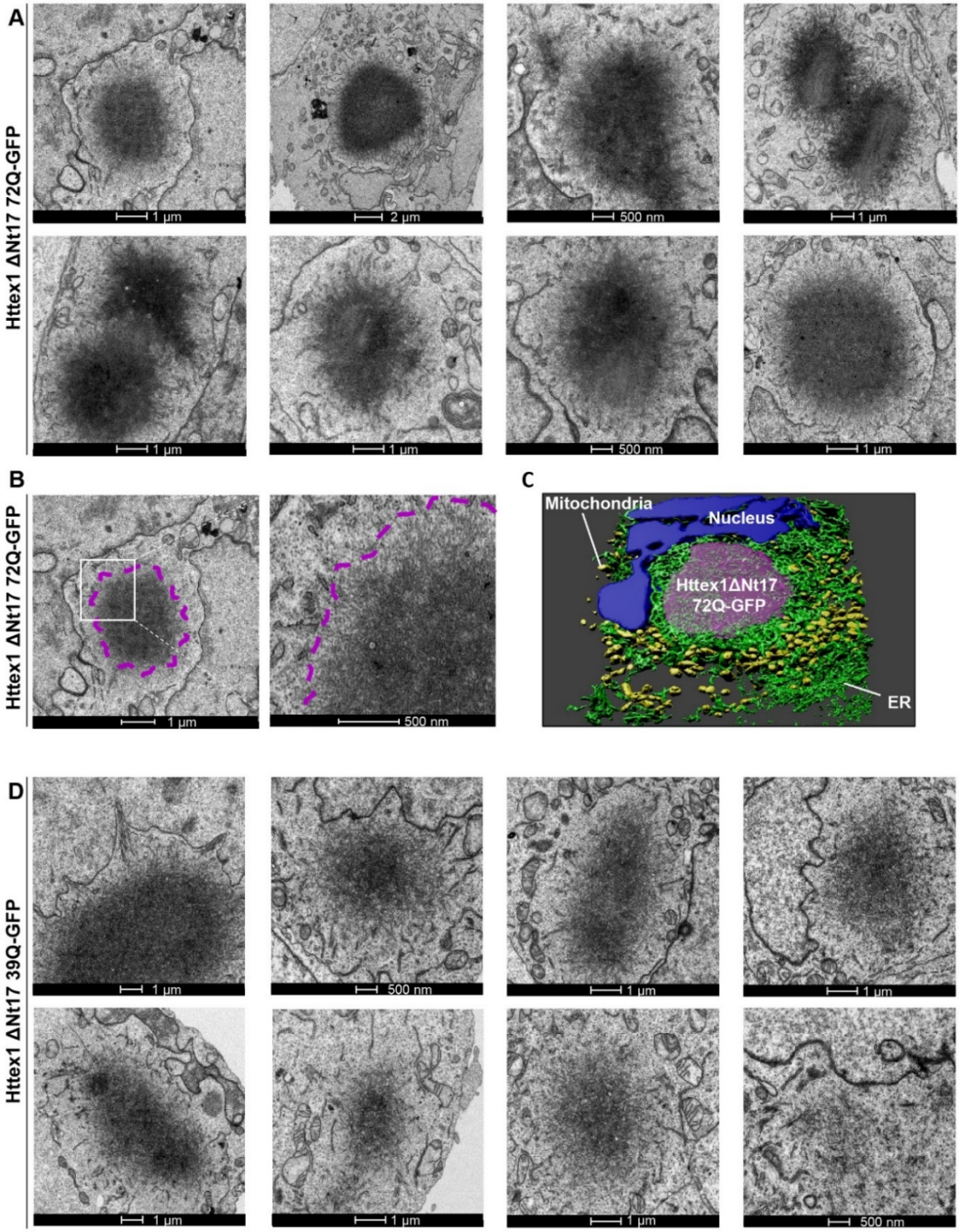

Figures S 18. Ultrastructural characterization of Httex1 ΔNt17 72Q-GFP and Httex1 ΔNt17 39Q-GFP inclusions.

A. 8 representative electron micrographs of Httex1 ΔNt17 72Q-GFP inclusions formed in HEK cells 48 h post-transfection. **B.** Httex1 ΔNt17 72Q-GFP cellular inclusion and higher magnification (white square) are displayed in the right-hand panel. Dashed lines delimit the inclusion. **C.** 3D model of Httex1 ΔNt17 72Q-GFP cellular inclusion (top view). Httex1 ΔNt17 72Q-GFP inclusion (purple), ER membranes (green), nucleus (blue), and mitochondria (yellow). **D.** 8 representative electron micrographs of Httex1 ΔNt17 39-GFP inclusions formed in HEK cells 48 h post-transfection. Scale bars = 2 µm, 1 µm, or 500 nm as indicated below the micrographs.

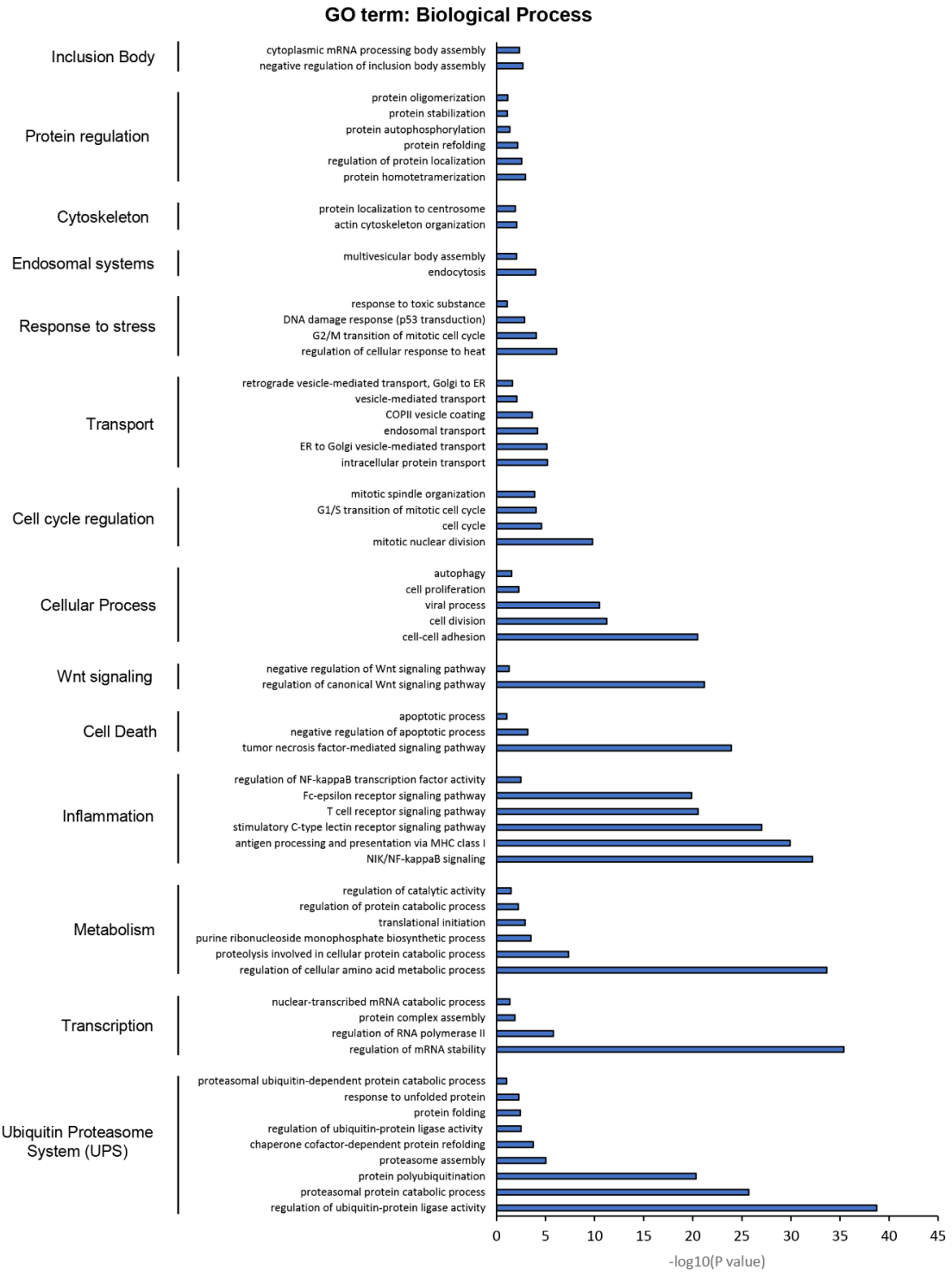

Figures S 19. Proteomic analysis of Httex1 72Q-GFP vs. GFP Urea soluble fraction from HEK cells.

Classification of the proteins significantly enriched in the Urea soluble fraction of HEK cells overexpressing Httex1 72Q or Httex1 16Q and extracted from the volcano plot (p-value<0.01) (Figure 3A). Analyses were performed using Gene Ontology (GO) enrichment analyses determined by DAVID analysis ($-\log_{10}$(p-value) >1).

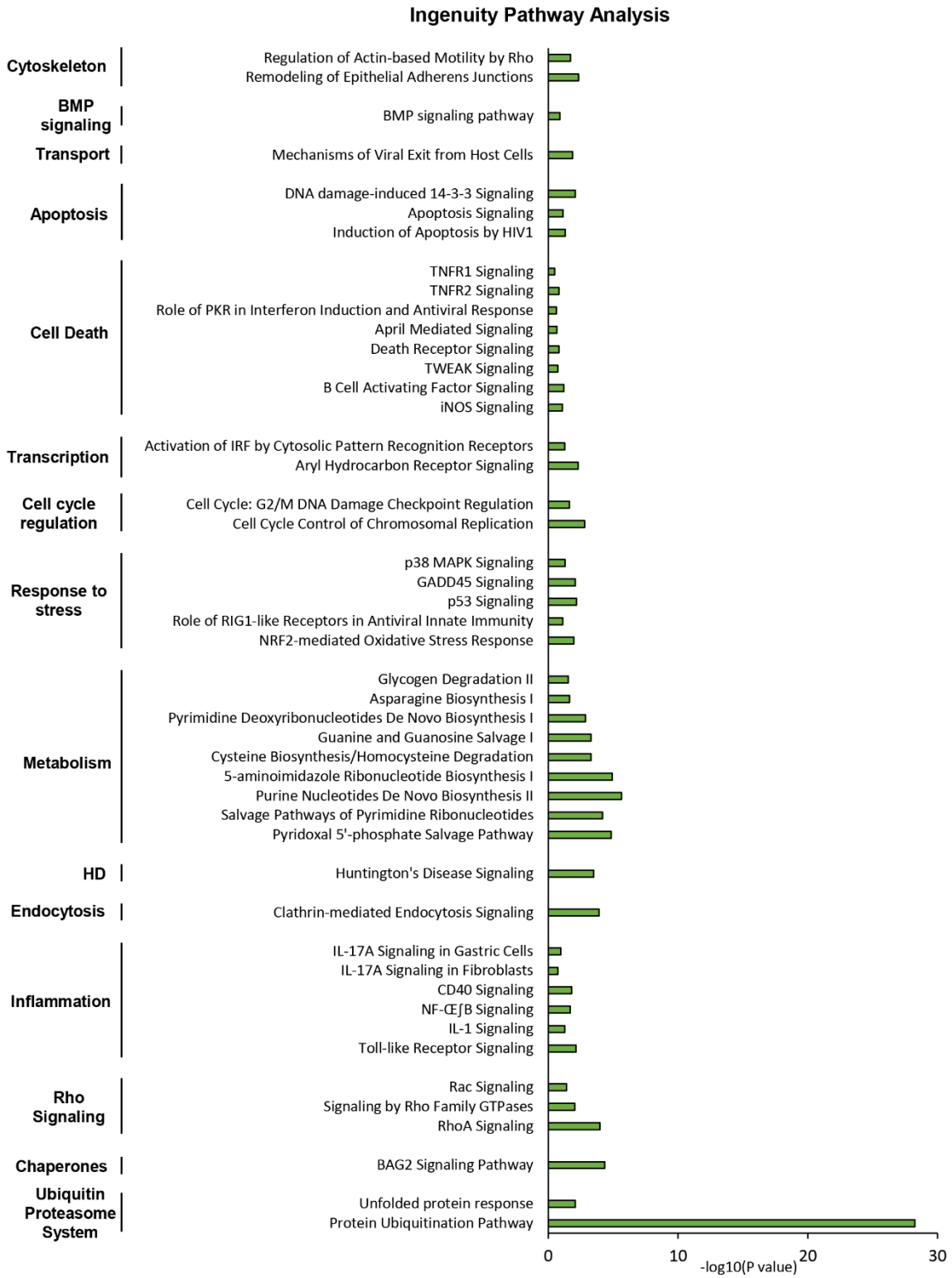

Figures S 20. **Ingenuity Pathway Analysis of Httex1 72Q-GFP vs. GFP Urea soluble fraction revealed strong enrichment of the Ubiquitin-Proteasome System (UPS).**

Canonical pathways enriched in the Urea soluble fraction of Httex1 72Q-GFP vs. Httex1 GFP extracted from the volcano plot in Figure 9A. Analyses were performed using Ingenuity Pathway Analysis (IPA).

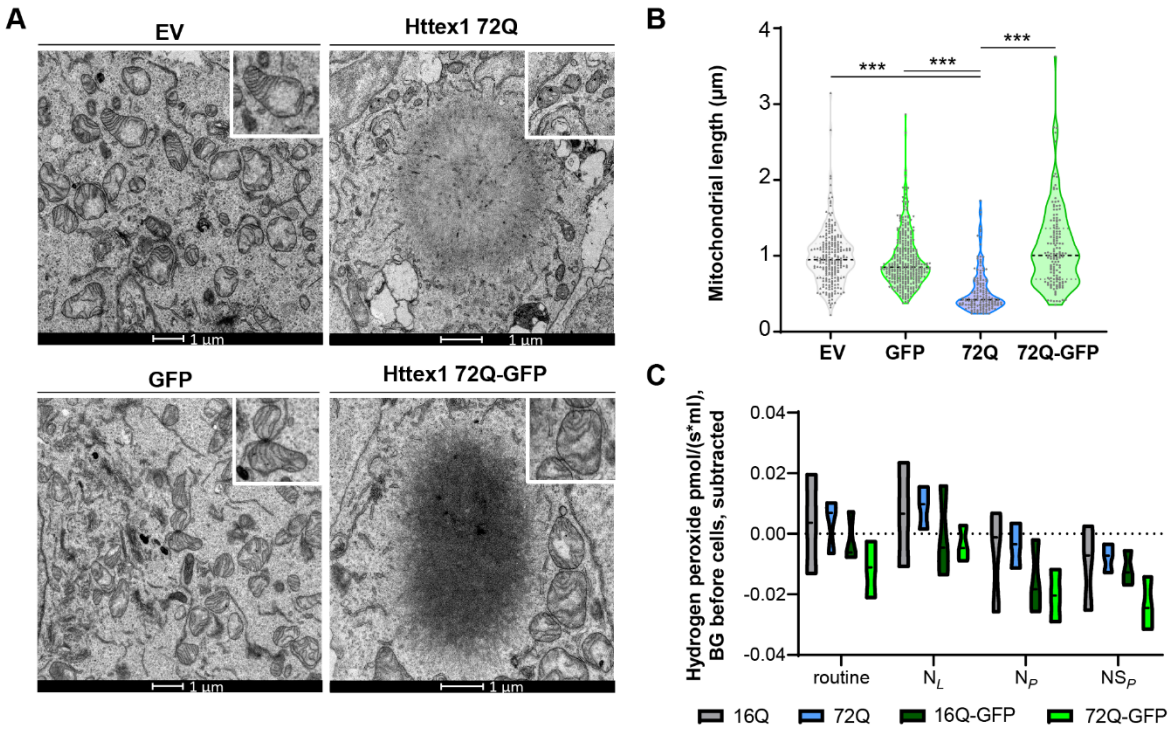

Figures S 21. **The formation of 72Q Httex1 inclusions induces mitochondrial alterations.**

A. Electron micrographs of mitochondria in HEK cells overexpressing empty vector (EV), Httex1 72Q, GFP or Httex1 72Q-GFP. The insets depict higher magnification of the mitochondria found at the periphery of Httex1 inclusions or representative in EV and GFP controls. Scale bars = 1 µm. **B.** Measurement of the mitochondrial length reveals a significant reduction of the size of the mitochondria profile located in the proximity of the inclusions. **C.** Mitochondrial reactive oxygen species (ROS) were measured in HEK cells overexpressing Httex1 16Q, Httex1 16Q-GFP, Httex1 72Q or Httex1 72Q-GFP for 48 h. The produced mitochondrial ROS were measured using Amplex red fluorometry (superoxide was transformed by superoxide dismutase to detectable levels of hydrogen peroxide). No significant differences in mitochondrial ROS levels were detected in the HEK cells overexpressing Httex1 72Q, compared to Httex1 72Q-GFP. The graph presents the median, minimum and maximum values of three independent experiments. ANOVA followed by Tukey honest significant difference [HSD] post hoc test was performed. *P < 0.05, **P < 0.005, ***P < 0.001.

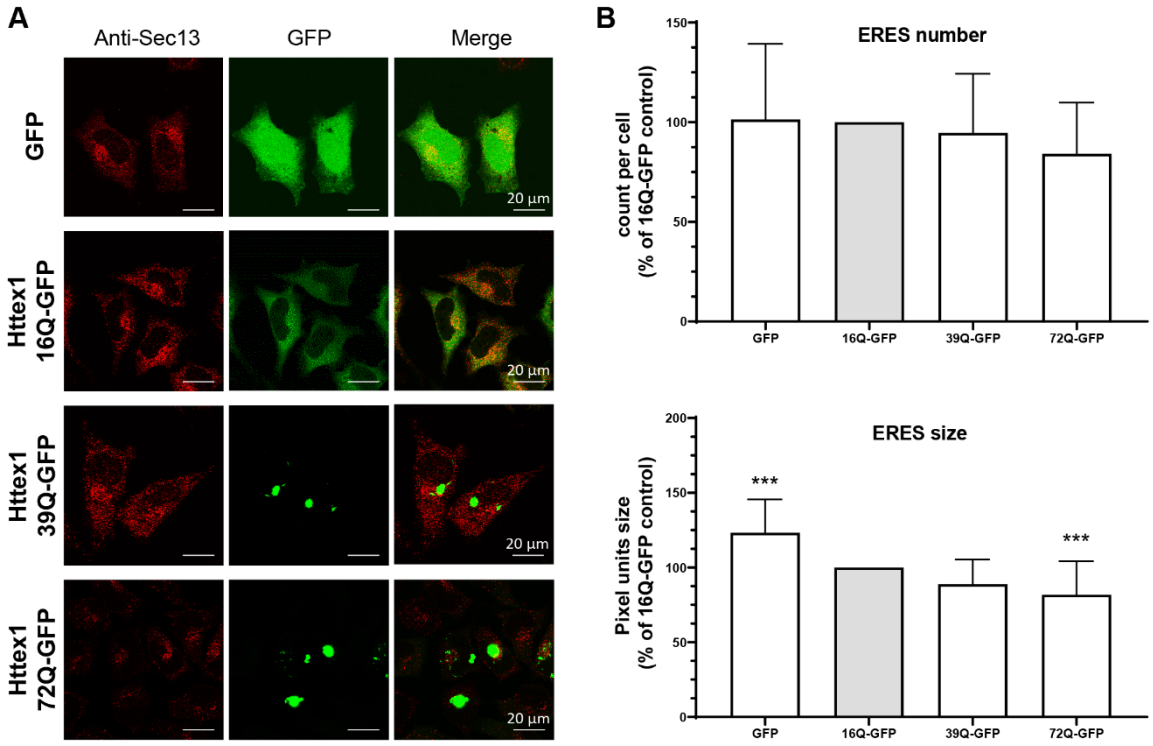

Figures S 22. Httex1-GFP inclusion formation induces the size reduction of ER-exit sites.

A. Representative confocal images of HeLa cells transfected with Httex1 16Q-GFP, 39Q-GFP or 72Q-GFP or GFP (as the negative control). Cells were fixed 48 h after transfection and immunostained. Httex1-GFP or GFP was detected by fluorescence, and ER exit sites were detected using the Sec13 antibody (red). Scale bars = 20 µm. **B**. ERES number and size quantifications from confocal imaging were performed using FIJI. The graphs represent the mean ± SD of three independent experiments presented as the relative percentage of the Httex1 16Q-GFP control. ANOVA followed by Tukey honest significant difference [HSD] post hoc test was performed. *P < 0.05, **P < 0.005, ***P < 0.001.

Specific features	Httex1 72Q	Httex1 72Q-GFP
Actin F at the periphery of inclusions	+++	-
Ring detection of Htt Ab	+++	++ (+center faintly)
Core/shell organization	+++	-
Thickness and spacing of fibrils in periphery	Thin fibrils and more spacing than the core	Thick fibrils, more inter-space compare to tag-free
polyQ influence on ultrastructure	Yes (lose core/shell organization)	No
Recruitment of membranous organelles	++ in core and +++ in periphery	Few but interactions at the periphery
Nuclear inclusions	Lose core/shell arrangement and the recruitment of membranous organelles No interactions with nuc. mb.	No overall change in morphology No interactions with nuc. mb.
Lipids	++ Neutral lipids in core specific for 72Q not 39Q	-
Mitochondrial morphology	Loss of cristae	normal
Fragmentation of mitochondrial profile	++	-
Mitochondrial respiration	++	+
ER impact	++ ERES modulation	+ ERES modulation
Main pathways proteomic	Endolysosome, UPS, cytoskeleton, nucleoplasm, ER to Golgi transport	Endolysosome, UPS, cytoskeleton, nucleoplasm, ER to Golgi transport, mitochondria
Differences in proteomic pathways	Infection/inflammation, mRNA stability	UPS more enriched, mitochondria, metabolism

Figures S 23. **Tag-free and GFP Httex1 cellular inclusions reveal distinct features in HEK cells.**

The table summarizes the key distinct features between Httex1 72Q and Httex1 72Q-GFP at the cellular, ultrastructural, proteomic composition and functional levels. Confocal analysis revealed a ring-like detection of Httex1 inclusions by Htt antibodies and colocalized with filamentous actin only for tag-free Httex1 72Q. Our results demonstrated that the core and shell structural organization of tag-free Httex1 is influenced by the subcellular environment and the polyQ length but not by the presence of Nt17 domain. The addition of GFP to the C-terminal part of Httex1 induced a differential structural organization. Indeed, no core and shell organization were detected for Httex1 72Q-GFP inclusions, independently of the polyQ length. We demonstrated that neutral lipids are specifically recruited into tag-free Httex1 cellular inclusions in a polyQ length-dependent manner. Moreover, tag-free Httex1 72Q inclusion formation induced mitochondrial fragmentation, increased mitochondrial respiration and led to ER-exit site remodeling. In contrast, Httex1 72Q-GFP inclusion formation did not lead to mitochondrial fragmentation but to reduced mitochondrial respiration and ERES modulation compared to Httex1 72Q. Finally, our quantitative proteomic analysis revealed 55% differences between the co-aggregated proteins with Httex1 72Q compared to Httex1 72Q-GFP. Httex1 72Q inclusions were found to have a specific enrichment of infection and inflammation-related proteins, while Httex1 72Q-GFP exhibited a stronger UPS-related protein enrichment, as well as an enrichment of mitochondria and metabolic-related pathways.

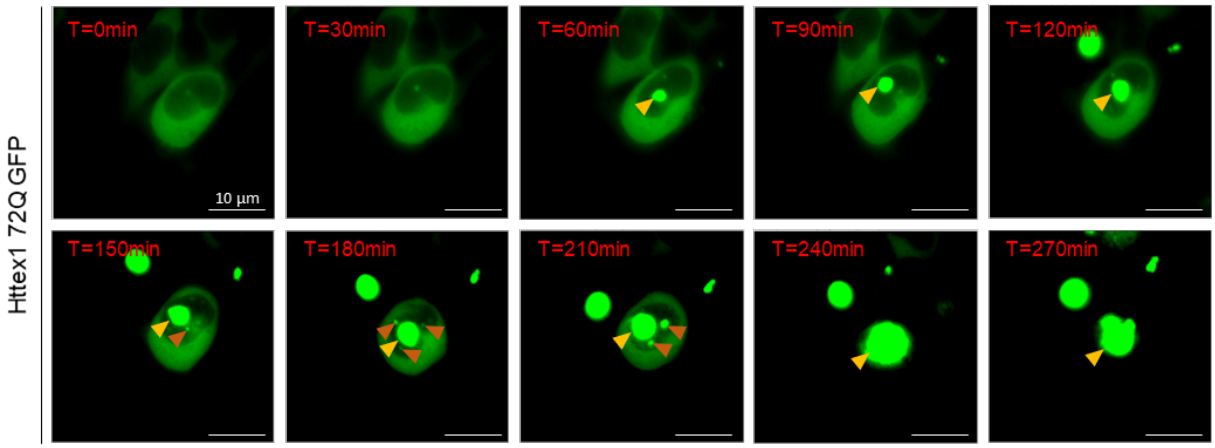

Figures S 24. Droplets and fusion events observed in HEK cells transfected with Httex1 72Q-GFP.

The time-lapse represents the GFP fluorescence observed by live-cell microscopy of Httex1 72Q-GFP aggregation. The yellow arrowhead shows the main Httex1 72Q-GFP inclusion that fuses with smaller surrounding droplets (orange arrowheads) over time. Scale bars = 10 µm.

Chapter III: Nuclear and cytoplasmic huntingtin inclusions exhibit distinct biochemical composition, interactome and ultrastructural properties

Abstract

Huntington's disease (HD) is characterized by the polyglutamine (polyQ) expansion within the huntingtin protein (Htt), leading to the formation of neuronal inclusion and neurodegeneration. Although the gene responsible for the disease is known, we still do not understand well the cellular mechanisms leading to aggregation and inclusion formation. In this study using primary neurons, we clearly established that neuronal intranuclear inclusions evolve over time from small aggregates to large granulo-filamentous inclusions and that this process is associated with increased cellular toxicity. The analysis of the protein content of neuronal intranuclear inclusions revealed a failure of the cellular degradation machineries to clear Httex1 inclusions, as well as the sequestration of transcription regulators. These findings suggest that identifying modifiers of Htt inclusion growth and aberrant secondary interactions with other proteins and organelles represent an alternative strategy for interfering with Htt-induced toxicity and slowing disease progression, especially after disease onset. Our results uncover novel biochemical and ultrastructural features of neuronal intranuclear Httex1 inclusions as well as aggregation mechanisms over time.

1. Introduction

The use of mammalian overexpression-based cellular models (including non-differentiated neuronal cells) are very useful to assess huntingtin exon 1 (Httex1) inclusion formation and are still being extensively used by scientists in the field of Huntington's disease (HD)[149,195,265,270,310,408,504–507]. The deep investigation of Httex1 aggregation and inclusion formation in mammalian cells using HEK cells (Chapter II) allowed us to unravel specific cellular mechanisms of Httex1 inclusion formation, and predominantly cytoplasmic inclusions. We demonstrated that the length of the polyglutamine (polyQ) stretch but not the first 17 amino acids (Nt17 domain) modulates the ultrastructural properties of Httex1 cytoplasmic inclusions. In addition, we revealed a striking difference in the composition and ultrastructure of Httex1 inclusions with and without the presence of a GFP tag at the C-terminal part of the protein.

In order to investigate Htt aggregation in a neuronal context, several studies used neuronal cell types to model the expression of mutant Htt, but without robust biochemical and ultrastructural analysis of the neuronal inclusions, and often relying on tags fused to Htt[120,195,283,332,409]. For example, although the STHDhQ111/Q111 cells are mouse striatal-like neurons expressing a humanized exon 1, the level of Htt inclusions formation is very low in these cells[297,298]. Similarly, in the absence of overexpression-based methods using patient-derived cells, very few Htt inclusions are observed[301,302,508]. Therefore, these models do not allow interrogating the entire process of Htt aggregation, inclusion formation and maturation of the endogenous proteins in cells.

As one of the key objectives of our study is to decipher the sequence (Nt17, polyQ repeat length, and GFP) determinants of Htt inclusion formation, we selected a lentiviral-based neuronal model of Httex1 expression that is characterized by abundant Htt inclusions formation in which manipulations of the Htt sequence are possible. Indeed, we investigated Httex1 inclusions formation in primary cortical neurons and investigated how sequences flanking the polyQ domain or the presence of a GFP tag influences: 1) the level and kinetics of aggregation

in neurons (confocal and image-based quantification), 2) the subcellular localization of the newly formed aggregates (confocal imaging), 3) their ultrastructural properties (CLEM and tomography analyses), 4) their protein composition (biochemistry and proteomic analyses) and 5) their toxicity properties (cell death assays).

In addition, our group recently reported that sequences outside exon1 influence Htt aggregation[175]. In this study, *Kolla et al.* demonstrated that Htt171 aggregation is driven by phase separation events via a complex interplay between the helical domain (residues 104-171) and the polyQ domain. Moreover, site-specific phosphorylation of Htt outside exon1 (T107 and S116) has also been shown to modulate Htt aggregation. Htt171 fragment was previously shown to form inclusions formation in cells[264,308,509] and mice[510]. In contrast, the Htt586 fragment —which is naturally produced by caspase-6 cleavage of the huntingtin protein[85,104,131,276]— does not aggregate or form inclusions in cells[273,274]. Discrepancies were reported *in vivo* on the use of the caspase-6 fragment in transgenic mice. In one study, the Htt586 148Q mice under the beta-actin promoter did not recapitulate HD motor and behavioral phenotypes, and only a few aggregates were observed compared to the shorter Httex1 fragment[511]. However, a different study with HD mice expressing Htt586 82Q under the prion promoter reported motor deficits, brain atrophy and massive inclusion formation[106]. Interestingly, a third study showed that the caspase-6 cleavage site of Htt was required for neuronal dysfunction and neurodegeneration in a YAC mice model[109]. In order to explore the role of fragment length in regulating Htt inclusions formation, we conducted a preliminary image-based analysis of long N-terminal Htt fragments expression and aggregation in primary neurons.

2. Results

2.1 Expression of Httex1 72Q in primary cortical neurons leads to the formation of dense and filamentous nuclear inclusions

Following the results obtained in our mammalian cellular model of HD showing predominantly cytoplasmic inclusions, we next investigated the sequence determinants of Htt aggregation and inclusion formation in primary cortical neurons over time.

First, confocal microscopy confirmed that none of the Httex1 16Q constructs (Httex1 16Q and ΔNt17 Httex1 16Q) overexpressed in neurons induced the formation of aggregates up to 14 days post-transduction (D14). Conversely, overexpression of Httex1 72Q induced the formation of round nuclear inclusions in almost 100% of transduced neurons, already at D3 (Figures 1A-B and S1). Less than 1% of the neurons showed cytoplasmic inclusions, either as puncta or with the ring-like morphology. Although no changes in the subcellular distribution of the inclusions were observed up to D14, we observed significant changes in the size and shape of the nuclear inclusions over time (Figure 1C). At D3, the majority of the nuclear inclusions were detected as small (< 1 μm) nuclear puncta (94%), and only a few appeared as large (~ 3-4 μm) inclusions (Figure 1D). The ratio of small and large nuclear inclusions shifted slightly over time from 50:50 at D7 to 43:57 at D14 (Figure 1D).

We next characterized the ultrastructural properties of the nuclear Httex1 72Q inclusions by CLEM. At D7, these inclusions appeared as dense and roughly round aggregates without distinctive core and shell structural organization (Figures 2A and S2A). In these thin sections, the intranuclear Httex1 72Q inclusions appeared darker than the surrounding nucleoplasm and structurally different from the nucleolus (Figure 2A and controls Figure S2C-D). The high density of these aggregates made it challenging to determine if they were made of filamentous structures.

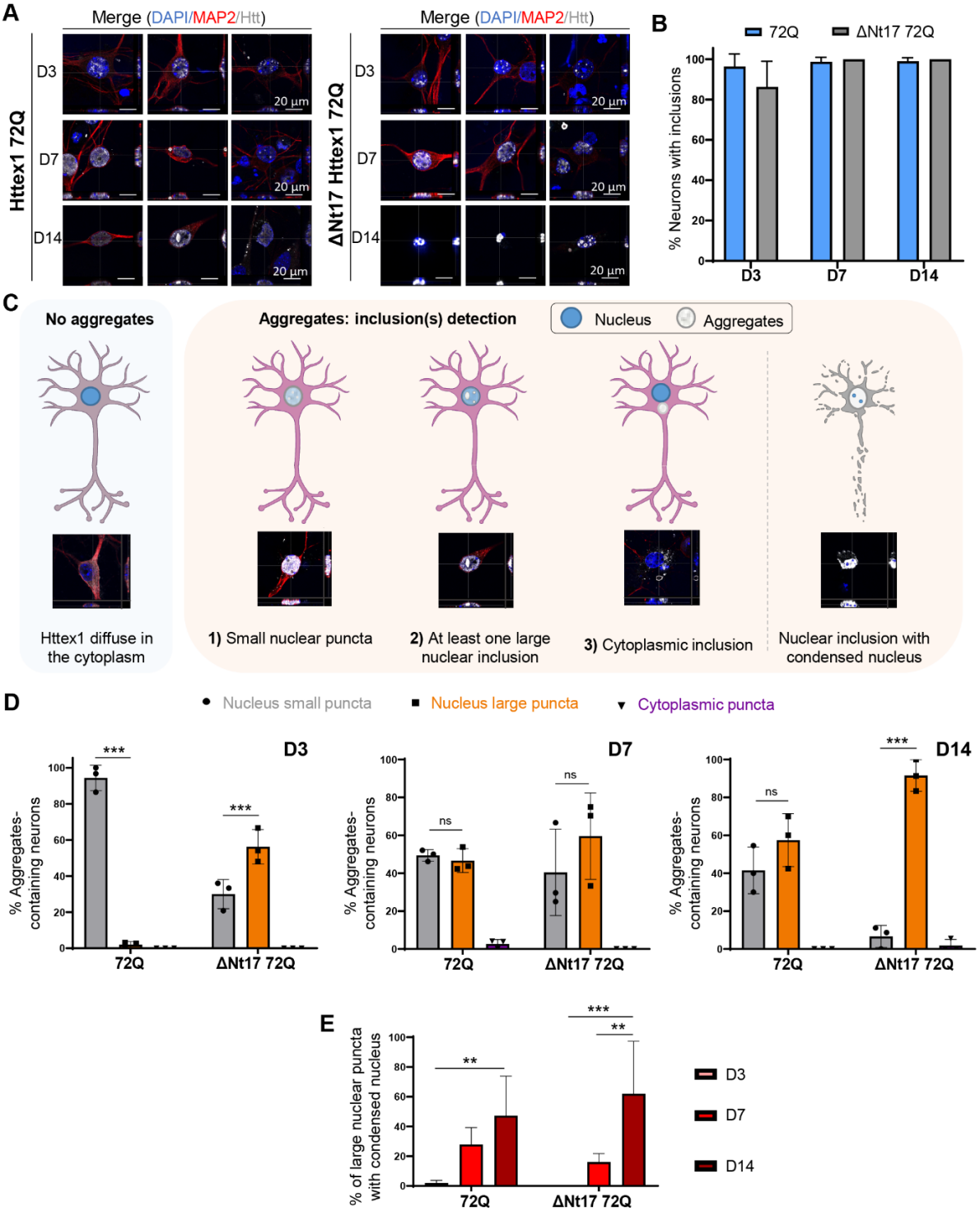

Figure 1. Confocal microscopy analysis and classification of the Httex1 inclusions formed in neurons revealed their morphological heterogeneity over time.

A. Httex1 expression was detected by ICC staining combined with confocal imaging in primary cortical neurons, 3- (D3), 7- (D7) and 14- (D14) days after lentiviral transduction. Httex1 mutants were detected with the MAB5492 antibody. The nucleus was counterstained with DAPI (blue), and MAP2 was used to visualize the neurons (red). Scale bar = 20 µm. **B.** Image-based quantification of the number of neurons containing Httex1 inclusions over time. The

graphs represent the mean ± SD of 3 independent experiments. **C.** Primary neurons were classified via the detection of Httex1 as diffuse or by the morphology of the detected Httex1 aggregates: 1) Small nuclear puncta; 2) at least one large nuclear inclusion, and 3) cytoplasmic inclusion. In addition, a subclass was created for neurons containing a large nuclear inclusion associated with nuclear condensation. **D.** Image-based quantification and classification of the different morphologies of Httex1 inclusions based on the panel C. Statistical analysis: ANOVA followed by a Tukey honest significant difference [HSD] post hoc test was performed, *P < 0.05, **P < 0.005, ***P < 0.001. **E.** Image-based quantification of neurons containing a large nuclear inclusion with a nuclear condensation. Statistical analysis: Two-way ANOVA followed by a HSD post hoc test was performed, *P < 0.05, **P < 0.005, ***P < 0.001.

However, using electron tomography (ET), we were able to visualize and confirm the presence of filamentous structures inside these nuclear inclusions (Figure 2B and movie 3). The segmented filaments did not appear to be closely stacked in parallel but rather organized as a network of tortuous filaments. Neither EM nor ET imaging revealed the presence of membranous-, organelle- or vesicle-like structures inside or at the periphery of these inclusions. Although removal of the Nt17 domain (Figure 2C) did not alter the ultrastructural properties or composition of the inclusions, it accelerated the formation of large aggregates significantly. As early as D3, ~60% of the neurons overexpressing ΔNt17 Httex1 72Q already contained large nuclear inclusions, compared to only ~6% for Httex1 72Q (Figure 1D). At D14, almost all the aggregates formed in the ΔNt17 Httex1 72Q overexpressing neurons converted into the large nuclear inclusions (~90%) (Figure 1D), compared to 57% for Httex1 72Q.

Finally, among the small aggregates dispersed throughout the nucleus, a few were observed near the nuclear membrane, which often appeared damaged and ruptured (Figures S2A). Our data are in line with previous EM studies from human HD patients[432] and HD mice models[102,512] showing nuclear ultrastructural changes, including altered nuclear membrane shape, nuclear invagination and increased nuclear pore density in neurons bearing Httex1 inclusions. Consistent with these observations, the nuclei containing Httex1 72Q inclusions showed enhanced nuclear condensation over time (Figure 1E), indicating increased neuronal toxicity, consistent with previous reports in HD patients[513] and HD mice model[512].

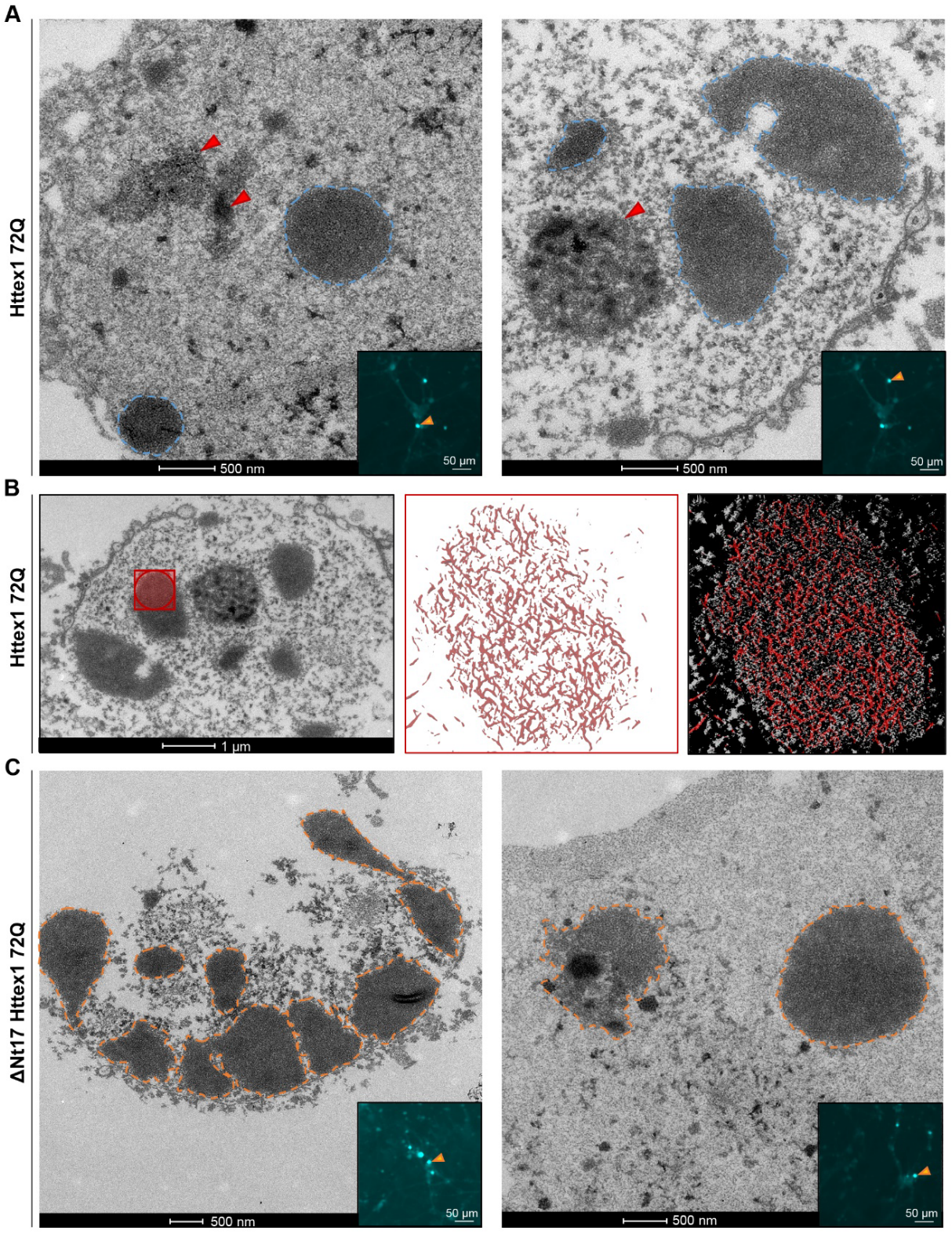

Figure 2. Ultrastructural analysis of the nuclear Httex1 72Q inclusions formed in primary cortical neurons shows granular and filamentous structures by CLEM and Tomography.

A. Representative electron micrographs of Httex1 72Q inclusions formed 7 days after lentiviral transduction in mouse cortical primary neurons. Blue dashed lines represent the inclusions, and the red arrowheads the nucleolus. Scale bar = 500 nm for the EM images and 50 µm for

the fluorescent image (inset). **B.** Electron micrograph and corresponding tomogram (selected area in red) of a neuronal Httex1 72Q inclusion. Segmentation of the tomogram reveals the presence of a multitude of filaments. **C.** Representative electron micrographs of ΔNt17 Httex1 72Q inclusions formed seven days after lentiviral transduction in mouse cortical primary neurons. Orange dashed lines represent the inclusions, and the red arrowheads the nucleolus. Scale bar = 500 nm for the EM images and 50 µm for the fluorescent image (inset).

Interestingly, despite the presence of the large inclusions as early as D3 in the neurons overexpressing ΔNt17 Httex1 72Q, we did not observe an earlier onset of cell death or a higher level of toxicity over time in these neurons compared to those overexpressing Httex1 72Q (Figure 1E). This suggests a lack of correlation between cell death level and the size of the inclusions, with the large inclusions being less toxic. These results demonstrate the formation of condensed mutant Httex1 fibrillar aggregates within intranuclear inclusions in neurons and suggest that the process of their formation and maturation is directly linked to neuronal dysfunctions and cell death.

2.2 The use of Httex1-GFP in primary neurons leads to a differential structural organization and toxic properties of Httex1 inclusions

We also assessed how the presence of the GFP tag might influence the kinetics of aggregation, the morphology, subcellular localization and toxicity of the nuclear inclusions in primary cortical neurons (Figures 3 and S3). First, we observed that the presence of the GFP tag slows down the aggregation rate of Httex1 72Q: in contrast to the tag-free Httex1 72Q, the aggregation was significantly delayed, as evidenced by the absence of nuclear or cytoplasmic aggregates or inclusions at D3 (Figure 3A-B). However, at D7, almost all the Httex1 72Q-GFP proteins appeared in the form of small nuclear puncta (~35%) or large nuclear inclusions (~60%) (Figure 3C). The proportion of small puncta *vs.* large inclusions did not change over time, up to D14 (Figure 3C). Interestingly, the subcellular localization, the morphology and size distribution of the inclusions observed by confocal imaging were not impacted by the presence of the GFP tag.

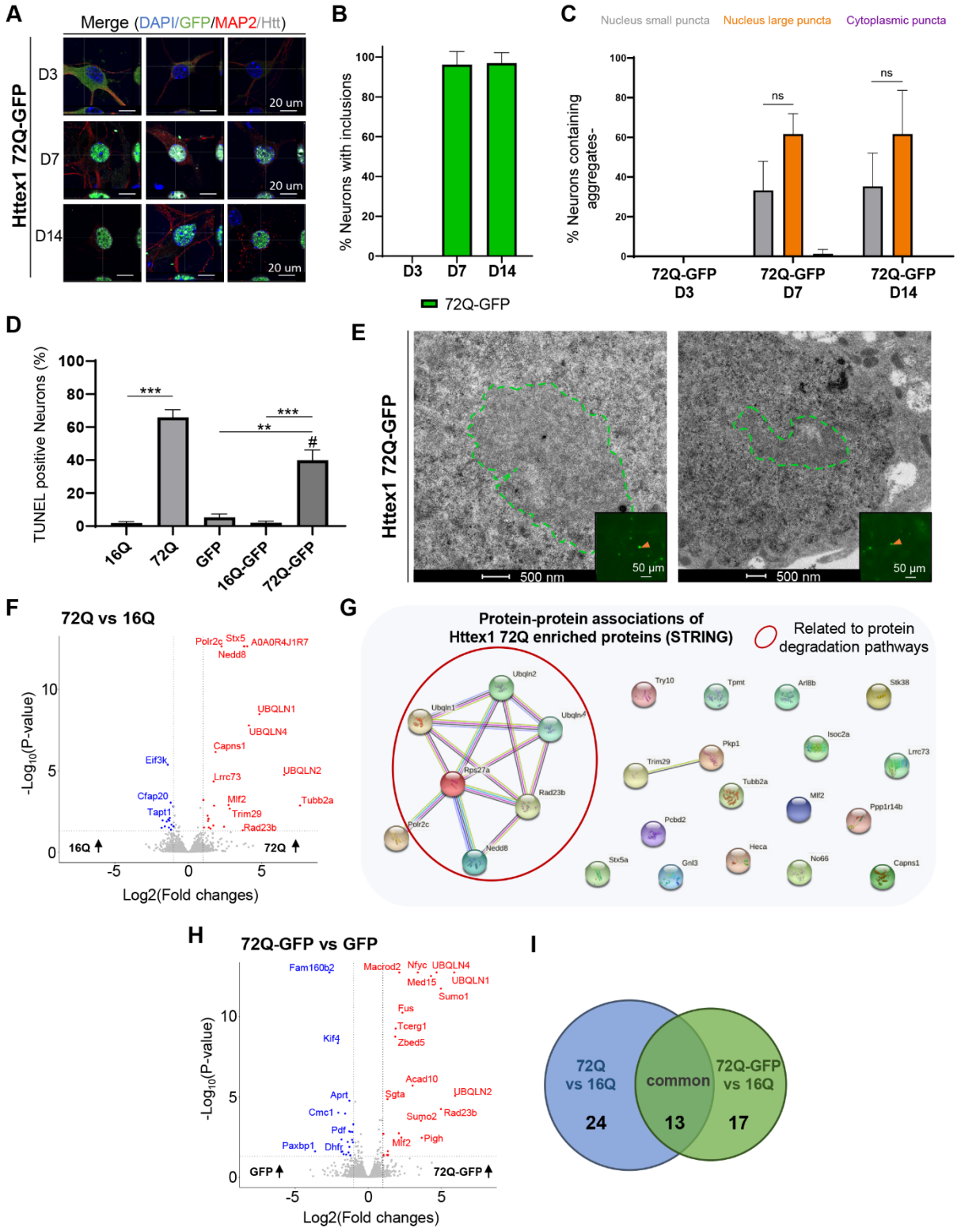

Figure 3. The presence of the GFP tag alters the kinetic, ultrastructural properties, protein content and toxicity of Httex1 72Q inclusions in primary neurons.

A. Httex1 72Q-GFP expression was detected by ICC staining combined with confocal imaging in primary cortical neurons, 3- (D3), 7- (D7) and 14- (D14) days after lentiviral transduction. Httex1 was directly visualized with GFP (green) as diffuse, small puncta or large inclusions.

The nucleus was counterstained with DAPI (blue), and MAP2 was used to detect the neurons (red). Scale bar = 20 µm. **B.** Image-based quantification of the number of transduced neurons bearing Httex1 72Q-GFP inclusions over time. The graphs represent the mean ± SD of 3 independent experiments. ANOVA followed by a Tukey honest significant difference [HSD] post hoc test was performed. *P < 0.05, **P < 0.005, ***P < 0.001. **C.** The image-based pipeline Figure 5C was used to classify the morphology (small nuclear puncta *vs.* large nuclear inclusion), and subcellular localization (cytosol *vs.* nucleus) of the inclusions formed upon overexpression of Httex1 72Q-GFP in neurons overtime **D.** TUNEL (Terminal dUTP Nick End-Labeling) assay showed an increased level of DNA fragmentation ($TUNEL^+$) in the neuronal population (positive for the neuronal marker NeuN+) in conditions of overexpression of Httex1 72Q and Httex1 72Q-GFP but not Httex1 16Q, Httex1 16Q-GFP or GFP alone. The graphs represent the mean ± SD of 3 independent experiments. ANOVA followed by a Tukey honest significant difference [HSD] post hoc test was performed. *P < 0.05, **P < 0.005, ***P < 0.001. #P < 0.05 comparison between 72Q and 72Q-GFP. **E.** Representative electron micrographs of Httex1 72Q-GFP inclusions formed after 7 days post lentiviral transduction in mouse cortical primary neurons. Green dashed lines represent the inclusions. Scale bars = 500 nm for the EM images and scale bars = 50 µm for the fluorescent image (inset). **F.** Urea soluble proteins from primary neurons expressing Httex1 72Q or Httex1 16Q of 3 independent experiments were extracted 7 days after lentiviral transduction and analyzed using LC-MS/MS. Identified proteins were plotted using a volcano plot comparing Httex1 72Q vs. Httex1 16Q. Black dotted lines represent the false discovery rate (FDR) <0.05, and an absolute log2 fold change threshold of 1 which were used for assigning significance for the subsequent analysis. 23 proteins upregulated are in red, and the14 downregulated are in blue. The non-significant proteins are in grey. **G.** Visualization of the upregulated Httex1 72Q proteins compared to Httex1 16Q and protein-protein associations using the online platform STRING underscores an association between proteins related to protein degradation pathways (red circle). **H.** Urea soluble proteins from primary neurons expressing Httex1 72Q-GFP or GFP of 3 independent experiments were extracted 7 days after lentiviral transduction and analyzed using LC-MS/MS. Identified proteins were plotted using a volcano plot comparing Httex1 72Q-GFP *vs*. GFP. Black dotted lines represent the false discovery rate (FDR) <0.05 and an absolute log2 fold change threshold of 1 which were used for assigning significance for the subsequent analysis. Upregulated proteins for Httex1 72Q-GFP are represented in red, downregulated in blue and non-significant proteins in grey. **I.** Venn diagram comparison of proteins enriched in Httex1 72Q *vs.* Httex1 16Q (blue) to Httex1 72Q-GFP *vs.* Httex1 16Q (green). 24 proteins were unique to Httex1 72Q *vs.* Httex1 16Q (44.4%), 17 unique to Httex1 72Q-GFP *vs.* Httex1 16Q (31.5%) and 13 (24.1%) common to both co-aggregated proteins.

However, the Httex1 72Q-GFP aggregates exhibited a significantly reduced toxicity compared to tag-free Httex1 72Q in neurons (Figure S3D). Even at D14, chromatin condensation did not exceed 10% in these neurons (Figure S3D), whereas ~50% of the neurons overexpressing the tag-free Httex1 72Q construct were already dead (Figure 1E). In addition, the TUNEL cell death assay revealed a dramatic increase (~60%) in DNA fragmentation in the cortical neurons

bearing the intranuclear Httex1 72Q inclusions compared to only 40% in neurons expressing Httex1 72Q-GFP (Figure 3D).

Next, we investigated how the presence of the GFP tag might impact the ultrastructural properties of these neuronal inclusions (Figures 3E and S4). The nuclear inclusions formed in the presence of the GFP tag exhibited a round shape but displayed a less dark staining density compared to the inclusions formed by the untagged Httex1 72Q protein (Figure 2A). Due to their lower density, the presence of filamentous structures organized as an entangled arrangement throughout the GFP tagged inclusion could be detected. Finally, these inclusions were localized throughout the nucleus but always distant from the nuclear membrane (Figure S4).

Altogether, our results demonstrate that the addition of the GFP significantly slows the initiation of mutant Httex1 fibrillization and inclusion formation in the nucleus but accelerates the maturation of the aggregates once formed, resulting in predominantly large inclusions with reduced toxicity in neurons. The lack of physical interaction between the Httex1 72Q-GFP inclusions and the nuclear envelope and/or the absence of small puncta aggregates in neurons expressing Httex1-72Q-GFP could explain their reduced toxicity (Figures 3D-E).

2.3 The Httex1 72Q and Httex1 72Q-GFP nuclear and cytoplasmic inclusions exhibit distinct proteome composition

To gain further insight into the biochemical composition of the Htt nuclear inclusions, the molecular interactions and mechanisms driving their formation and maturation, we next investigated the proteome content of nuclear inclusions formed in primary neurons (Figure S5). Proteomic analysis showed that 23 proteins were significantly enriched in the Httex1 72Q inclusions compared to Httex1 16Q (Figure 3F). These proteins were analyzed by protein-protein association using the online platform STRING (Figure 3G) and classified using GO term analysis by Cellular component, Molecular function and Biological process (Figure S6).

The proteins identified include the transcription factors PCBD2 and Mlf2, the RNA/DNA binding protein (GNL3), DNA-dependent RNA polymerase (Polr2c), histone lysine demethylase (No66), DNA genome nucleotide excision repair (Rad23B) and proteins linked to chromosome segregation (ARL8B and Tubb2a). In line with our results, ARL8B, Tubb2A, Polr2 sub-units, Mlf2, GNL3 and Rad23B proteins were also found enriched in the insoluble fractions of Q175 HD mice brains[514] and Tubb2a in R6/2 mice[486] nuclear inclusions. Interestingly, the gene expression level of these nuclear proteins was also significantly increased in HD post-mortem brain (PCBD2)[515] and symptomatic HD patients (Mlf2, GNL3, Polr2 and ARL8B)[516]. Altogether, this suggests that the loss of key nuclear proteins due to their sequestration by the pathological Htt inclusion is compensated in neurons by increasing gene expression levels. However, this seems insufficient to compensate for the loss of their biological functions, as reflected by the high level of nuclear alterations observed in our neuronal HD model, including chromatin condensation, nuclear fragmentation, and nuclear envelope integrity loss (Figure 2).

In addition to the nuclear proteins, STRING analysis (Figure 3G), together with GO term classification of cellular components (Figure S6A), the molecular functions (Figure S6B), and the biological process annotations (Figure S6C) revealed the enrichment of a cluster of proteins [Ubiquilin (ubqln) 1, 2 and 4; Rps27a, Rad23B and Nedd8, red circle, Figure 3G] related to the protein degradation machinery, including the UPS, autophagy and ERAD pathways. In line with our findings, all these proteins were also found enriched in the insoluble fractions of the Q175 HD mice brains, while the Ubiquilin family members (Ubqln 1, 2 or 4)[517–519] were also shown to be sequestered in R6/2 mice nuclear inclusions[486] and in the Httex1 nuclear inclusions formed in the PC12 neuronal rat precursor[520]. Interestingly, ubiquilin proteins have been previously shown to translocate from the cytoplasm to the nucleus or have an upregulated expression level in the nucleoplasm concomitantly with the early stage of the formation of the neurofibrillary tangles in AD post-mortem brain tissues[521]. Furthermore, Nedd8, originally shown to colocalize with ubiquitin and the proteasome components in the cytoplasmic inclusions[522,523] found in several neurodegenerative disorders, has recently been

shown to promote nuclear protein aggregation as a defense mechanism against proteotoxicity[524]. Moreover, our analysis revealed 5 proteins known as Htt interactors (based on the HDinHD database) among the proteins significantly different between Httex1 72Q compared to Httex1 16Q in primary neurons (Table S1).

Finally, we also assessed how the presence of the GFP tag might influence the protein content of the neuronal intranuclear inclusions (Figure 3H). Similar to the Httex1 72Q aggregates, ~45% of the proteins enriched in the insoluble fraction of the Httex1 72Q-GFP aggregates were related to nuclear biological processes and functions, including transcription factors (Mlf2[520], nfyc-1, TCERG1, Med15), DNA-chromatin binding proteins (ZBED5, N6AMT1 and Actl6b), DNA genome nucleotide excision repair protein (Rad23B), the DNA/RNA-binding protein FUS. In addition, Httex1 72Q-GFP aggregates were also enriched in proteins from the promyelocytic leukemia nuclear bodies (Sumo 1 and 2) known as nuclear membraneless compartments involved in genome maintenance such as DNA repair, DNA damage response, telomere homeostasis, and which is also associated with apoptosis signaling pathways (Figure S7). Furthermore, proteins from the ubiquitin-proteasome system (Bag5, Fus, Rad23b, Sgta, Sumo1, Sumo2, Ubqln1, Ubqln2, Ubqln4), the ERAD (Sgta, Ubqln1, Ubqln2), autophagy (Ubqln1, Ubqln2, Ubqln4) and sumoylation (Sumo1, Sumo2) pathways were also highly enriched in the insoluble fraction of the Httex1 72Q-GFP aggregates (Figure S7A-B). Interestingly, the proteome of the Httex1 72Q-GFP aggregates formed in our HD neuronal model shared 40% of the proteins also found enriched in the insoluble fraction of Httex1 74Q-GFP nuclear inclusions formed in the PC12 neuronal rat precursor cell line[520]. This highlights a strong similarity between the pathways and proteins involved in the aggregation of Httex1 and inclusion formation in rodent neuronal cells.

We next compared the proteins identified between tag-free Httex1 72Q inclusions and Httex1 72Q-GFP (Figure 3I). 24 proteins were unique to Httex1 72Q (44.4%), 17 unique to Httex1 72Q-GFP (31.5%) and only 13 (24.1%) common to both type of inclusions. Most of the unique

proteins found in the tag-free or GFP-tagged Httex1 72Q inclusions were related to nuclear functions, the ubiquitin-proteasome system, ERAD and autophagy pathways. Moreover, among the 13 common proteins, most were linked to the protein degradation machinery (i.e., ubiquilins 1, 2 and 4, and the Rad23b and Nedd8 proteins).

Although the tag-free Httex1 72Q and Httex1 72Q-GFP inclusions share several proteins related to the degradation machinery, more than 75% of the co-aggregating proteins are different, which could explain the drastic differences in neuronal toxicity associated with each type of these inclusions.

2.4 Use of longer Htt fragments in neurons

Based on our recent work indicating the importance of sequences outside of Httex1 in the aggregation properties of Htt^{175}, we also investigated the aggregation properties of longer N-terminal Htt fragments in primary neurons. Similar to our confocal-based quantification of Httex1 aggregation (Figure 1), we characterized the expression of Htt171 and Htt586 in primary neurons (Figure 4). To address this, we used lentiviruses to assess the expression of Htt171 and Htt586 with either 18Q or 82Q in cortical mouse primary neurons and could observe inclusion formation only for Htt171 82Q over time (Figure 4). Moreover, Htt171 82Q formed nuclear puncta only at D7 and D14 (Figure 4A, bottom left panel). Image-based quantification demonstrated that even if no inclusions were detected at D3, unlike Httex1 72Q (Figure 1), the majority of aggregate-containing neurons were detected as large puncta for Htt171 82Q already at D7 (Figure 4B). Large puncta were also significantly dominant at D14 for Htt171 82Q compared to similar levels of small and large puncta observed for Httex1 72Q. Interestingly, large Htt171 82Q puncta are associated with a condensed nucleus only at D14 (Figure 4C), which could indicate delayed toxicity compared to Httex1 72Q, where nuclear condensation was already observed at D7 for more than 20% of neurons with large nuclear aggregates (Figure 1E).

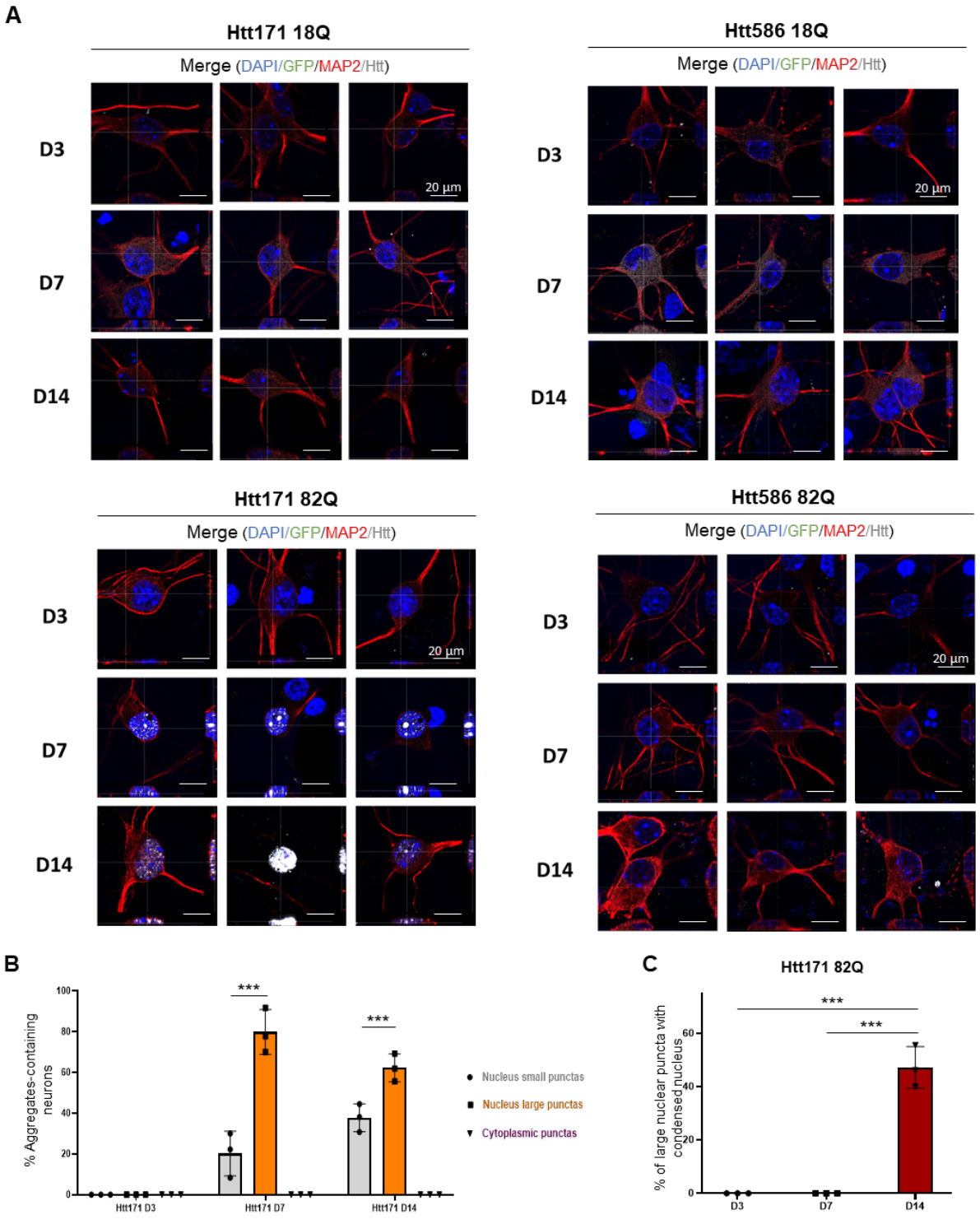

Figure 4. Confocal microscopy analysis of infected neurons shows a delayed aggregation for Htt171 82Q and no aggregates formed for Htt586 82Q.

A. Htt171 18Q & 82Q and Htt586 18Q & 82Q expression were detected by ICC staining combined with confocal imaging in primary cortical neurons after 3-, 7- and 14- days lentiviral transduction. Htt was detected with the MAB5492 antibody as diffuse, small puncta or

inclusions. Neurons were identified using MAP2 antibody (red) and the nucleus was counterstained with DAPI (blue). Scale bar = 20 µm. **B.** Image-based quantification and classification of the different morphologies of Httex1 inclusions based on Figure 1C. In each condition, approximately 150 neurons were quantified for each condition. The graphs represent the mean ± SD of 3 independent experiments. Statistical analysis: Two-way ANOVA, indicating an interaction between the type of puncta and time, and multiple comparison analysis by a Tukey honest significant difference [HSD] post hoc test was performed. Differences are represented between the conditions with an asterisk: *P < 0.05, **P < 0.005, ***P < 0.001. **C.** Image-based quantification of neurons containing a large nuclear inclusion with a nuclear condensation. The graphs represent the mean ± SD of 3 independent experiments. Statistical analysis: One-way ANOVA, multiple comparison analysis by a Tukey honest significant difference [HSD] post hoc test was performed. Differences are represented between the different timepoints with an asterisk: *P < 0.05, **P < 0.005, ***P < 0.001.

The expression of Htt586 18Q or 82Q did not result in any inclusions formation in neurons, as evident by the diffuse signal in the cytoplasm from D3 to D14 (Figure 4A, top and bottom right panels).

Overall, we demonstrated that no visible aggregates were formed up to14 days post-induction of expression in primary cortical neurons using the Htt586 fragment and that the pattern of inclusion formation in cells expressing Ht171 82Q is different from Httex1 72Q with a delayed apparition of Htt puncta. Such results suggest that more studies should be conducted in primary neurons using longer N-terminal fragments with sequences outside exon1, Htt in order to assess their role on Htt expression, proteolysis and aggregation.

3. Discussion

3.1 Neuronal intranuclear Httex1 inclusions appear as granulo-filamentous structures

Our results on neuronal intranuclear inclusions revealed that tag-free mutant Httex1 expression in primary neurons leads to the formation of granulo-filamentous nuclear inclusions, similar to previous ultrastructural studies performed in HD patients brains and *in vivo* models of HD, including R6/2 mice[102,133] and transgenic rat[525]. However, in most of these studies, the ultrastructural properties of the filaments were less evident compared to the well-resolved filamentous structure we and others[195] showed using electron tomography. For example, Tagawa and colleagues also observed nuclear inclusions of tag-free Httex1, but their data did not reveal the level of ultrastructural details and insights that our study provides[120].

Moreover, while a highly organized network of fibrils could be easily detected in both the cytoplasmic and nuclear inclusions in HEK cells (Chapter II), the filamentous structures inside the nuclear inclusions formed in neurons were only detectable by electron tomography. This highlights that the structural organization of the nuclear inclusions is cell-type dependent. They mostly appeared as a network of tortuous filaments as previously described for the neuronal intranuclear inclusions detected in R6/2 mice[102,133] and transgenic rat[525] with a membraneless and fine granular structure with the presence of filamentous structures. Similarly, patients with neuronal intranuclear inclusions were described as granulo-filamentous by Difiglia *et al.*[81] due to the immune detection of a mixture of granules and filaments. Interestingly, previous EM analyses of the intranuclear inclusions formed in the neurons of transgenic HD mice expressing Httex1 (115 to 156 polyQ tract) revealed similar structures to the ones depicted in (Chapter II, Figure 5) with rare detection of filamentous structures inside the inclusions but were unable to unravel any additional structural details[102]. In addition, Tagawa and colleagues[120] could detect amorphous deposits in the cytoplasm and nucleus of primary neurons based on EM, but without great structural details of the inclusions to detect granular or filamentous elements.

The overexpression of Httex1 72Q was highly toxic in neurons in contrast to HEK cells indicating cell-type dependent toxic properties that might arise from the different subcellular repartition of the inclusions but also the robustness of the cells. Moreover, this differential toxicity underscores distinct Htt mechanisms of aggregation or interaction with cellular proteins or differences in the resilience of the different cells based, for example, on distinct oxidative stress tolerance and immune functions/inflammation.

In addition, the removal of the Nt17 domain did not reduce the level of aggregation in neurons (Figure 1B) in contrast to what we previously observed in HEK cells[292] and a previous study by Shen *et al.*[149]. The level of neurons overexpressing Httex1 could explain this difference. In our study, aggregates were detected in ~90-100 % of the transduced neurons (Figure 1B). However, we observed major differences in the repartition of the small puncta *vs.* the large nuclear inclusions, with the latest being predominantly detected in ΔNt17 Httex1 compared to Httex1 72Q over time (Figure 1D). We speculate that such differences can come from the absence of the Nt17 domain, which prevents targeting Httex1 for protein degradation, in particular via phosphorylation[141,154,160]. Large inclusions could also be favored by the intermolecular capacity of ΔNt17 to form more lateral association[292]. We also demonstrated that the Nt17 domain was not altering the final structure of large Httex1 inclusions, similar to cytoplasmic and nuclear inclusions in HEK cells.

3.2 The protein degradation machinery fails to clear neuronal intranuclear Httex1 inclusions

Interestingly, our quantitative neuronal proteomic analysis demonstrated similar pathways enrichment related to degradation machineries (UPS, autophagy and ERAD) inside the neuronal inclusions and those formed in HEK cells. Few proteins were similar (RAD23B, UBQLN4, RPS27A, MLF2, UBQLN2) in Httex1 72Q aggregate fraction from HEK cells and neurons but still indicating a conserved mechanism for protein degradation of aggregated

Httex1 independent of the cell type. It is interesting that despite the difference of ultrastructure and subcellular repartition of the majority of the inclusions, Httex1 72Q expression indicates a failure of the protein degradation machinery to clear inclusions. The sequestration of UPS components such as ubiquilins and Rad23B is in line with previous cellular studies[283,457,459,463,474] and patient-based analysis[460]. ER defects and ERAD-related protein enrichment were also observed in HEK cells and previous studies[274,332,440–443]. Saturation of the UPS and ERAD pathways to clear misfolded Httex1 aggregates is known to occur in HD and to be associated with autophagy activation as an attempt to clear Htt inclusions[160,456,463,465,474,487,526]. In parallel, a great proportion of proteins enriched in neuronal intranuclear inclusions were related to nuclear functions such as transcription factors, RNA/DNA and chromatin binding proteins previously reported in HD mice models and HD *post-mortem* brains[486,514–520]. Our proteomic analysis demonstrates that the sequestration of key nuclear proteins inside the neuronal intranuclear Htt inclusions is associated with nuclear morphological changes, chromatin condensation and DNA fragmentation, supporting the hypothesis that the nucleus might be the primary site of cellular dysfunctions in neurons.

Our proteomic analysis also revealed the enrichment of several biological processes and signaling pathways related to RNA binding proteins, transcription factors, RNA splicing, mRNA processing, and stability, as well as chromatin and nucleotide-binding proteins (Figure 3C). Dysregulation of transcriptional gene pathways has been reported in several animal and cell HD models[527–529] as well as in HD post-mortem tissues and HD peripheral blood cells[530–532]. Our findings support the hypothesis that sequestration of the key regulators of transcription inside the Htt inclusions could be one of the causative mechanisms of transcription dysregulation in HD.

3.3 GFP strongly influences the biochemical and structural properties of neuronal intranuclear Httex1 inclusions

First, our imaging results revealed that the use of Httex1 72Q-GFP in neurons changed the proportion of small and large nuclear aggregates compared to tag-free Httex1 72Q, with a delay of inclusion formation. Moreover, neuronal Httex1 72Q-GFP nuclear inclusions were not as large and dense as tag-free Httex1 72Q inclusions allowing the better detection of fibrillar structures by CLEM. Httex1 72Q-GFP nuclear inclusions looked similar to pale nuclear inclusions observed in Httex1 51Q transgenic rat with filamentous structures detected by EM[533]. The different structural organization and impact on the nuclear membrane might explain the reduced toxicity compared to tag-free Httex1 72Q inclusions. Similar to our results, intraneuronal nuclear Httex1 97Q-GFP inclusion from Bäuerlein and colleagues in primary neurons did not display vesicles or endomembranes and contained many visible fibrillar structures using Cryo-ET[195].

To date, no study has compared the protein content of Htt inclusions formed in the presence or absence of a fluorescent solubilizing tag. To address this gap, we have compared the proteome of Httex1 72Q inclusions in the presence or absence of the GFP tag. Our results show that although the top two biological processes enriched in the Httex1 inclusions were similar, namely, the protein quality control machinery (UPS system, autophagy pathway, and the chaperones network), and the transcriptional-related pathways, the degree of enrichment of proteins as well as the class of proteins enriched was different in both types of inclusions.

In the protein content of neuronal intranuclear inclusions, despite common protein degradation pathways, Httex1 72Q-GFP expression in neurons results in more than 75% differences among the co-aggregating proteins with tag-free Httex1 72Q. Our proteomic data suggest that the failure of the protein degradation machinery to clear off the tag-free Httex1 72Q inclusions, on the one hand, combined with the biological dysfunctions of key nuclear proteins, on the other hand, could explain the high toxic properties of the nuclear inclusions formed in primary neurons.

Finally, in primary neurons, the use of Httex1 72Q-GFP changed dramatically the kinetics of inclusion formation and the proportion of small and large nuclear aggregates compared to tag-free Httex1 72Q. Moreover, neuronal Httex1 72Q-GFP nuclear inclusions were smaller and less dense compared to the tag-free Httex1 72Q inclusions, exhibited a distinct proteome composition and interacted less with the nuclear membrane. These differences could explain the reduced toxicity of Httex1 72Q-GFP inclusions compared to tag-free Httex1 72Q inclusions.

4. Conclusion

Overall, we revealed that mutant Httex1 expression in primary neurons evolves over time from small aggregates to large granulo-filamentous nuclear inclusions, with the sequestration of proteins from the cellular clearance mechanisms to induce toxicity and eventually neurodegeneration. Our work provides important and novel insights that not only advance our understanding of the mechanisms of Htt aggregation but also point to new directions for therapeutic interventions. We show that Htt aggregation and inclusion formation in the cytosol and nucleus occur via different mechanisms and lead to the formation of inclusions with distinct biochemical and ultrastructural properties. These observations suggest that the two types of inclusions may exert their toxicity via different mechanisms and may require different strategies to interfere with their formation, maturation and toxicity. We also showed the importance of assessing the protein sequence determinants and modulators of Htt aggregation using N-terminal Htt fragments longer than exon1.

Furthermore, our work suggests that identifying modifiers of Htt inclusion growth and aberrant secondary interactions with other proteins and organelles represent an alternative and strategy for interfering with Htt-induced toxicity and slowing disease progression, especially after disease onset. Therefore, we believe that targeting inclusion growth and maturation represents a viable therapeutic strategy.

5. Materials and Methods

DNA constructs and purification

SIN-PGK expression vector encoding for Httex1 16Q, Httex1 16Q-GFP, Httex1 72Q, and Httex1 72Q-GFP, ΔN17-Httex1 16Q, ΔN17-Httex1 16Q-GFP, ΔN17-Httex1 72Q, and ΔN17-Httex1 72Q-GFP were purchased from GeneArt (Germany). Plasmids were transformed into Chemo-competent E. coli stable 3 cells (Stbl3) from Life Technologies (Switzerland), and Maxiprep plasmid purification (Life Technologies, Switzerland) was performed following the manufacturer's instructions. Lentiviruses particles were produced according to Barde *et al*.[534]

Mouse primary cortical cell culture and lentiviral transduction

Primary cortical neurons were isolated from P0 pups of WT mice (C57BL/6JRccHsd, Harlan) as described previously[211,535]. Neurons were plated in 6-well plates for biochemical analysis at a density of 500 000 cells/ml, or in 24-well plates containing glass coverslips at a density of 125 000 cells/ml, all previously coated with poly-l-lysine 0.1% w/v in water (Sigma-Aldrich). Cortical primary neurons were transduced as previously described[536] with Httex1 lentiviruses particles at a multiplicity of infection (MOI) 2 after 5 or 7 days *in vitro* (DIV). All procedures were approved by the Swiss Federal Veterinary Office (authorization number VD 3392).

Immunocytochemistry (ICC)

At the indicated time-point, primary cortical neurons were washed twice with PBS pH 7.4 (1X) (Life Technologies, Switzerland) and fixed in 3.7% formaldehyde (Sigma-Aldrich, Switzerland) in PBS (PFA) for 15 min at room temperature (RT). After a blocking step with 3% BSA (Sigma-Aldrich, Switzerland) diluted in 0.1% Triton X-100 (Applichem, Germany) in PBS (PBST) for

30 min at RT, cells were incubated with the primary antibodies (Chapter II, Figure S1) anti-Htt raised against the Nt17 domain (2B7, CHDI [Cure Huntington's Disease Initiative]; Ab109115, Abcam) or the PolyQ (MW1, CHDI) or Proline-Rich Domain (PRD) (MAB5492, Millipore; 4C9, CHDI; N18, Santa-Cruz and EGT 414), or against Htt (S830) at a dilution of 1/500 in PBST for 2 h at RT. Cells were then rinsed five times in PBST and incubated for 1 h at RT with the secondary donkey anti-mouse Alexa647, donkey anti-rabbit Alexa647, or donkey anti-goat 568 antibodies (Life Technologies, Switzerland) used at a dilution of 1/800 in PBST and DAPI (Sigma-Aldrich, Switzerland) at 2µg/ml, all diluted in PBST. In addition, cortical neurons were detected with a MAP2 antibody.

Cells were then washed five times in PBST, and a last one in double-distilled H2O, before being mounted in polyvinyl alcohol (PVA) mounting medium with DABCO (Sigma-Aldrich, Switzerland). Cells were examined with a confocal laser-scanning microscope (Inverted Leica SP8, Germany) with a 63x/1.4 oil objective (HC PL APO) and analyzed using LASX Leica software.

Image-based quantification Httex1 expression in primary neurons

A minimum of five areas per condition was imaged for each independent experiment, as described above. Each experiment was performed three times. The cell counter feature was used in the LASX Leica software to quantify the morphological expression of Httex1 in neurons at the different time points. The classification was done according to Figure 1C with the detection of Httex1 classified as diffuse; small nuclear puncta; large nuclear inclusion, or cytoplasmic inclusion. In each condition, approximately 150 neurons were quantified for each condition, and a minimum of three independent experiments was performed.

Correlative light and electron microscopy (CLEM)

Primary cortical neurons grown on gridded glass dishes (MatTek Corporation, Ashland, MA, USA) or manually annotated 13mm plastic coverslips [Thermanox 174950] (Thermo Fisher Scientific, Waltham, USA) were washed 7 days post-transduction with either Empty vector (EV), Httex1 72Q, or Httex1 72Q-GFP. Then cells were fixed for 2 h with 1% glutaraldehyde (Electron Microscopy Sciences, USA) and 2.0% PFA in 0.1 M phosphate buffer (PB) at pH 7.4. After washing with PBS, ICC was performed as described above. Intra-cellular inclusions were stained with an Htt antibody (Millipore MAB5492, aa 1-82), and the cells of interest were imaged with a fluorescence confocal microscope (LSM700, Carl Zeiss Microscopy) with a 40x objective. The precise position of the selected cells was recorded using the alpha-numeric grid etched on the dish bottom. The cells were then fixed further with 2.5% glutaraldehyde and 2.0% PFA in 0.1 M PB at pH 7.4 for another 2 h. After five washes of 5 min with 0.1 M cacodylate buffer at pH 7.4, cells were post-fixed with 1% osmium tetroxide in the same buffer for 1 h and then washed with double-distilled water before being contrasted with 1% uranyl acetate water for 1 h. The cells were then dehydrated in increasing concentrations of alcohol (2 × 50%, 1 × 70%, 1 × 90%, 1 × 95%, and 2 × 100%) for 3 min each wash. Dehydrated cells were infiltrated with Durcupan resin (Electron Microscopy Sciences, Hatfield, PA, USA) diluted with absolute ethanol at 1: 2 for 30 min, at 1: 1 for 30 min, at 2: 1 for 30 min, and twice with pure Durcupan for 30 min each. After 2 h of incubation in fresh Durcupan resin, the dishes were transferred into a 65°C oven so that the resin could polymerize overnight. Once the resin had hardened, the glass CS on the bottom of the dish was removed by repeated immersion in hot water (60°C), followed by liquid nitrogen. The cell of interest was then located using the previously recorded alpha-numeric coordinates, and a razor blade was used to cut this region away from the rest of the resin. This piece was then glued to a resin block with acrylic glue and trimmed with a glass knife using an ultramicrotome (Leica Ultracut UCT, Leica Microsystems). Next, ultrathin sections (50–60 nm) were cut serially from the face with a diamond knife (Diatome, Biel, Switzerland) and collected on 2 mm single-slot copper grids coated with

formvar plastic support film. Sections were contrasted with uranyl acetate and lead citrate and imaged with a transmission electron microscope (Tecnai Spirit EM, FEI, The Netherlands) operating at 80 kV acceleration voltage and equipped with a digital camera (FEI Eagle, FEI).

Electron tomography (ET) on neuronal intranuclear inclusions

The previous EM grids generated with Httex1 transduced primary neurons were used to collect six tilt series with the Tomo 4.0 software (Thermo Fisher Scientific) on a Tecnai F20 TEM operated at 200 kV (Thermo Fisher Scientific), on a Falcon III DD camera (Thermo Fisher Scientific) in linear mode at 29'000× magnification. The tilt series were recorded from -58° to 58° using a continuous tilt scheme, with an increment of 2°. Tilt series alignments and tomogram reconstruction were performed with Inspect3D v4.1.2 (Thermo Fisher Scientific) using 22 iterations of SIRT.

The resulting tomogram was subjected for filling missing wedge with a new deep learning-based tool in EMAN2 build after 03/20/2020[537]. Missing wedge corrected tomograms were subjected for template-free, semi-automated convolutional neural network (CNN) based semi-automated tomogram annotation in EMAN2. Six tomograms were imported into EMAN2 project manager and shrunk by factor of two. The tomograms were then inspected slice by slice, and annotated by manual selection of a few 64x64 pixel tiles containing elongated features resembled fibrils, in order to train the CNN. In addition, quite a few regions in the tomogram which do not contain elongated features, were manually annotated as negative examples. Selected positive examples were manually segmented with pixel accuracy. Both positive and negative examples were provided for the training of the neural network. The trained CNN was then applied to the original tomogram for complete annotation. Images and movies were generated with 3dmod from IMOD package[538,539].

Preparation of samples for mass spectrometry

Samples were generated in triplicate for quantitative mass spectrometry analysis. At the indicated time-point, primary neurons were lysed in PBS supplemented by 0.5% NP40, 0.5% Triton x100, 1% protease cocktail inhibitor (Sigma PB340), and 1% Phenylmethanesulfonyl Fluoride (PMSF, Applichem). Cell lysates were incubated at 4°C for 20 min and then cleared by centrifugation at 4°C for 20 min at 20,000g. Supernatants were collected as non-ionic soluble protein fractions. Pellets were washed and resuspended in PBS supplemented by 2% N-Lauroylsarcosine sodium salt (Sarkosyl, Sigma) with protease inhibitors. The pellets were briefly sonicated with a fine probe [3 times, 3 sec at the amplitude of 60% (Sonic Vibra Cell, Blanc Labo, Switzerland)], incubated 5 min on ice, then centrifuged at 100,000g for 30 min at 4°C. Supernatants were collected as Sarkosyl soluble fractions. Pellets were washed with the previous buffer and resuspended in PBS supplemented by 2% Sarkosyl and 8M Urea and briefly sonicated as done previously. Laemmli buffer 4x was added to samples before being boiled at 95°C for five minutes. Samples were then separated on a 16% SDS-PAGE gel before being analyzed by Coomassie staining and WB.

For WB analyses, nitrocellulose membranes were blocked overnight with Odyssey blocking buffer (LiCor, Switzerland) and then incubated at RT for 2 h with Htt primary antibodies (MAB5492, Millipore, Switzerland) diluted in PBS (1/5000). Membranes were washed in PBS-Tween 1% and then incubated with fluorescently labeled secondary antibody diluted in PBS (1/5000) for 1 h at RT before a final wash in PBS-Tween 1%. The protein detection was performed by fluorescence using Odyssey CLx from LiCor. The signal intensity was quantified using Image Studio 3.1 from LiCor.

For proteomic identification, the samples separated by SDS-PAGE were then stained with Coomassie blue (25% Isopropanol [Fisher scientific, United-States], 10% acetic acid [Fisher scientific, United-States], and 0.05% Coomassie brilliant R250 [Applichem, Germany]. Each gel lane was entirely sliced and proteins were In-gel digested as previously described[495].

Peptides were desalted on stagetips[496] and dried under a vacuum concentrator. For LC-MS/MS analysis, resuspended peptides were separated by reversed-phase chromatography on a Dionex Ultimate 3000 RSLC nano UPLC system connected in-line with an Orbitrap Lumos (Thermo Fisher Scientific, Waltham, USA). Protein identification and quantification were performed with the search engine MaxQuant 1.6.2.10[497]. The mouse Uniprot database and Httex1 Sequence was used. Carbamidomethylation was set as a fixed modification, whereas oxidation (M), phosphorylation (S, T, Y), acetylation (Protein N-term), and glutamine to pyroglutamate were considered as variable modifications. A maximum of two missed cleavages was allowed. "Match between runs" was enabled. A minimum of 2 peptides was allowed for protein identification, and the false discovery rate (FDR) cut-off was set at 0.01 for both peptides and proteins. Label-free quantification and normalization were performed by Maxquant using the MaxLFQ algorithm, with the standard settings[498]. In Perseus[499], reverse proteins, contaminants, and proteins identified only by sites were filtered out. Data from the Urea fraction were analyzed separately following the same workflow. Biological replicates were grouped together, and protein groups containing a minimum of two LFQ values in at least one group were conserved. Missing values were imputed with random numbers using a gaussian distribution (width = 0.7, down-shift = 1.9 for Urea fraction). Differentially expressed proteins were highlighted by a two-sample t-test, followed by a permutation-based correction (False Discovery Rate). Significant hits were determined by a volcano plot-based strategy, combining t-test P-values with ratio information[500]. Significance curves in the volcano plot corresponded to a S0 value of 0.5 and a FDR cut-off of 0.05. Further graphical displays were generated using homemade programs written in R (version 3.6.1)[540]. A bioinformatics pipeline was implemented using the Differential Enrichment analysis of Proteomic data (DEP)[519]. DEP has been shown to have greater sensitivity for detecting true differences between conditions compared to pairwise between-condition t-tests, as the overall variability of all samples is used to inform the variance-stabilising normalization and differential statistical test approach. This pipeline was implemented in R (4.0.3 (2020-10-10)) and the code is available here:

https://github.com/jannahastings/httex-proteomics-202107. In the comparative analysis, known HTT interactor proteins were selected using the HDinHD dataset (https://www.hdinhd.org/) and restricted to the human and mouse datasets among cell- or animal-based studies exclusively.

Toxicity assays in primary neurons

The culture supernatant of primary cortical neurons was collected at the indicated time-point, and the level of lactic acid dehydrogenase (LDH) was measured using the CytoTox 96® Non-Radioactive Cytotoxicity Assay (Promega, Switzerland) as previously described[211]. The absorbance at 490 nm was measured using a Tecan infinite M200 Pro plate reader (Tecan, Maennedorf, Switzerland), which proportionally indicates the number of cells with a permeabilized membrane leading to LDH release in the culture media.

In addition, DNA fragmentation-associated cell death was measured by TUNEL assay as previously described[541]. In brief, cortical neurons were washed and fixed in 4% PFA for 15 min at RT at the indicated time-points. Neurons were permeabilized in 0.1% Triton X-100 in 0.1% citrate buffer, pH 6.0, before being incubated with the terminal deoxynucleotide transferase and TMR red dUTP (In Situ Cell Death Detection kit; Roche, Switzerland) for 1 h at 37 °C. ICC was next performed as described above. A minimum of one hundred neurons was counted for each condition and for each independent experiment, done in triplicate.

Statistical Analysis

All experiments were independently repeated at least 3 times. The statistical analyses were performed using Student's *t*-test, one-way ANOVA test followed by a Tukey-Kramer or HSD *post-hoc* tests, two-way ANOVA and repeated measures ANOVA using GraphPad Prism 9.1.1. The data were regarded as statistically significant at $p<0.05$.

6. Contributions

This chapter together with chapter II, as a hybrid version, was sent as a major revision to Nature Communications, and is now accepted with the title:

"Nuclear and cytoplasmic huntingtin inclusions exhibit distinct biochemical composition, interactome and ultrastructural properties"

Biorxiv version*: https://doi.org/10.1101/2020.07.29.226977*

Nature communication article (doi) : https://doi.org/10.1038/s41467-021-26684-z

Nathan Riguet[1], Anne-Laure Mahul-Mellier[1], Niran Maharjan[1], Johannes Burtscher[1], Marie Croisier[2], Graham Knott[2], Janna Hastings[1,3], Alice Patin[1], Veronika Reiterer[4], Hesso Farhan[4], Sergey Nasarov[1] and Hilal A. Lashuel[1]*

*Correspondence: hilal.lashuel@epfl.ch

Affiliations:

[1]Laboratory of Molecular and Chemical Biology of Neurodegeneration, Brain Mind Institute, Ecole Polytechnique Fédérale de Lausanne (EPFL), 1015 Lausanne, Switzerland.

[2]BIO EM facility (BIOEM), EPFL, 1015 Lausanne, Switzerland.

[3] Bioinformatics Competence Centre (BICC), EPFL, 1015 Lausanne, Switzerland.

[4]Institute of Pathophysiology, Medical University of Innsbruck, Innsbruck, Austria.

Author contributions

H.A.L conceived and supervised the study. H.A.L, N.R and A.L.M.M designed all the experiments and wrote the paper. N.R performed and analyzed the confocal imaging, the electron microscopy, quantitative proteomic experiments and the biochemistry experiments. A.L.M.M analyzed the proteomic data. M.C prepared the samples for CLEM and acquired the EM and ET images. G.K supervised the EM-related experiments and contributed to the interpretation of the data. S.N generated, annotated and analyzed the tomograms. J.H. analyzed the proteomic data. All authors reviewed and contributed to the writing.

7. Supplementary Figures

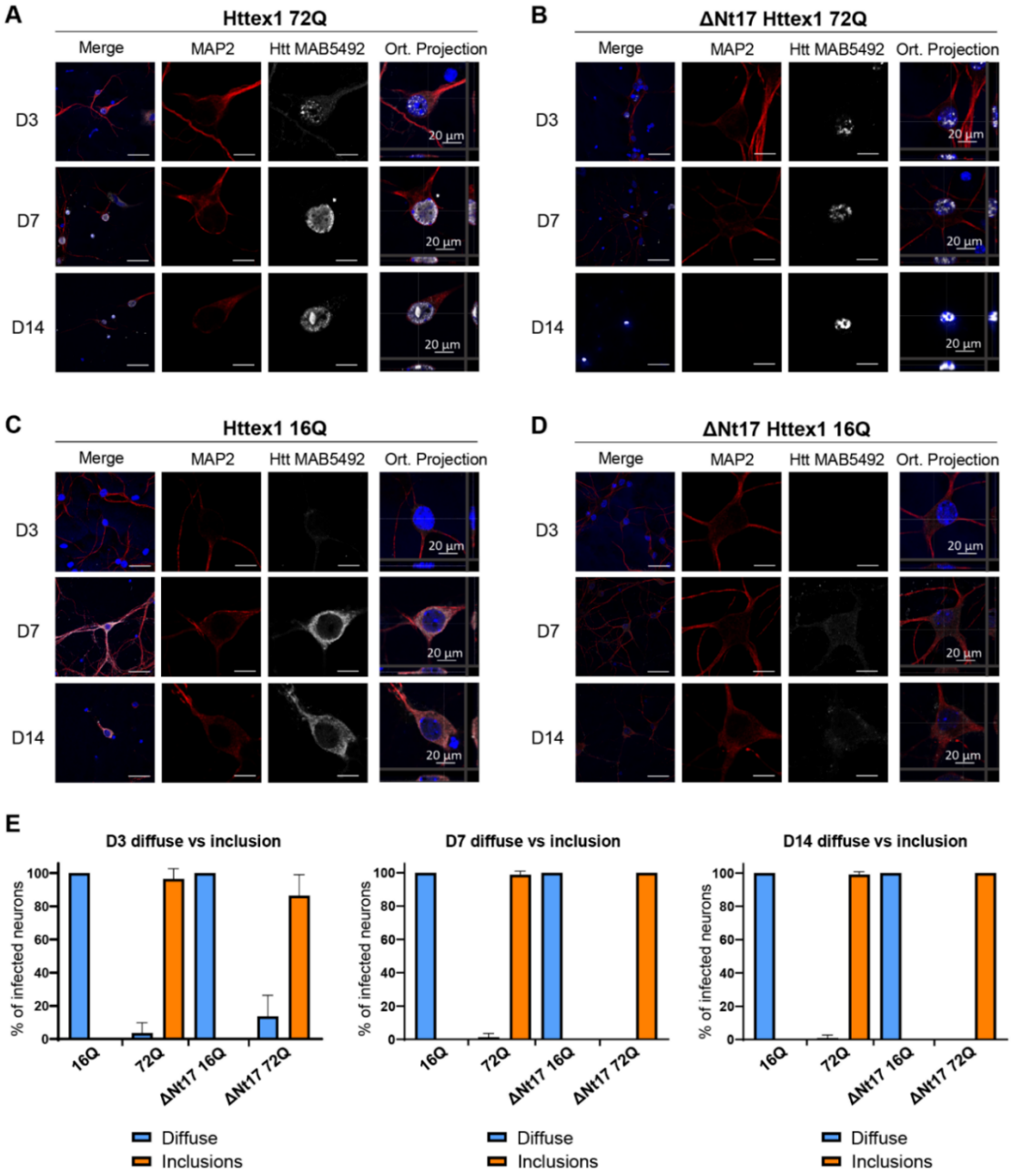

Figures S 1. Most of the neurons overexpressing Httex1 72Q show the presence of nuclear aggregates.

Representative images of Httex1 expression of **A.** Httex1 72Q; **B.** ΔNt17 Httex1 72Q; **C.** Httex1 72Q; **D.** ΔNt17 Httex1 72Q; detected by ICC staining combined with confocal imaging in primary cortical neurons at 3 (D3), 7 (D7) and 14 (D14) days after lentiviral transduction. Httex1 was detected with the MAB5492 antibody (grey) and the neurons with the MAP2 antibody (red). The nucleus was counterstained with DAPI (blue). Scale bar = 20 µm. **E.** Image-based quantification of neurons expressing Httex1 as diffuse protein or containing Httex1 inclusions at D3, D7 and D14. The graphs represent the mean ± SD of 3 independent experiments. ANOVA followed by a Tukey honest significant difference [HSD] post hoc test was performed. ***P < 0.001.

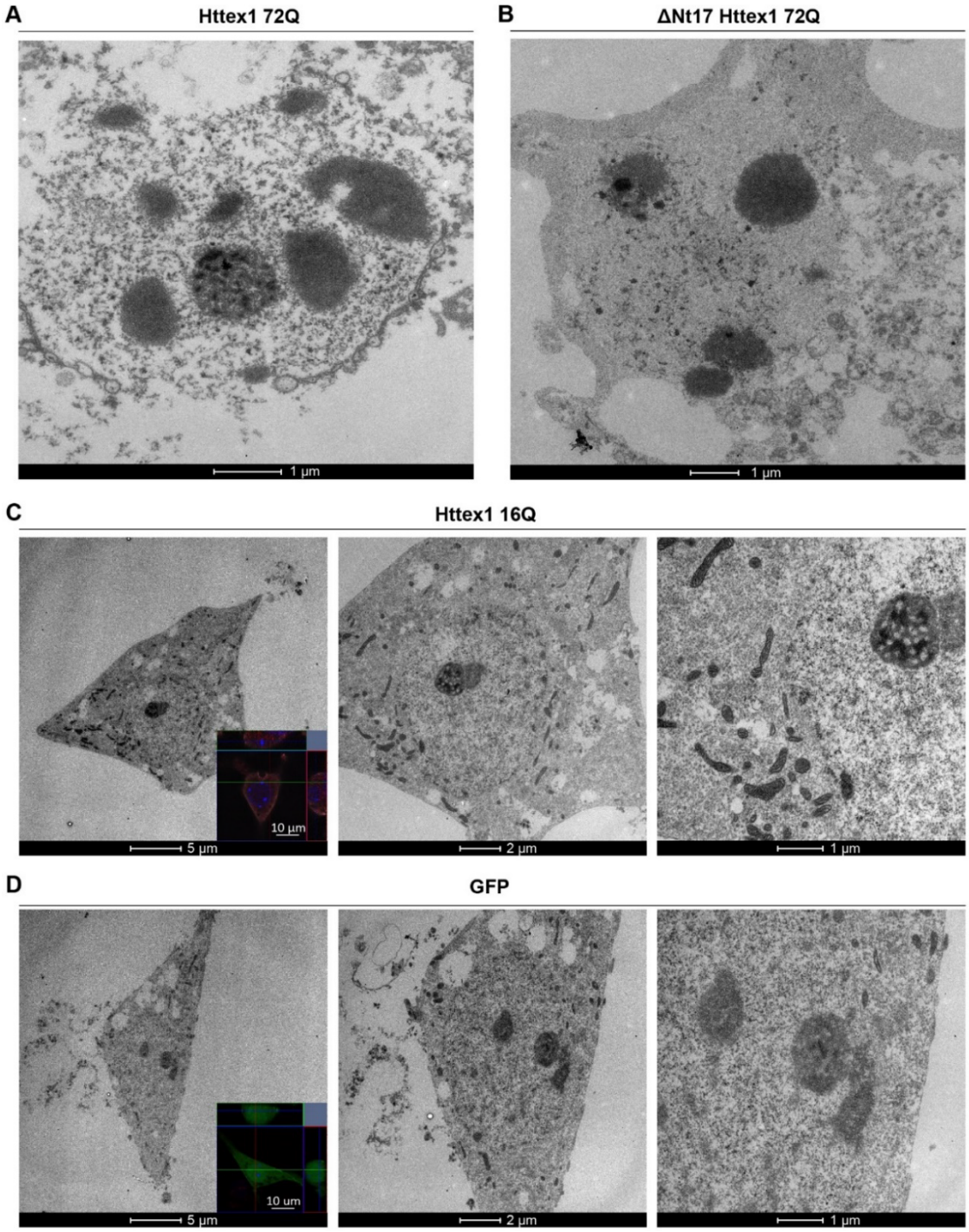

Figures S 2. **Representative electron micrographs of primary neurons expressing Httex1 showing inclusion formation by Httex1 72Q and ΔNt17 Httex1 72Q, but not 16Q, or GFP.**

Representative electron micrographs of **A.** Httex1 16Q and **B.** GFP, transduced neuron selected by fluorescence using CLEM. The fluorescence images (insets) were acquired by confocal imaging. Httex1 was detected with the MAB5492 antibody, the neurons with the MAP2 antibody (red) and the GFP in green. The nucleus was counterstained with DAPI (blue). **C.** Representative electron micrograph of Httex1 72Q transduced neurons at low magnification showing disruption of the nuclear envelop and cellular integrity from close up image Figure 2A (right panel). **D.** Representative electron micrograph of ΔNt17 Httex1 72Q transduced neurons. Scale bars = 500 nm for the EM images and 50 µm for the fluorescent images (insets).

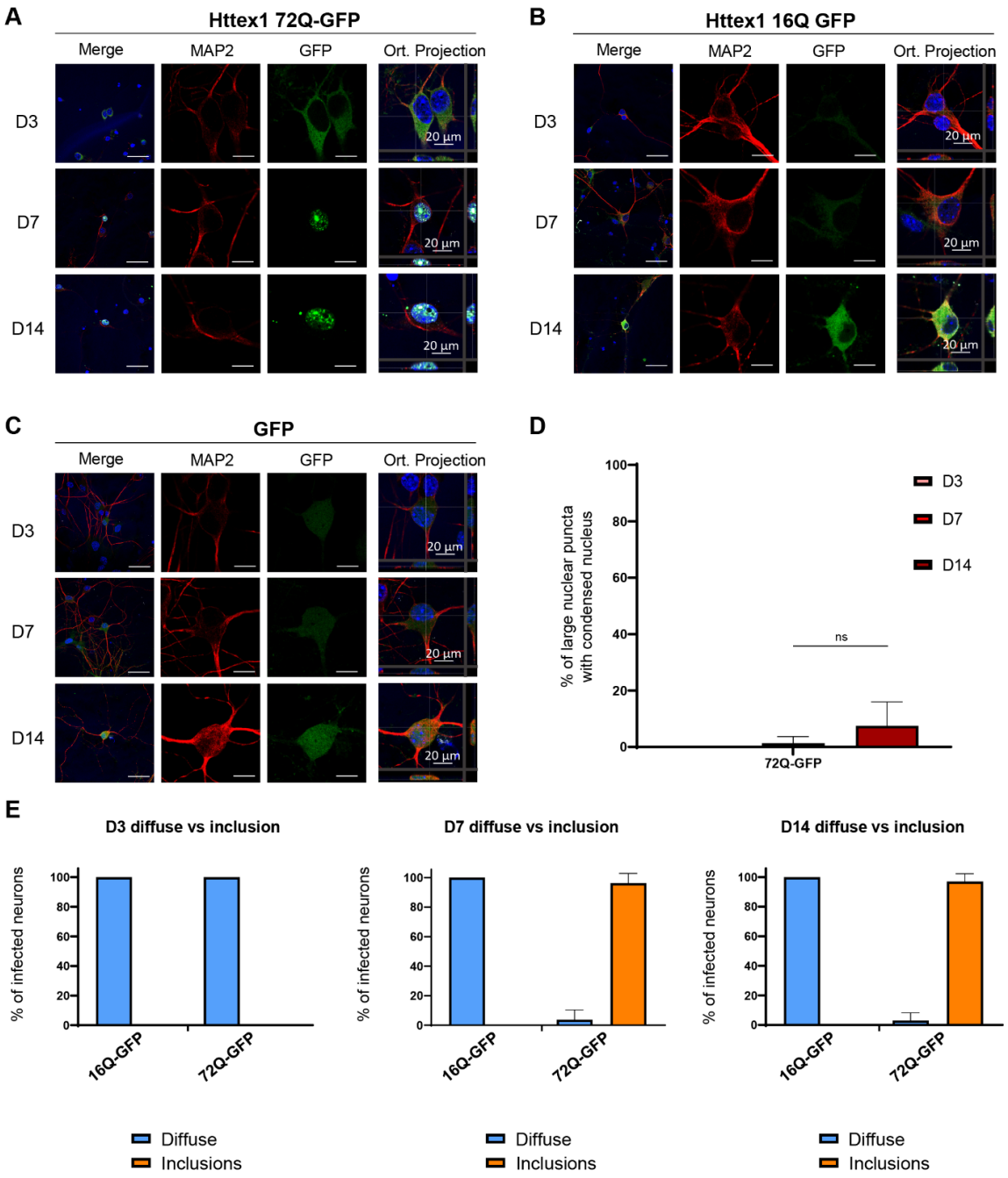

Figures S 3. Neurons overexpressing Httex1 72Q-GFP show the presence of nuclear aggregates only from D7.

Representative images of Httex1 expression of Httex1-GFP and GFP expression of **A.** Httex1 72Q-GFP; **B.** ΔNt17 Httex1 72Q-GFP; **C.** GFP; detected by ICC staining combined with confocal imaging in primary cortical neurons at 3 (D3), 7 (D7) and 14 (D14) days after lentiviral transduction. Httex1 was visualized with the GFP, and the neurons were detected with the MAP2 antibody (red). The nucleus was counterstained with DAPI (blue). Scale bar = 20 µm. **D.** Image-based quantification of neurons containing a large nuclear inclusion with a nuclear condensation. **E.** Image-based quantification of neurons expressing Httex1 as diffuse protein or containing Httex1 inclusions at D3, D7 and D14. **D-E.** The graphs represent the mean ± SD of 3 independent experiments. ANOVA followed by a Tukey honest significant difference [HSD] post hoc test was performed, *P < 0.05, **P < 0.005, ***P < 0.001.

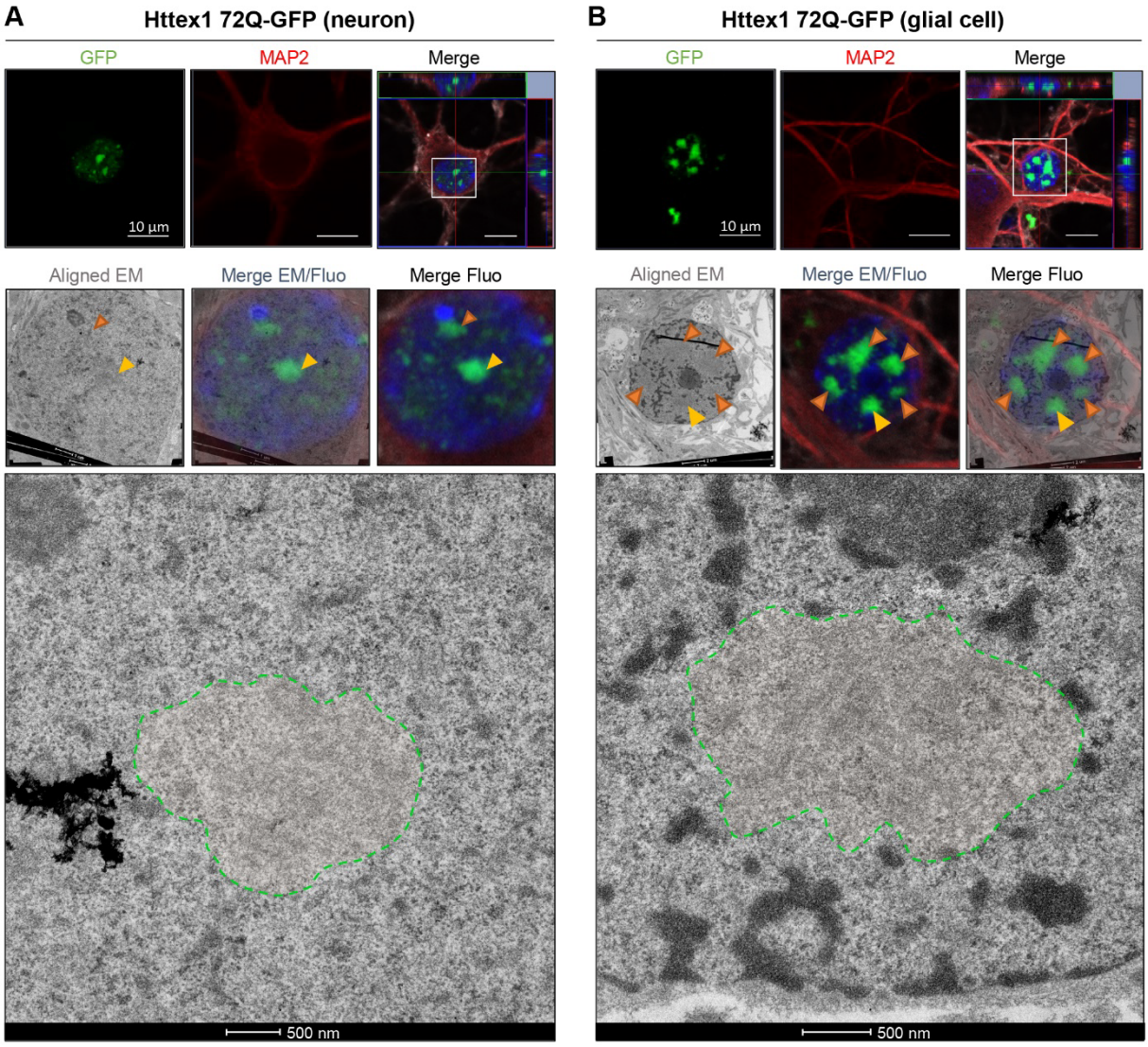

Figures S 4. CLEM analysis of the ultrastructure properties of Httex1 72Q-GFP formed in glial cells and neurons.

Seven days post-transduction, a selected neuron **(A)** and glial cell **(B)** were fixed and subjected to ICC staining in order to image and localize Httex1 72Q-GFP inclusions by confocal microscopy (upper panels). Httex1 was detected with GFP, the nucleus was counterstained with DAPI (blue), and the neurons were detected using MAP2 antibodies (red). Scale bars = 10 µm. Fluorescence images allowed the selection of the cell of interest and to correct the alignment of the inclusions with the electron micrographs (middle panels, orange arrowheads: Httex1 72Q-GFP nuclear inclusions; yellow arrowheads: selected inclusion). Selected inclusions could be successfully segmented (green-dotted lines, lower panels. Scale bars = 500 nm.

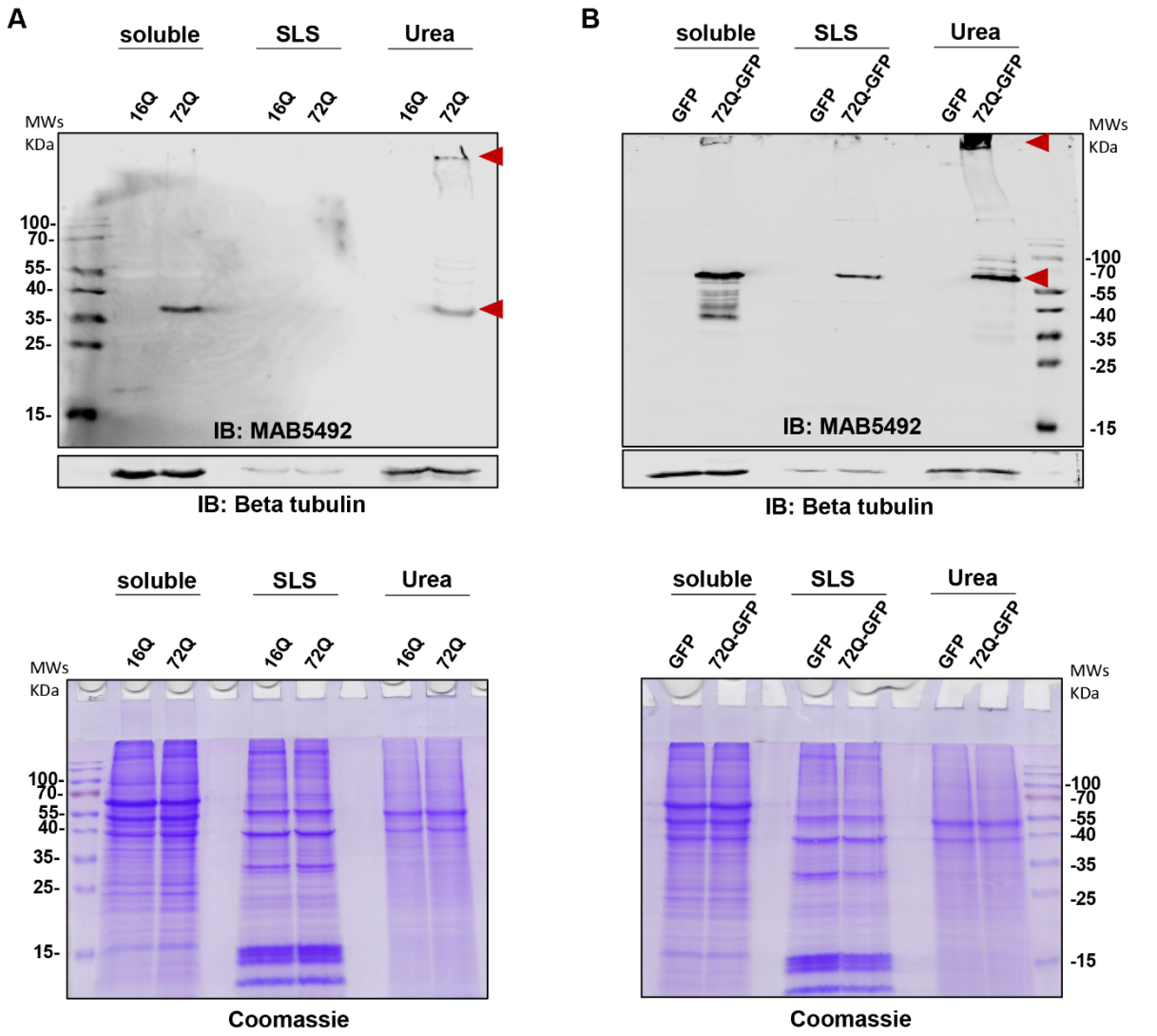

Figures S 5. **The enrichment of Httex1 aggregates in the soluble urea fraction of primary neurons was confirmed by Western Blot analysis.**

Cell fractionation from transduced primary neurons was performed as detailed in Figure S11A. **A-B.** Httex1 16Q and Httex1 72Q (**A**) or GFP and Httex1 72Q-GFP (**B**) protein expression levels (upper panel) in the different detergent fractions and total proteins (lower panel) were assessed by WB and Coomassie staining. The aggregation-prone Httex1 constructs (Httex1 72Q and Httex1 72Q-GFP) could successfully be detected in the last aggregate Urea fraction (red arrowheads) but not the controls Httex1 16Q and GFP. Httex1 was detected by WB using antibody MAB5492 and Beta tubulin was used as the loading control.

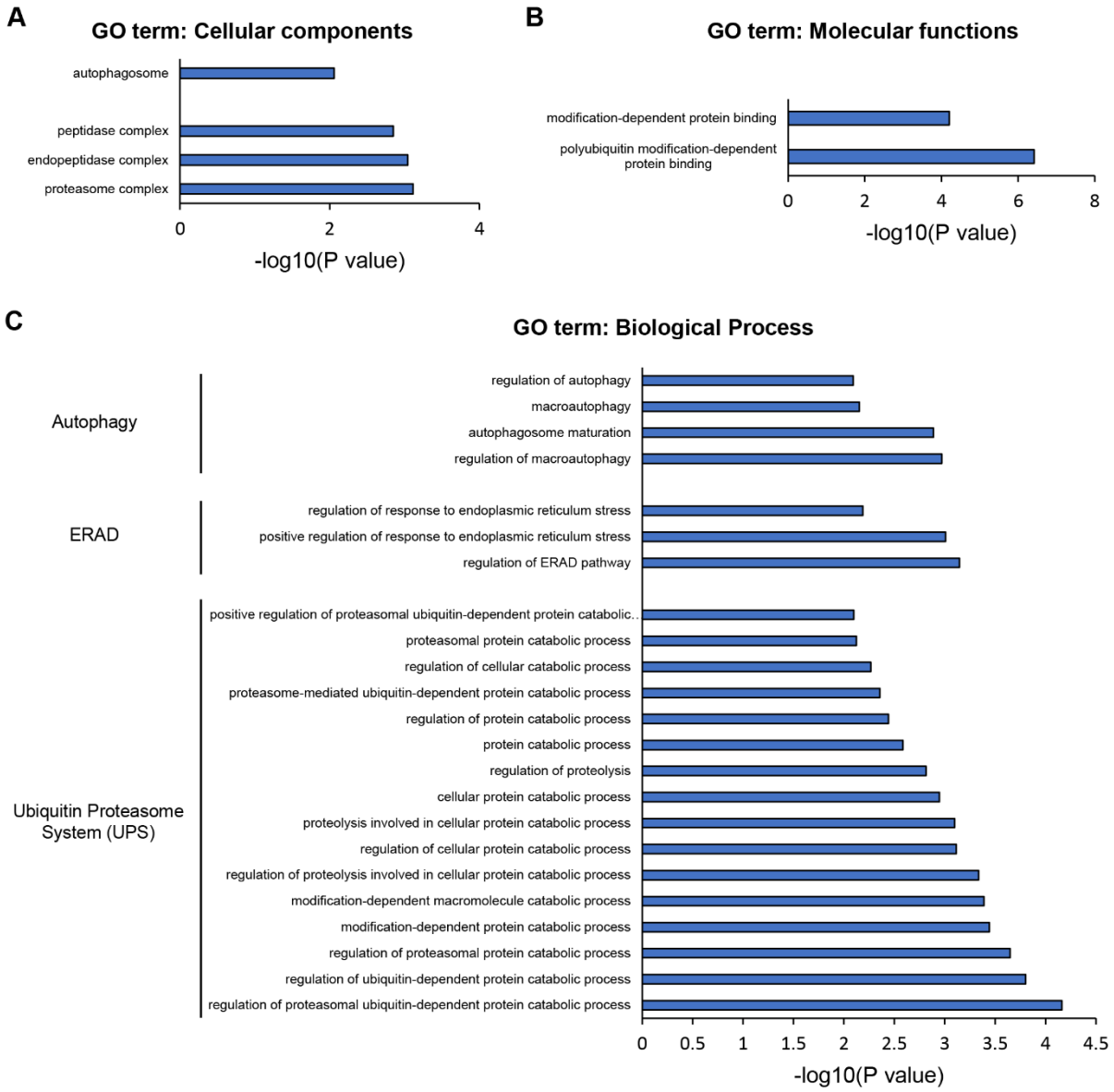

Figures S 6. Proteomic analysis of Httex1 72Q vs. Httex1 16Q Urea soluble fraction revealed strong enrichment of the Ubiquitin-Proteasome System.

Cellular components (**A**), Molecular functions (**B**) and biological processes (**C**) enriched in the Urea soluble fraction of Httex1 72Q vs. Httex1 16Q extracted from the volcano plot (p-value<0.01) (Figure 3F). Analyses were performed using Gene Ontology (GO) enrichment analyses determined by DAVID analysis ($-\log_{10}$(p-value) >1).

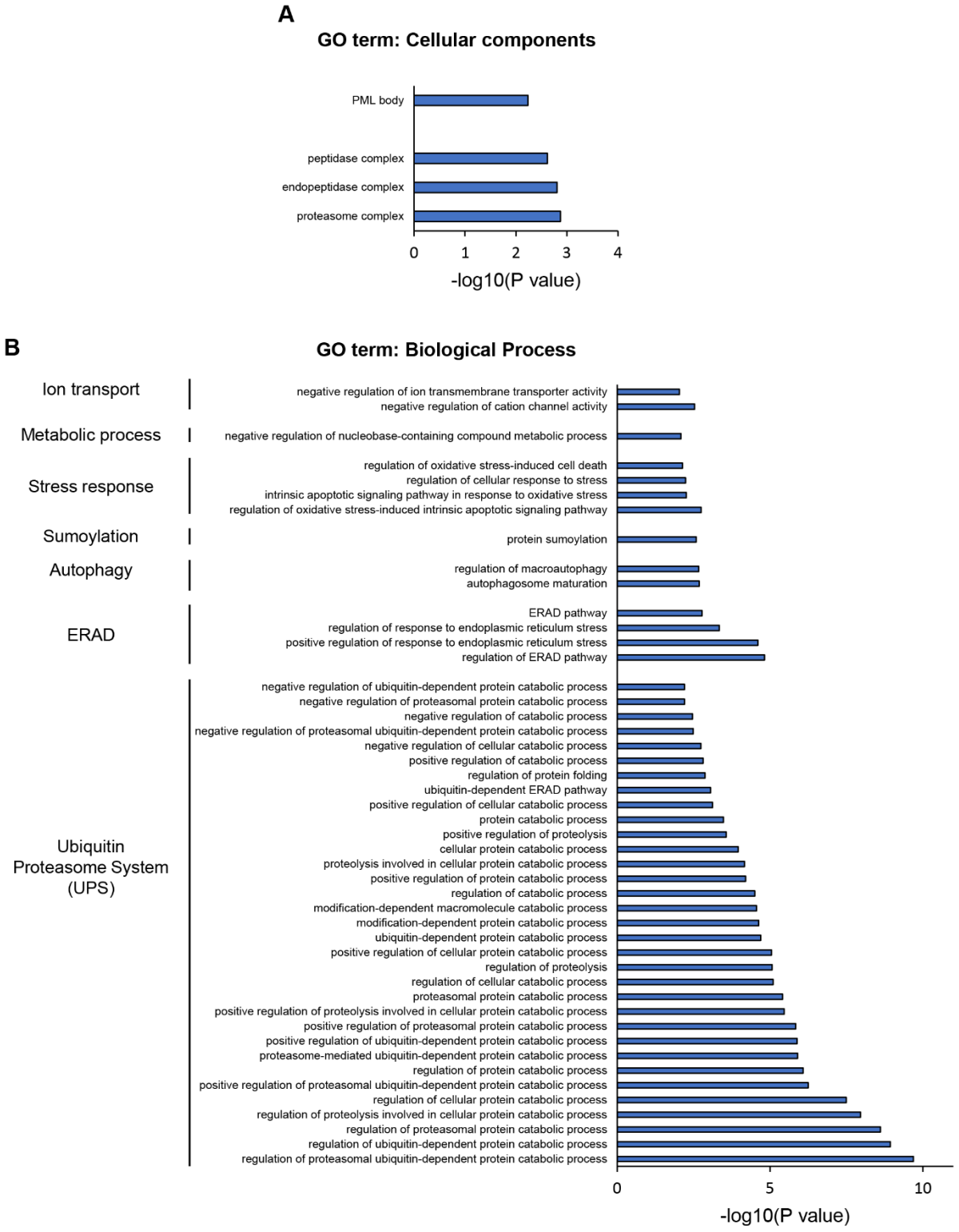

Figures S 7. Proteomic analysis of Httex1 72Q-GFP vs. GFP Urea soluble fraction revealed strong enrichment of the Ubiquitin-Proteasome System.

Cellular components (**A**), Molecular functions (B) and biological processes (**C**) enriched in the Urea soluble fraction of Httex1 72Q vs. Httex1 16Q extracted from the volcano plot (p-value<0.01) (Figure 3H). Analyses were performed using Gene Ontology (GO) enrichment analyses determined by DAVID analysis ($-\log_{10}$(p-value) >1).

Chapter IV: Discussion and future perspectives

Discussion

The primary objectives of this thesis were to 1) develop an integrated pipeline for the characterization of Htt cellular inclusions at the biochemical, ultrastructural, and functional levels; and 2) use this pipeline to elucidate the molecular, cellular, and structural determinants of cytoplasmic and nuclear Htt inclusion formation. Our ultimate goal was to use the knowledge gained from these studies to reassess current hypotheses and working models on the mechanisms of huntingtin aggregation and how it contributes to cellular dysfunctions and neurodegeneration in HD. Our results confirm previous findings and shed new light on the complex mechanisms associated with different stages of inclusion formation and suggest that future therapeutic strategies should account for the complexity of the process within the different cellular compartments and at various stages of disease progression.

Our detailed analyses of the ultrastructure of Httex1 72Q inclusions revealed their fibrillar nature but also showed a previously unreported core and shell structural organization for cytoplasmic mutant Httex1 inclusions. Additionally, we showed that Httex1 72Q is composed of highly organized radiating Htt fibrils that are densely packed at the core compared to the periphery, where the fibrils remain highly organized but less densely packed. Furthermore, the periphery of the inclusions is decorated by membranous organelles and cytoskeletal proteins. The formation of this complex organization of the Httex1 inclusions was strongly dependent on the length of the polyQ repeat as well as its subcellular localization. We demonstrated that the formation of neuronal intranuclear inclusions matures from small aggregates to large granulo-filamentous inclusions, inducing nuclear condensation.

Additionally, our quantitative proteomic analysis showed that the formation and maturation of inclusions are accompanied by the sequestration of proteins related to some of the major

cellular pathways dysregulated in HD, such as the inflammation and transcriptomic pathways, the actin cytoskeleton, and the quality control machinery, including the ubiquitin-proteasome system, the autophagy pathway, and the chaperones related to protein folding and proteostasis. Altogether, our findings suggest that the formation of Huntingtin inclusions is driven primarily by the polyQ repeat domain and involves the active recruitment and sequestration of lipids, proteins, and membranous organelles. The periphery of the Httex1 inclusion might act as an active site for Htt fibril growth and the interaction of the radiating Htt fibrils with the cellular compartments, leading to functional disruption of these organelles, which could ultimately contribute to cellular dysfunction and neurodegeneration.

Most of the existing studies on cellular models of HD do not perform thorough ultrastructural and biochemical characterization of Htt aggregates, impeding the detailed interpretation of the investigated mechanisms. Moreover, the great majority of Htt cellular studies rely on constructs containing additional sequences or tags to help purify or visualize the protein. Our findings highlighted the limitation of existing models of Htt aggregation and underscored the critical importance of having a comprehensive characterization of the different models of Htt inclusions.

To what extent do Htt inclusions in cells resemble Htt inclusions in HD brains?

Our studies revealed several shared morphological properties between the inclusions we observed in the cellular models and those in HD patient brains (Figures 1 and 2). In addition, our work not only complements previous studies but also provides a more detailed characterization of the ultrastructural properties of Htt inclusions and systematic analysis of their proteome, which was not investigated in previous morphological studies of Htt inclusions. Although several groups have reported on electron microscopy or proteomic studies of Htt inclusions from cells and animal models of HD, examination of the ultrastructural and proteome of inclusions is rarely reported on the same model system.

Neuronal intranuclear inclusions in HD brains and *in vivo* models of HD are all detected and described as predominantly granular with the appearance of filamentous structures (Figure 1A-E). In other studies, neuronal intranuclear inclusions in primary neurons were observed at low magnification and described as protein deposits by Tagawa *et al.* (Figure 1F) and more recently as a highly fibrillar inclusion body by Bäuerlein and colleagues (Figure 1G). Our electron tomography data on nuclear neuronal Htt inclusion clearly demonstrated that they are composed of primarily fibrillar Httex1 aggregates, in addition to granular structures (Chapter III, Figure 2), similar to previous ultrastructural studies performed in HD patient brains and *in vivo* (Figure 1).

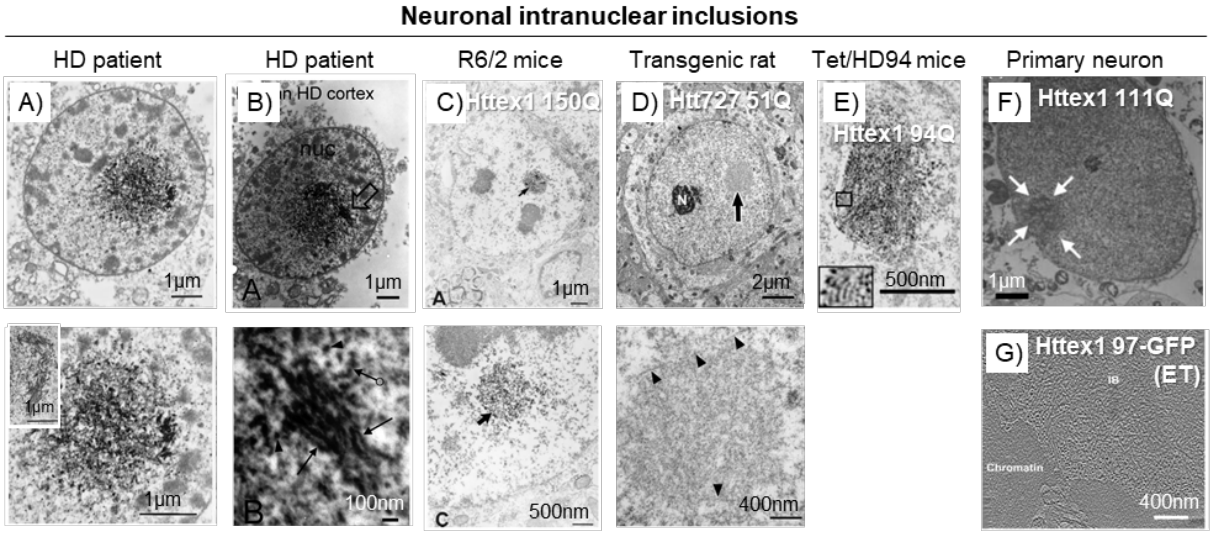

Figure 1. Comparison of huntingtin nuclear inclusions observed by EM-based techniques in HD patient brains, *in vivo* and cellular models of HD.

A) EM of a neuronal intranuclear inclusion (NII) in the HD cortex with immunoperoxidase labeling (Ab1). Upper panel: The NII in a cortical neuron appears as a dense and membraneless aggregate. Lower panel: Higher magnification of NII shows the presence of labeled granules and filaments within the inclusion. **B)** mHtt was detected by EM and immunoperoxidase labeling with a primary antibody targeting the Nt17 domain. EM images are from a cortical neuron. The NII is highly heterogeneous with the presence of granular/oligomeric and fibrillar structures. Stacks of labeled fibrils were detected in the inclusion and magnified in the lower panel. **C)** EM localization of NII from the transgenic R6/2 mice. DAB labeling confirmed the presence of Htt. **D)** EM of one striatal NII from a transgenic rat expressing Htt727 with 51Q. Top panel: Round intranuclear aggregate (large arrow) slightly larger than the adjacent nucleolus (N). Lower panel: High magnification of the NII reveals a granular and fibrillar (arrowheads) morphology. **E)** NII detected in the cortex and striatum of Tet/HD94 mice by EM. **F)** EM analysis of cortical neurons expressing Htt111 with the presence of NII (arrows). **G)** Cryo-ET of an NII from a Htt97Q-GFP-transfected neuron. Figure adapted

from: A) DiFiglia and colleagues[81]; B) Legleiter and colleagues[113]; C) Davies and colleagues[102]; D) Petrasch-Parwez and colleagues[533]; E) Díaz-Hernández and colleagues[445]; F) Tagawa and colleagues[120]; and G) Bäuerlein and colleagues[195], with permissions. The Copyright 2004 Society for Neuroscience applies to Díaz-Hernández and colleagues'[445] publication.

Cytoplasmic inclusions from *post-mortem* HD patients were also described by DiFiglia *et al.* as containing granules and filaments surrounded by the accumulation of mitochondria (Figure 2A). These share similar features to what we observed for the cytoplasmic tag-free Httex1 72Q inclusions in our mammalian cellular system. (Chapter II, Figure 1). Similarly, neuritic inclusions from transgenic rats and mice were shown to be composed of mostly granular structures but also contained filaments (Figure 2B-C), as well as mitochondria surrounding the inclusion (Figure 2B). In primary neurons, Tagawa and colleagues observed cytoplasmic inclusions of tag-free Httex1 packed against the nucleus, similar to what we observed in HEK cells, but they did not further characterize the ultrastructural properties of these inclusions (Figure 2D, upper panel). In contrast, Httex1 72Q-GFP or Httex1 97Q-GFP neuronal cytoplasmic inclusions were predominantly fibrillar, as reported by Miller *et al*. by EM and by Bäuerlein *et al.* by ET. (Figure 2D, lower panel and Figure 2F).

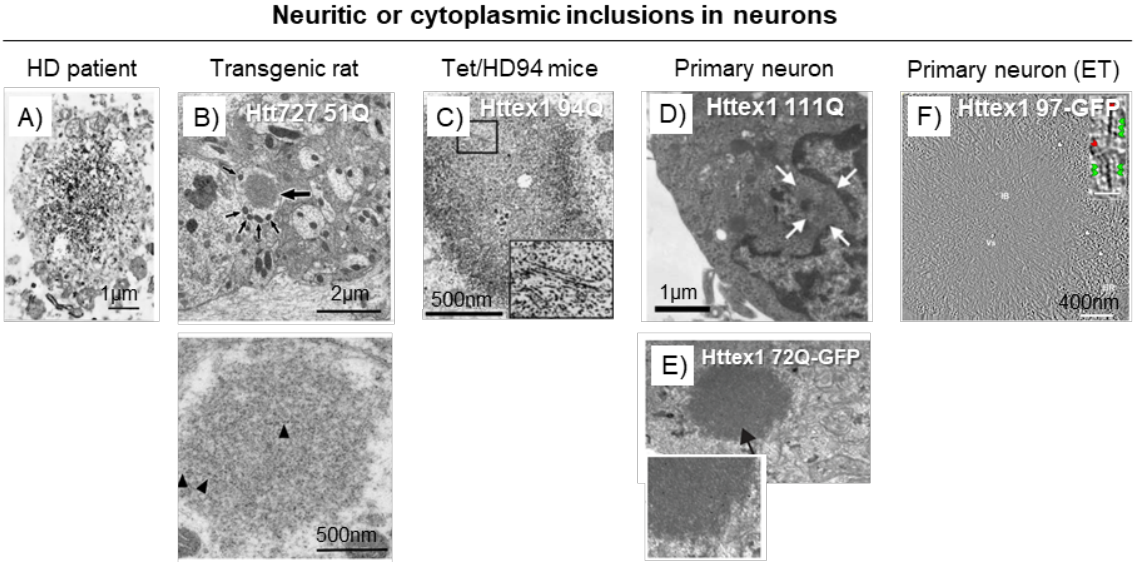

Figure 2. Comparison of huntingtin neuritic and cytoplasmic neuronal inclusions observed by EM-based techniques in HD patient brains, *in vivo* and cellular models of HD.

A) EM of one human dystrophic neurite in the HD cortex with immunoperoxidase labeling (Ab1) containing an aggregate with immunoreactive granules and filaments and surrounded by mitochondria. **B)** Ultrastructure of one dendritic inclusion with the accumulation of mitochondria in proximity. The magnification (lower panel) reveals granular and fibrillar (arrowheads) structures. **C)** EM analysis of a dystrophic neurite inclusion found in the cortex of Tet/HD94 mice. **D)** EM analysis of cortical neurons expressing Htt111 showed the presence of perinuclear aggregates (arrows). **E)** EM showed the presence of a granular Htt inclusion found in a striatal neuron transfected with mutant Httex1-GFP. **F)** Cryo-ET of a cytoplasmic inclusion detected in a Htt97Q-GFP-transfected mouse primary neuron. Figure adapted from: A) DiFiglia and colleagues[81]; B) Petrasch-Parwez and colleagues[533]; C) Díaz-Hernández and colleagues[445]; D) Tagawa and colleagues[120]; E) Miller and colleagues[329]; and F) Bäuerlein and colleagues[195], with permissions. The Copyright 2004 Society for Neuroscience applies to Díaz-Hernández and colleagues'[445] publication.

Ultrastructural characterization of Htt inclusions was also previously conducted in non-neuronal mammalian cells, where they were detected predominantly in the cytoplasm (Figure 3). As discussed in the previous chapters, the core and shell organization we detected for tag-free Httex1 72Q cytoplasmic inclusions was also observed by Qin *et al.* but using a longer fragment than Httex1 (FLAG-tagged Htt1-969 fragment; 100Q), by immunoperoxidase labeling (Figure 3B). Tagawa and colleagues provided EM images of cytoplasmic tag-free Httex1-111Q inclusions in HeLa cells and showed that they also displayed a core and shell morphology at low magnification. However, they did not report high-resolution data on the ultrastructural properties of these inclusions or assess their biochemical composition, simply describing them qualitatively as amorphous deposits (Figure 3C).

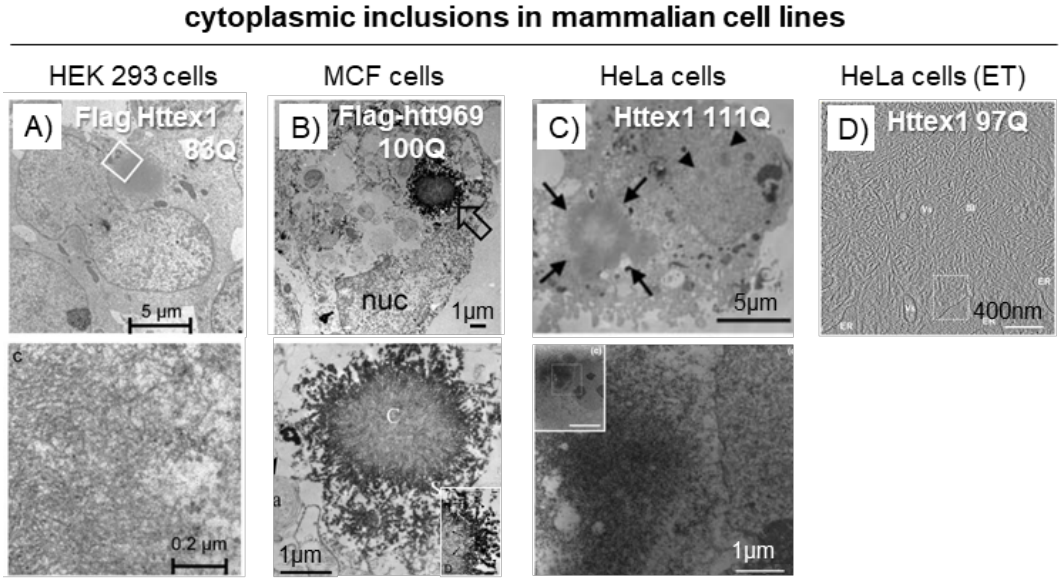

Figure 3. Comparison of huntingtin cytoplasmic inclusions found in mammalian cells.

A. EM of HEK cells with one perinuclear Httex1 83Q aggregates, 3–5 days post-transfection. Higher magnification reveals the presence of HDQ83 fibrils with a diameter of ~10 nm. **B)** EM of MCF-7 showed one cytoplasmic Htt FH969–100Q inclusion by immunoperoxidase using a FLAG tag. The inclusion was in close proximity to several mitochondria. Radiating fibrils were detected in the core (C) and shell (S). **C)** EM analysis of HeLa cells expressing Htt111 reveals a large cytoplasmic aggregate (black arrows). Lower panel: Immune detection of a large cytoplasmic aggregate (N-18). **D)** Cryo-ET of a Htt97Q-transfected HeLa cell. Figure adapted from A) Waelter and colleagues[268]; B) Qin and colleagues[165]; C) Tagawa and colleagues[120]; and D) Bäuerlein and colleagues[195], with permissions. The Copyright 2007 Society for Neuroscience applies to Qin and colleagues'[165] publication.

Altogether, the observations summarized in Figures 1, 2 and 3, demonstrate that many of the features of inclusions seen in HD brains can be reproduced in our cellular models, including 1) the formation of granulo-filamentous neuronal intranuclear inclusions, 2) the accumulation of mitochondria in the periphery of the cytoplasmic inclusions, and 3) the presence of Actin-F associated with the inclusions. However, many of these features were observed only with tag-free mutant Httex1 proteins. This underscores the critical importance of using tag-free native Htt sequences to investigate the mechanisms of inclusion formation and ultrastructural properties in cells.

How does Httex1 inclusion formation contribute to cellular toxicity?

The contribution of Htt aggregation and inclusion formation to cellular toxicity is complex and not fully understood. Discrepancies were observed with, on the one hand, the deleterious sequestration of key cellular factors by Htt inclusion formation, and on the other hand, the protective effect of inclusions by the sequestration of toxic soluble oligomeric or aggregated forms of Htt. It was previously shown that the overexpression of mutant Httex1 in mammalian cells and primary neurons was sufficient to induce cell death[311–318]. In our work, we demonstrated that the toxicity induced by mHtt aggregation and inclusion formation depended on the cell type.

In HEK cells, we detected ER and mitochondrial defects (ERES remodeling, increased mitochondrial respiration, mitochondrial fragmentation, and inner cristae damage) but without ROS production and mitochondrial outer membrane permeabilization. ER and mitochondrial dysfunctions such as mitochondrial fragmentation[489–491] and reduced ER dynamics[195] were previously observed in cellular models of HD and suggest that the modulation of the ER-mitochondrial network is an adaptive mechanism upon mHtt misfolding and aggregation. Moreover, the colocalization of Httex1 inclusions with aggresome markers (HDAC6, p62, and vimentin) and the sequestration of proteins, membranes, and organelles related to the UPS, chaperones, ERAD, inflammation, and stress granules indicate an adaptative mechanism to clear aggregates. Then, the detection of proteins related to autophagosomes and apoptosis by proteomic analysis is in line with the significant caspase 3 activity measured in cells, but only at a relatively late time point (96 hours post-transfection). Therefore, we cannot rule out that the observed proteotoxicity might partially arise from soluble oligomers, but the physical interactions of inclusions with cellular components and the recruitment of essential proteins indicate that Htt inclusions are, to some extent, harmful to the cells. Overall, we observed a strong resilience in HEK cells despite a high level of inclusions after mHttex1 expression for 48 h (Chapter II). In a study by Waelter *et al.*, HEK cell viability measured by their metabolic

activity was decreased four days post-induction of Httex1 expression and correlated with the formation of insoluble fibrillar aggregates[268]. Similar to our results, the authors suggest a key role of Httex1 aggregation on toxicity by interfering with the protein degradation machinery such as the proteasome, as well as the sequestration of regulatory proteins.

In primary neurons, enhanced nuclear condensation and DNA fragmentation increased over time, but we noticed a lack of correlation between the size of the nuclear inclusions (small versus large puncta) and cell death levels. In the study by Shen and colleagues, the authors suggest that Httex1 toxicity in cortico-striatal slices might arise from different structural conformers rather than the size of the aggregates[149]. Moreover, similar to our results in primary neurons, the authors observed similar levels of neuronal toxicity with and without the presence of the Nt17 domain, despite a higher number of inclusions relocated in the nucleus. Our proteomic analysis revealed the sequestration of transcription factors and proteins related to the UPS, ERAD and autophagy. Interestingly, it was demonstrated that the Nedd8 ubiquitin-related protein was involved in a protective mechanism against proteotoxicity by inducing the aggregation of misfolded proteins and trying to reduce proteasome burden in cells[524] and was detected in Lewy bodies from PD brains[522]. Also, our results showed that the formation of neuronal intranuclear inclusions with the presence of fibrillar aggregates is linked to DNA fragmentation and toxicity by intrinsic apoptosis. Interestingly, Ramdzan *et al*. overexpressed Httex1 97Q in cells with a large fluorescent tag (mCherry or Cerulean) and observed that early soluble or disordered aggregates showed death by apoptosis (caspase 3/7 activation)[504]. By contrast, they reported that mature inclusion formation was associated with apoptosis suppression, quiescence entry and delayed necrosis, and therefore suggested a model that integrates both early and late, mature toxic processes. Our results suggest that primary neurons are more susceptible to cell death compared to HEK cells. However, the comparison of the two cellular models should take into account that Httex1 expression was assessed for a longer time period in primary neurons, as well as the different subcellular localization of the

inclusions. Therefore, although our results and previous cellular studies suggest that nuclear mHtt aggregates are potentially more toxic[143,147,446,542], the cell type appears to be a major factor, and both cytoplasmic and nuclear aggregates contribute to cellular dysfunctions.

Overall, our studies indicate that although cells expressing mutant Httex1 initiate coping mechanisms such as the upregulation of the protein degradation machineries, increased mitochondrial respiration and inflammation to clear mutant aggregates, the process of inclusion formation and maturation is linked to cellular dysfunction and cell death. Therefore, even if the formation of Httex1 inclusions associated with stress granules and aggresome features might be protective at first, the overload of clearance mechanisms, the physical interactions, and the sequestration of cellular components transfer toxic properties to the inclusions.

Future perspectives

Toward more disease-relevant models of HD pathology formation

The cellular models we describe in this thesis were based on manipulating the expression of one Htt fragment, Httex1. While there is strong evidence that Httex1 is produced in the brain and accumulates in pathological aggregates of HD animal models, it is also clear that it is not the only polyQ-containing fragment being produced in neurons. Biochemical studies on brain-derived Htt inclusions have consistently shown the presence of multiple Htt fragments of variable length. Whether these fragments have physiological roles or are the products of pathogenic processes remains unclear. Furthermore, the aggregation propensity of many of these fragments remains unexplored. Therefore, we believe that more systematic studies are needed to determine the distribution of Htt species and how they vary in different brain regions and cell types affected or not by Htt aggregation.

Furthermore, a more detailed characterization of Htt aggregates from the post-mortem brains of HD patients at the biochemical and structural levels is essential to guiding the development and validation of more disease-relevant cellular models that recapitulate the complexity and pathological diversity of Htt in HD. Toward this goal, we have initiated a collaboration with Prof. Richard Faull at the New Zealand Human Brain Bank at the University of Auckland to obtain brain tissues from HD patients and controls. The primary objectives of this project are to 1) identify the biologically relevant forms of Htt species under normal and pathological conditions, 2) develop and optimize methods for the isolation and characterization of Htt species from *post-mortem* HD brains, and 3) capture the morphological, structural, and biochemical diversity of Htt pathology in different brain regions as well as from different disease severities. Preliminary results using an expanded panel of antibodies revealed the presence of several Htt fragments in the soluble fraction of brain lysates from HD cases as well as controls. Further studies are needed to determine, with more precision, which fragments are associated with pathology formation and which of these fragments can aggregate and participate in the initiation of Htt aggregation.

The need for label-free methods to monitor and study Htt aggregation and inclusions formation in cells and *in vivo*

Understanding the role of protein aggregation in the pathogenesis of HD requires the development of novel methods that allow monitoring of the various stages of Htt aggregation that lead to inclusions under physiological-like conditions and in the absence of any sequence modifications that could alter the biophysical and cellular properties of the protein. We previously demonstrated that large tags such as GFP could interfere with Htt fibrilization, alter the surface accessibility of the fibrils, but also strongly modify the ultrastructural and biochemical properties of cytoplasmic and nuclear Httex1 inclusions. Therefore, our results stress the need to develop label-free methods to monitor Htt aggregation and inclusion formation in cells. Towards this goal, we worked in close collaboration with Prof. Aleksandra Radenovic, Dr. Kristine Grussmayer and Dr. Vytautas Navikas in the Laboratory of Nanoscale Biology (LBEN, EPFL) to develop label-free quantitative phase contrast-based methods for label-free monitoring of Htt, as well as super-resolution techniques to assess Htt early dynamics. Preliminary results are encouraging and demonstrate the feasibility of detecting unlabeled Httex1 cellular inclusions by quantitative phase contrast. These preliminary and promising results have led to the development of a new project aimed at unraveling the early dynamics of Htt cellular aggregation and inclusion formation using a combination of super-resolution imaging and novel label-free methods.

References

1. Cattaneo E, Rigamonti D, Goffredo D, Zuccato C, Squitieri F, Sipione S. Loss of normal huntingtin function: new developments in Huntington's disease research. *Trends Neurosci*. 2001;24(3):182-188. doi:10.1016/S0166-2236(00)01721-5

2. Rosenblatt A, Leroi I. Neuropsychiatry of Huntington's disease and other basal ganglia disorders. *Psychosomatics*. 2000;41(1):24-30. doi:10.1016/S0033-3182(00)71170-4

3. Reiner A, Dragatsis I, Dietrich P. *Genetics and Neuropathology of Huntington's Disease*. Vol 98. Elsevier Inc.; 2011. doi:10.1016/B978-0-12-381328-2.00014-6

4. Bates GP, Dorsey R, Gusella JF, et al. Huntington disease. *Nat Rev Dis Prim*. 2015;1:15005. doi:10.1038/nrdp.2015.5

5. Rawlins MD, Wexler NS, Wexler AR, et al. The Prevalence of Huntington ' s Disease. *Neuroepidemiology*. 2016;46:144-153. doi:10.1159/000443738

6. Baig SS, Strong M, Quarrell OW. The global prevalence of Huntington's disease: a systematic review and discussion. *Neurodegener Dis Manag*. 2016;6(4):331-343. doi:10.2217/nmt-2016-0008

7. Pringsheim T, Wiltshire K, Day L, Dykeman J, Steeves T, Jette N. The incidence and prevalence of Huntington's disease: A systematic review and meta-analysis. *Mov Disord*. 2012;27(9):1083-1091. doi:10.1002/mds.25075

8. Margolis RL, Ross CA. Diagnosis of Huntington disease. *Clin Chem*. 2003;49(10):1726-1732. doi:10.1373/49.10.1726

9. Ross CA, Aylward EH, Wild EJ, et al. Huntington disease: natural history, biomarkers and prospects for therapeutics. *Nat Rev Neurol*. 2014;10(4):204-216. doi:10.1038/nrneurol.2014.24

10. Ross CA, Tabrizi SJ. Huntington's disease: from molecular pathogenesis to clinical treatment. *Lancet Neurol*. 2011;10(1):83-98. doi:10.1016/S1474-4422(10)70245-3

11. Stout JC, Paulsen JS, Queller S, et al. Neurocognitive Signs in Prodromal Huntington Disease. *Neuropsychology*. 2011;25(1):1-14. doi:10.1037/a0020937.Neurocognitive

12. Vonsattel JPG, DiFiglia M. Huntington disease. *J Neuropathol Exp Neurol*. 1998;57(5):369-384. doi:10.1016/B978-0-444-63233-3.00017-8

13. Bence NF, Sampat RM, Kopito RR. Impairment of the ubiquitin-proteasome system by protein aggregation. *Science (80-)*. 2001;292(5521):1552-1555. doi:10.1126/science.292.5521.1552

14. Kegel KB, Kim M, Sapp E, et al. Huntingtin expression stimulates endosomal-lysosomal activity, endosome tubulation, and autophagy. *J Neurosci*. 2000;20(19):7268-7278. doi:10.1523/jneurosci.20-19-07268.2000

15. Kegel KB, Meloni AR, Yi Y, et al. Huntingtin is present in the nucleus, interacts with the transcriptional corepressor C-terminal binding protein, and represses transcription. *J Biol Chem*. 2002;277(9):7466-7476. doi:10.1074/jbc.M103946200

16. Kumar A, Vaish M, Ratan RR. Transcriptional dysregulation in Huntington's disease: a failure of adaptive transcriptional homeostasis. *Drug Discov Today*. 2014;19(7):956-962. doi:10.1016/j.drudis.2014.03.016.Transcriptional

17. Gu M, Gash MT, Mann VM, Javoy-Agid F, Cooper JM, Schapira AHV. Mitochondrial defect in Huntington's disease caudate nucleus. *Ann Neurol*. 1996;39(3):385-389.

doi:10.1002/ana.410390317

18. Panov A V, Gutekunst C, Leavitt BR, et al. Early mitochondrial calcium defects in Huntington ' s disease are a direct effect of polyglutamines. *Nat Neurosci*. 2002;5(8):731-736. doi:10.1038/nn884

19. Cowan CM, Raymond LA. Selective Neuronal Degeneration in Huntington's Disease. *Curr Top Dev Biol*. 2006;75:25-71. doi:10.1016/S0070-2153(06)75002-5

20. Zuccato C, Ciammola A, Rigamonti D, et al. Loss of Huntingtin-Mediated BDNF Gene Transcription in Huntington's Disease. *Science (80-)*. 2001;293:493-498. doi:10.1126/science.1059581

21. Liot G, Zala D, Pla P, Mottet G, Piel M, Saudou F. Mutant Huntingtin Alters Retrograde Transport of TrkB Receptors in Striatal Dendrites. *J Neurosci*. 2013;33(15):6298-6309. doi:10.1523/JNEUROSCI.2033-12.2013

22. Rosas HD, Koroshetz WJ, Chen YI, et al. Evidence for more widespread cerebral pathology in early HD: An MRI-based morphometric analysis. *Neurology*. 2003;60(10):1615-1620. doi:10.1212/01.WNL.0000065888.88988.6E

23. Singh-Bains MK, Mehrabi NF, Sehji T, et al. Cerebellar degeneration correlates with motor symptoms in Huntington disease. *Ann Neurol*. 2019;85(3):396-405. doi:10.1002/ana.25413

24. Nana AL, Kim EH, Thu DCV, et al. Widespread heterogeneous neuronal loss across the cerebral cortex in Huntington's disease. *J Huntingtons Dis*. 2014;3(1):45-64. doi:10.3233/JHD-140092

25. De La Monte SM, Vonsattel JP, Richardson EP. Morphometric demonstration of atrophic changes in the cerebral cortex, white matter, and neostriatum in Huntington's disease. *J Neuropathol Exp Neurol*. 1988;47(5):516-525. doi:10.1097/00005072-198809000-00003

26. Vonsattel J-P, Myers RH, Stevens TJ, Ferrante RJ, Bird ED, Richardson EP. Neuropathological Classification of Huntington's Disease. *J Neuropathol Exp Neurol*. 1985;44(6):559-577. doi:10.1097/00005072-198511000-00003

27. Gusella JF, Wexler NS, Conneally PM, et al. A polymorphic DNA marker genetically linked to Huntington's disease. *Nature*. 1983;306(5940):234-238. doi:10.1038/306234a0

28. The Huntington's Disease Collaborative Research Group. A Novel Gene Containing a Trinucleotide That Is Expanded and Unstable on Huntington's Disease Chromosomes. *Cell*. 1993;72(6):971-983.

29. Kremer B, Goldberg P, Andrew SE, et al. A Worldwide study of the huntington's disease mutation. The sensitivity and specificity of measuring CAG repeats. *N Engl J Med*. 1994;330(20):1401-106.

30. Read AP. Huntington's disease : testing the test. *Nat Genet*. 1993;4(4):329-330.

31. La Spada AR, Taylor JP. Polyglutamines placed into context. *Neuron*. 2003;38(5):681-684. doi:10.1016/S0896-6273(03)00328-3

32. Orr HT, Zoghbi HY. Trinucleotide repeat disorders. *Annu Rev Neurosci*. 2007;30:575-621. doi:10.1146/annurev.neuro.29.051605.113042

33. Orr HT. Polyglutamine Neurodegeneration: Expanded Glutamines Enhance Native Functions. *Curr Opin Genet Dev*. 2012;22(3):251-255. doi:10.1146/annurev-cellbio-

092910-154240.Sensory

34. McNeil SM, Novelletto A, Srinidhi J, et al. Reduced penetrance of the Huntington's disease mutation. *Hum Mol Genet*. 1997;6(5):775-779. doi:10.1093/hmg/6.5.775

35. Semaka A, Collins JA, Hayden MR. Unstable familial transmissions of huntington disease alleles with 27-35 CAG repeats (intermediate alleles). *Am J Med Genet Part B Neuropsychiatr Genet*. 2010;153B(1):314-320. doi:10.1002/ajmg.b.30970

36. JM L, EM R, JH L, et al. CAG repeat expansion in Huntington disease determines age at onset in a fully dominant fashion. *Neurology*. 2012;78(10):690-695.

37. Consortium GM of HD. CAG Repeat Not Polyglutamine Length Determines Timing of Huntington's Disease Onset. *Cell*. 2019;178(4):887-900.e14. doi:10.1016/j.cell.2019.06.036

38. Gusella JF, Macdonald ME. Huntington's disease: the case for genetic modifiers. *Genome Med*. 2009:1-6.

39. Myers RH. Huntington's Disease Genetics. *NeuroRx*. 2004;1(2):255-262.

40. Andresen JM, Gayán J, Cherny SS, et al. Replication of twelve association studies for Huntington's disease residual age of onset in large Venezuelan kindreds. *J Med Genet*. 2007;44:44-50. doi:10.1136/jmg.2006.045153

41. U.S.–Venezuela Collaborative Research Project T, Wexler NS. Venezuelan kindreds reveal that genetic and environmental factors modulate Huntington's disease age of onset. *Proc Natl Acad Sci*. 2004;101(10):3498-3503.

42. Wexler NS, Young AB, Tanzi RE, et al. Homozygotes for Huntington's disease. *Nature*. 1987;326(6109):194-197. doi:10.1038/326194a0

43. Squitieri F, Gellera C, Cannella M, et al. Homozygosity for CAG mutation in Huntington disease is associated with a more severe clinical course. *Brain*. 2003;126(4):946-955. doi:10.1093/brain/awg077

44. van der Burg JM, Björkqvist M, Brundin P. Beyond the brain: widespread pathology in Huntington's disease. *Lancet Neurol*. 2009;8(8):765-774. doi:10.1016/S1474-4422(09)70178-4

45. Carroll JB, Bates GP, Steffan J, Saft C, Tabrizi SJ. Treating the whole body in Huntington's disease. *Lancet Neurol*. 2015;14(11):1135-1142. doi:10.1016/S1474-4422(15)00177-5

46. Strong T V, Tagle DA, Valdes JM, et al. Widespread expression of the disease gene in brain and nonneural tissues. *Nat Genet*. 1993;5(3):259-265.

47. Panov A V., Lund S, Greenamyre JT. Ca2+-induced permeability transition in human lymphoblastoid cell mitochondria from normal and Huntington's disease individuals. *Mol Cell Biochem*. 2005;269(1-2):143-152. doi:10.1007/s11010-005-3454-9

48. Sathasivam K, Woodman B, Mahal A, et al. Centrosome disorganization in fibroblast cultures derived from R6/2 Huntington's disease (HD) transgenic mice and HD patients. *Hum Mol Genet*. 2001;10(21):2425-2435. doi:10.1093/hmg/10.21.2425

49. Almeida S, Sarmento-Ribeiro AB, Januário C, Rego AC, Oliveira CR. Evidence of apoptosis and mitochondrial abnormalities in peripheral blood cells of Huntington's disease patients. *Biochem Biophys Res Commun*. 2008;374(4):599-603. doi:10.1016/j.bbrc.2008.07.009

50. J N, SB F, JR O, et al. Targeted disruption of the Huntington's disease gene results in

embryonic lethality and behavioral and morphological changes in heterozygotes. *Cell*. 1995;81(5):811-823. doi:10.1016/0092-8674(95)90542-1

51. Zeitlin S, Liu J, Chapman DL, Papaioannou VE, Efstratiadis A. Increased apoptosis and early embryonic lethality in mice nullizygous for the Huntington's disease gene homologue. *Nat Genet*. 1995;11(2):155-163.

52. Sørensen SA, Fenger K. Causes of death in patients with Huntington's disease and in unaffected first degree relatives. *J Med Genet*. 1992;29(12):911-914. doi:10.1136/jmg.29.12.911

53. Thul PJ, Akesson L, Wiking M, et al. A subcellular map of the human proteome. *Science (80-)*. 2017;356(6340):eaal3321. doi:10.1126/science.aal3321

54. Hughes AC, Mort M, Elliston L, et al. Identification of novel alternative splicing events in the huntingtin gene and assessment of the functional consequences using structural protein homology modelling. *J Mol Biol*. 2014;426(7):1428-1438. doi:10.1016/j.jmb.2013.12.028

55. Ruzo A, Ismailoglu I, Popowski M, et al. Discovery of novel isoforms of Huntingtin reveals a new hominid-specific exon. *PLoS One*. 2015;10(5):e0127687. doi:10.1371/journal.pone.0127687

56. Saudou F, Humbert S. The Biology of Huntingtin. *Neuron*. 2016;89(5):910-926. doi:10.1016/j.neuron.2016.02.003

57. Xia J, DH L, J T, M V, R T. Huntingtin contains a highly conserved nuclear export signal. *Hum Mol Genet*. 2003;12(12):1393-1403. doi:10.1093/hmg/ddg156

58. Maiuri T, Woloshansky T, Xia J, Truant R. The huntingtin N17 domain is a multifunctional CRM1 and Ran-dependent nuclear and cilial export signal. *Hum Mol Genet*. 2013;22(7):1383-1394. doi:10.1093/hmg/dds554

59. Guo Q, Bin Huang, Cheng J, et al. The cryo-electron microscopy structure of huntingtin. *Nature*. 2018;555(7694):117-120. doi:10.1038/nature25502

60. Harding RJ, Loppnau P, Ackloo S, et al. Design and characterization of mutant and wildtype huntingtin proteins produced from a toolkit of scalable eukaryotic expression systems. *J Biol Chem*. 2019;294(17):6986-7001. doi:10.1074/jbc.RA118.007204

61. Harding RJ, Deme JC, Hevler JF, et al. HAP40 orchestrates huntingtin structure for 1 differential interaction with polyglutamine 2 expanded exon 1. *bioRxiv*. 2021. https://doi.org/10.1101/2021.04.02.438217.

62. Vijayvargia R, Epand R, Leitner A, et al. Huntingtin's spherical solenoid structure enables polyglutamine tract-dependent modulation of its structure and function. *Elife*. 2016;5(MARCH2016):1-16. doi:10.7554/eLife.11184

63. Seefelder M, Alva V, Huang B, et al. The evolution of the huntingtin-associated protein 40 (HAP40) in conjunction with huntingtin. *BMC Evol Biol*. 2020;20(1):1-18. doi:10.1186/s12862-020-01705-5

64. Harjes P, Wanker EE. The hunt for huntingtin function: Interaction partners tell many different stories. *Trends Biochem Sci*. 2003;28(8):425-433. doi:10.1016/S0968-0004(03)00168-3

65. Gauthier LR, Charrin BC, Borrell-Pagès M, et al. Huntingtin controls neurotrophic support and survival of neurons by enhancing BDNF vesicular transport along microtubules. *Cell*. 2004;118(1):127-138. doi:10.1016/j.cell.2004.06.018

66. Elias S, Thion MS, Yu H, et al. Huntingtin regulates mammary stem cell division and differentiation. *Stem Cell Reports*. 2014;2(4):491-506. doi:10.1016/j.stemcr.2014.02.011

67. Haremaki T, Deglincerti A, Brivanlou AH. Huntingtin is required for ciliogenesis and neurogenesis during early Xenopus development. *Dev Biol*. 2015;408(2):305-315. doi:10.1016/j.ydbio.2015.07.013

68. Caviston JP, Ross JL, Antony SM, Tokito M, Holzbaur ELF. Huntingtin facilitates dynein/dynactin-mediated vesicle transport. *Proc Natl Acad Sci U S A*. 2007;104(24):10045-10050. doi:10.1073/pnas.0610628104

69. Mackenzie KD, Lim Y, Duffield MD, Chataway T, Zhou XF, Keating DJ. Huntingtin-associated protein-1 (HAP1) regulates endocytosis and interacts with multiple trafficking-related proteins. *Cell Signal*. 2017;35:176-187. doi:10.1016/j.cellsig.2017.02.023

70. Caviston JP, Zajac AL, Tokito M, Holzbaur ELF. Huntingtin coordinates the dynein-mediated dynamic positioning of endosomes and lysosomes. *Mol Biol Cell*. 2011;22(4):478-492. doi:10.1091/mbc.E10-03-0233

71. Wong YC, Holzbaur ELF. The Regulation of Autophagosome Dynamics by Huntingtin and HAP1 Is Disrupted by Expression of Mutant Huntingtin, Leading to Defective Cargo Degradation. *J Neurosci*. 2014;34(4):1293-1305. doi:10.1523/JNEUROSCI.1870-13.2014

72. Zala D, Hinckelmann MV, Saudou F. Huntingtin's Function in Axonal Transport Is Conserved in Drosophila melanogaster. *PLoS One*. 2013;8(3):e60162. doi:10.1371/journal.pone.0060162

73. Baquet ZC. Early Striatal Dendrite Deficits followed by Neuron Loss with Advanced Age in the Absence of Anterograde Cortical Brain-Derived Neurotrophic Factor. *J Neurosci*. 2004;24(17):4250-4258. doi:10.1523/JNEUROSCI.3920-03.2004

74. Godin JD, Colombo K, Molina-Calavita M, et al. Huntingtin Is Required for Mitotic Spindle Orientation and Mammalian Neurogenesis. *Neuron*. 2010;67(3):392-406. doi:10.1016/j.neuron.2010.06.027

75. Karam A, Tebbe L, Weber C, et al. A novel function of Huntingtin in the cilium and retinal ciliopathy in Huntington's disease mice. *Neurobiol Dis*. 2015;80:15-28. doi:10.1016/j.nbd.2015.05.008

76. Keryer G, Pineda JR, Liot G, et al. Ciliogenesis is regulated by a huntingtin-HAP1-PCM1 pathway and is altered in Huntington disease. *J Clin Invest*. 2011;121(11):4372-4382. doi:10.1172/JCI57552

77. Marcora E, Gowan K, Lee JE. Stimulation of NeuroD activity by huntingtin and huntingtin-associated proteins HAP1 and MLK2. *Proc Natl Acad Sci U S A*. 2003;100(16):9578-9583. doi:10.1073/pnas.1133382100

78. Takano H, Gusella JF. The predominantly HEAT-like motif structure of huntingtin and its association and coincident nuclear entry with dorsal, an NF-kB/Rel/dorsal family transcription factor. *BMC Neurosci*. 2002;3:15. doi:10.1186/1471-2202-3-15

79. Steffan JS, Kazantsev A, Spasic-Boskovic O, et al. The Huntington's disease protein interacts with p53 and CREB-binding protein and represses transcription. *Proc Natl Acad Sci U S A*. 2000;97(12):6763-6768. doi:10.1073/pnas.100110097

80. Zuccato C, Tartari M, Crotti A, et al. Huntingtin interacts with REST/NRSF to modulate the transcription of NRSE-controlled neuronal genes. *Nat Genet*. 2003;35(1):76-83.

doi:10.1038/ng1219

81. DiFiglia M, Sapp E, Chase KO, et al. Aggregation of Huntingtin in Neuronal Intranuclear Inclusions and Dystrophic Neurites in Brain. *Science (80-)*. 1997;277(5334):1990-1993. doi:10.1126/science.277.5334.1990

82. Sieradzan KA, Mechan AO, Jones L, Wanker EE, Nukina N, Mann DMA. Huntington's disease intranuclear inclusions contain truncated, ubiquitinated huntingtin protein. *Exp Neurol*. 1999;156(1):92-99. doi:10.1006/exnr.1998.7005

83. Wellington CL, Singaraja R, Ellerby L, et al. Inhibiting caspase cleavage of huntingtin reduces toxicity and aggregate formation in neuronal and nonneuronal cells. *J Biol Chem*. 2000;275(26):19831-19838. doi:10.1074/jbc.M001475200

84. Lunkes A, Lindenberg KS, Ben-Haem L, et al. Proteases acting on mutant huntingtin generate cleaved products that differentially build up cytoplasmic and nuclear inclusions. *Mol Cell*. 2002;10(2):259-269. doi:10.1016/S1097-2765(02)00602-0

85. Wellington CL, Ellerby LM, Gutekunst C-A, et al. Caspase cleavage of mutant huntingtin precedes neurodegeneration in Huntington's disease. *J Neurosci*. 2002;22(18):7862-7872. doi:10.1038/35096019

86. Iuchi S, Hoffner G, Verbeke P, Djian P, Green H. Oligomeric and polymeric aggregates formed by proteins containing expanded polyglutamine. *Proc Natl Acad Sci U S A*. 2003;100(5):2409-2414. doi:10.1073/pnas.0437660100

87. Zhou H, Cao F, Wang Z, et al. Huntingtin forms toxic NH2-terminal fragment complexes that are promoted by the age-dependent decrease in proteasome activity. *J Cell Biol*. 2003;163(1):109-118. doi:10.1083/jcb.200306038

88. Kim YJ, Yi Y, Sapp E, et al. Caspase 3-cleaved N-terminal fragments of wild-type and mutant huntingtin are present in normal and Huntington's disease brains, associate with membranes, and undergo calpaindependent proteolysis. *Proc Natl Acad Sci U S A*. 2001;98(22):12784-12789. doi:10.1073/pnas.221451398

89. Becher MW, Kotzuk JA, Sharp AH, et al. Intranuclear neuronal inclusions in Huntington's disease and dentatorubral and pallidoluysian atrophy: Correlation between the density of inclusions and IT15 CAG triplet repeat length. *Neurobiol Dis*. 1998;4(6):387-397. doi:10.1006/nbdi.1998.0168

90. Schilling G, Klevytska A, Tebbenkamp ATN, et al. Characterization of huntingtin pathologic fragments in Human Huntington disease, transgenic mice, and cell models. *J Neuropathol Exp Neurol*. 2007;66(4):313-320. doi:10.1097/nen.0b013e318040b2c8

91. Gourfinkel-An I, Cancel G, Duyckaerts C, et al. Neuronal distribution of intranuclear inclusions in huntington's disease with adult onset. *Neuroreport*. 1998;9(8):1823-1826. doi:10.1097/00001756-199806010-00028

92. Maat-Schieman M, Roos R, Losekoot M, et al. Neuronal intranuclear and neuropil inclusions for pathological assessment of Huntington's disease. *Brain Pathol*. 2007;17(1):31-37. doi:10.1111/j.1750-3639.2006.00040.x

93. Herndon ES, Hladik CL, Qihc HTA, Shang P. Neuroanatomical Profile of Polyglutamine Immunoreactivity in Huntington Disease Brains. *J Neuropathol Exp Neurol*. 2009;68(3):250-261. doi:10.1097/NEN.0b013e318198d320.Neuroanatomical

94. Gutekunst C a, Li SH, Yi H, et al. Nuclear and neuropil aggregates in Huntington's disease: relationship to neuropathology. *J Neurosci*. 1999;19(7):2522-2534. doi:10.1523/jneurosci.5389-07.2008

95. Van Roon-Mom WMC, Hogg VM, Tippett LJ, Faull RLM. Aggregate distribution in frontal and motor cortex in Huntington's disease brain. *Neuroreport*. 2006;17(6):667-670. doi:10.1097/00001756-200604240-00022

96. Sathasivam K, Neueder A, Gipson TA, et al. Aberrant splicing of HTT generates the pathogenic exon 1 protein in Huntington disease. *Proc Natl Acad Sci*. 2013;110(6):2366-2370. doi:10.1073/pnas.1221891110

97. Mende-Mueller LM, Toneff T, Hwang SR, Chesselet MF, Hook VYH. Tissue-specific proteolysis of huntingtin (htt) in human brain: Evidence of enhanced levels of N- and C-terminal htt fragments in Huntington's disease striatum. *J Neurosci*. 2001;21(6):1830-1837. doi:10.1523/jneurosci.21-06-01830.2001

98. Sapp E, Valencia A, Li X, et al. Native mutant huntingtin in human brain: Evidence for prevalence of full-length monomer. *J Biol Chem*. 2012;287(16):13487-13499. doi:10.1074/jbc.M111.286609

99. Schut MH, Patassini S, Kim EH, et al. Effect of post-mortem delay on N-terminal huntingtin protein fragments in human control and Huntington disease brain lysates. *PLoS One*. 2017;12(6):1-13. doi:10.1371/journal.pone.0178556

100. Toneff T, Mende-Mueller L, Wu Y, et al. Comparison of huntingtin proteolytic fragments in human lymphoblast cell lines and human brain. *J Neurochem*. 2002;82(1):84-92. doi:10.1046/j.1471-4159.2002.00940.x

101. Sun B, Fan W, Balciunas A, et al. Polyglutamine repeat length-dependent proteolysis of huntingtin. *Neurobiol Dis*. 2002;11(1):111-122. doi:10.1006/nbdi.2002.0539

102. Davies SW, Turmaine M, Cozens BA, et al. Formation of Neuronal Intranuclear Inclusions Underlies the Neurological Dysfunction in Mice Transgenic for the HD Mutation. *Cell*. 1997;90(3):537-548. doi:10.1016/s0092-8674(00)80513-9. PMID: 9267033.

103. Hackam AS, Singaraja R, Wellington CL, et al. The influence of huntingtin protein size on nuclear localization and cellular toxicity. *J Cell Biol*. 1998;141(5):1097-1105. doi:10.1083/jcb.141.5.1097

104. Landles C, Sathasivam K, Weiss A, et al. Proteolysis of mutant huntingtin produces an exon 1 fragment that accumulates as an aggregated protein in neuronal nuclei in huntington disease. *J Biol Chem*. 2010;285(12):8808-8823. doi:10.1074/jbc.M109.075028

105. Crook ZR, Housman D. Huntington's Disease: Can Mice Lead the Way to Treatment? *Neuron*. 2011;69(3):423-435. doi:10.1016/j.neuron.2010.12.035

106. Roby EW, Ratovitski T, Wang X, Watkin E. Transgenic Mouse Model Expressing the Caspase 6 Fragment of Mutant Huntingtin. *J Neurosci*. 2012;32(1):183-193. doi:10.1523/JNEUROSCI.1305-11.2012.Transgenic

107. O'Brien R, DeGiacomo F, Holcomb J, et al. Integration-independent transgenic huntington disease fragment mouse models reveal distinct phenotypes and life span in vivo. *J Biol Chem*. 2015;290(31):19287-19306. doi:10.1074/jbc.M114.623561

108. Rechsteiner M, Rogers SW. PEST sequences and regulation by proteolysis. *Trends Biochem Sci*. 1996;21(7):267-271. doi:10.1016/0968-0004(96)10031-1

109. Graham RK, Deng Y, Slow EJ, et al. Cleavage at the Caspase-6 Site Is Required for Neuronal Dysfunction and Degeneration Due to Mutant Huntingtin. *Cell*. 2006;125(6):1179-1191. doi:10.1016/j.cell.2006.04.026

110. Neueder A, Landles C, Ghosh R, et al. The pathogenic exon 1 HTT protein is produced by incomplete splicing in Huntington's disease patients. *Sci Rep*. 2017;7(1):1307. doi:10.1038/s41598-017-01510-z

111. Bañez-Coronel M, Ayhan F, Tarabochia AD, et al. RAN Translation in Huntington Disease. *Neuron*. 2015;88(4):667-677. doi:10.1016/j.neuron.2015.10.038

112. Vonsattel JPG, Keller C, Amaya MDP. Neuropathology of Huntington's disease. In: *Handbook of Clinical Neurology*. Vol 89. ; 2008:599-618. doi:10.1007/7854_2014_354

113. Legleiter J, Mitchell E, Lotz GP, et al. Mutant huntingtin fragments form oligomers in a polyglutamine length-dependent manner in Vitro and in Vivo. *J Biol Chem*. 2010;285(19):14777-14790. doi:10.1074/jbc.M109.093708

114. Hoffner G, Djian P. Polyglutamine Aggregation in Huntington Disease: Does Structure Determine Toxicity? *Mol Neurobiol*. 2014;52(3):1297-1314. doi:10.1007/s12035-014-8932-1

115. Slow EJ, van Raamsdonk J, Rogers D, et al. Selective striatal neuronal loss in a YAC128 mouse model of Huntington disease. *Hum Mol Genet*. 2003;12(13):1555-1567. doi:10.1093/hmg/ddg169

116. Slow EJ, Graham RK, Osmand AP, et al. Absence of behavioral abnormalities and neurodegeneration in vivo despite widespread neuronal huntingtin inclusions. *Proc Natl Acad Sci U S A*. 2005;102(32):11402-11407. doi:10.1073/pnas.0503634102

117. Arrasate M, Mitra S, Schweitzer ES, Segal MR, Finkbeiner S. Inclusion body formation reduces levels of mutant huntingtin and the risk of neuronal death. *Nature*. 2004;431(7010):805-810. doi:10.1038/nature02998

118. Li H, Li SH, Johnston H, Shelbourne PF, Li XJ. Amino-terminal fragments of mutant huntingtin show selective accumulation in striatal neurons and synaptic toxicity. *Nat Genet*. 2000;25(4):385-389. doi:10.1038/78054

119. Martindale D, Hackam A, Wieczorek A, et al. Length of huntingtin and its polyglutamine tract influences localization and frequency of intracellular aggregates. *Nat Genet*. 1998;18(2):150-154. doi:10.1038/ng0598-51

120. Tagawa K, Hoshino M, Okuda T, et al. Distinct aggregation and cell death patterns among different types of primary neurons induced by mutant huntingtin protein. *J Neurochem*. 2004;89(4):974-987. doi:10.1111/j.1471-4159.2004.02372.x

121. Qin Z-H, Gu Z-L. Huntingtin processing in pathogenesis of Huntington disease. *Acta Pharmacol Sin*. 2004;25(10):1243-1249.

122. Chánez-Cárdenas ME, Vázquez-Contreras E. The aggregation of huntingtin and α-synuclein. *J Biophys*. 2012;2012. doi:10.1155/2012/606172

123. Ciammola A, Sassone J, Alberti L, et al. Increased apoptosis, huntingtin inclusions and altered differentiation in muscle cell cultures from Huntington's disease subjects. *Cell Death Differ*. 2006;13(12):2068-2078. doi:10.1038/sj.cdd.4401967

124. Denis HL, Lamontagne-Proulx J, St-Amour I, et al. Platelet abnormalities in Huntington's disease. *J Neurol Neurosurg Psychiatry*. 2019;90(3):272-283. doi:10.1136/jnnp-2018-318854

125. Sathasivam K, Hobbs C, Turmaine M, et al. Formation of polyglutamine inclusions in non-CNS tissue. *Hum Mol Genet*. 1999;8(5):813-822. doi:10.1093/hmg/8.5.813

126. Tanaka M, Machida Y, Niu S, et al. Trehalose alleviates polyglutamine-mediated

pathology in a mouse model of Huntington disease. *Nat Med*. 2004;10(2):148-154. doi:10.1038/nm985

127. Orth M, Cooper JM, Bates GP, Schapira AHV. Inclusion formation in Huntington's disease R6/2 mouse muscle cultures. *J Neurochem*. 2003;87(1):1-6. doi:10.1046/j.1471-4159.2003.02009.x

128. Arrasate M, Finkbeiner S. Protein aggregates in Huntington's disease. *Exp Neurol*. 2012;238(1):1-11. doi:10.1016/j.expneurol.2011.12.013

129. Franich NR, Hickey MA, Zhu C, et al. Phenotype onset in Huntington's disease knock-in mice is correlated with the incomplete splicing of the mutant huntingtin gene. *J Neurosci Res*. 2019;97(12):1590-1605. doi:10.1002/jnr.24493

130. Mangiarini L, Sathasivam K, Seller M, et al. Exon 1 of the HD gene with an expanded CAG repeat is sufficient to cause a progressive neurological phenotype in transgenic mice. *Cell*. 1996;87(3):493-506. doi:10.1016/S0092-8674(00)81369-0

131. Barbaro BA, Lukacsovich T, Agrawal N, et al. Comparative study of naturally occurring Huntingtin fragments in Drosophila points to exon 1 as the most pathogenic species in Huntington's disease. *Hum Mol Genet*. 2015;24(4):913-925. doi:10.1093/hmg/ddu504

132. Scherzinger E, Sittler A, Schweiger K, et al. Self-assembly of polyglutamine-containing huntingtin fragments into amyloid-like fibrils: Implications for Huntington's disease pathology. *Proc Natl Acad Sci U S A*. 1999;96(8):4604-4609. doi:10.1073/pnas.96.8.4604

133. Scherzinger E, Lurz R, Turmaine M, et al. Huntingtin-Encoded Polyglutamine Expansions Form Amyloid-like Protein Aggregates In Vitro and In Vivo. *Cell*. 1997;90(3):549-558. doi:10.1016/s0092-8674(00)80514-0. PMID: 9267034.

134. Hollenbach B, Scherzinger E, Schweiger K, Lurz R, Lehrach H, Wanker EE. Aggregation of truncated GST-HD exon 1 fusion proteins containing normal range and expanded glutamine repeats. *Philos Trans R Soc L B Biol Sci*. 1999;354(1386):991-994. doi:10.1098/rstb.1999.0450

135. Ansaloni A, Wang ZM, Jeong JS, Ruggeri FS, Dietler G, Lashuel HA. One-pot semisynthesis of exon 1 of the Huntingtin protein: New tools for elucidating the role of posttranslational modifications in the pathogenesis of Huntington's disease. *Angew Chem Int Ed Engl*. 2014;53(29):1928-1933. doi:10.1002/anie.201307510

136. Vieweg S, Mahul-Mellier A-L, Ruggeri FS, et al. The Nt17 domain and its helical conformation regulate the aggregation, cellular properties and neurotoxicity of mutant huntingtin exon 1. *J Mol Biol*. 2021;433(21):167222. doi:10.1016/j.jmb.2021.167222

137. Steffan JS, Agrawal N, Pallos J, et al. SUMO modification of Huntingtin and Huntington's disease pathology. *Science (80-)*. 2004;304(5667):100-104. doi:10.1126/science.1092194

138. Rockabrand E, Slepko N, Pantalone A, et al. The first 17 amino acids of Huntingtin modulate its sub-cellular localization, aggregation and effects on calcium homeostasis. *Hum Mol Genet*. 2007;16(1):61-77. doi:10.1093/hmg/ddl440

139. Tam S, Spiess C, Auyeung W, et al. The chaperonin TRiC blocks a huntingtin sequence element that promotes the conformational switch to aggregation. *Nat Struct Mol Biol*. 2009;16(12):1279-1285. doi:10.1038/nsmb.1700

140. Thakur AK, Jayaraman M, Mishra R, et al. Polyglutamine disruption of the huntingtin exon1 N-terminus triggers a complex aggregation mechanism. *Nat Struct Mol Biol*. 2009;16(4):380-389. doi:10.1038/nsmb.1570.Polyglutamine

141. Thompson LM, Aiken CT, Kaltenbach LS, et al. IKK phosphorylates Huntingtin and targets it for degradation by the proteasome and lysosome. *J Cell Biol*. 2009;187(7):1083-1099. doi:10.1083/jcb.200909067

142. Gu X, Greiner ER, Mishra R, et al. Serines 13 and 16 Are Critical Determinants of Full-length Human Mutant Huntingtin-Induced Disease Pathogenesis in HD Mice. *Neuron*. 2009;64(6):828-840. doi:10.1016/j.neuron.2009.11.020.Serines

143. Zheng Z, Li A, Holmes BB, Marasa JC, Diamond MI. An N-terminal nuclear export signal regulates trafficking and aggregation of huntingtin (Htt) protein exon 1. *J Biol Chem*. 2013;288(9):6063-6071. doi:10.1074/jbc.M112.413575

144. Ross CA, Poirier MA. What is the role of protein aggregation in neurodegeneration? *Nat Rev Mol Cell Biol*. 2005;6(11):891-898. doi:10.1038/nrm1742

145. Arndt JR, Chaibva M, Legleiter J. The emerging role of the first 17 amino acids of huntingtin in Huntington's disease. *Biomol Concepts*. 2015;6(1):33-46. doi:10.1002/aur.1474.Replication

146. Aiken CT, Steffan JS, Guerrero CM, et al. Phosphorylation of threonine 3: Implications for huntingtin aggregation and neurotoxicity. *J Biol Chem*. 2009;284(43):29427-29436. doi:10.1074/jbc.M109.013193

147. Atwal RS, Xia J, Pinchev D, Taylor J, Epand RM, Truant R. Huntingtin has a membrane association signal that can modulate huntingtin aggregation, nuclear entry and toxicity. *Hum Mol Genet*. 2007;16(21):2600-2615. doi:10.1093/hmg/ddm217

148. Williamson TE, Vitalis A, Crick SL, Pappu R V. Modulation of Polyglutamine Conformations and Dimer Formation by the N-Terminus of Huntingtin. *J Mol Biol*. 2010;396(5):1295-1309. doi:10.1016/j.jmb.2009.12.017

149. Shen K, Calamini B, Fauerbach JA, et al. Control of the structural landscape and neuronal proteotoxicity of mutant Huntingtin by domains flanking the polyQ tract. *Elife*. 2016;5:e18065. doi:10.7554/eLife.18065

150. Monsellier E, Redeker V, Ruiz-Arlandis G, Bousset L, Melki R. Molecular interaction between the chaperone Hsc70 and the N-terminal flank of huntingtin exon 1 modulates aggregation. *J Biol Chem*. 2015;290(5):2560-2576. doi:10.1074/jbc.M114.603332

151. Gu X, Cantle JP, Greiner ER, et al. N17 Modifies Mutant Huntingtin Nuclear Pathogenesis and Severity of Disease in HD BAC Transgenic Mice. *Neuron*. 2015;85(4):726-741. doi:10.1016/j.neuron.2015.01.008

152. Watkin EE, Arbez N, Waldron-Roby E, et al. Phosphorylation of mutant huntingtin at serine 116 modulates neuronal toxicity. *PLoS One*. 2014;9(2):39-45. doi:10.1371/journal.pone.0088284

153. Bustamante MB, Ansaloni A, Pedersen JF, et al. Detection of huntingtin exon 1 phosphorylation by Phos-Tag SDS-PAGE: Predominant phosphorylation on threonine 3 and regulation by IKKβ. *Biochem Biophys Res Commun*. 2015;463(4):1317-1322. doi:10.1016/j.bbrc.2015.06.116

154. Cariulo C, Azzollini L, Verani M, et al. Phosphorylation of huntingtin at residue T3 is decreased in Huntington's disease and modulates mutant huntingtin protein conformation. *Proc Natl Acad Sci*. 2017;114(50):E10809-E10818. doi:10.1073/pnas.1705372114

155. Jeong H, Then F, Melia TJ, et al. Acetylation Targets Mutant Huntingtin to Autophagosomes for Degradation. *Cell*. 2009;137(1):60-72. doi:10.1016/j.cell.2009.03.018

156. Chiki A, DeGuire SM, Ruggeri FS, et al. Mutant Exon1 Huntingtin Aggregation is Regulated by T3 Phosphorylation-Induced Structural Changes and Crosstalk between T3 Phosphorylation and Acetylation at K6. *Angew Chemie Int Ed*. 2017;56(19):5202-5207. doi:10.1002/anie.201611750

157. Morozko EL, Smith-Geater C, Monteys AM, et al. PIAS1 modulates striatal transcription, DNA damage repair, and SUMOylation with relevance to Huntington's disease. *Proc Natl Acad Sci U S A*. 2021;118(4):e2021836118. doi:10.1073/pnas.2112001118

158. Ehrnhoefer DE, Sutton L, Hayden MR. Small changes, big impact: Posttranslational modifications and function of huntingtin in Huntington disease Dagmar. *Neuroscientist*. 2011;17(5):475-492. doi:10.1177/1073858410390378.Small

159. Chiki A, Zhang Z, Rajasekhar K, et al. Investigating crosstalk among PTMs provides novel insight into the structural basis underlying the differential effects of Nt17 PTMs on mutant Httex1 aggregation. *Front Mol Biosci*. 2021;8:694. doi:10.3389/fmolb.2021.686086

160. Hegde RN, Chiki A, Petricca L, et al. TBK1 phosphorylates mutant Huntingtin and suppresses its aggregation and toxicity in Huntington's disease models. *EMBO J*. 2020;39(17):e104671. doi:10.15252/embj.2020104671

161. Falk AS, Bravo-Arredondo JM, Varkey J, Pacheco S, Langen R, Siemer AB. Structural Model of the Proline-Rich Domain of Huntingtin Exon-1 Fibrils. *Biophys J*. 2020;119(10):2019-2028. doi:10.1016/j.bpj.2020.10.010

162. Kim MW, Chelliah Y, Kim SW, Otwinowski Z, Bezprozvanny I. Secondary Structure of Huntingtin Amino-Terminal Region. *Structure*. 2009;17(9):1205-1212. doi:10.1016/j.str.2009.08.002

163. Lakhani V V., Ding F, Dokholyan N V. Polyglutamine induced misfolding of Huntingtin Exon1 is modulated by the flanking sequences. *PLoS Comput Biol*. 2010;6(4):e1000772. doi:10.1371/journal.pcbi.1000772

164. Gao YG, Yan XZ, Song AX, et al. Structural Insights into the Specific Binding of Huntingtin Proline-Rich Region with the SH3 and WW Domains. *Structure*. 2006;14(12):1755-1765. doi:10.1016/j.str.2006.09.014

165. Qin Z, Wang Y, Sapp E, et al. Huntingtin Bodies Sequester Vesicle-Associated Proteins by a Polyproline-Dependent Interaction. *J Neurosci*. 2004;24(1):269-281. doi:10.1523/JNEUROSCI.1409-03.2004

166. Chen S, Berthelier V, Hamilton JB, O'Nuallain B, Wetzel R. Amyloid-like features of polyglutamine aggregates and their assembly kinetics. *Biochemistry*. 2002;41(23):7391-7399. doi:10.1021/bi011772q

167. Poirier MA, Li H, Macosko J, Cai S, Amzel M, Ross CA. Huntingtin spheroids and protofibrils as precursors in polyglutamine fibrilization. *J Biol Chem*. 2002;277(43):41032-41037. doi:10.1074/jbc.M205809200

168. Sivanandam VN, Jayaraman M, Hoop CL, Kodali R, Wetzel R, Van Der Wel PCA. The aggregation-enhancing huntingtin N-terminus is helical in amyloid fibrils. *J Am Chem Soc*. 2011;133(12):4558-4566. doi:10.1021/ja110715f

169. Thakur AK, Jayaraman M, Mishra R, et al. Polyglutamine disruption of the huntingtin exon 1 N terminus triggers a complex aggregation mechanism. *Nat Struct Mol Biol*. 2009;16(4):380-389. doi:10.1038/nsmb.1570

170. Tycko R. Amyloid Polymorphism: Structural Basis and Neurobiological Relevance. *Neuron*. 2015;86(3):632-645. doi:10.1016/j.neuron.2015.03.017

171. André W, Sandt C, Dumas P, Djian P, Hoffner G. Structure of inclusions of huntington's disease brain revealed by synchrotron infrared microspectroscopy: Polymorphism and relevance to cytotoxicity. *Anal Chem*. 2013;85(7):3765-3773. doi:10.1021/ac400038b

172. Boatz JC, Piretra T, Lasorsa A, Matlahov I, Conway JF, van der Wel PCA. Protofilament Structure and Supramolecular Polymorphism of Aggregated Mutant Huntingtin Exon 1. *J Mol Biol*. 2020;432(16):4722-4744. doi:10.1016/j.jmb.2020.06.021

173. Isas JM, Langen R, Siemer AB. Solid-State Nuclear Magnetic Resonance on the Static and Dynamic Domains of Huntingtin Exon-1 Fibrils. *Biochemistry*. 2015;54(25):3942-3949. doi:10.1021/acs.biochem.5b00281

174. Nazarov S, Chiki A, Boudeffa D, Lashuel HA. The structural basis of huntingtin (Htt) fibril polymorphism, revealed by cryo-EM of exon 1 Htt fibrils. *bioRxiv*. 2021.

175. Kolla R, Gopinath P, Ricci J, Reif A, Rostami I, Lashuel HA. A New Chemoenzymatic Semisynthetic Approach Provides Insight into the Role of Phosphorylation beyond Exon1 of Huntingtin and Reveals N-Terminal Fragment Length-Dependent Distinct Mechanisms of Aggregation. *J Am Chem Soc*. 2021;143(26):9798-9812. doi:10.1021/jacs.1c03108

176. Shimomura O, Johnson FH, Saiga Y. Extraction, purification and properties of aequorin, a bioluminescent protein from the Luminous Hydromedusan, Aequorea. *J Cell Comp Physiol*. 1962;59:223-239. doi:10.1002/jcp.1030590302

177. Prasher DC, Eckenrode VK, Ward WW, Prendergast FG, Cormier MJ. Primary structure of the Aequorea victoria green-fluorescent protein. *Gene*. 1992;111(2):229-233. doi:10.1016/0378-1119(92)90691-H

178. Chalfie M, Tu Y, Euskirchen G, Ward William W, Prasher Douglas C. Green fluorescent protein as a marker for gene expression. *Science (80-)*. 1994;263(5148):802-805.

179. Yang F, Moss LG, Phillips GN. The Molecular Structure of Green Fluorescent Protein. *Nat Biotechnol*. 1996;14(10):1246-1251. doi:doi: 10.1038/nbt1096-1246. PMID: 9631087.

180. Stauber RH, Horie K, Carney P, et al. Development and applications of enhanced green fluorescent protein mutants. *Biotechniques*. 1998;24(3):462-471. doi:10.2144/98243rr01

181. Arpino JAJ, Rizkallah PJ, Jones DD. Crystal Structure of Enhanced Green Fluorescent Protein to 1.35 Å Resolution Reveals Alternative Conformations for Glu222. *PLoS One*. 2012;7(10):e47132. doi:10.1371/journal.pone.0047132

182. Brazelton TR, Blau HM. Optimizing Techniques for Tracking Transplanted Stem Cells In Vivo. *Stem Cells*. 2005;23(9):1251-1265. doi:10.1634/stemcells.2005-0149

183. Swenson ES, Price JG, Brazelton T, Krause DS. Limitations of Green Fluorescent Protein as a Cell Lineage Marker. *Stem Cells*. 2007;25(10):2593-2600. doi:10.1634/stemcells.2007-0241

184. Wiedenmann J, Oswald F, Nienhaus GU. Fluorescent proteins for live cell imaging: Opportunities, limitations, and challenges. *IUBMB Life*. 2009;61(11):1029-1042. doi:10.1002/iub.256

185. Tao W, Evans B-G, Yao J, et al. Enhanced Green Fluorescent Protein Is a Nearly Ideal Long-Term Expression Tracer for Hematopoietic Stem Cells, Whereas DsRed-Express Fluorescent Protein Is Not. *Stem Cells*. 2007;25(3):670-678. doi:10.1634/stemcells.2006-0553

186. Huang WY, Aramburu J, Douglas PS, Izumo S. Transgenic expression of green fluorescence protein can cause dilated cardiomyopathy. *Nat Med*. 2000;6(5):482-483. doi:10.1038/74914

187. Liu HS, Jan MS, Chou CK, Chen PH, Ke NJ. Is green fluorescent protein toxic to the living cells? *Biochem Biophys Res Commun*. 1999;260(3):712-717. doi:10.1006/bbrc.1999.0954

188. Baens M, Noels H, Broeckx V, et al. The dark side of EGFP: Defective polyubiquitination. *PLoS One*. 2006;1(1):e54. doi:10.1371/journal.pone.0000054

189. Masino L, Kelly G, Leonard K, Trottier Y, Pastore A. Solution structure of polyglutamine tracts in GST-polyglutamine fusion proteins. *FEBS Lett*. 2002;513(2-3):267-272. doi:10.1016/S0014-5793(02)02335-9

190. Bulone D, Masino L, Thomas DJ, San Biagio PL, Pastore A. The interplay between polyQ and protein context delays aggregation by forming a reservoir of protofibrils. *PLoS One*. 2006;1(1):e111. doi:10.1371/journal.pone.0000111

191. Atwal RS, Desmond CR, Caron N, et al. Kinase inhibitors modulate huntingtin cell localization and toxicity. *Nat Chem Biol*. 2011;7(7):453-460. doi:10.1038/nchembio.582

192. Dahlgren PR, Karymov MA, Bankston J, et al. Atomic force microscopy analysis of the Huntington protein nanofibril formation. *Nanomedicine Nanotechnology, Biol Med*. 2005;1(1):52-57. doi:10.1016/j.nano.2004.11.004

193. Vieweg S, Ansaloni A, Wang ZM, Warner JB, Lashuel HA. An intein-based strategy for the production of tag-free huntingtin exon 1 proteins enables new insights into the polyglutamine dependence of Httex1 aggregation and fibril formation. *J Biol Chem*. 2016;291(23):12074-12086. doi:10.1074/jbc.M116.713982

194. Riguet N, Mahul-Mellier A-L, Maharjan N, et al. Nuclear and cytoplasmic huntingtin inclusions exhibit distinct biochemical composition, interactome and ultrastructural properties. *bioRxiv*. 2021.

195. Bäuerlein FJB, Saha I, Mishra A, et al. In Situ Architecture and Cellular Interactions of PolyQ Inclusions. *Cell*. 2017;171(1):179-187.e10. doi:10.1016/j.cell.2017.08.009

196. McLean PJ, Kawamata H, Hyman BT. α-Synuclein-enhanced green fluorescent protein fusion proteins form proteasome sensitive inclusions in primary neurons. *Neuroscience*. 2001;104(3):901-912. doi:10.1016/S0306-4522(01)00113-0

197. Kothawala A, Kilpatrick K, Novoa JA, Segatori L. Quantitative Analysis of a-Synuclein Solubility in Living Cells Using Split GFP Complementation. *PLoS One*. 2012;7(8):e43505. doi:10.1371/journal.pone.0043505

198. Schwach G, Tschemmernegg M, Pfragner R, Ingolic E, Schreiner E, Windisch M. Establishment of stably transfected rat neuronal cell lines expressing α-synuclein GFP fusion proteins. *J Mol Neurosci*. 2010;41(1):80-88. doi:10.1007/s12031-009-9289-1

199. Outeiro TF, Putcha P, Tetzlaff JE, et al. Formation of toxic oligomeric α-synuclein species in living cells. *PLoS One*. 2008;3(4):e1867. doi:10.1371/journal.pone.0001867

200. Cabantous S, Terwilliger TC, Waldo GS. Protein tagging and detection with engineered self-assembling fragments of green fluorescent protein. *Nat Biotechnol*. 2005;23(1):102-107. doi:10.1038/nbt1044

201. Hansen C, Björklund T, Petit GH, et al. A novel α-synuclein-GFP mouse model displays progressive motor impairment, olfactory dysfunction and accumulation of α-synuclein-GFP. *Neurobiol Dis*. 2013;56:145-155. doi:10.1016/j.nbd.2013.04.017

202. Unni VK, Weissman TA, Rockenstein E, Masliah E, McLean PJ, Hyman BT. In vivo imaging of α-synuclein in mouse cortex demonstrates stable expression and differential subcellular compartment mobility. *PLoS One*. 2010;5(5):e10589. doi:10.1371/journal.pone.0010589

203. Elabi O, Gaceb A, Carlsson R, et al. Human α-synuclein overexpression in a mouse model of Parkinson's disease leads to vascular pathology, blood brain barrier leakage and pericyte activation. *Sci Rep*. 2021;11(1):1120. doi:10.1038/s41598-020-80889-8

204. Caputo A, Liang Y, Raabe TD, et al. Snca-gfp knock-in mice reflect patterns of endogenous expression and pathological seeding. *eNeuro*. 2020;7(4):ENEURO.0007-20.2020. doi:10.1523/ENEURO.0007-20.2020

205. Schaser AJ, Stackhouse TL, Weston LJ, et al. Trans-synaptic and retrograde axonal spread of Lewy pathology following pre-formed fibril injection in an in vivo A53T alpha-synuclein mouse model of synucleinopathy. *Acta Neuropathol Commun*. 2020;8(1):150. doi:10.1186/s40478-020-01026-0

206. Volpicelli-Daley LA, Luk KC, Lee VMY. Addition of exogenous α-synuclein preformed fibrils to primary neuronal cultures to seed recruitment of endogenous α-synuclein to Lewy body and Lewy neurite-like aggregates. *Nat Protoc*. 2014;9(9):2135-2146. doi:10.1038/nprot.2014.143

207. Afitska K, Fucikova A, Shvadchak V V., Yushchenko DA. Modification of C Terminus Provides New Insights into the Mechanism of α-Synuclein Aggregation. *Biophys J*. 2017;113(10):2182-2191. doi:10.1016/j.bpj.2017.08.027

208. Jarvela TS, Chaplot K, Lindberg I. A protease protection assay for the detection of internalized alpha-synuclein pre-formed fibrils. *PLoS One*. 2021;16(1):e0241161. doi:10.1371/journal.pone.0241161

209. Karpowicz RJ, Haney CM, Mihaila TS, Sandler RM, Petersson EJ, Lee VMY. Selective imaging of internalized proteopathic α-synuclein seeds in primary neurons reveals mechanistic insight into transmission of synucleinopathies. *J Biol Chem*. 2017;292(32):13482-13497. doi:10.1074/jbc.M117.780296

210. Trinkaus VA, Riera-Tur I, Martínez-Sánchez A, et al. In situ architecture of neuronal α-Synuclein inclusions. *Nat Commun*. 2021;12(1):2110. doi:10.1038/s41467-021-22108-0

211. Mahul-Mellier A-L, Burtscher J, Maharjan N, et al. The process of Lewy body formation, rather than simply α-synuclein fibrillization, is one of the major drivers of neurodegeneration. *Proc Natl Acad Sci U S A*. 2020;117(9):4971-4982. doi:10.1073/1913904117

212. Ochiishi T, Doi M, Yamasaki K, et al. Development of new fusion proteins for visualizing amyloid-β oligomers in vivo. *Sci Rep*. 2016;6:22712. doi:10.1038/srep22712

213. Waldo GS, Standish BM, Berendzen J, Terwilliger TC. Rapid protein-folding assay using green fluorescent protein. *Nat Biotechnol*. 1999;17(7):691-695. doi:10.1038/10904

214. Wurth C, Guimard NK, Hecht MH. Mutations that reduce aggregation of the alzheimer's Aβ42 peptide: An unbiased search for the sequence determinants of Aβ amyloidogenesis. *J Mol Biol*. 2002;319(5):1279-1290. doi:10.1016/S0022-2836(02)00399-6

215. Hussein RM, Hashem RM, Rashed LA. Evaluation of the amyloid beta-GFP fusion protein as a model of amyloid beta peptides-mediated aggregation: A study of DNAJB6 chaperone. *Front Mol Neurosci*. 2015;8:40. doi:10.3389/fnmol.2015.00040

216. Azizyan RA, Garro A, Radkova Z, et al. Establishment of Constraints on Amyloid Formation Imposed by Steric Exclusion of Globular Domains. *J Mol Biol*. 2018;430(20):3835-3846. doi:10.1016/j.jmb.2018.05.038

217. Kfoury N, Holmes BB, Jiang H, Holtzman DM, Diamond MI. Trans-cellular propagation of Tau aggregation by fibrillar species. *J Biol Chem*. 2012;287(23):19440-19451. doi:10.1074/jbc.M112.346072

218. Gorlovoy P, Larionov S, Pham TTH, Neumann H. Accumulation of tau induced in neurites by microglial proinflammatory mediators. *FASEB J*. 2009;23(8):2502-2513. doi:10.1096/fj.08-123877

219. Fitzpatrick AWP, Falcon B, He S, et al. Cryo-EM structures of tau filaments from Alzheimer's disease. *Nature*. 2017;547(7662):185-190. doi:10.1038/nature23002

220. Kaniyappan S, Tepper K, Biernat J, et al. FRET-based Tau seeding assay does not represent prion-like templated assembly of Tau filaments. *Mol Neurodegener*. 2020;15(1):39. doi:10.1186/s13024-020-00389-1

221. Shillcock JC, Hastings J, Riguet N, Lashuel H. Non-monotonic fibril surface occlusion by GFP tags from coarse-grained molecular simulations. *bioRxiv*. 2021.

222. DeGuire SM, Ruggeri FS, Fares MB, et al. N-terminal Huntingtin (Htt) phosphorylation is a molecular switch regulating Htt aggregation, helical conformation, internalization, and nuclear targeting. *J Biol Chem*. 2018;293(48):18540-18558. doi:10.1074/jbc.RA118.004621

223. Shahmoradian SH, Lewis AJ, Genoud C, et al. Lewy pathology in Parkinson's disease consists of crowded organelles and lipid membranes. *Nat Neurosci*. 2019;22(7):1099-1109. doi:10.1038/s41593-019-0423-2

224. Pouladi MA, Morton AJ, Hayden MR. Choosing an animal model for the study of Huntington's disease. *Nat Rev Neurosci*. 2013;14(10):708-721. doi:10.1038/nrn3570

225. Menalled LB, Chesselet M-F. Mouse models of Huntington's disease. *Trends Pharmacol Sci*. 2002;23(1):32-39. doi:10.1242/dmm.002451

226. Ehrnhoefer DE, Butland SL, Pouladi MA, Hayden MR. Mouse models of Huntington disease: variations on a theme. *Dis Model Mech*. 2009;2(3-4):123-129. doi:10.1242/dmm.002451

227. McGeer EG, McGeer PL. Duplication of biochemical changes of Huntington's chorea by intrastriatal injections of glutamic and kainic acids. *Nature*. 1976;263(5577):517-519. doi:https://doi.org/10.1038/263517a0

228. Schwarcz R, Foster AC, French ED, Whetsell WO, Köhler C. Excitotoxic models for neurodegenerative disorders. *Life Sci*. 1984;35(1):19-32. doi:10.1016/0024-3205(84)90148-6

229. Beal MF, Kowall NW, Ellison DW, Mazurek MF, Swartz KJ, JB M. Replication of the neurochemical characteristics of Huntington's disease by quinolinic acid. *Nature*. 1986;321(6066):168-171.

230. Coyle JT, Schwarcz R. Lesion of striatal neurons with kainic acid provides a model for Huntington's chorea. *Nature*. 1976;263(5574):244-246. doi:10.1038/263244a0

231. Beal MF, Ferrante RJ, Swartz KJ, Kowall NW. Chronic quinolinic acid lesions in rats closely resemble Huntington's disease. *J Neurosci*. 1991;11(6):1649-1659. doi:10.1523/jneurosci.11-06-01649.1991

232. Ferrante RJ, Kowall NW, Cipolloni PB, Storey E, Beal MF. Excitotoxin Lesions in Primates as a Model for Huntington's Disease: Histopathologic and Neurochemical Characterization. *Exp Neurol*. 1993;119(1):46-71. doi:10.1006/exnr.1993.1006

233. Brouillet E, Jenkins BG, Hyman BT, et al. Age-Dependent Vulnerability of the Striatum to the Mitochondrial Toxin 3-Nitropropionic Acid. *J Neurochem*. 1993;60(1):356-359. doi:10.1111/j.1471-4159.1993.tb05859.x

234. Beal MF, Brouillet E, Jenkins B, Henshaw R, Rosen B, Hyman BT. Age-Dependent Striatal Excitotoxic Lesions Produced by the Endogenous Mitochondrial Inhibitor Malonate. *J Neurochem*. 1993;61(3):1147-1150. doi:10.1111/j.1471-4159.1993.tb03633.x

235. Hodgson JG, Agopyan N, Gutekunst CA, et al. A YAC mouse model for Huntington's disease with full-length mutant huntingtin, cytoplasmic toxicity, and selective striatal neurodegeneration. *Neuron*. 1999;23(1):181-192. doi:10.1016/S0896-6273(00)80764-3

236. Gray M, Shirasaki DI, Cepeda C, et al. Full-Length Human Mutant Huntingtin with a Stable Polyglutamine Repeat Can Elicit Progressive and Selective Neuropathogenesis in BACHD Mice. *J Neurosci*. 2008;28(24):6182-6195. doi:10.1523/JNEUROSCI.0857-08.2008

237. Yu-Taeger L, Petrasch-Parwez E, Osmand AP, et al. A novel BACHD transgenic rat exhibits characteristic neuropathological features of Huntington disease. *J Neurosci*. 2012;32(44):15426-15438. doi:10.1523/JNEUROSCI.1148-12.2012

238. Hemachandra Reddy P, Williams M, Charles V, et al. Behavioural abnormalities and selective neuronal loss in HD transgenic mice expressing mutated full-length HD cDNA. *Nat Genet*. 1998;20(2):198-202. doi:10.1038/2510

239. Wheeler VC, Gutekunst CA, Vrbanac V, et al. Early phenotypes that presage late-onset neurodegenerative disease allow testing of modifiers in Hdh CAG knock-in mice. *Hum Mol Genet*. 2002;11(6):633-640. doi:10.1093/hmg/11.6.633

240. Menalled LB, Sison JD, Dragatsis I, Zeitlin S, Chesselet MF. Time course of early motor and neuropathological anomalies in a knock-in mouse model of Huntington's disease with 140 CAG repeats. *J Comp Neurol*. 2003;465(1):11-26. doi:10.1002/cne.10776

241. Lin CH, Tallaksen-Greene S, Chien WM, et al. Neurological abnormalities in a knock-in mouse model of Huntington's disease. *Hum Mol Genet*. 2001;10(2):137-144. doi:10.1093/hmg/10.2.137

242. Heng MY, Tallaksen-Greene SJ, Detloff PJ, Albin RL. Longitudinal evaluation of the Hdh(CAG)150 knock-in murine model of Huntington's disease. *J Neurosci*. 2007;27(34):8989-8998. doi:10.1523/JNEUROSCI.1830-07.2007

243. Southwell AL, Smith-Dijak A, Kay C, et al. An enhanced Q175 knock-in mouse model of Huntington disease with higher mutant huntingtin levels and accelerated disease phenotypes. *Hum Mol Genet*. 2016;25(17):3654-3675. doi:10.1093/hmg/ddw212

244. Faber PW, Alter JR, MacDonald ME, Hart AC. Polyglutamine-mediated dysfunction and apoptotic death of a Caenorhabditis elegans sensory neuron. *Proc Natl Acad Sci U S A*. 1999;96(1):179-184. doi:10.1073/pnas.96.1.179

245. Lee AL, Ung HM, Sands LP, Kikis EA. A new Caenorhabditis elegans model of human huntingtin 513 aggregation and toxicity in body wall muscles. *PLoS One*. 2017;12(3):1-19. doi:10.1371/journal.pone.0173644

246. Parker JA, Connolly JB, Wellington C, Hayden M, Dausset J, Neri C. Expanded polyglutamines in Caenorhabditis elegans cause axonal abnormalities and severe dysfunction of PLM mechanosensory neurons without cell death. *Proc Natl Acad Sci U S A*. 2001;98(23):13318-13323. doi:10.1073/pnas.231476398

247. Jackson GR, Salecker I, Dong X, et al. Polyglutamine-expanded human huntingtin transgenes induce degeneration of Drosophila photoreceptor neurons. *Neuron*. 1998;21(3):633-642. doi:10.1016/S0896-6273(00)80573-5

248. Babcock DT, Ganetzky B. Transcellular spreading of huntingtin aggregates in the *Drosophila* brain. *Proc Natl Acad Sci*. 2015;112(39):E5427-E5433. doi:10.1073/pnas.1516217112

249. Krench M, Littleton JT. Modeling huntington disease in Drosophila: Insights into axonal transport defects and modifiers of toxicity. *Fly (Austin)*. 2013;7(4):229-236. doi:10.4161/fly.26279

250. Marsh JL, Pallos J, Thompson LM. Fly models of Huntington's disease. *Hum Mol Genet*. 2003;12(2):187-193. doi:10.1093/hmg/ddg271

251. Brand a H, Perrimon N. Targeted gene expression as a means of altering cell fates and generating dominant phenotypes. *Development*. 1993;118(2):401-415.

252. Schiffer NW, Broadley SA, Hirschberger T, et al. Identification of anti-prion compounds as efficient inhibitors of polyglutamine protein aggregation in a zebrafish model. *J Biol Chem*. 2007;282(12):9195-9203. doi:10.1074/jbc.M607865200

253. Jacobsen JC, Bawden CS, Rudiger SR, et al. An ovine transgenic Huntington's disease model. *Hum Mol Genet*. 2010;19(10):1873-1882. doi:10.1093/hmg/ddq063

254. Handley RR, Reid SJ, Brauning R, et al. Brain urea increase is an early Huntington's disease pathogenic event observed in a prodromal transgenic sheep model and HD cases. *Proc Natl Acad Sci U S A*. 2017;114(52):E11293-E11302. doi:10.1073/pnas.1711243115

255. Reid SJ, Patassini S, Handley RR, et al. Further molecular characterisation of the OVT73 transgenic sheep model of huntington's disease identifies cortical aggregates. *J Huntingtons Dis*. 2013;2(3):279-295. doi:10.3233/JHD-130067

256. Yang D, Wang CE, Zhao B, et al. Expression of Huntington's disease protein results in apoptotic neurons in the brains of cloned transgenic pigs. *Hum Mol Genet*. 2010;19(20):3983-3994. doi:10.1093/hmg/ddq313

257. Yan S, Tu Z, Liu Z, et al. A Huntingtin Knockin Pig Model Recapitulates Features of Selective Neurodegeneration in Huntington's Disease. *Cell*. 2018;173(4):989-1002.e13. doi:10.1016/j.cell.2018.03.005

258. E S, PB C, RJ F, NW K, MF B. Movement disorder following excitotoxin lesions in primates. *Neuroreport*. 1994;5(10):1259-1261. doi:https://doi.org/10.1097/00001756-199406020-00026

259. Kendall AL, David F, Rayment G, Torres EM, Annett LE, Dunnett SB. The influence of excitotoxic basal ganglia lesions on motor performance in the common marmoset. *Brain*. 2000;123(7):1442-1458. doi:10.1093/brain/123.7.1442

260. Palfi S, Brouillet E, Jarraya B, et al. Expression of mutated huntingtin fragment in the putamen is sufficient to produce abnormal movement in non-human primates. *Mol Ther*. 2007;15(8):1444-1451. doi:10.1038/sj.mt.6300185

261. Yang SH, Cheng PH, Banta H, et al. Towards a transgenic model of Huntington's

disease in a non-human primate. *Nature*. 2008;453(7197):921-924. doi:10.1038/nature06975

262. Lunkes A, Mandel JL. A cellular model that recapitulates major pathogenic steps of Huntington's disease. *Hum Mol Genet*. 1998;7(9):1355-1361. doi:10.1093/hmg/7.9.1355

263. Kim M, Lee HS, LaForet G, et al. Mutant Huntingtin expression in clonal striatal cells: Dissociation of inclusion formation and neuronal survival by caspase inhibition. *J Neurosci*. 1999;19(3):964-973. doi:10.1523/jneurosci.19-03-00964.1999

264. Cooper JK, Schilling G, Peters MF, et al. Truncated N-terminal fragments of huntingtin with expanded glutamine repeats form nuclear and cytoplasmic aggregates in cell culture. *Hum Mol Genet*. 1998;7(5):783-790. doi:10.1093/hmg/7.5.783

265. Kim YE, Hosp F, Frottin F, et al. Soluble Oligomers of PolyQ-Expanded Huntingtin Target a Multiplicity of Key Cellular Factors. *Mol Cell*. 2016;63(6):950-964. doi:10.1016/j.molcel.2016.07.022

266. Peskett TR, Rau F, O'Driscoll J, Patani R, Lowe AR, Saibil HR. A Liquid to Solid Phase Transition Underlying Pathological Huntingtin Exon1 Aggregation. *Mol Cell*. 2018;70(4):588-601.e6. doi:10.1016/j.molcel.2018.04.007

267. Ghosh R, Wood-Kaczmar A, Dobson L, et al. Expression of mutant exon 1 huntingtin fragments in human neural stem cells and neurons causes inclusion formation and mitochondrial dysfunction. *FASEB J*. 2020;34(6):8139-8154. doi:10.1096/fj.201902277RR

268. Waelter S, Boeddrich A, Lurz R, et al. Accumulation of mutant huntingtin fragments in aggresome-like inclusion bodies as a result of insufficient protein degradation. *Mol Biol Cell*. 2001;12(5):1393-1407. doi:10.1091/mbc.12.5.1393

269. Sahl SJ, Lau L, Vonk WIM, Weiss LE, Frydman J, Moerner WE. Delayed emergence of subdiffraction-sized mutant huntingtin fibrils following inclusion body formation. *Q Rev Biophys*. 2016;49. doi:10.1017/S0033583515000219

270. Luo H, Cao L, Liang X, Du A, Peng T, Li H. Herp Promotes Degradation of Mutant Huntingtin: Involvement of the Proteasome and Molecular Chaperones. *Mol Neurobiol*. 2018;55(10):7652-7668. doi:10.1007/s12035-018-0900-8

271. Kaytor MD, Wilkinson KD, Warren ST. Modulating huntingtin half-life alters polyglutamine-dependent aggregate formation and cell toxicity. *J Neurochem*. 2004;89(4):962-973. doi:10.1111/j.1471-4159.2004.02376.x

272. Chen MZ, Mok SA, Ormsby AR, Muchowski PJ, Hatters DM. N-terminal fragments of huntingtin longer than residue 170 form visible aggregates independently to polyglutamine expansion. *J Huntingtons Dis*. 2017;6(1):79-91. doi:10.3233/JHD-160207

273. Warby SC, Doty CN, Graham RK, et al. Activated caspase-6 and caspase-6-cleaved fragments of huntingtin specifically colocalize in the nucleus. *Hum Mol Genet*. 2008;17(15):2390-2404. doi:10.1093/hmg/ddn139

274. El-Daher M-T, Hangen E, Bruyere J, et al. Huntingtin proteolysis releases non-polyQ fragments that cause toxicity through dynamin 1 dysregulation. *EMBO J*. 2015;34(17):2255-2271. doi:10.15252/embj.201490808

275. Ratovitski T, Gucek M, Jiang H, et al. Mutant huntingtin N-terminal fragments of specific size mediate aggregation and toxicity in neuronal cells. *J Biol Chem*. 2009;284(16):10855-10867. doi:10.1074/jbc.M804813200

276. Graham RK, Deng Y, Carroll J, et al. Cleavage at the 586 amino acid caspase-6 site in mutant huntingtin influences caspase-6 activation in vivo. *J Neurosci*. 2010;30(45):15019-15029. doi:10.1523/JNEUROSCI.2071-10.2010

277. Kegel KB, Sapp E, Alexander J, et al. Polyglutamine expansion in huntingtin alters its interaction with phospholipids. *J Neurochem*. 2009;110(5):1585-1597. doi:10.1111/j.1471-4159.2009.06255.x

278. Atwal RS, Xia J, Pinchev D, Taylor J, Epand RM, Truant R. Huntingtin has a membrane association signal that can modulate huntingtin aggregation, nuclear entry and toxicity. *Hum Mol Genet*. 2007;16(21):2600-2615. doi:10.1093/hmg/ddm217

279. Mantha N, Das NG, Das SK. Recent Trends in Detection of Huntingtin and Preclinical Models of Huntington's Disease. *ISRN Mol Biol*. 2014:190976. doi:10.1155/2014/190976

280. Hazeki N, Tukamoto T, Goto J, Kanazawa I. Formic acid dissolves aggregates of an N-terminal huntingtin fragment containing an expanded polyglutamine tract: Applying to quantification of protein components of the aggregates. *Biochem Biophys Res Commun*. 2000;277(2):386-393. doi:10.1006/bbrc.2000.3682

281. Oguro A, Kubota H, Shimizu M, Ishiura S, Atomi Y. Protective role of the ubiquitin binding protein Tollip against the toxicity of polyglutamine-expansion proteins. *Neurosci Lett*. 2011;503(3):234-239. doi:10.1016/j.neulet.2011.08.043

282. Cornett J, Cao F, Wang C-E, et al. Polyglutamine expansion of huntingtin impairs its nuclear export. *Nat Genet*. 2005;37(2):198-204. doi:10.1038/ng1503

283. Juenemann K, Jansen AHP, van Riel L, et al. Dynamic recruitment of ubiquitin to mutant huntingtin inclusion bodies. *Sci Rep*. 2018;8(1):1405. doi:10.1038/s41598-018-19538-0

284. Andrew SE, Paul Goldberg Y, Kremer B, et al. The relationship between trinucleotide (CAG) repeat length and clinical features of Huntington's disease. *Nat Genet*. 1993;4(4):398-403. doi:10.1038/ng0893-398

285. Yanai A, Huang K, Kang R, et al. Palmitoylation of huntingtin by HIP14is essential for its trafficking and function. *Nat Neurosci*. 2006;9(6):824-831. doi:10.1038/nn1702

286. Li S-H, Cheng AL, Zhou H, et al. Interaction of Huntington disease protein with transcriptional activator Sp1. *Mol Cell Biol*. 2002;22(5):1277-1287. doi:10.1128/MCB.22.5.1277

287. Iwata A, Riley BE, Johnston JA, Kopito RR. HDAC6 and microtubules are required for autophagic degradation of aggregated Huntingtin. *J Biol Chem*. 2005;280(48):40282-40292. doi:10.1074/jbc.M508786200

288. Aron R, Pellegrini P, Green EW, et al. Deubiquitinase Usp12 functions noncatalytically to induce autophagy and confer neuroprotection in models of Huntington's disease. *Nat Commun*. 2018;9(1). doi:10.1038/s41467-018-05653-z

289. Neueder A, Dumas AA, Benjamin AC, Bates GP. Regulatory mechanisms of incomplete huntingtin mRNA splicing. *Nat Commun*. 2018;9(1):3955. doi:10.1038/s41467-018-06281-3

290. Klaips CL, Gropp MHM, Hipp MS, Hartl FU. Sis1 potentiates the stress response to protein aggregation and elevated temperature. *Nat Commun*. 2020;11(1):6271. doi:10.1038/s41467-020-20000-x

291. Nguyen T, Hamby A, Massa SM. Clioquinol down-regulates mutant huntingtin expression in vitro and mitigates pathology in a Huntington's disease mouse model.

Proc Natl Acad Sci U S A. 2005;102(33):11840-11845. doi:10.1073/pnas.0502177102

292. Sophie Vieweg, Mahul-Mellier A-L, Ruggeri FS, et al. Towards deciphering the Nt17 code: How the sequence and conformation of the first 17 amino acids in Huntingtin regulate the aggregation, cellular properties and neurotoxicity of mutant Httex1. *bioRxiv*. 2021:6.

293. Scior A, Buntru A, Arnsburg K, et al. Complete suppression of Htt fibrilization and disaggregation of Htt fibrils by a trimeric chaperone complex. *EMBO J*. 2018;37(2):282-299. doi:10.15252/embj.201797212

294. Singer E, Hunanyan L, Melkonyan MM, Weber JJ, Danielyan L, Nguyen HP. The novel alpha-2 adrenoceptor inhibitor beditin reduces cytotoxicity and huntingtin aggregates in cell models of huntington's disease. *Pharmaceuticals*. 2021;14(3). doi:10.3390/ph14030257

295. Gerson JE, Safren N, Fischer S, et al. Ubiquilin-2 differentially regulates polyglutamine disease proteins. *Hum Mol Genet*. 2020;29(15):2596-2610. doi:10.1093/hmg/ddaa152

296. Jiang M, Zhang X, Liu H, et al. Nemo-like kinase reduces mutant huntingtin levels and mitigates Huntington's disease. *Hum Mol Genet*. 2020;29(8):1340-1352. doi:10.1093/hmg/ddaa061

297. Wang Q, Liang G, Yang H, Wang S, Eckenhoff MF, Wei H. The common inhaled anesthetic isoflurane increases aggregation of huntingtin and alters calcium homeostasis in a cell model of Huntington's disease. *Toxicol Appl Pharmacol*. 2011;250(3):291-298. doi:10.1016/j.taap.2010.10.032

298. Trettel F, Rigamonti D, Hilditch-Maguire P, et al. Dominant phenotypes produced by the HD mutation in STHdh(Q111) striatal cells. *Hum Mol Genet*. 2000;9(19):2799-2809. doi:10.1093/hmg/9.19.2799

299. Milakovic T, Quintanilla RA, Johnson GVW. Mutant Huntingtin expression induces mitochondrial calcium handling defects in clonal striatal cells: Functional consequences. *J Biol Chem*. 2006;281(46):34785-34795. doi:10.1074/jbc.M603845200

300. Connor B. Concise Review: The Use of Stem Cells for Understanding and Treating Huntington's Disease. *Stem Cells*. 2018;36(2):146-160. doi:10.1002/stem.2747

301. Hung CLK, Maiuri T, Bowie LE, et al. A patient-derived cellular model for Huntington's disease reveals phenotypes at clinically relevant CAG lengths. *Mol Biol Cell*. 2018;29(23):2809-2820. doi:10.1091/mbc.E18-09-0590

302. Consortium H iPSC. Induced pluripotent stem cells from patients with huntington's disease show CAG repeat expansion associated phenotypes. *Cell Stem Cell*. 2012;11(2):264-278. doi:10.1016/j.stem.2012.04.027

303. Osipovitch M, Asenjo Martinez A, Mariani JN, et al. Human ESC-Derived Chimeric Mouse Models of Huntington's Disease Reveal Cell-Intrinsic Defects in Glial Progenitor Cell Differentiation. *Cell Stem Cell*. 2019;24(1):107-122.e7. doi:10.1016/j.stem.2018.11.010

304. Victor MB, Richner M, Olsen HE, et al. Striatal neurons directly converted from Huntington's disease patient fibroblasts recapitulate age-associated disease phenotypes. *Nat Neurosci*. 2018;21(3):1307. doi:10.1038/s41593-018-0075-7

305. Holley SM, Kamdjou T, Reidling JC, et al. Therapeutic effects of stem cells in rodent models of Huntington's disease: Review and electrophysiological findings. *CNS Neurosci Ther*. 2018;24(4):329-342. doi:10.1111/cns.12839

306. Ferrante RJ, Gutekunst CA, Persichetti F, et al. Heterogeneous topographic and cellular distribution of huntingtin expression in the normal human neostriatum. *J Neurosci*. 1997;17(9):3052-3063. doi:10.1523/jneurosci.17-09-03052.1997

307. Sisodia SS. Nuclear inclusions in glutamine repeat disorders: Are they pernicious, coincidental, or beneficial? *Cell*. 1998;95(1):1-4. doi:10.1016/S0092-8674(00)81743-2

308. Saudou F, Finkbeiner S, Devys D, Greenberg ME. Huntingtin acts in the nucleus to induce apoptosis but death does not correlate with the formation of intranuclear inclusions. *Cell*. 1998;95(1):55-56. doi:10.1016/S0092-8674(00)81782-1

309. Yu Z-X, Li S-H, Nguyen H-P, Li X-J. Huntingtin inclusions do not deplete polyglutamine-containing transcription factors in HD mice. *Hum Mol Genet*. 2002;11(8):905-914. doi:10.1093/hmg/11.8.905

310. Cisbani G, Cicchetti F. An in vitro perspective on the molecular mechanisms underlying mutant huntingtin protein toxicity. *Cell Death Dis*. 2012;3(8):1-12. doi:10.1038/cddis.2012.121

311. Wang H, Lim PJ, Karbowski M, Monteiro MJ. Effects of overexpression of Huntingtin proteins on mitochondrial integrity. *Hum Mol Genet*. 2009;18(4):737-752. doi:10.1093/hmg/ddn404

312. Ye C, Zhang Y, Wang W, Wang J, Li H. Inhibition of neurite outgrowth and promotion of cell death by cytoplasmic soluble mutant huntingtin stably transfected in mouse neuroblastoma cells. *Neurosci Lett*. 2008;442(1):63-68. doi:10.1016/j.neulet.2008.05.119

313. Olshina MA, Angley LM, Ramdzan YM, et al. Tracking mutant huntingtin aggregation kinetics in cells reveals three major populations that include an invariant oligomer pool. *J Biol Chem*. 2010;285(28):21807-21816. doi:10.1074/jbc.M109.084434

314. Hackam AS, Hodgson JG, Singaraja R, et al. Evidence for both the nucleus and cytoplasm as subcellular sites of pathogenesis in Huntington's disease in cell culture and in transgenic mice expressing mutant huntingtin. *Philos Trans R Soc B Biol Sci*. 1999;354(1386):1047-1055.

315. Wang HQ, Xu YX, Zhao XY, et al. Overexpression of F0F1-ATP synthase α suppresses mutant huntingtin aggregation and toxicity in vitro. *Biochem Biophys Res Commun*. 2009;390(4):1294-1298. doi:10.1016/j.bbrc.2009.10.139

316. Arango M, Holbert S, Zala D, et al. CA150 expression delays striatal cell death in overexpression and knock-in conditions for mutant huntingtin neurotoxicity. *J Neurosci*. 2006;26(17):4649-4659. doi:10.1523/JNEUROSCI.5409-05.2006

317. Zala D, Benchoua A, Brouillet E, et al. Progressive and selective striatal degeneration in primary neuronal cultures using lentiviral vector coding for a mutant huntingtin fragment. *Neurobiol Dis*. 2005;20(3):785-798. doi:10.1016/j.nbd.2005.05.017

318. Poirier MA, Jiang H, Ross CA. A structure-based analysis of huntingtin mutant polyglutamine aggregation and toxicity: Evidence for a compact beta-sheet structure. *Hum Mol Genet*. 2005;14(6):765-774. doi:10.1093/hmg/ddi071

319. Igarashi S, Morita H, Bennett KM, et al. Inducible PC12 cell model of Huntington's disease shows toxicity and decreased histone acetylation. *Neuroreport*. 2003;14(4):565-568. doi:10.1097/00001756-200303240-00007

320. Dong G, Ferguson JM, Duling AJ, et al. Modeling pathogenesis of Huntington's disease with inducible neuroprogenitor cells. *Cell Mol Neurobiol*. 2011;31(5):737-747. doi:10.1007/s10571-011-9679-0

321. Yang H, Hu HY. Sequestration of cellular interacting partners by protein aggregates: implication in a loss-of-function pathology. *FEBS J*. 2016;283(20):3705-3717. doi:10.1111/febs.13722

322. Park SH, Kukushkin Y, Gupta R, et al. PolyQ proteins interfere with nuclear degradation of cytosolic proteins by sequestering the Sis1p chaperone. *Cell*. 2013;154(1):134-145. doi:10.1016/j.cell.2013.06.003

323. Schaffar G, Breuer P, Boteva R, et al. Cellular toxicity of polyglutamine expansion proteins: Mechanism of transcription factor deactivation. *Mol Cell*. 2004;15(1):95-105. doi:10.1016/j.molcel.2004.06.029

324. Harding RJ, Tong YF. Proteostasis in Huntington's disease: Disease mechanisms and therapeutic opportunities. *Acta Pharmacol Sin*. 2018;39(5):754-769. doi:10.1038/aps.2018.11

325. Yamamoto A, Lucas JJ, Hen R. Reversal of Neuropathology and Motor Dysfunction in a Conditional Model of Huntington's Disease. *Cell*. 2000;101(1):57-66.

326. Sánchez I, Mahlke C, Yuan J. Pivotal role of oligomerization in expanded polyglutamine neurodegenerative disorders. *Nature*. 2003;421(6921):373-379. doi:10.1038/nature01301

327. Martín-Aparicio E, Yamamoto A, Hernández F, Hen R, Avila J, Lucas JJ. Proteasomal-dependent aggregate reversal and absence of cell death in a conditional mouse model of Huntington's disease. *J Neurosci*. 2001;21(22):8772-8781. doi:10.1523/jneurosci.21-22-08772.2001

328. King MA, Goemans CG, Hafiz F, Prehn JHM, Wyttenbach A, Tolkovsky AM. Cytoplasmic inclusions of Htt exon1 containing an expanded polyglutamine tract suppress execution of apoptosis in sympathetic neurons. *J Neurosci*. 2008;28(53):14401-14415. doi:10.1523/JNEUROSCI.4751-08.2008

329. Miller J, Arrasate M, Shaby BA, Mitra S, Masliah E, Finkbeiner S. Quantitative relationships between huntingtin levels, polyglutamine length, inclusion body formation, and neuronal death provide novel insight into huntington's disease molecular pathogenesis. *J Neurosci*. 2010;30(31):10541-10550. doi:10.1523/JNEUROSCI.0146-10.2010

330. Bodner RA, Outeiro TF, Altmann S, et al. Pharmacological promotion of inclusion formation: a therapeutic approach for Huntington's and Parkinson's diseases. *Proc Natl Acad Sci U S A*. 2006;103(11):4246-4251. doi:10.1073/pnas.0511256103

331. Lajoie P, Snapp EL. Formation and toxicity of soluble polyglutamine oligomers in living cells. *PLoS One*. 2010;5(12):e15245. doi:10.1371/journal.pone.0015245

332. Leitman J, Ulrich Hartl F, Lederkremer GZ. Soluble forms of polyQ-expanded huntingtin rather than large aggregates cause endoplasmic reticulum stress. *Nat Commun*. 2013;4:2753. doi:10.1038/ncomms3753

333. Takahashi T, Kikuchi S, Katada S, Nagai Y, Nishizawa M, Onodera O. Soluble polyglutamine oligomers formed prior to inclusion body formation are cytotoxic. *Hum Mol Genet*. 2008;17(3):345-356. doi:10.1093/hmg/ddm311

334. Nucifora LG, Burke KA, Feng X, et al. Identification of novel potentially toxic oligomers formed in vitro from mammalian-derived expanded huntingtin exon-1 protein. *J Biol Chem*. 2012;287(19):16017-16028. doi:10.1074/jbc.M111.252577

335. McColgan P, Tabrizi SJ. Huntington's disease: a clinical review. *Eur J Neurol*. 2017:24-34. doi:10.1111/ene.13413

336. Caron NS, Dorsey ER, Hayden MR. Therapeutic approaches to Huntington disease: from the bench to the clinic. *Nat Rev Drug Discov*. 2018;17(10):729-750. doi:10.1038/nrd.2018.133

337. Tabrizi SJ, Flower MD, Ross CA, Wild EJ. Huntington disease: new insights into molecular pathogenesis and therapeutic opportunities. *Nat Rev Neurol*. 2020;16(10):529-546. doi:10.1038/s41582-020-0389-4

338. Benjamin CM, Adam S, Wiggins S, et al. Proceed with Care: Direct Predictive Testing for Huntington Disease. *Am J Hum Genet*. 1994;55(4):606-615.

339. Group HS. Unified Huntington's Disease Rating Scale: Reliability and Consistency. *Mov Disord*. 1996;11(2):136-142.

340. Pettibone DJ, Totaro JA, Pflueger AB. Tetrabenazine-induced depletion of brain monoamines: Characterization and interaction with selected antidepressants. *Eur J Pharmacol*. 1984;102(3-4):425-430. doi:10.1016/0014-2999(84)90562-4

341. Group HS. Tetrabenazine as antichorea therapy in Huntington disease: A randomized controlled trial. *Neurology*. 2006;66(33):366-372. doi:10.1212/01.wnl.0000259143.52138.5c

342. Group HS. Effect of deutetrabenazine on chorea among patients with huntington disease : A randomized clinical trial. *JAMA - J Am Med Assoc*. 2016;316(1):40-50. doi:10.1001/jama.2016.8655

343. Adam OR, Jankovic J. Symptomatic Treatment of Huntington Disease. *Neurotherapeutics*. 2008;5(2):181-197. doi:https://doi.org/10.1016/j.nurt.2008.01.008

344. Rodrigues FB, Wild EJ. Huntington's Disease Clinical Trials Corner: April 2020. *J Huntingtons Dis*. 2020;9(2):185-197. doi:10.3233/JHD-200002

345. Wang G, Liu X, Gaertig MA, Li S, Li XJ. Ablation of huntingtin in adult neurons is nondeleterious but its depletion in young mice causes acute pancreatitis. *Proc Natl Acad Sci U S A*. 2016;113(12):3359-3364. doi:10.1073/pnas.1524575113

346. Dietrich P, Johnson IM, Alli S, Dragatsis I. Elimination of huntingtin in the adult mouse leads to progressive behavioral deficits, bilateral thalamic calcification, and altered brain iron homeostasis. *PLoS Genet*. 2017;13(7):e1006846. doi:10.1371/journal.pgen.1006846

347. Ambrose CM, Duyao MP, Barnes G, et al. Structure and expression of the Huntington's disease gene: Evidence against simple inactivation due to an expanded CAG repeat. *Somat Cell Mol Genet*. 1994;20(1):27-38. doi:10.1007/BF02257483

348. Kordasiewicz HB, Stanek LM, Wancewicz E V., et al. Sustained Therapeutic Reversal of Huntington's Disease by Transient Repression of Huntingtin Synthesis. *Neuron*. 2012;74(6):1031-1044. doi:10.1016/j.neuron.2012.05.009

349. Grondin R, Kaytor MD, Ai Y, et al. Six-month partial suppression of Huntingtin is well tolerated in the adult rhesus striatum. *Brain*. 2012;135(4):1197-1209. doi:10.1093/brain/awr333

350. McBride JL, Pitzer MR, Boudreau RL, et al. Preclinical safety of RNAi-mediated HTT suppression in the rhesus macaque as a potential therapy for Huntington's disease. *Mol Ther*. 2011;19(12):2152-2162. doi:10.1038/mt.2011.219

351. Hu J, Matsui M, Gagnon KT, et al. Allele-specific silencing of mutant huntingtin and ataxin-3 genes by targeting expanded CAG repeats in mRNAs. *Nat Biotechnol*. 2009;27(5):478-484. doi:10.1038/nbt.1539

352. Gagnon KT, Pendergraff HM, Deleavey GF, et al. Allele-selective inhibition of mutant huntingtin expression with antisense oligonucleotides targeting the expanded CAG repeat. *Biochemistry*. 2010;49(47):10166-10178. doi:10.1021/bi101208k

353. Pfister EL, Kennington L, Straubhaar J, et al. Five siRNAs Targeting Three SNPs May Provide Therapy for Three-Quarters of Huntington's Disease Patients. *Curr Biol*. 2009;19(9):774-778. doi:10.1016/j.cub.2009.03.030

354. Carroll JB, Warby SC, Southwell AL, et al. Potent and selective antisense oligonucleotides targeting single-nucleotide polymorphisms in the huntington disease gene / allele-specific silencing of mutant huntingtin. *Mol Ther*. 2011;19(12):2178-2185. doi:10.1038/mt.2011.201

355. Zhang Y, Engelman J, Friedlander RM. Allele-specific silencing of mutant Huntington's disease gene. *J Neurochem*. 2009;108(1):82-90. doi:10.1111/j.1471-4159.2008.05734.x

356. Kay C, Collins JA, Skotte NH, et al. Huntingtin haplotypes provide prioritized target panels for allele-specific silencing in huntington disease patients of european ancestry. *Mol Ther*. 2015;23(11):1759-1771. doi:10.1038/mt.2015.128

357. Lindow M, Vornlocher HP, Riley D, et al. Assessing unintended hybridization-induced biological effects of oligonucleotides. *Nat Biotechnol*. 2012;30(10):920-923. doi:10.1038/nbt.2376

358. Franich NR, Fitzsimons HL, Fong DM, Klugmann M, During MJ, Young D. AAV vector-mediated RNAi of mutant Huntingtin expression is neuroprotective in a novel genetic rat model of Huntington's disease. *Mol Ther*. 2008;16(5):947-956. doi:10.1038/mt.2008.50

359. Wild EJ, Tabrizi SJ. Therapies targeting DNA and RNA in Huntington's disease. *Lancet Neurol*. 2017;16(10):837-847. doi:10.1016/S1474-4422(17)30280-6

360. Chen ZJ, Kren BT, Wong PYP, Low WC, Steer CJ. Sleeping Beauty-mediated down-regulation of huntingtin expression by RNA interference. *Biochem Biophys Res Commun*. 2005;329(2):646-652. doi:10.1016/j.bbrc.2005.02.024

361. Harper SQ, Staber PD, He X, et al. RNA interference improves motor and neuropathological abnormalities in a Huntington's disease mouse model. *Proc Natl Acad Sci U S A*. 2005;102(16):5820-5825. doi:10.1073/pnas.0501507102

362. Miniarikova J, Zimmer V, Martier R, et al. AAV5-miHTT gene therapy demonstrates suppression of mutant huntingtin aggregation and neuronal dysfunction in a rat model of Huntington's disease. *Gene Ther*. 2017;24(10):630-639. doi:10.1038/gt.2017.71

363. Valles A, Evers MM, Stam A, et al. Widespread and sustained target engagement in Huntington s disease minipigs upon intrastriatal microRNA-based gene therapy. *Sci Transl Med*. 2021;13(588):eabb8920. doi:10.1126/scitranslmed.abb8920

364. Rocha NP, Colpo GD, Teixeira AL, Stimming EF. Clinical Trials for Huntington Disease. *Pract Neurol*. 2020;(June):69-74.

365. Tabrizi SJ, Leavitt BR, Landwehrmeyer GB, et al. Targeting Huntingtin Expression in Patients with Huntington's Disease. *N Engl J Med*. 2019;380(24):2307-2316. doi:10.1056/nejmoa1900907

366. Klug A. The discovery of zinc fingers and their applications in gene regulation and genome manipulation. *Annu Rev Biochem*. 2010;79:213-231. doi:10.1146/annurev-biochem-010909-095056

367. Garriga-Canut M, Agustín-Pavón C, Herrmann F, et al. Synthetic zinc finger repressors

reduce mutant huntingtin expression in the brain of R6/2 mice. *Proc Natl Acad Sci U S A*. 2012;109(45):E3136-45. doi:10.1073/pnas.1206506109

368. Malankhanova TB, Malakhova AA, Medvedev SP, Zakian SM. Modern Genome Editing Technologies in Huntington's Disease Research. *J Huntingtons Dis*. 2017;6(1):19-31. doi:10.3233/JHD-160222

369. Fink KD, Deng P, Gutierrez J, et al. Allele-specific reduction of the mutant huntingtin allele using transcription activator-like effectors in human huntington's disease fibroblasts. *Cell Transplant*. 2016;25(4):677-686. doi:10.3727/096368916X690863

370. Adli M. The CRISPR tool kit for genome editing and beyond. *Nat Commun*. 2018;9(1):1911. doi:10.1038/s41467-018-04252-2

371. Dabrowska M, Juzwa W, Krzyzosiak WJ, Olejniczak M. Precise Excision of the CAG Tract from the Huntingtin Gene by Cas9 Nickases. *Front Neurosci*. 2018;12:75. doi:10.3389/fnins.2018.00075

372. Monteys AM, Ebanks SA, Keiser MS, Davidson BL. CRISPR/Cas9 Editing of the Mutant Huntingtin Allele In Vitro and In Vivo. *Mol Ther*. 2017;25(1):12-23. doi:10.1016/j.ymthe.2016.11.010

373. Shin JW, Kim KH, Chao MJ, et al. Permanent inactivation of Huntington's disease mutation by personalized allele-specific CRISPR/Cas9. *Hum Mol Genet*. 2016;25(20):4566-4576. doi:10.1093/hmg/ddw286

374. Xu X, Tay Y, Sim B, et al. Reversal of Phenotypic Abnormalities by CRISPR/Cas9-Mediated Gene Correction in Huntington Disease Patient-Derived Induced Pluripotent Stem Cells. *Stem Cell Reports*. 2017;8(3):619-633. doi:10.1016/j.stemcr.2017.01.022

375. Theil D, Valdez R, Darribat K, Doelemeyer A, Sivasankaran R, Hartmann A. Orally administered branaplam does not impact neurogenesis in juvenile mice, rats, and dogs. *Biol Open*. 2021;10(10):bio058551. doi:10.1242/bio.058551

376. Tai YF, Pavese N, Gerhard A, et al. Imaging microglial activation in Huntington's disease. *Brain Res Bull*. 2007;72(2-3):148-151. doi:10.1016/j.brainresbull.2006.10.029

377. Tai YF, Pavese N, Gerhard A, et al. Microglial activation in presymptomatic Huntington's disease gene carriers. *Brain*. 2007;130(7):1759-1766. doi:10.1093/brain/awm044

378. Crotti A, Glass CK. The choreography of neuroinflammation in Huntington's disease. *Trends Immunol*. 2015;36(6):364-373. doi:10.1016/j.it.2015.04.007

379. Palpagama TH, Waldvogel HJ, Faull RLM, Kwakowsky A. The Role of Microglia and Astrocytes in Huntington's Disease. *Front Mol Neurosci*. 2019;12(October):1-15. doi:10.3389/fnmol.2019.00258

380. Crotti A, Benner C, Kerman B, et al. Mutant Huntingtin promotes autonomous microglia activation via myeloid lineage-determining factors. *Nat Neurosci*. 2014;17(4):513-521. doi:10.1038/jid.2014.371

381. Dalrymple A, Wild EJ, Joubert R, et al. Proteomic profiling of plasma in Huntington's disease reveals neuroinflammatory activation and biomarker candidates. *J Proteome Res*. 2007;6(7):2833-2840. doi:10.1021/pr0700753

382. Garcia-Miralles M, Hong X, Tan LJ, et al. Laquinimod rescues striatal, cortical and white matter pathology and results in modest behavioural improvements in the YAC128 model of Huntington disease. *Sci Rep*. 2016;6:31652. doi:10.1038/srep31652

383. Brück W, Pförtner R, Pham T, et al. Reduced astrocytic NF-κB activation by laquinimod

protects from cuprizone-induced demyelination. *Acta Neuropathol*. 2012;124(3):411-424. doi:10.1007/s00401-012-1009-1

384. Mishra MK, Wang J, Keough MB, et al. Laquinimod reduces neuroaxonal injury through inhibiting microglial activation. *Ann Clin Transl Neurol*. 2014;1(6):409-422. doi:10.1002/acn3.67

385. Dobson L, Träger U, Farmer R, et al. Laquinimod dampens hyperactive cytokine production in Huntington's disease patient myeloid cells. *J Neurochem*. 2016;137(5):782-794. doi:10.1111/jnc.13553

386. Biotech A. Active Biotech provides update on laquinimod in Huntington's disease. 2018. http://www.activebiotech.com/en.

387. Monk R, Connor B. Cell reprogramming to model huntington's disease: A comprehensive review. *Cells*. 2021;10(7):1565. doi:10.3390/cells10071565

388. Kratter IH, Zahed H, Lau A, et al. Serine 421 regulates mutant huntingtin toxicity and clearance in mice. *J Clin Invest*. 2016;126(9):3585-3597. doi:10.1172/JCI80339

389. Evers MM, Tran HD, Zalachoras I, et al. Preventing formation of toxic N-terminal huntingtin fragments through antisense oligonucleotide-mediated protein modification. *Nucleic Acid Ther*. 2014;24(1):4-12. doi:10.1089/nat.2013.0452

390. Casaca-Carreira J, Toonen LJA, Evers MM, Jahanshahi A, van-Roon-Mom WMC, Temel Y. In vivo proof-of-concept of removal of the huntingtin caspase cleavage motif-encoding exon 12 approach in the YAC128 mouse model of Huntington's disease. *Biomed Pharmacother*. 2016;84:93-96. doi:10.1016/j.biopha.2016.09.007

391. Kim S, Kim K-T. Therapeutic Approaches for Inhibition of Protein Aggregation in Huntington's Disease. *Exp Neurobiol*. 2014;23(1):36-44. doi:10.5607/en.2014.23.1.36

392. Wood NI, Pallier PN, Wanderer J, Morton AJ. Systemic administration of Congo red does not improve motor or cognitive function in R6/2 mice. *Neurobiol Dis*. 2007;25(2):342-353. doi:10.1016/j.nbd.2006.09.015

393. Im J, Kim S, Jeong YH, et al. Preparation and evaluation of BBB-permeable trehalose derivatives as potential therapeutic agents for Huntington's disease. *Medchemcomm*. 2013;4(2):310-316. doi:10.1039/c2md20112g

394. Chopra V, Fox JH, Lieberman G, et al. A small-molecule therapeutic lead for Huntington's disease: preclinical pharmacology and efficacy of C2-8 in the R6/2 transgenic mouse. *Proc Natl Acad Sci U S A*. 2007;104(42):16685-16689. doi:10.1073/pnas.0707842104

395. Nagai Y, Fujikake N, Ohno K, et al. Prevention of polyglutamine oligomerization and neurodegeneration by the peptide inhibitor QBP1 in Drosophila. *Hum Mol Genet*. 2003;12(11):1253-1260. doi:10.1093/hmg/ddg144

396. Zou J, Guo Y, Guettouche T, Smith DF, Voellmy R. Repression of heat shock transcription factor HSF1 activation by HSP90 (HSP90 complex) that forms a stress-sensitive complex with HSF1. *Cell*. 1998;94(4):471-480. doi:10.1016/S0092-8674(00)81588-3

397. Fujikake N, Nagai Y, Popiel HA, Okamoto Y, Yamaguchi M, Toda T. Heat shock transcription factor 1-activating compounds suppress polyglutamine-induced neurodegeneration through induction of multiple molecular chaperones. *J Biol Chem*. 2008;283(38):26188-26197. doi:10.1074/jbc.M710521200

398. Yokota SI, Kayano T, Ohta T, et al. Proteasome-dependent degradation of cytosolic

chaperonin CCT. *Biochem Biophys Res Commun*. 2000;279(2):712-717. doi:10.1006/bbrc.2000.4011

399. Milnerwood AJ, Gladding CM, Pouladi MA, et al. Early Increase in Extrasynaptic NMDA Receptor Signaling and Expression Contributes to Phenotype Onset in Huntington's Disease Mice. *Neuron*. 2010;65(2):178-190. doi:10.1016/j.neuron.2010.01.008

400. Okamoto SI, Pouladi MA, Talantova M, et al. Balance between synaptic versus extrasynaptic NMDA receptor activity influences inclusions and neurotoxicity of mutant huntingtin. *Nat Med*. 2009;15(12):1407-1413. doi:10.1038/nm.2056

401. Ryskamp D, Wu J, Geva M, et al. The sigma-1 receptor mediates the beneficial effects of pridopidine in a mouse model of Huntington disease. *Neurobiol Dis*. 2017;97(Pt A):46-59. doi:10.1016/j.nbd.2016.10.006

402. Reilmann R, McGarry A, Grachev ID, et al. Safety and efficacy of pridopidine in patients with Huntington's disease (PRIDE-HD): a phase 2, randomised, placebo-controlled, multicentre, dose-ranging study. *Lancet Neurol*. 2019;18(2):165-176. doi:10.1016/S1474-4422(18)30391-0

403. Mann JJ, Kaplan RD, Bird ED. Elevated postmortem monoamine oxidase B activity in the caudate nucleus in hUntington's disease compared to schizophrenics and controls. *J Neural Transm*. 1986;65(3-4):277-283. doi:10.1007/BF01249088

404. Ooi J, Hayden MR, Pouladi MA. Inhibition of Excessive Monoamine Oxidase A/B Activity Protects Against Stress-induced Neuronal Death in Huntington Disease. *Mol Neurobiol*. 2015;52(3):1850-1861. doi:10.1007/s12035-014-8974-4

405. Beaumont V, Zhong S, Lin H, et al. Phosphodiesterase 10A Inhibition Improves Cortico-Basal Ganglia Function in Huntington's Disease Models. *Neuron*. 2016;92(6):1220-1237. doi:10.1016/j.neuron.2016.10.064

406. Gruber A, Hornburg D, Antonin M, et al. Molecular and structural architecture of polyQ aggregates in yeast. *Proc Natl Acad Sci*. 2018;115(15):E3446-E3453. doi:10.1073/pnas.1717978115

407. Wang H, Lim PJ, Yin C, Rieckher M, Vogel BE, Monteiro MJ. Suppression of polyglutamine-induced toxicity in cell and animal models of Huntington's disease by ubiquilin. *Hum Mol Genet*. 2006;15(6):1025-1041. doi:10.1093/hmg/ddl017

408. Lu M, Banetta L, Young LJ, et al. Live-cell super-resolution microscopy reveals a primary role for diffusion in polyglutamine-driven aggresome assembly. *J Biol Chem*. 2019;294(1):257-268. doi:10.1074/jbc.RA118.003500

409. Kim YE, Hosp F, Frottin F, et al. Soluble Oligomers of PolyQ-Expanded Huntingtin Target a Multiplicity of Key Cellular Factors. *Mol Cell*. 2016;63(6):951-964. doi:10.1016/j.molcel.2016.07.022

410. Hazeki N, Tsukamoto T, Yazawa I, et al. Ultrastructure of nuclear aggregates formed by expressing an expanded polyglutamine. *Biochem Biophys Res Commun*. 2002;294(2):429-440. doi:10.1016/S0006-291X(02)00498-9

411. Aktar F, Burudpakdee C, Polanco M, et al. The huntingtin inclusion is a dynamic phase-separated compartment. *Life Sci Alliance*. 2019;2(5):e201900489. doi:10.26508/lsa.201900489

412. Miao K, Wei L. Live-Cell Imaging and Quantification of PolyQ Aggregates by Stimulated Raman Scattering of Selective Deuterium Labeling. *ACS Cent Sci*. 2020;6(4):478-486. doi:10.1021/acscentsci.9b01196

413. Chongtham A, Bornemann DJ, Barbaro BA, et al. Effects of flanking sequences and cellular context on subcellular behavior and pathology of mutant HTT. *Hum Mol Genet*. 2020;29(4):674-688. doi:10.1093/hmg/ddaa001

414. Matsumoto G, Kim S, Morimoto RI. Huntingtin and mutant SOD1 form aggregate structures with distinct molecular properties in human cells. *J Biol Chem*. 2006;281(7):4477-4485. doi:10.1074/jbc.M509201200

415. Costa V, Scorrano L. Shaping the role of mitochondria in the pathogenesis of Huntington ' s disease. *EMBO J*. 2012;31(8):1853-1864. doi:10.1038/emboj.2012.65

416. Sapp E, Schwarz C, Chase K, et al. Huntingtin localization in brains of normal and Huntington's disease patients. *Ann Neurol*. 1997;42(4):604-612. doi:10.1002/ana.410420411

417. DiFiglia M, Sapp E, Chase K, et al. Huntingtin is a cytoplasmic protein associated with vesicles in human and rat brain neurons. *Neuron*. 1995;14(5):1075-1081. doi:10.1016/0896-6273(95)90346-1

418. Sahoo B, Singer D, Kodali R, Zuchner T, Wetzel R. Aggregation behavior of chemically synthesized, full-length huntingtin exon1. *Biochemistry*. 2014;53(24):3897-3907. doi:10.1021/bi500300c

419. Di Pardo A, Monyror J, Morales LC, et al. Mutant huntingtin interacts with the sterol regulatory element-binding proteins and impairs their nuclear import. *Hum Mol Genet*. 2020;29(3):418-431. doi:10.1093/hmg/ddz298

420. Di Pardo A, Maglione V. The S1P Axis: New Exciting Route for Treating Huntington's Disease. *Trends Pharmacol Sci*. 2018;39(5):468-480. doi:10.1016/j.tips.2018.02.009

421. Valenza M, Rigamonti D, Goffredo D, et al. Dysfunction of the cholesterol biosynthetic pathway in Huntington's disease. *J Neurosci*. 2005;25(43):9932-9939. doi:10.1523/JNEUROSCI.3355-05.2005

422. Del Toro D, Xifró X, Pol A, et al. Altered cholesterol homeostasis contributes to enhanced excitotoxicity in Huntington's disease. *J Neurochem*. 2010;115(1):153-167. doi:10.1111/j.1471-4159.2010.06912.x

423. Croce KR, Yamamoto A. A role for autophagy in Huntington's disease. *Neurobiol Dis*. 2019;122:16-22. doi:10.1016/j.nbd.2018.08.010

424. Snapp EL, Hegde RS, Francolini M, et al. Formation of stacked ER cisternae by low affinity protein interactions. *J Cell Biol*. 2003;163(2):257-269. doi:10.1083/jcb.200306020

425. McCaughey J, Miller VJ, Stevenson NL, et al. TFG Promotes Organization of Transitional ER and Efficient Collagen Secretion. *Cell Rep*. 2016;15(8):1648-1659. doi:10.1016/j.celrep.2016.04.062

426. Witte K, Schuh AL, Hegermann J, et al. TFG-1 function in protein secretion and oncogenesis. *Nat Cell Biol*. 2011;13(5):550-558. doi:10.1038/ncb2225

427. Ratovitski T, Chighladze E, Arbez N, et al. Huntingtin protein interactions altered by polyglutamine expansion as determined by quantitative proteomic analysis. *Cell Cycle*. 2012;11(10):2006-2021. doi:10.4161/cc.20423

428. Ray PD, Huang B-W, Tsuji Y. Reactive oxygen species (ROS) homeostasis and redox regulation in cellular signaling. *Cell Signal*. 2012;24(5):981-990. doi:10.1016/j.cellsig.2012.01.008

429. Chang DTW, Rintoul GL, Pandipati S, Reynolds IJ. Mutant huntingtin aggregates impair mitochondrial movement and trafficking in cortical neurons. *Neurobiol Dis*. 2006;22(2):388-400. doi:10.1016/j.nbd.2005.12.007

430. Forno LS, Norville RL. Ultrastructure of Lewy bodies in the stellate ganglion. *Acta Neuropathol*. 1976;34(3):183-197. doi:10.1007/BF00688674

431. Gai WP, Yuan HX, Li XQ, Power JTH, Blumbergs PC, Jensen PH. In situ and in vitro study of colocalization and segregation of α-synuclein, ubiquitin, and lipids in Lewy bodies. *Exp Neurol*. 2000;166(2):324-333. doi:10.1006/exnr.2000.7527

432. Tellez-Nagel I, Johnson AB, Terry RD. Studies on brain biopsies of patients with Huntington's chorea. *J Neuropathol Exp Neurol*. 1974;33(2):308-332.

433. Choo YS, Johnson GVW, MacDonald M, Detloff PJ, Lesort M. Mutant huntingtin directly increases susceptibility of mitochondria to the calcium-induced permeability transition and cytochrome c release. *Hum Mol Genet*. 2004;13(14):1407-1420. doi:10.1093/hmg/ddh162

434. Song W, Chen J, Petrilli A, et al. Mutant huntingtin binds the mitochondrial fission GTPase dynamin-related protein-1 and increases its enzymatic activity. *Nat Med*. 2011;17(3):377-382. doi:10.1038/nm.2313

435. Brennan WA, Bird ED, Aprille JR. Regional Mitochondrial Respiratory Activity in Huntington's Disease Brain. *J Neurochem*. 1985;44(6):1948-1950. doi:10.1111/j.1471-4159.1985.tb07192.x

436. Gu M, Gash MT, Mann VM, Javoy-Agid F, Cooper JM, Schapira AHV. Mitochondrial defect in Huntington's disease caudate nucleus. *Ann Neurol*. 1996;39(3):385-389. doi:10.1002/ana.410390317

437. Browne SE, Bowling AC, MacGarvey U, et al. Oxidative damage and metabolic dysfunction in huntington's disease: Selective vulnerability of the basal ganglia. *Ann Neurol*. 1997;41(5):646-653. doi:10.1002/ana.410410514

438. Stephens DJ. De novo formation, fusion and fission of mammalian COPII-coated endoplasmic reticulum exit sites. *EMBO Rep*. 2003;4(2):210-217. doi:10.1038/sj.embor.embor736

439. Farhan H, Weiss M, Tani K, Kaufman RJ, Hauri HP. Adaptation of endoplasmic reticulum exit sites to acute and chronic increases in cargo load. *EMBO J*. 2008;27(15):2043-2054. doi:10.1038/emboj.2008.136

440. Vidal R, Caballero B, Couve A, Hetz C. Converging pathways in the occurrence of endoplasmic reticulum (ER) stress in Huntington's disease. *Curr Mol Med*. 2011;11(1):1-12. doi:10.2174/156652411794474419

441. Jiang R, Diaz-Castro B, Looger LL, Khakh BS. Dysfunctional Calcium and Glutamate Signaling in Striatal Astrocytes from Huntington's Disease Model Mice. *J Neurosci*. 2016;36(12):3453-3470. doi:10.1523/JNEUROSCI.3693-15.2016

442. Lee KS, Huh S, Lee S, et al. Altered ER-mitochondria contact impacts mitochondria calcium homeostasis and contributes to neurodegeneration in vivo in disease models. *Proc Natl Acad Sci U S A*. 2018;115(38):E8844-E8853. doi:10.1073/pnas.1815900115

443. Higo T, Hamada K, Hisatsune C, et al. Mechanism of ER Stress-Induced Brain Damage by IP(3) Receptor. *Neuron*. 2010;68(5):865-878. doi:10.1016/j.neuron.2010.11.010

444. Suopanki J, Götz C, Lutsch G, et al. Interaction of huntingtin fragments with brain membranes - Clues to early dysfunction in Huntington's disease. *J Neurochem*.

2006;96(3):870-884. doi:10.1111/j.1471-4159.2005.03620.x

445. Díaz-Hernández M, Moreno-Herrero F, Gómez-Ramos P, et al. Biochemical, ultrastructural, and reversibility studies on huntingtin filaments isolated from mouse and human brain. In: *Journal of Neuroscience*. Vol 24. ; 2004:9361-9371. doi:10.1523/JNEUROSCI.2365-04.2004

446. Peters MF, Nucifora FC, Kushi J, et al. Nuclear targeting of mutant huntingtin increases toxicity. *Mol Cell Neurosci*. 1999;14(2):121-128. doi:10.1006/mcne.1999.0773

447. Benn CL, Landles C, Li H, et al. Contribution of nuclear and extranuclear polyQ to neurological phenotypes in mouse models of Huntington's disease. *Hum Mol Genet*. 2005;14(20):3065-3078. doi:10.1093/hmg/ddi340

448. Greiner ER, Yang XW. Huntington's disease: Flipping a switch on huntingtin. *Nat Chem Biol*. 2011;7(7):412-414. doi:10.1038/nchembio.604

449. Michalek M, Salnikov ES, Werten S, Bechinger B. Membrane interactions of the amphipathic amino terminus of huntingtin. *Biochemistry*. 2013;52(5):847-858. doi:10.1021/bi301325q

450. Burke KA, Kauffman KJ, Umbaugh CS, Frey SL, Legleiter J. The interaction of polyglutamine peptides with lipid membranes is regulated by flanking sequences associated with huntingtin. *J Biol Chem*. 2013;288(21):14993-15005. doi:10.1074/jbc.M112.446237

451. Chaibva M, Gao X, Jain P, Campbell WA, Frey SL, Legleiter J. Sphingomyelin and GM1 Influence Huntingtin Binding to, Disruption of, and Aggregation on Lipid Membranes. *ACS Omega*. 2018;3(1):273-285. doi:10.1021/acsomega.7b01472

452. Lin HK, Boatz JC, Krabbendam IE, et al. Fibril polymorphism affects immobilized non-amyloid flanking domains of huntingtin exon1 rather than its polyglutamine core. *Nat Commun*. 2017;8:15462. doi:10.1038/ncomms15462

453. Bugg CW, Isas JM, Fischer T, Patterson PH, Langen R. Structural features and domain organization of huntingtin fibrils. *J Biol Chem*. 2012;287(38):31739-31746. doi:10.1074/jbc.M112.353839

454. Li L, Liu H, Dong P, et al. Real-time imaging of Huntingtin aggregates diverting target search and gene transcription. *Elife*. 2016;5:e17056. doi:10.7554/eLife.17056.001

455. Posey AE, Ruff KM, Harmon TS, et al. Profilin reduces aggregation and phase separation of huntingtin N-terminal fragments by preferentially binding to soluble monomers and oligomers. *J Biol Chem*. 2018;293(10):3734-3746. doi:10.1074/jbc.RA117.000357

456. Labbadia J, Morimoto RI. Huntington's disease: Underlying molecular mechanisms and emerging concepts. *Trends Biochem Sci*. 2013;38(8):378-385. doi:10.1016/j.tibs.2013.05.003

457. Schipper-Krom S, Juenemann K, Jansen AH, et al. Dynamic recruitment of active proteasomes into polyglutamine initiated inclusion bodies. *FEBS Lett*. 2014;588(1):151-159. doi:10.1016/j.febslet.2013.11.023

458. Huang ZN, Her LS. The Ubiquitin Receptor ADRM1 Modulates HAP40-Induced Proteasome Activity. *Mol Neurobiol*. 2017;54(9):7382-7400. doi:10.1007/s12035-016-0247-y

459. Hipp MS, Patel CN, Bersuker K, et al. Indirect inhibition of 26S proteasome activity in a cellular model of Huntington's disease. *J Cell Biol*. 2012;196(5):573-587.

doi:10.1083/jcb.201110093

460. Bennett EJ, Shaler TA, Woodman B, et al. Global changes to the ubiquitin system in Huntington's disease. *Nature*. 2007;448(7154):704-708. doi:10.1038/nature06022

461. Schipper-Krom S, Juenemann K, Reits EAJ. The ubiquitin-proteasome system in huntington's disease: Are proteasomes impaired, initiators of disease, or coming to the rescue? *Biochem Res Int*. 2012;2012:837015. doi:10.1155/2012/837015

462. Bansal M, Moharir SC, Swarup G. Autophagy receptor optineurin promotes autophagosome formation by potentiating LC3-II production and phagophore maturation. *Commun Integr Biol*. 2018;11(2):1-4. doi:10.1080/19420889.2018.1467189

463. N'Diaye EN, Debnath J, Brown EJ. Ubiquilins accelerate autophagosome maturation and promote cell survival during nutrient starvation. *Autophagy*. 2009;5(4):573-575. doi:10.4161/auto.5.4.8312

464. Baker B, Geng S, Chen K, et al. Alteration of lysosome fusion and low-grade inflammation mediated by super-low-dose endotoxin. *J Biol Chem*. 2015;290(10):6670-6678. doi:10.1074/jbc.M114.611442

465. Lu K, Psakhye I, Jentsch S. Autophagic clearance of PolyQ proteins mediated by ubiquitin-Atg8 adaptors of the conserved CUET protein family. *Cell*. 2014;158(3):549-563. doi:10.1016/j.cell.2014.05.048

466. Shimizu M, Oguro-Ando A, Ohoto-Fujita E, Atomi Y. *Toll-Interacting Protein Pathway: Degradation of an Ubiquitin-Binding Protein*. Vol 534. 1st ed. Elsevier Inc.; 2014. doi:10.1016/B978-0-12-397926-1.00018-4

467. Shen WC, Li HY, Chen GC, Chern Y, Tu PH. Mutations in the ubiquitin-binding domain of OPTN/optineurin interfere with autophagy- mediated degradation of misfolded proteins by a dominant-negative mechanism. *Autophagy*. 2015;11(4):685-700. doi:10.4161/auto.36098

468. Korac J, Schaeffer V, Kovacevic I, et al. Ubiquitin-independent function of optineurin in autophagic clearance of protein aggregates. *J Cell Sci*. 2013;126(Pt2):580-592. doi:10.1242/jcs.114926

469. Schwab C, Yu S, McGeer EG, McGeer PL. Optineurin in Huntington's disease intranuclear inclusions. *Neurosci Lett*. 2012;506(1):149-154. doi:10.1016/j.neulet.2011.10.070

470. Maruyama H, Kawakami H. Optineurin and amyotrophic lateral sclerosis. *Geriatr Gerontol Int*. 2013;13(3):528-532. doi:10.1111/ggi.12022

471. Deng Z, Purtell K, Lachance V, Wold MS, Chen S, Yue Z. Autophagy Receptors and Neurodegenerative Diseases. *Trends Cell Biol*. 2017;27(7):491-504. doi:10.1016/j.tcb.2017.01.001

472. Suhr ST, Senut MC, Whitelegge JP, Faull KF, Cuizon DB, Gage FH. Identities of sequestered proteins in aggregates from cells with induced polyglutamine expression. *J Cell Biol*. 2001;153(2):283-294. doi:10.1083/jcb.153.2.283

473. Kazantsev A, Preisinger E, Dranovsky A, Goldgaber D, Housman D. Insoluble detergent-resistant aggregates form between pathological and nonpathological lengths of polyglutamine in mammalian cells. *Proc Natl Acad Sci U S A*. 1999;96(20):11404-11409. doi:10.1073/pnas.96.20.11404

474. Hjerpe R, Bett JS, Keuss MJ, et al. UBQLN2 Mediates Autophagy-Independent Protein Aggregate Clearance by the Proteasome. *Cell*. 2016;166(4):935-949.

doi:10.1016/j.cell.2016.07.001

475. Liu KY, Shyu YC, Barbaro BA, et al. Disruption of the nuclear membrane by perinuclear inclusions of mutant huntingtin causes cell-cycle re-entry and striatal cell death in mouse and cell models of Huntington's disease. *Hum Mol Genet*. 2015;24(6):1602-1616. doi:10.1093/hmg/ddu574

476. Firdaus WJJ, Wyttenbach A, Giuliano P, Kretz-Remy C, Currie RW, Arrigo AP. Huntingtin inclusion bodies are iron-dependent centers of oxidative events. *FEBS J*. 2006;273(23):5428-5441. doi:10.1111/j.1742-4658.2006.05537.x

477. Cha JJ. Transcriptional dysregulation in Huntington ' s disease. *Trends Neurosci*. 2000:387-392.

478. Moumné L, Betuing S, Caboche J. Multiple Aspects of Gene Dysregulation in Huntington's Disease. *Front Neurol*. 2013;4(October):1-10. doi:10.3389/fneur.2013.00127

479. Valor L, Viosca J, Lopez-Atalaya J, Barco A. Lysine Acetyltransferases CBP and p300 as Therapeutic Targets in Cognitive and Neurodegenerative Disorders. *Curr Pharm Des*. 2013;19(28):5051-5064. doi:10.2174/13816128113199990382

480. Faber PW, Barnes GT, Srinidhi J, Chen J, Gusella JF, MacDonald ME. Huntingtin interacts with a family of WW domain proteins. *Hum Mol Genet*. 1998;7(9):1463-1474. doi:10.1093/hmg/7.9.1463

481. Gao YG, Yang H, Zhao J, Jiang YJ, Hu HY. Autoinhibitory structure of the WW domain of HYPB/SETD2 regulates its interaction with the proline-rich region of huntingtin. *Structure*. 2014;22(3):378-386. doi:10.1016/j.str.2013.12.005

482. Dunah AW, Jeong H, Griffin A, et al. Sp1 and TAFII130 transcriptional activity disrupted in early Huntington's disease. *Science (80-)*. 2002;296(5576):2238-2243. doi:10.1126/science.1072613

483. Yamanaka T, Miyazaki H, Oyama F, et al. Mutant Huntingtin reduces HSP70 expression through the sequestration of NF-Y transcription factor. *EMBO J*. 2008;27(6):827-839. doi:10.1038/emboj.2008.23

484. Holbert S, Denghien I, Kiechle T, et al. The Gln-Ala repeat transcriptional activator CA150 interacts with huntingtin: Neuropathologic and genetic evidence for a role in Huntington's disease pathogenesis. *Proc Natl Acad Sci U S A*. 2001;98(4):1811-1816. doi:10.1073/pnas.98.4.1811

485. Van Roon-Mom WMC, Reid SJ, Jones AL, MacDonald ME, Faull RLM, Snell RG. Insoluble TATA-binding protein accumulation in Huntington's disease cortex. *Mol Brain Res*. 2002;109(1-2):1-10. doi:10.1016/S0169-328X(02)00450-3

486. Hosp F, Gutiérrez-Ángel S, Schaefer MH, et al. Spatiotemporal Proteomic Profiling of Huntington's Disease Inclusions Reveals Widespread Loss of Protein Function. *Cell Rep*. 2017;21(8):2291-2303. doi:10.1016/j.celrep.2017.10.097

487. Rusten TE, Filimonenko M, Rodahl LM, Stenmark H, Simonsen A. ESCRTing autophagic clearance of aggregating proteins. *Autophagy*. 2008;4(2):233-236. doi:10.4161/auto.5396

488. Kopito RR. Aggresomes, inclusion bodies and protein aggregation. *Trends Cell Biol*. 2000;10(12):524-530. doi:10.1016/S0962-8924(00)01852-3

489. Bossy-Wetzel E, Petrilli A, Knott AB. Mutant Huntintin and Mitochondrial Dysfunction. *Trends Neurosci*. 2008;31(12):609-616. doi:10.1016/j.tins.2008.09.004.MUTANT

490. Manczak M, P. Hemachandra R. Mitochondrial division inhibitor 1 protects against mutant huntingtin-induced abnormal mitochondrial dynamics and neuronal damage in Huntington's disease. *Hum Mol Genet*. 2015;24(25):7308-7325. doi:10.1093/hmg/ddv429

491. Yin X, Manczak M, Reddy PH. Mitochondria-targeted molecules MitoQ and SS31 reduce mutant huntingtin-induced mitochondrial toxicity and synaptic damage in Huntington's disease. *Hum Mol Genet*. 2016;25(9):1739-1753. doi:10.1093/hmg/ddw045

492. Ugalde CL, Annesley SJ, Gordon SE, et al. Misfolded α-synuclein causes hyperactive respiration without functional deficit in live neuroblastoma cells. *Dis Model Mech*. 2020;13(1):dmm040899. doi:10.1242/dmm.040899

493. Horn A, Raavicharla S, Shah S, Cox D, Jaiswal JK. Mitochondrial fragmentation enables localized signaling required for cell repair. *J Cell Biol*. 2020;219(5):e201909154. doi:10.1083/jcb.201909154

494. Jordan M, Schallhorn A, Wurm FM, Francisco SS. Transfecting mammalian cells : optimization of critical parameters affecting calcium-phosphate precipitate formation. *Nucleic Acids Res*. 1996;24(4):596-601.

495. Dorin-Semblat D, Demarta-Gatsi C, Hamelin R, et al. Malaria parasite-infected erythrocytes secrete PfCK1, the Plasmodium homologue of the pleiotropic protein kinase casein kinase 1. *PLoS One*. 2015;10(12):1-22. doi:10.1371/journal.pone.0139591

496. Rappsilber J, Mann M, Ishihama Y. Protocol for micro-purification, enrichment, pre-fractionation and storage of peptides for proteomics using StageTips. *Nat Protoc*. 2007;2(8):1896-1906. doi:10.1038/nprot.2007.261

497. Cox J, Mann M. MaxQuant enables high peptide identification rates, individualized p.p.b.-range mass accuracies and proteome-wide protein quantification. *Nat Biotechnol*. 2008;26(12):1367-1372. doi:10.1038/nbt.1511

498. Cox J, Hein MY, Luber CA, Paron I, Nagaraj N, Mann M. Accurate proteome-wide label-free quantification by delayed normalization and maximal peptide ratio extraction, termed MaxLFQ. *Mol Cell Proteomics*. 2014;13(9):2513-2526. doi:10.1074/mcp.M113.031591

499. Tyanova S, Temu T, Sinitcyn P, et al. The Perseus computational platform for comprehensive analysis of (prote)omics data. *Nat Methods*. 2016;13(9):731-740. doi:10.1038/nmeth.3901

500. Hubner NC, Bird AW, Cox J, et al. Quantitative proteomics combined with BAC TransgeneOmics reveals in vivo protein interactions. *J Cell Biol*. 2010;189(4):739-754. doi:10.1083/jcb.200911091

501. Makrecka-Kuka M, Krumschnabel G, Gnaiger E. High-resolution respirometry for simultaneous measurement of oxygen and hydrogen peroxide fluxes in permeabilized cells, tissue homogenate and isolated mitochondria. *Biomolecules*. 2015;5(3):1319-1338. doi:10.3390/biom5031319

502. Pesta D, Gnaiger E. High-Resolution Respirometry: OXPHOS Protocols for Human Cells and Permeabilized Fibers from Small Biopsies of Human Muscle BT - Mitochondrial Bioenergetics: Methods and Protocols. In: Palmeira CM, Moreno AJ, eds. Totowa, NJ: Humana Press; 2012:25-58. doi:10.1007/978-1-61779-382-0_3

503. Burtscher J, Zangrandi L, Schwarzer C, Gnaiger E. Differences in mitochondrial function

in homogenated samples from healthy and epileptic specific brain tissues revealed by high-resolution respirometry. *Mitochondrion*. 2015;25:104-112. doi:10.1016/j.mito.2015.10.007

504. Ramdzan YM, Trubetskov MM, Ormsby AR, et al. Huntingtin Inclusions Trigger Cellular Quiescence, Deactivate Apoptosis, and Lead to Delayed Necrosis. *Cell Rep*. 2017;19(5):919-927. doi:10.1016/j.celrep.2017.04.029

505. Ylä-Anttila P, Gupta S, Masucci MG. The Epstein-Barr virus deubiquitinase BPLF1 targets SQSTM1/p62 to inhibit selective autophagy. *Autophagy*. 2021;00(00):1-15. doi:10.1080/15548627.2021.1874660

506. Sun Y, Jiang X, Pan R, et al. Escins Isolated from Aesculus chinensis Bge. Promote the Autophagic Degradation of Mutant Huntingtin and Inhibit its Induced Apoptosis in HT22 cells. *Front Pharmacol*. 2020;11(February):1-20. doi:10.3389/fphar.2020.00116

507. Goold R, Flower M, Moss DH, et al. FAN1 modifies Huntington's disease progression by stabilizing the expanded HTT CAG repeat. *Hum Mol Genet*. 2019;28(4):650-661. doi:10.1093/hmg/ddy375

508. Mehta SR, Tom CM, Wang Y, et al. Human Huntington's Disease iPSC-Derived Cortical Neurons Display Altered Transcriptomics, Morphology, and Maturation. *Cell Rep*. 2018;25(4):1081-1096.e6. doi:10.1016/j.celrep.2018.09.076

509. Carnemolla A, Michelazzi S, Agostoni E. PIN1 modulates huntingtin levels and aggregate accumulation: An in vitro model. *Front Cell Neurosci*. 2017;11(May):1-12. doi:10.3389/fncel.2017.00121

510. Schilling G, Becher MW, Sharp AH, et al. Intranuclear inclusions and neuritic aggregates in transgenic mice expressing a mutant N-terminal fragment of huntingtin. *Hum Mol Genet*. 1999;8(3):397-407. doi:10.1093/hmg/8.3.397

511. O'Brien R, DeGiacomo F, Holcomb J, et al. Integration-independent transgenic huntington disease fragment mouse models reveal distinct phenotypes and life span in vivo. *J Biol Chem*. 2015;290(31):19287-19306. doi:10.1074/jbc.M114.623561

512. Gasset-Rosa F, Chillon-Marinas C, Goginashvili A, et al. Polyglutamine-Expanded Huntingtin Exacerbates Age-Related Disruption of Nuclear Integrity and Nucleocytoplasmic Transport. *Neuron*. 2017;94(1):48-57.e4. doi:10.1016/j.neuron.2017.03.027

513. Maiuri T, Hung CLK, Suart C, et al. DNA Repair in Huntington's Disease and Spinocerebellar Ataxias: Somatic Instability and Alternative Hypotheses. *J Huntingtons Dis*. 2021;10(1):165-173. doi:10.3233/JHD-200414

514. Sap KA, Guler AT, Bezstarosti K, et al. Global proteome and ubiquitinome changes in the soluble and insoluble fractions of Q175 huntington mice brains. *Mol Cell Proteomics*. 2019;18(9):1705-1720. doi:10.1074/mcp.RA119.001486

515. Hodges A, Hughes G, Brooks S, et al. Brain gene expression correlates with changes in behavior in the R6/1 mouse model of Huntington's disease. *Genes, Brain Behav*. 2008;7(3):288-299. doi:10.1111/j.1601-183X.2007.00350.x

516. Christodoulou CC, Zachariou M, Tomazou M, et al. Investigating the transition of pre-symptomatic to symptomatic huntington's disease status based on omics data. *Int J Mol Sci*. 2020;21(19):7414. doi:10.3390/ijms21197414

517. Safren N, Chang L, Dziki KM, Monteiro MJ. Signature changes in ubiquilin expression in the R6/2 mouse model of Huntington's disease. *Brain Res*. 2015;1597:37-46. doi:10.1016/j.brainres.2014.12.008

518. Safren N, El Ayadi A, Chang L, et al. Ubiquilin-1 overexpression increases the lifespan and delays accumulation of huntingtin aggregates in the R6/2 mouse model of Huntington's disease. *PLoS One*. 2014;9(1):e87513. doi:10.1371/journal.pone.0087513

519. Sticker A, Goeminne L, Martens L, Clement L. Robust summarization and inference in proteome-wide label-free quantification. *Mol Cell Proteomics*. 2020;19(7):1209-1219. doi:10.1074/mcp.RA119.001624

520. Wear MP, Kryndushkin D, O'Meally R, Sonnenberg JL, Cole RN, Shewmaker FP. Proteins with intrinsically disordered domains are preferentially recruited to polyglutamine aggregates. *PLoS One*. 2015;10(8):e0136362. doi:10.1371/journal.pone.0136362

521. Mizukami K, Abrahamson EE, Mi Z, et al. Immunohistochemical analysis of ubiquilin-1 in the human hippocampus: Association with neurofibrillary tangle pathology. *Neuropathology*. 2014;34(1):11-18. doi:10.1111/neup.12055

522. Dil Kuazi A, Kito K, Abe Y, Shin RW, Kamitani T, Ueda N. NEDD8 protein is involved in ubiquitinated inclusion bodies. *J Pathol*. 2003;199(2):259-266. doi:10.1002/path.1283

523. Mori F, Nishie M, Piao YS, et al. Accumulation of NEDD8 in neuronal and glial inclusions of neurodegenerative disorders. *Neuropathol Appl Neurobiol*. 2005;31(1):53-61. doi:10.1111/j.1365-2990.2004.00603.x

524. Maghames CM, Lobato-Gil S, Perrin A, et al. NEDDylation promotes nuclear protein aggregation and protects the Ubiquitin Proteasome System upon proteotoxic stress. *Nat Commun*. 2018;9(1):4376. doi:10.1038/s41467-018-06365-0

525. Petrasch-Parwez E, Nguyen H, Löbbecke-Schumacher, Habbes H, et al. Cellular and subcellular localization of Huntingtin aggregates in the brain of a rat transgenic for Huntington disease. *J Comp Neurol*. 2007;501(5):716-730. doi:10.1002/cne

526. Ya Zhou, Peskett TR, Landles C, et al. Correlative light and electron microscopy reveals that mutant huntingtin dysregulates the endolysosomal pathway in presymptomatic Huntington's disease. *J Chem Inf Model*. 2021.

527. Culver BP, DeClercq J, Dolgalev I, et al. Huntington's Disease Protein Huntingtin Associates with its own mRNA. *J Huntingtons Dis*. 2016;5(1):39-51. doi:10.3233/JHD-150177

528. Bowles KR, Stone T, Holmans P, Allen ND, Dunnett SB, Jones L. SMAD transcription factors are altered in cell models of HD and regulate HTT expression. *Cell Signal*. 2017;31:1-14. doi:10.1016/j.cellsig.2016.12.005

529. Feyeux M, Bourgois-Rocha F, Redfern A, et al. Early transcriptional changes linked to naturally occurring Huntington's disease mutations in neural derivatives of human embryonic stem cells. *Hum Mol Genet*. 2012;21(17):3883-3895. doi:10.1093/hmg/dds216

530. Borovecki F, Lovrecic L, Zhou J, et al. Genome-wide expression profiling of human blood reveals biomarkers for Huntington's disease. *Proc Natl Acad Sci U S A*. 2005;102(31):11023-11028. doi:10.1073/pnas.0504921102

531. Runne H, Kuhn A, Wild EJ, et al. Analysis of potential transcriptomic biomarkers for Huntington's disease in peripheral blood. *Proc Natl Acad Sci U S A*. 2007;104(36):14424-14429. doi:10.1073/pnas.0703652104

532. Mastrokolias A, Ariyurek Y, Goeman JJ, et al. Huntington's disease biomarker progression profile identified by transcriptome sequencing in peripheral blood. *Eur J Hum Genet*. 2015;23(10):1349-1356. doi:10.1038/ejhg.2014.281

533. Petrasch-Parwez E, Nguyen H-P, Löbbecke-Schumacher M, et al. Cellular and Subcellular Localization of Huntington Aggregates in the Brain of a Rat Transgenic for Huntington Disease. *J Comp Neurol*. 2007;501(October 2007):716-730. doi:10.1002/cne

534. Barde I, Salmon P, Trono D. Production and Titration of Lentiviral Vectors. *Curr Protoc Neurosci*. 2010:1-23. doi:10.1002/0471142301.ns0421s53

535. Steiner P, Floyd Sarria JC, Glauser L, Magnin S, Catsicas S, Hirling H. Modulation of receptor cycling by neuron-enriched endosomal protein of 21 kD. *J Cell Biol*. 2002;157(7):1197-1209. doi:10.1083/jcb.200202022

536. Mahul-Mellier AL, Fauvet B, Gysbers A, et al. C-Abl phosphorylates α-synuclein and regulates its degradation: Implication for α-synuclein clearance and contribution to the pathogenesis of parkinson's disease. *Hum Mol Genet*. 2014;23(11):2858-2879. doi:10.1093/hmg/ddt674

537. Chen M, Dai W, Sun SY, et al. Convolutional neural networks for automated annotation of cellular cryo-electron tomograms. *Nat Methods*. 2017;14(10):983-985. doi:10.1038/nmeth.4405

538. Kremer JR, Mastronarde DN, McIntosh JR. Computer visualization of three-dimensional image data using IMOD. *J Struct Biol*. 1996;116(1):71-76. doi:10.1006/jsbi.1996.0013

539. Pettersen EF, Goddard TD, Huang CC, et al. UCSF Chimera - A visualization system for exploratory research and analysis. *J Comput Chem*. 2004;25(13):1605-1612. doi:10.1002/jcc.20084

540. CoreTeam R. *R: A Language and Environment for Statistical Computing.* Vol 2.; 2019.

541. Gavrieli Y, Sherman Y, Ben-Sasson SA. Identification of programmed cell death in situ via specific labeling of nuclear DNA fragmentation. *J Cell Biol*. 1992;119(3):493-501. doi:10.1083/jcb.119.3.493

542. Yang W, Dunlap JR, Andrews RB, Wetzel R. Aggregated polyglutamine peptides delivered to nuclei are toxic to mammalian cells. *Hum Mol Genet*. 2002;11(23):2905-2917. doi:10.1093/hmg/11.23.2905

Curriculum Vitae

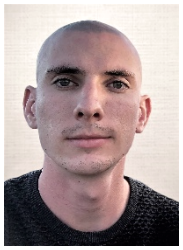

NATHAN RIGUET

Address: Route de Chavannes 66, 1007 Lausanne, Switzerland
Phone: +41 78 402 65 19 || **Email:** nathanriguet@gmail.com

PROFILE

Motivated Neurosciences doctorate student with strong interest in Health and Life Sciences, specialized in neurodegenerative diseases.
Solid theoretical and practical expertise in cell biology, primary neurons and related analytical techniques from image-based to biochemical characterizations. Robust experience in confocal microscopy, live imaging, electron microscopy and biochemistry, along with mass spectrometry-based proteomics data analysis and statistics.
Dynamic, fast learning, adaptable person and team-worker.

EDUCATION

ECOLE POLYTECHNIQUE FÉDÉRALE DE LAUSANNE (EPFL), LAUSANNE, SWITZERLAND
Ph.D. in NEUROSCIENCES| 09/2017 – Present
PhD Thesis: "An integrative approach to elucidate the mechanisms and dynamics of Huntingtin aggregation and inclusion formation in neuronal models of Huntington's Disease"
EPFL PhD Program in Neuroscience (EDNE).

ÉCOLE SUPÉRIEURE DE PHYSIQUE ET DE CHIMIE INDUSTRIELLES DE LA VILLE DE PARIS (ESPCI) AND PARIS DESCARTES UNIVERSITY, PARIS, FRANCE
MASTER OF SCIENCE (2nd Year) Bioengineering and Innovation in Neurosciences (BIN) | 09/2016 – 07/2017

DIDEROT AND DESCARTES UNIVERSITIES, PARIS, FRANCE
MASTER OF SCIENCE (1st Year) Cellular biology, physiology and pathology - Neurosciences| 09/2015 – 06/2016

ASTON UNIVERSITY, BIRMINGHAM, ENGLAND
BACHELOR OF SCIENCE (Final year) Biological science and Human biology | 09/2014 – 06/2015

UNIVERSITY RENNES II, RENNES, FRANCE
BACHELOR OF SCIENCE (1st, and 2nd years) Molecular and cellular science and Human biology | 09/2012 – 06/2014

EXPERIENCE

ÉCOLE POLYTECHNIQUE FÉDÉRALE DE LAUSANNE (EPFL), LAUSANNE, SWITZERLAND
Teaching assistant: Physiology practicals to 3rd year Bachelor students| 2018 – 2020
Supervision of bachelor projects: Dynamic analysis of Huntingtin aggregation and inclusion formation| 2018
Development of neuronal models of HD aggregation based on the Human pathology| 2021
MSc Thesis: Nt17 domain controls Huntingtin-exon1 localization and aggregation in cells (Lashuel lab) | 2017

HOPITAL ROBERT DEBRÉ – INSERM UMR1141, PARIS, FRANCE
Internship: "Study of physiopathology of tauopathies in zebrafish model" Supervised by Dr. Nadia Soussi-Yanicostas | 2016

ASTON UNIVERSITY, BIRMINGHAM, ENGLAND
BSc Thesis: "Determining the effects of Nicotinamide mononucleotide in the protection of neuronal cells from oxidative stress" Supervised by Dr. Eric Hill | 2015

SCA SOCIETY, LE THEIL SUR HUISNE, FRANCE
Quality Agent: laboratory service (Sampling, testing, control, data entry, reporting) | Summers 2012 to 2015

PUBLICATIONS

ORIGINAL RESEARCH ARTICLES

- **Nathan Riguet**, Anne-Laure Mahul-Mellier, Niran Maharjan, Johannes Burtscher, Alice Patin, Marie Croisier, Graham Knott and Hilal A. Lashuel. Disentangling the sequence, cellular and ultrastructural determinants of Huntingtin nuclear and cytoplasmic inclusion formation. Published in **Nature Communications. Doi:** 10.1038/s41467-021-26684-z

- Sophie Vieweg, Anne-Laure Mahul-Mellier, Francesco S. Ruggeri, **Nathan Riguet**, Sean M. DeGuire, Anass Chiki, Urszula Cendrowska, Giovanni Dietler, Hilal A. Lashuel. Towards deciphering the Nt17 code: How the sequence and conformation of the first 17 amino acids in Huntingtin regulate the aggregation, cellular properties and neurotoxicity of mutant Httex1. Published in **Journal of Molecular Biology. Doi:** 10.1016/j.jmb.2021.167222

- Julian C. Shillcock, Janna Hastings, **Nathan Riguet**, Hilal A. Lashuel. Non-monotonic fibril surface occlusion by GFP tags from coarse-grained molecular simulations. Published in **Computational and Structural Biotechnology Journal**. Doi: 10.1016/j.csbj.2021.12.017

- Bryan Frey, Abdelrahman AlOkda, Matthew. P. Jackson, **Nathan Riguet**, James A. Duce and Hilal A. Lashuel. Monitoring alpha-synuclein oligomerization and aggregation using bimolecular fluorescence complementation assays: what you see is not always what you get. Published in **Journal of Neurochemistry**. Doi: 10.1111/jnc.15275

CONFERENCES PROCEEDINGS

- **Nathan Riguet** *et al.* Mechanisms of inclusion formation in Huntington's disease: Lessons from cellular models. February 2021 – BMI Progress report, EPFL (Switzerland)

- **Nathan Riguet** *et al.* Deciphering the complexity and ultrastructure properties of Huntingtin exon 1 inclusions and their impact on cellular organelles using Correlative Light and Electron Microscopy (CLEM). **March 2020** - CIME day, EPFL (Switzerland) - **Best poster award**

- **Nathan Riguet** *et al.* Correlative light electron microscopy (CLEM) studies provide new insight into the architecture and structural properties of Htt inclusions and their impact on cellular organelles. **February 2019** - CHDI conference, Palm springs (USA)
  May 2019 - Meeting of the Neuroleman network and doctoral schools, Les Diablerets (Switzerland)

SELECTED COURSES AND FORMATION

- Advanced Microscopy for Life Science
- Image Processing for Life Science
- Understanding statistics and experimental design
- Data management (certificate), Wordpress base
- Safety in P2
- Expérimentation Animale - Module 1 (Valid certification)

SKILLS/ QUALIFICATIONS

TECHNICAL/ ANALYTICAL SKILLS

Cellular Biology

- Preparation of primary cultures (dissection of brain pups), mamalian cell lines, transfection, lentivirus production and infection, protein and fibril treatments, immunoprecipitation, immunocitochemistry

Molecular Biology

- Transformation, plasmid purification, amplification, cloning, analysis of sequenced products, PCR mutagenesis

Imaging

- Light microscopy: confocal, live cell imaging, Superesolution (PALM)
  Electron microscopy: Correlative light electron microscopy (CLEM), EM grid preparation (negative stain and imaging (Techicai Spirit 80kv)

Biochemical analysis

- Detergent fractionation of cellular, animal and Human samples, western blotting, filter trap, Coomassie

SOFTWARE'S/ BIOINFORMATICS TOOLS

- Proficient in Microsoft Office Word, Excel, PowerPoint, GraphPad
- Image analysis: Fiji, Zen and LASX softwares (Zeiss and Leica), photoshop, Blender
- Bioinformatic tools for proteomic analysis (Byonic, Scaffold, Cytoscape, DAVID and STRING analysis)
- Webmanager: wordpress

LANGUAGES

- French (native)
- English (fluent)

COMMUNICATION SKILLS

- Excellent oral and written communication.
- Easy adaptation face to new situations.
- Ability to effectively communicate with specialists from different fields.
- Collaboration with leading researchers in Engineering, Pathologists, Chemistry and Bioinformatic.
- Able to work independently and within a team.

HOBBIES

- Sports (Basketball, Tennis, hiking)
- Travelling
- Committee member of the Defi Parkinson association (https://www.defi-parkinson.ch/)